The Emission and Atmospheric Oxidation of Biogenic Volatile Organic Compounds from Sitka Spruce

A thesis submitted to

THE NATIONAL UNIVERSITY OF IRELAND, CORK

for the degree of

DOCTOR OF PHILOSOPHY

by

Hayley Furnell

Based on research carried out at

School of Chemistry

&

Environmental Research Institute

Supervisor: *Prof. John Wenger*

Head of School: *Prof. Anita McGuire*

University College Cork October 2023

Table of Contents

Declaration

This is to certify that the work I am submitting is my own and has not been submitted for another degree, either at University College Cork or elsewhere. All external references and sources are clearly acknowledged and identified within the contents. I have read and understood the regulations of University College Cork concerning plagiarism and intellectual property.

Hayley Furnell

Acknowledgements

I would like to thank my supervisor Prof. John Wenger for his guidance, advice and support over the last few years. I also want to express my immense gratitude to Julien Kammer for all the time he has spent teaching and helping me throughout this PhD.

I would like to thank Astrid Wingler for all her advice, and for providing me with equipment I would not have otherwise had access to. I would like to thank the group at Teagasc Food Research Centre, Kieran Kilcawley, David Mannion and particularly Iwona Skibinska, for accommodating the analysis of my samples. I would like to thank Fermoy Woodland Nurseries for supplying the Sitka spruce trees.

I would like to thank the members of CRAC who helped me along the way, particularly Dean Venables for the use of his laboratory, Niall O'Sullivan for his help operating the ToF-CIMS and the ERI chamber, and Satheesh Chandran and Mixtli Campos for their help running experiments in IASC.

I would like to thank my Granny for accommodating me for the duration of my time at UCC, and my cousin Sara Leacy for all her advice.

I would like to thank Don Mahon and Natalie Tate for their support, understanding, enthusiasm and belief in everything I do.

Dedication

For my Grandparents

Abstract

Biogenic volatile organic compounds (BVOCs) emitted by plants undergo chemical reactions in the atmosphere resulting in the formation of oxidised products and secondary organic aerosols (SOA), which have a large impact on climate. In this work an on-line time-of-flight chemical ionisation mass spectrometer (ToF-CIMS) was used in laboratory studies to identify the main BVOCs emitted from the main plantation tree species in Ireland, *Picea Sitchensis* (Sitka spruce). Experiments have also been conducted to assess the atmospheric oxidation pathways of the BVOCs emitted by Sitka spruce and their SOA formation potential.

The ToF-CIMS was used in combination with off-line gas chromatography-mass spectrometry to identify the BVOC emissions from three Sitka spruce trees maintained in a plant growth chamber under conditions relevant to the Irish climate. Fifty-two of the seventy-four BVOCs emitted from Sitka spruce were oxygenated compounds, with piperitone ($C_{10}H_{16}O$), an oxygenated monoterpene, being the dominant emission. Other prevalent emissions included isoprene and five monoterpenes (myrcene, β-phellandrene, δ-limonene, α-pinene, and camphene). Temperature, light intensity and stress were all found to alter the emission profiles, with different BVOCs exhibiting different responses. At the current conditions of the Irish climate the annual BVOC flux for isoprene was found to exceed that for piperitone, although this is expected to change in a warming climate.

A series of simulation chamber experiments was performed to determine, for the first time, the kinetics, products and mechanisms for the gas-phase reaction of piperitone with the main atmospheric oxidant the hydroxyl radical ($OH^{\bullet}$). The rate coefficient was determined by the relative rate method and used to calculate an atmospheric lifetime of under 2 hours. Calculations based on structure activity relationships identified the reaction with $OH^{\bullet}$ as the dominant loss pathway for piperitone and was used to identify its most reactive sites. The ToF-CIMS detected thirty-three gas-phase oxidation products, and formation mechanisms for seventeen

of the products have been proposed. The results from these experiments provide new and useful information on the atmospheric fate of piperitone.

Oxidation experiments were also conducted with $OH^{\bullet}$ on all the BVOCs emitted by a Sitka spruce tree, to identify oxidation products, reaction pathways and determine the SOA formation potential of whole Sitka spruce BVOC emissions. Eight gas-phase BVOCs were identified as key reactive emissions, and upon reaction with $OH^{\bullet}$ led to the formation of twenty-five gas-phase products and ninety-nine particle-phase products. Eight of these products were identified as originating from the oxidation of piperitone, myrcene and isoprene across the gas-phase and particle-phase, with the majority of the remining products resulting from oligomerisation reactions. Rapid SOA formation was observed soon after the onset of oxidation, likely due to the formation of low volatility oxidation products which caused new particle formation. SOA yields were estimated to be around 15%.

Overall, this work has produced a wealth of new information on the emission and atmospheric oxidation of BVOCs emitted from Sitka spruce, which will be valuable to decision makers in the forestry sector. Moreover, the research highlights the importance of assessing BVOC emissions and the associated SOA formation potential prior to establishing tree plantations.

Chapter 1 Introduction

1.1 Earth's Atmosphere

The atmosphere is the body of air surrounding the Earth, and is held in place by gravity[1]. Neglecting water vapour, the atmosphere is composed of approximately 78% molecular nitrogen (N_2), 21% molecular oxygen (O_2) and 1% argon (Ar), with a minority attributed to trace gases. The atmosphere extends from ground level and experiences a decrease in pressure with increasing altitude, with no defined boundary between the atmosphere and outer space. The atmosphere is divided into five layers; exosphere, thermosphere, mesosphere, stratosphere and troposphere. Each layer is characterised by temperature, altitude and pressure[2], with distinct boundaries between the layers, Figure 1.1.

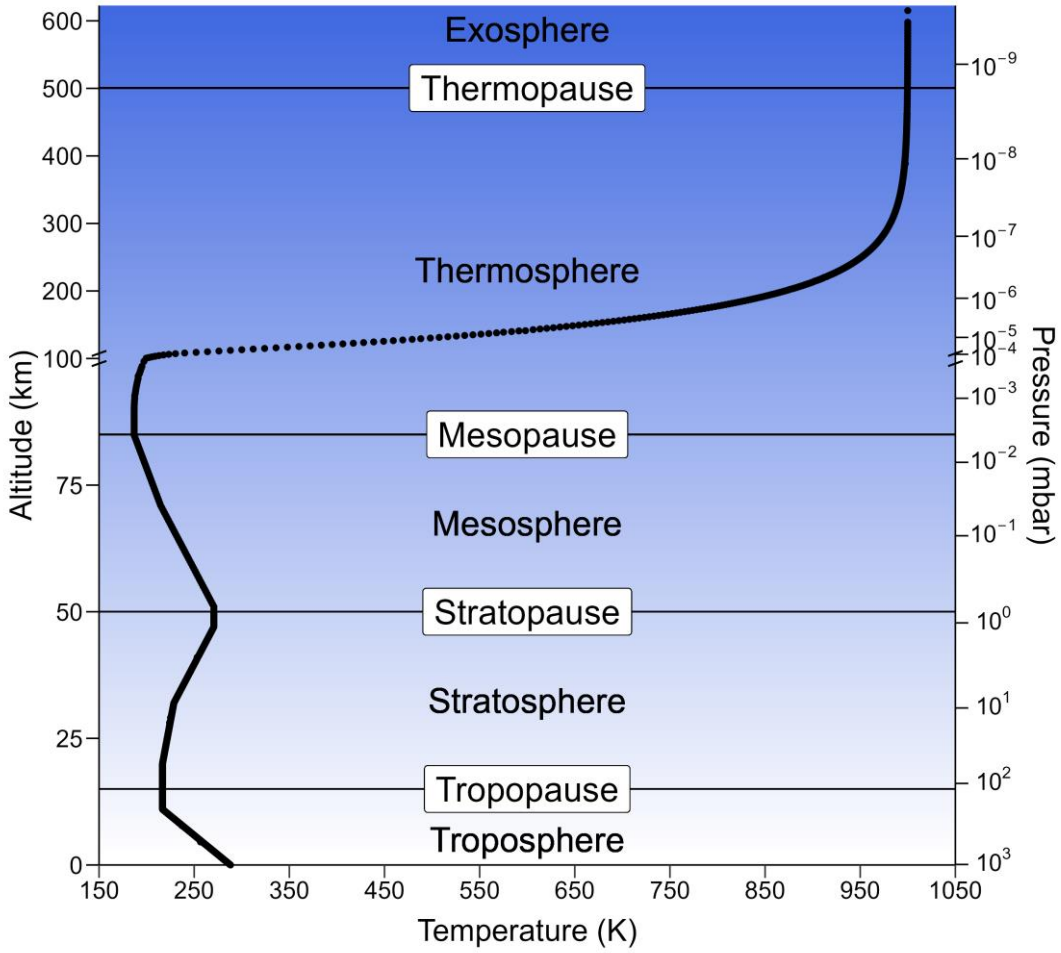

Figure 1.1 *Layers of the Earth's atmosphere showing altitude, pressure and temperature. Data taken from US Standard Atmosphere, 1976[3].*

The furthest atmospheric layer from the Earth's surface is the exosphere. The thermopause, at an altitude of 500 km, marks the lower boundary of the exosphere which extends upwards. The density of the exosphere is very low and similar to a vacuum, making it the thinnest of the atmospheric layers[2]. It is composed primarily of N_2, O_2 and carbon dioxide (CO_2). The temperature in the exosphere is over 1000 K, and is relatively constant throughout[1].

The thermosphere is located between the mesopause at an altitude of 85 km, and the thermopause at 500 km. The absorption of solar radiation at wavelengths below 200 nm by N_2 and O_2, causes the temperature in the thermosphere to increase with increasing altitude. The pressure at the base of the thermosphere is approximately 10^{-3} mbar, making it slightly denser than the exosphere[1, 2, 4].

The mesosphere extends from the stratopause at 50 km to the mesopause at 85 km. Pressure ranges from approximately 1 mbar to 10^{-3} mbar in the mesosphere. The temperature in the mesosphere decreases with increasing altitude. At approximately 188 K, the mesopause is the coldest part of the atmosphere[1, 2].

At an altitude of 15 km the tropopause marks the lower boundary for the stratosphere. The pressure in the stratosphere ranges between 10^2 mbar at the tropopause and 1 mbar at the stratopause. The stratosphere is characterised by a high concentration of ozone (O_3), which absorbs solar radiation to undergo photodissociation. The excess energy following absorption is released as heat, and leads to an increase in temperature which increases with altitude in the stratosphere[1, 2, 4].

The troposphere is the lowest atmospheric layer, and is composed of two separate layers, the boundary layer and the free troposphere. The troposphere extends from the Earth's surface to the tropopause at 15 km, and experiences a decrease in temperature with increasing altitude. The troposphere is the most dense of the atmospheric layers, and contains approximately 80% of the mass of the atmosphere. The composition of the troposphere is significantly more diverse than the

compositions of the other atmospheric layers. The troposphere contains all emissions from the Earth's surface and almost all of the water vapour in the atmosphere. The interactions between the various entities in the troposphere, including gases, aerosols and particles, determine the weather and climate at the Earth's surface[1, 2, 4].

1.2 Volatile Organic Compounds

Volatile organic compounds (VOCs) are compounds that are predominantly found in the gas-phase at ambient temperatures[5]. VOCs are composed mainly of carbon and hydrogen and may contain other elements including oxygen, nitrogen, sulphur, and halogens. They are emitted from a wide range of natural (biogenic) and man-made (anthropogenic) sources. The major biogenic sources of VOCs include plants[6] and oceans[7], while the dominant anthropogenic sources are fossil fuel burning[8] and solvent use[5]. The emission of VOCs from biogenic sources far exceeds the emission from anthropogenic sources[9], accounting for approximately 90% of VOCs emitted on a global basis[10, 11].

Once emitted into the atmosphere VOCs can have impacts on human health[12] and climate. Several VOCs are known to be toxic[13], with some compounds such as benzene and its derivatives, classed as carcinogenic[14] and mutagenic[15]. The oxidation of VOCs can lead to the formation of tropospheric O_3, which also has negative health impacts at high concentrations, aggravating conditions such as chronic pulmonary heart disease and asthma[16, 17]. VOCs indirectly impact climate through the formation of secondary organic aerosols (SOA)[18, 19], and by reducing the oxidant concentration available to react with the major greenhouse gas methane, prolonging its atmospheric lifetime[6] and contributing to global warming.

1.3 Oxidants

The dominant atmospheric oxidants are the hydroxyl radical ($OH^{\bullet}$), O_3 and the nitrate radical ($NO_3^{\bullet}$), which along with photolysis are responsible for initiating the atmospheric oxidation of VOCs. These oxidants are produced from a variety of natural and man-made sources.

$OH^{\bullet}$ is the dominant day time oxidant[20], and largely controls the oxidation capacity of the atmosphere. The main source of $OH^{\bullet}$ is the photolysis of O_3, at wavelengths below 320 nm[21] leading to the formation of O_2 and an oxygen radical, $^{\bullet}O(^1D)$[22] (Reaction 1.1), which can subsequently react with water vapour (H_2O) to produce two $OH^{\bullet}$ (Reaction 1.2).

$$O_3 \xrightarrow[< 320\ nm]{h\nu} O_2 + \dot{O}(^1D) \qquad \textbf{Reaction 1.1}$$

$$\dot{O}(^1D) + H_2O \longrightarrow \dot{O}H + \dot{O}H \qquad \textbf{Reaction 1.2}$$

Other minor sources of $OH^{\bullet}$ include the photolysis of nitrous acid (HONO) at wavelengths less than 400 nm[21, 23], producing $OH^{\bullet}$ and $NO^{\bullet}$ (Reaction 1.3);

$$HONO \xrightarrow[< 400\ nm]{h\nu} \dot{O}H + N\dot{O} \qquad \textbf{Reaction 1.3}$$

and the photolysis of formaldehyde (HCHO) at wavelengths below 330 nm producing $HO_2^{\bullet}$ (Reaction 1.4), which reacts with either O_3 (Reaction 1.5) or $NO^{\bullet}$ (Reaction 1.6), depending on ambient conditions[22, 24, 25].

$$HCHO \xrightarrow[< 330\ nm]{h\nu} \dot{H} + H\dot{C}OH \qquad \textbf{Reaction 1.4}$$

$$H\dot{O}_2 + O_3 \longrightarrow 2O_2 + \dot{O}H \qquad \textbf{Reaction 1.5}$$

$$H\dot{O}_2 + N\dot{O} \longrightarrow NO_2 + \dot{O}H \qquad \textbf{Reaction 1.6}$$

The oxidation of VOCs by $OH^{\bullet}$ in polluted air masses generates appreciable amounts of $HO_2^{\bullet}$, which readily reacts with $NO^{\bullet}$, thereby $OH^{\bullet}$ is regenerated[22]. Finally $OH^{\bullet}$ is also produced as a by product from the ozonolysis of alkenes[22, 26], which is the only non-photolytic source of $OH^{\bullet}$.

The ambient $OH^{\bullet}$ concentration depends on several factors including the time of day and location, with 1.6×10^6 molecules cm^{-3} estimated to be the global 12-hour average $OH^{\bullet}$ concentration[27]. The $OH^{\bullet}$ concentration follows a diurnal pattern which peaks at noon[23]. Around the world, $OH^{\bullet}$ concentrations are highest at the tropics, due to high solar irradiance and high water vapour concentrations[7, 28].

O_3 can be produced in the presence of sunlight, as well as in the dark. During the day the formation of ground level O_3 is initiated through the photolysis of nitrogen dioxide, (NO_2), Reaction 1.7.

$$NO_2 \xrightarrow[< 420\ nm]{h\nu} \dot{O}(^3P) + N\dot{O} \qquad \textit{Reaction 1.7}$$

$$\dot{O}(^3P) + O_2 + M \longrightarrow O_3 + M \qquad \textit{Reaction 1.8}$$

Biomass burning and fossil fuel burning are the main sources of NO_2[22]. NO_2 undergoes photolysis at wavelengths less than 420 nm[21, 29], to produce $^{\bullet}O(^3P)$ and $NO^{\bullet}$. $^{\bullet}O(^3P)$ will react with O_2 in the presence of a third body, M, to form O_3[21, 22], Reaction 1.8. M is usually a small stable molecule, typically N_2 or O_2, which acts as a diffusion pathway for the excess energy generated from the reaction[21]. O_3 photolysis can also lead to the regeneration of O_3, through the stabilisation of $^{\bullet}O(^1D)$ with M, producing $^{\bullet}O(^3P)$. At night the ground level O_3 concentration increases due to entrainment from the free troposphere[6, 21].

O_3 concentrations depend on several factors including altitude, location and season, with 7×10^{11} molecules cm^{-3} estimated to be the global 24-hour average O_3 concentration[27]. The highest O_3 concentration is found in the free troposphere[6, 26],

between approximately 2 km and 15 km above sea level. Elevated O_3 concentrations are found in the mid to high latitudes, due to enhanced O_3 formation and transport from the stratosphere[21]. O_3 concentrations are at a maximum in the summer due to enhanced photochemical activity[30].

O_3 in the stratosphere and free troposphere effectively filters solar radiation, reducing the amount of UV radiation reaching the Earth's surface. At ground level, high concentrations of O_3 have a negative impact on human health and biological processes, leading to plant stress and a reduction in crop yields, it also leads to an increase in surface temperatures due to the absorption of solar radiation[31].

$NO_3^\bullet$ is the dominant oxidant at night-time[21]. $NO_3^\bullet$ is produced from the reaction of NO_2 with O_3, Reaction 1.9.

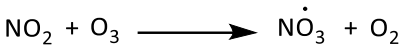

Reaction 1.9

$NO_3^\bullet$ undergoes rapid photooxidation upon exposure to sunlight, preventing $NO_3^\bullet$ oxidation from occurring during the day[32, 33], Reactions 1.10 and 1.11.

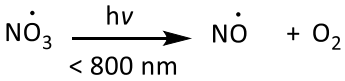

Reaction 1.10

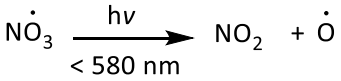

Reaction 1.11

The ambient nocturnal $NO_3^\bullet$ concentration is estimated to be 5 x 10^8 molecules cm^{-3} in urban areas[27]. $NO_3^\bullet$ concentrations are concentrated in urban areas near NO_x sources, and are quite low in rural areas. Although $NO_3^\bullet$ is typically associated with urban environments, $NO^\bullet$ has also been found to originate from certain soils. The oxidation of $NO^\bullet$ could be a source of $NO_3^\bullet$ in rural environments[22].

Photolysis is also a major loss pathway for VOCs containing carbonyl (>C=O) or nitro ($-NO_2$) functionalities[26]. In order for photolysis to occur, two criteria must be met; the incident light must have the correct wavelength to be absorbed by the VOC, and the light must have sufficient energy to dissociate the bond[34]. Due to the filtration of incoming solar radiation by O_3 in the stratosphere, the wavelength of light that reaches the troposphere is typically above 290 nm, therefore photolysis only occurs for VOCs that absorb in the actinic range[26].

1.4 VOC Oxidation

The fate of a VOC in the atmosphere depends on its reactivity towards the various atmospheric oxidants $OH^{\bullet}$, O_3 and $NO_3^{\bullet}$, as well as photolysis. The reactivity of a VOC depends on several factors including the functional groups present[35, 36], the structure of the VOC[37] and the nature of the oxidant[22, 38].

Laboratory studies involving the use of atmospheric simulation chambers (Figure 1.2) or flow tube reactors are used to study oxidation reactions. They are constructed from an inert material, typically Teflon[39, 40] or glass[41, 42], and are supplied with dry, clean air free of VOCs and oxidants[43].

Figure 1.2 *Photograph of the Irish atmospheric simulation chamber (IASC) at University College Cork, Ireland.*

A suite of instruments connected to the chamber is utilised to monitor the progress of the oxidation reaction through the decay of the reacting VOC and the formation of oxidised products, which takes the general form:

VOC + Oxidant ⟶ Products **_Reaction 1.12_**

The rate of a reaction is a measure of the change in concentration of reactants or products with time[44]. The rate of a reaction depends on several factors including temperature and pressure, and is defined by the rate coefficient (*k*) for the reaction. The temperature dependence of *k* values can be described using the Arrhenius equation over a limited temperature range, and displays a negative trend with increasing temperature[44]. The values for *k* can be used to determine the lifetime of VOCs in the atmosphere due to reaction with the various oxidants[27]. In the case of photolysis reactions *J* values are used to describe the reaction kinetics, which can also be determined from experiments performed using chambers.

As well as investigating reaction kinetics, chambers can also be used to determine the oxidation products and SOA produced during the reactions. On-line monitoring and assessment of oxidation products facilitates derivation of the oxidation mechanisms leading to their formation, and can also be used to investigate the SOA formation potential of VOCs.

1.5 Secondary Organic Aerosols

An aerosol is the suspension of solid and liquid particles in a gas. SOA are produced from the oxidation of VOCs which through a single oxidation step or multiple progressive oxidation steps generate products with sufficiently low volatility that partition into the particle-phase[18]. Partitioning can occur via two methods, nucleation leading to new particle formation[45] or deposition onto pre-existing particles[46]. A schematic for the formation of SOA is shown in Figure 1.3.

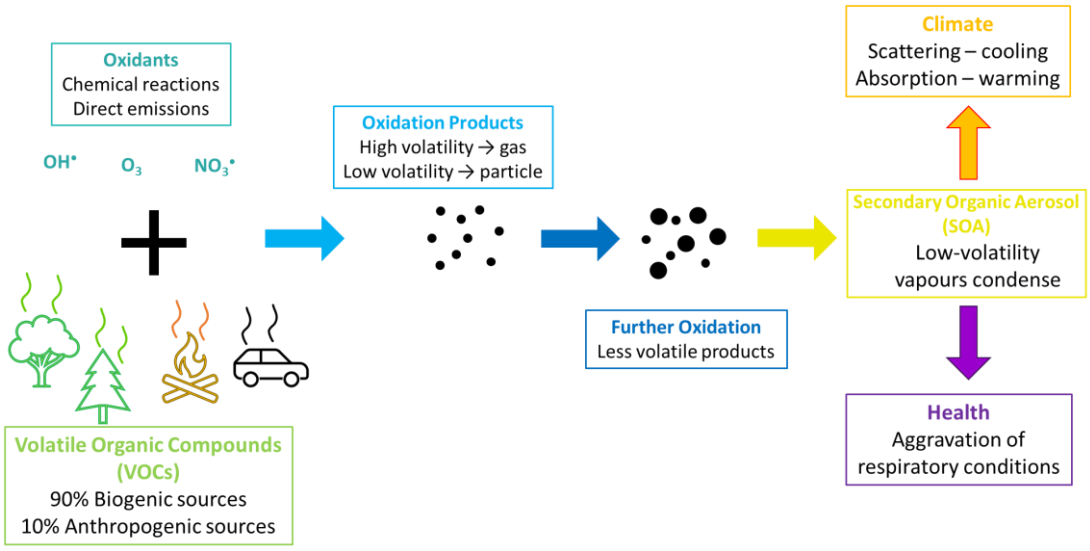

Figure 1.3 *Schematic of SOA formation from biogenic and anthropogenic VOCs.*

SOA have impacts on health and climate. Inhalation of SOA can lead to an accumulation of particles in the alveoli in the lungs[47], which cross the thin membrane and enter the bloodstream. People living in areas subject to high SOA concentrations have increased susceptibility to respiratory conditions and heart disease, as well as increased mortality from stroke and cardiorespiratory diseases[48].

SOA are a key component of photochemical smog, which leads to reduced visibility[49]. More importantly, SOA have significant direct and indirect climatic impacts, through their interaction with incoming solar radiation which alters the natural radiative balance[50]. SOA directly affect the climate through the reflection and scattering of incoming infra-red (IR) solar radiation. This reduces the amount reaching Earth and

has a cooling effect on the Earth's atmosphere[51, 52]. If the SOA contain light absorbing functionalities (chromophores) such as carbonyl or nitro groups, radiation can be absorbed and this has a warming effect on the climate[53, 54]. An example of this is brown carbon, which is formed through the oxidation of anthropogenic and biogenic VOCs[53] and absorbs in the near-UV and visible wavelength ranges.

SOA indirectly affect climate through their influence on clouds. SOA particles act as cloud condensation nuclei (CCN), leading to the formation of clouds[51, 55]. Clouds reflect incoming solar radiation reducing the amount that reaches Earth[52]. Changes in the concentrations or sizes of CCN will alter cloud formation and properties, and impact natural radiative processes[19]. Figure 1.4 shows the direct and indirect effects that aerosols have on radiative forcing.

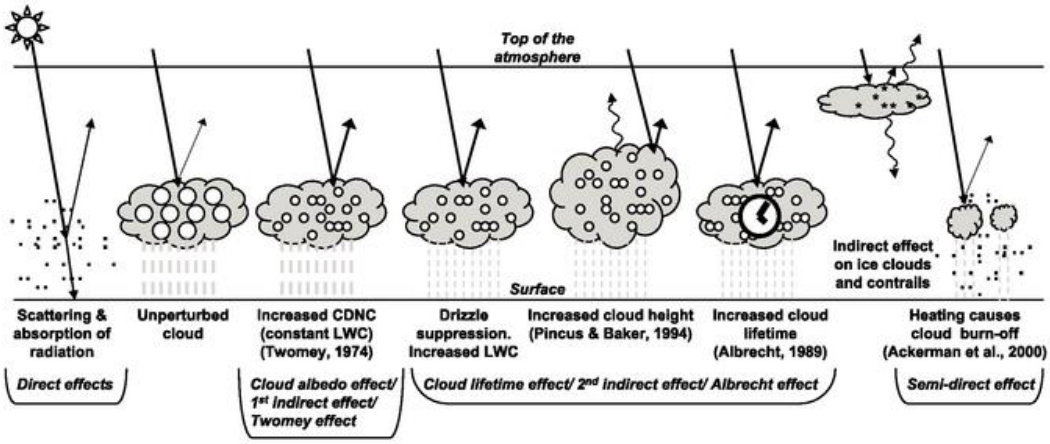

Figure 1.4 *Direct and indirect effects of aerosols on radiative forcing[56].*

The largest uncertainty regarding predictive global climate models is that associated with aerosols, and in particular their indirect impacts on clouds[57]. The composition of SOA determine their properties and health and climatic impacts[58]. There is a high degree of uncertainty associated with global SOA concentrations[59], with estimates for the biogenic SOA flux from 12 Tg year^{-1} to 70 Tg year^{-1}, and estimates for the anthropogenic sources between 2 Tg year^{-1} and 12 Tg year^{-1}. While the SOA estimates are largely variable, it is clear the SOA contribution originating from biogenic sources far exceeds that from anthropogenic sources. Therefore, it is important to determine

the chemical and physical properties of SOA produced from the most abundant VOCs released from biogenic sources into the atmosphere.

1.6 Biogenic Volatile Organic Compounds

VOCs emitted from plants, soils and aquatic plants are referred to as biogenic VOCs (BVOCs). BVOCs are emitted from the foliage, bark and roots of plants. BVOCs account for approximately 90% of global VOC emissions, and are over an order of magnitude more abundant than anthropogenic VOCs[11].

A significant amount of research has been conducted on the BVOC emissions from various plant species in an effort to determine their composition and potential climatic impacts[51, 60]. All plant species have been found to emit terpenes, which are hydrocarbons comprised of multiple C_5H_8 units[9, 61]. The most common terpenes are isoprene (C_5H_8), monoterpenes ($C_{10}H_{16}$) and sesquiterpenes ($C_{15}H_{24}$). Terpene BVOCs are emitted from coniferous plants[62], deciduous plants[19] and grasses[63]. Only one C_5H_8 isomer, isoprene, is emitted from plants, while multiple cyclic and linear monoterpene and sesquiterpene isomers exist.

Figure 1.5 shows the structures of isoprene, α-pinene a commonly emitted monoterpene and β-caryophyllene a commonly emitted sesquiterpene. BVOC emissions are dominated by terpenes, although smaller amounts of oxygenated compounds can also be emitted including acetone[15], methanol[64] and oxygenated monoterpenes[65, 66].

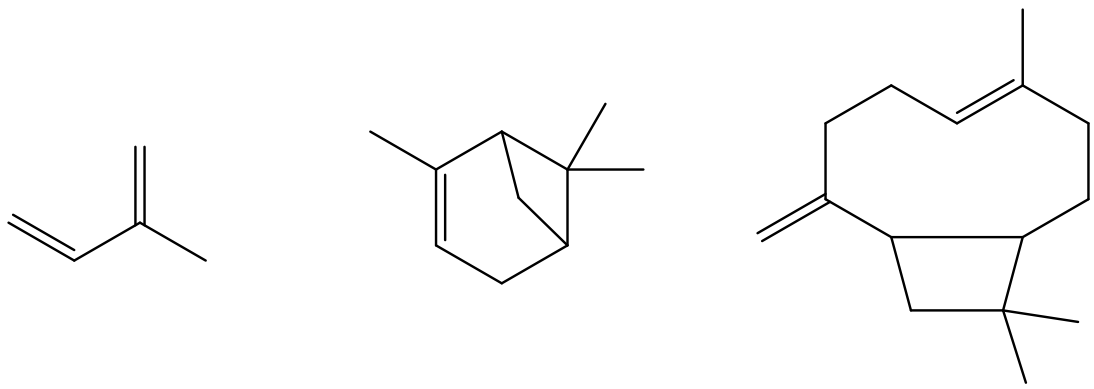

Figure 1.5 *Structures of isoprene (left), α-pinene (middle) and* β*-caryophyllene (right).*

The BVOCs emitted from a plant species depend on several factors. In general each species of plant emits a unique BVOC emission profile, typically with isoprene or two to three monoterpenes accounting for 60% to 90% of the BVOC emission flux[67, 68], with the remainder composed of other terpenes and oxygenated BVOCs. Depending on the emission flux, plant species are normally classed as high or low emitters, with the emissions from the leaves of deciduous plants usually much lower than those from the needles of coniferous plants[69, 70].

Two of the most well studied tree species are Scots pine and Norway spruce, which are typically found in the temperate and boreal regions of the Northern Hemisphere. The main BVOCs emitted from Scots pine are α-pinene and δ-carene, although other monoterpenes can also be emitted in significant amounts[71, 72]. The main BVOCs emitted from Norway spruce are α-pinene, β-pinene and limonene[73]. As both Scots pine and Norway spruce are found in the same locations, and emit similar BVOC profiles, the climate surrounding these forests is influenced by the SOA produced from the oxidation of these monoterpenes.

1.7 Monocultures

A monoculture is an area of land that is dedicated to growing a single plant species. In terms of forestry, this often means natural forests containing multiple native species are cleared, and replaced with a single, usually non-native species. An example of this are the oil palm plantations that have been established in place of natural rainforest across Asia, Africa and Latin America[31]. Large scale oil palm plantations (Figure 1.6) were established due to the worldwide demand for palm oil used in food, cosmetics and as a biofuel[31].

Figure 1.6 *Photograph of oil palm plantation in Asia[74].*

The mass planting of oil palm has had several negative impacts on the local areas. Oil palm plantations have led to widespread deforestation[75]. There has been a significant loss in biodiversity due to the removal of natural forest, as oil palm plantations tend to be devoid of other flora and fauna[76].

Since the establishment of oil palm plantations, the atmospheric composition of the air in areas surrounding the plantations has experienced significant changes. In

Southeast Asia the replacement of natural tropical rainforest with oil palm plantations has lead to a significant increase in ambient isoprene concentrations, and decrease in monoterpene concentrations[31]. Oil palm plantations are also associated with elevated NO_x concentrations relative to the natural forest, due to agro-industrial activity. In the presence of NO_x, the oxidation of isoprene can lead to the formation of ground level O_3. For remote oil palm plantations NO_x emissions are sufficiently low to maintain pre-plantation ground level O_3 concentrations. More intensive oil palm processing would increase NO_x emissions leading to an enhancement in O_3 formation. Elevated O_3 concentrations have been observed in regions where oil palm plantations are in close proximity to urban centres.

In Ireland a similar process is occurring. Natural forest comprised of predominantly native broadleaf species including oak, ash and birch, are cleared to make way for Sitka spruce monocultures. Sitka spruce is a non-native coniferous tree species, desired for its ability to rapidly grow in the Irish climate.

1.8 *Picea Sitchensis* (Sitka spruce)

In Ireland forestry accounts for approximately 11% of land cover, almost 50% of which is dedicated to *Picea Sitchensis* (Sitka spruce) monocultures. Sitka spruce is a naturally occurring species in the Western US, it was originally introduced to Ireland in the 19th century, with the first Sitka spruce plantations established at the start of the 20th century. Since then Sitka spruce has become the main plantation tree species in Ireland, Figure 1.7.

Figure 1.7 *Photograph of a Sitka spruce monoculture in Co. Cork Ireland.*

The widespread planting of Sitka spruce is favoured over native species because of its ability to grow quickly and straight, which facilitates wood production. Sitka spruce can grow to a height of approximately 30 m, with nearly all the foliage located at the top. This has the effect of blocking sunlight from reaching the forest floor, preventing the growth of flora that is commonly found in other forests, leading to a significant loss in biodiversity[77].

The climatic implications of planting Sitka spruce monocultures are largely unknown, as to date only a limited number of studies have characterised the BVOC emissions from Sitka spruce. The most recent study was conducted in 2004, and none were

conducted in Ireland. In all studies isoprene and monoterpenes were identified as BVOC emissions from Sitka spruce.

The first known study on the characterisation of BVOCs emitted from Sitka spruce was conducted in the US on twelve Sika spruce saplings housed in a controlled environmental chamber. A combination of gas- and liquid-chromatography were used to identify the BVOC emissions, which were comprised of isoprene, and four monoterpenes; camphene, α-pinene, β-pinene and myrcene. The emissions were dominated by isoprene, with myrcene identified as the main monoterpene emission. A very low concentration of β-phellandrene was also detected in the emissions of only one of the twelve Sitka spruce trees[78]. In a follow-up study the BVOC emissions of twelve 6 month old Sitka spruce saplings were analysed. Isoprene was found to dominate the emissions with the same four monoterpenes identified in the same ratios[79].

A study conducted in the UK, also using gas-chromatography analysis, found a difference in the BVOC composition and emission fluxes from a young Sitka spruce tree and a mature Sitka spruce tree naturally growing in a forest. The difference in fluxes was partly attributed to differences in the environmental conditions between the trees at the time of sampling. For both trees the emissions were dominated by myrcene, accounting for over 80% of the total BVOC flux. The other BVOCs consisted of isoprene, α-pinene, β-pinene and camphene, although the relative contributions were different, with the mature tree emitting more isoprene and the young tree emitting more monoterpenes. In the same work, the emissions of glasshouse grown 2 year old Sitka spruce trees, analysed in a laboratory under controlled environmental conditions, were composed almost entirely of isoprene, with minor contributions from the same three monoterpenes[80]. In an extension of this study it was found that β-phellandrene made a significant contribution to the overall Sitka spruce BVOC flux, and was the second highest monoterpene emission after myrcene[81]. These results are in contrast to those reported for Sitka spruce in the US, for which β-phellandrene was barely detected.

Another study in the UK, using a combination of proton transfer reaction-mass spectrometry (PTR-MS) and gas chromatography, analysed the BVOC emissions from a Sitka spruce tree. The BVOC emissions were composed predominantly of α-pinene, β-pinene, limonene and myrcene. Minor concentrations of several other monoterpenes; camphene, δ-carene, α-phellandrene, α-terpinene and γ-terpinene were also detected, as well as p-cymene and two $C_{10}H_{16}O$ oxygenated monoterpene isomers, piperitone and camphor. The emission of isoprene was not reported[82]. An extension of this study, using PTR-MS analysis only, found isoprene, an unidentified monoterpene mixture and small oxygenated compounds, methanol and acetaldehyde in the emissions of 9 year old Sitka spruce[83].

Several studies have also been conducted to determine the composition of Sitka spruce resin. Resin originating from the needles and branches was found to be composed of mainly myrcene, camphor and piperitone[84-88]. Other monoterpenes including β-pinene[84], β-phellandrene[84, 85], and several oxygenated compounds including 1,8-cineole[87] and isopentyl isovalerate[89] were also identified in various studies. The composition of the cortical resin in the main trunk was found to be quite different to that in the needles and branches. The monoterpenes α-pinene, β-pinene and β-phellandrene were found to dominate the composition of Sitka spruce cortical resin[86, 90].

Two studies analysing the soil in Sitka spruce forests covered with fallen needles, found the composition of the soil emissions to be quite similar to the needle BVOC emissions. The soil BVOC emissions were mainly composed of β-myrcene, α-pinene, β-pinene, δ-limonene and camphene. Both studies focussed on the detection of isoprene and monoterpenes, and did not report the detection of oxygenated compounds.

There is a discrepancy between the results of studies identifying the composition of the BVOCs emitted from Sitka spruce. Some studies focussed solely on the detection of isoprene and monoterpenes, with others also reporting the detection of oxygenated compounds. All studies were conducted under different conditions, and

none were performed in Ireland. In order to assess the BVOC emissions from Sitka spruce monocultures in Ireland, it is important that the work is performed at conditions relevant to the Irish climate.

1.9 Aims and Thesis Overview

1.9.1 Aims of Thesis

The aims of this work were to:

- Identify and determine the emission fluxes of the main BVOCs emitted by Sitka spruce under conditions relevant to the Irish climate.
- Assess the atmospheric reactivity of the main BVOC emitted by Sitka spruce, through determination of its reaction kinetics, product formation and oxidation mechanisms.
- Perform oxidation reactions on the whole Sitka spruce BVOC emissions, to identify oxidation products, determine oxidation pathways and to assess the SOA formation potential of Sitka spruce BVOC emissions.

1.9.2 Overview of Thesis

Chapter 1 provides an overview of the research topic presented in this thesis. A description of VOCs, regarding their sources, oxidation, SOA formation potential and climatic impacts following the formation of SOA are presented. The importance of knowing the composition of VOCs produced from high emitting sources is provided, with a review of the BVOCs emitted by Sitka spruce, Ireland's main plantation tree species.

A description of the main instrumentation used in this work is provided in Chapter 2. All work involved the use of a high resolution time-of-flight chemical ionisation mass spectrometer (ToF-CIMS), with experiments carried out at two separate laboratories; Environmental Research Institute, University College Cork (ERI, UCC) and at the Irish Atmospheric Simulation Chamber facility University College Cork (IASC, UCC).

An overview of the BVOCs emitted by Sitka spruce is provided in Chapter 3. The composition of the BVOC emissions was determined using a combination of on-line ToF-CIMS analysis with off-line thermal desorption gas-chromatography mass

spectrometry (TD-GC/MS) analysis. The response of the BVOC emission fluxes to changes in environmental conditions were assessed and emission pathways were identified. Standardised BVOC emission fluxes were determined and the contributions of BVOC emissions to the carbon balance for Sitka spruce was calculated. An extrapolation procedure was applied to estimate the total BVOC flux from all Sitka spruce trees in Ireland.

Chapter 4 focussed on the oxidation of piperitone, the main BVOC emitted by the Sitka spruce trees in Chapter 3. Rate coefficients for the reactions of piperitone with $OH^{\bullet}$, O_3 and $NO_3^{\bullet}$ were estimated using structure activity relationships. Relative rate experiments were conducted to determine the rate coefficient for the reaction of piperitone with $OH^{\bullet}$. A series of oxidation experiments was carried out using an atmospheric simulation chamber to identify the main reaction products from the reaction of piperitone with $OH^{\bullet}$. Oxidation mechanisms were proposed for the formation of some of the main products.

The work described in Chapter 5 involved the oxidation of the BVOC emissions from a Sitka spruce tree. The BVOC emissions were transferred into an atmospheric simulation chamber and oxidised with $OH^{\bullet}$. Oxidation mechanisms were proposed for some products. The formation of SOA was investigated, and SOA formation yields were determined.

Chapter 6 provides a summary and perspectives of all work carried out, with suggestions for future research on this topic.

Chapter 2 Instrumentation

2.1 ToF-CIMS

The main instrument used in this work was a ToF-CIMS (Time-of-Flight Chemical Ionisation Mass Spectrometer, Aerodyne C4Q-106). The ToF-CIMS is an on-line instrument designed to monitor the composition and temporal evolution of atmospheric trace gases. The instrument was developed by researchers at Tofwerk and Aerodyne[91]. The ToF-CIMS is a highly sensitive instrument, capable of detecting VOCs at ppt concentration levels[92], with a high (1 Hz) time resolution[92, 93]. Chemical ionisation is a soft ionisation technique, which imparts minimal excess energy to the newly formed ion, resulting in little fragmentation[94] and easier identification of the analytes. Chemical ionisation is suitable for use with a variety of reagent ions[91, 93, 95], thus, enabling the detection of a wide range of atmospheric gases. The instrument has been used in laboratory studies to investigate the atmospheric oxidation of VOCs in simulation chambers[96]; and also in field studies, to measure ambient concentrations of atmospheric VOCs of biogenic[93, 97] and anthropogenic[98] origin.

2.1.1 Instrument Overview

A schematic of the ToF-CIMS is shown in Figure 2.1. The instrument consists of six distinct regions. Ambient air is admitted into the instrument through the gas-phase inlet and flows into the ion molecule reactor (IMR) where it undergoes chemical ionisation, to produce ions which travel through a series of focussing lenses and ion optics to the time-of-flight (ToF) region. In the ToF region the ions are separated according to their mass-to-charge ratio.

The ToF-CIMS used in this work was fitted with a vacuum ultraviolet (VUV) ion source (Tofwerk)[92], which consists of a krypton lamp that generates UV light at two wavelengths, 116.49 nm and 123.58 nm. N_2 is flowed at a rate between 0.25 L min^{-1} and 0.5 L min^{-1} over a heated permeation tube containing the reagent ion precursor and into the VUV ion source, where reagent ion precursor absorbs the UV radiation, leading to the formation of reagent ions. The flow of reagent ions subsequently passes into the IMR region[92].

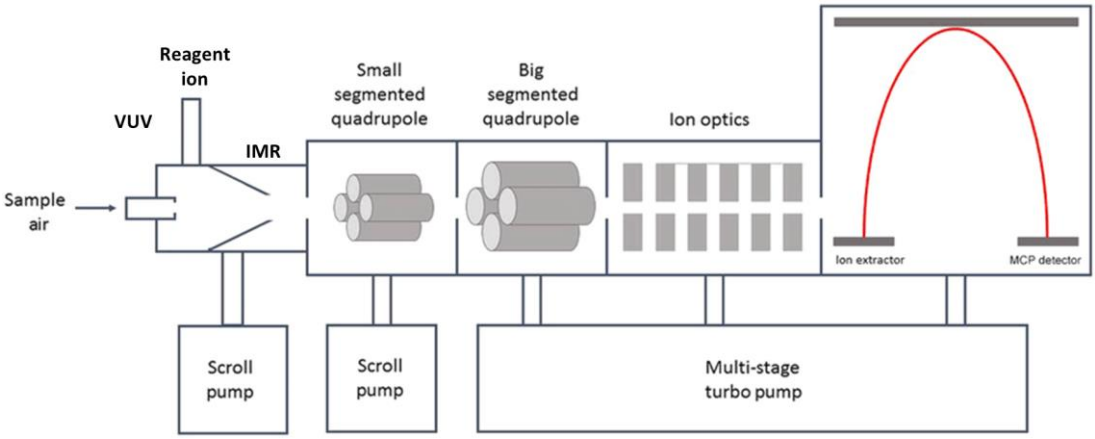

Figure 2.1 *Schematic of ToF-CIMS, adapted from Sanchez et al., 2016[99].*

The IMR is a small tapered stainless steel chamber in which the gas-phase analytes undergo chemical ionisation upon interaction with the reagent ions. Ambient air is admitted into the IMR at a flow rate of 2 L min^{-1}, through a critical orifice. Heating of the interior surface of the IMR to 60 °C, prevents loss of VOCs to the IMR walls[100]. The flows of reagent ions and sample air are orthogonal to each other and collide in the IMR[91]. Due to the large excess of reagent ions, ionisation of neutral gas-phase molecules proceeds, with negligible loss in reagent ion concentration[101]. The ionisation process that occurs depends on the properties of the analyte and reagent ion[93]. The pressure of the IMR also influences the ionisation process, with higher pressures promoting cluster formation[100]. In this work, the IMR was maintained at a pressure of 70 mbar or 120 mbar, depending on the choice of reagent ion. This was achieved with the use of a scroll pump (SH112), operating at a rate of 100 L min^{-1}. A voltage of -100 V was applied to the IMR to focus the ions through a critical orifice at the back of the IMR and into the small segmented quadrupole (SSQ)[91].

The SSQ consists of a short six-piece segmented quadrupole, to which a radio frequency field is applied. An electric field is generated, which as the ions pass through, focusses them into a beam[91]. The strength of the electric field can be adjusted, a strong field can lead to the dissociation of weakly bound ion clusters[102]. The pressure in the SSQ was maintained at 2 mbar for this work, with the use of a scroll pump (TriScroll 600)[103]. The voltages applied to the SSQ were set to 0 V, in order to reduce declustering, and enhance ion transmission through the instrument[100].

Following passage through the SSQ, the ions are admitted into the big segmented quadrupole (BSQ). The BSQ is a radio frequency only quadrupole, maintained at a pressure of 10^{-3} mbar by a turbo pump[103].

After the BSQ the ion beam enters the primary beam chamber (PBC), which consists of a series of ion optics, composed of ion lenses, flanges and deflectors[103]. The purpose of the PBC is to focus the ions into a single beam and accelerate it to the orthogonal extractor[91]. The pressure in the PBC was maintained at 10^{-4} mbar, with the use of the turbo pump[103].

In the ToF analyser the ions are held on the orthogonal extractor until a strong electric field is applied, causing the ions to accelerate through the ToF region[103]. The pressure in the ToF analyser was maintained at 10^{-6} mbar with the turbo pump[104]. The ions initially travel through the ToF region towards the reflector, where they experience a repulsion and are forced towards the detector. The ToF-CIMS is equipped with two microchannel plate detectors (MCP), arranged in a chevron configuration. The MCPs consist of an array of electron multiplier channels. When an ion enters a channel on the front MCP, electrons are released, which enter the second MCP, releasing further electrons. The current at the back of the second MCP is measured and converted to an ion concentration[103].

Operation of the ToF CIMS is performed through TofDaq, the software suite for data acquisition and control. The voltages and pressures applied to the various regions of the instrument are adjusted through TofDaq. Conditions for each measurement mode were optimised and reloaded as necessary. The voltages and pressures used in operating the ToF-CIMS were loaded and applied at least 30 minutes prior to commencing any measurements to allow the instrument time to initiate and ensure stability of the ion signals.

2.1.2 Reagent Ions

The choice of reagent ion determines the range of compounds the ToF-CIMS is capable of detecting[105]. No single reagent ion is suited to ionising all gas-phase molecules, and it is common practice to select a reagent ion which ionises the largest range of target analytes. The reagent ions chosen for this work were the benzene cation ($C_6H_6^+$) and iodide anion (I^-). $C_6H_6^+$ was selected for its affinity to ionise hydrocarbons and VOCs with a low oxygen content[106]. I^- was selected for its ability to detect VOCs with a high oxygen content[105], such as those produced during atmospheric oxidation experiments.

The $C_6H_6^+$ reagent ion was generated from the ionisation of gaseous benzene, via two methods. A 0.25 L min^{-1} flow of N_2 (BOC, oxygen free) was passed over a liquid benzene permeation tube (6-PD-1400-C45, Carl Stuart Group) placed inside ¾" stainless steel tubing which was wrapped in a heat strip and maintained at 50 °C. Alternatively, 0.02 L min^{-1} N_2 was passed over a volume of liquid benzene in a gas cell (Kin-Tek) and diluted with a 0.15 L min^{-1} flow of N_2. The vapourised benzene produced by these methods was passed into the ion source where upon absorption of VUV radiation, $C_6H_6^+$ was formed via the ejection of an electron[107].

For the generation of I^- ions, a 0.4 L min^{-1} flow of N_2 was passed over a methyl iodide (CH_3I) permeation tube (PD-4600-U30, Carl Stuart Group), heated to 50 °C with a heat strip. Alternatively, a flow of 0.45 L min^{-1} N_2 (Irish Oxygen, 2 Grade) was passed over a CH_3I permeation tube (PD-4600-U30, Carl Stuart Group), heated to 90 °C with a GC oven (Agilent), and into the ToF-CIMS. Upon entering the VUV ion source an amount of CH_3I absorbs the UV radiation, leading to the ejection of photoelectrons[92]. The photoelectrons interact with CH_3I molecules, leading to dissociation and the formation of I^-. During instrument operation the I^- ion was the dominant peak in the mass spectrum, significant signals were also observed for iodide clusters and interference from H_2O, O_2 and NO_3[108].

2.1.3 Tuning

Tuning of the ToF-CIMS was performed following installation of the VUV ion source and movement of the instrument. Tuning is an automated process carried out with specialised software, Thuner (version 1.7.0). The purpose of tuning is to optimise the response of the instrument to the analytes of interest. For $C_6H_6^+$ mode, this relates to the detection of hydrocarbons and VOCs with a low oxygen content (O_0 - O_2)[93]. For I^- mode this encompasses a wide range of oxygenated compounds (O_2 - O_7)[105].

The ToF-CIMS must be supplied with a stable tracer signal that it measures during tuning. For tuning in $C_6H_6^+$ mode β-pinene ($C_{10}H_{16}$) was used, and for I^- mode formic acid (CH_3COOH) was used. Home-made permeation tubes of β-pinene (purity 99%, Sigma Aldrich) and formic acid (purity 89%, Sigma Aldrich) were made using liquid standards. To generate a stable signal, the permeation tube was placed inside a ½" piece of stainless steel tubing and filtered air was passed over the tube at a flow rate of 3 L min^{-1}. The ToF-CIMS sub-sampled 2 L min^{-1} from this flow, with the remainder of the flow being vented. The reference signal was monitored for at least 12 hours to ensure stability of the signal.

Thuner can be used to optimise for sensitivity and resolution[109]. The focus of the tuning procedure depends on the appearance of the mass spectrum. Thuner operates by performing a series of steps (a sequence) in which the voltages applied to the SSQ and BSQ are varied within a range, and the response of the tracer compound is measured. The voltages are optimised during each step, and utilised as the input for the next step in the sequence[110].

For each step in the sequence the ion definitions are assigned. The tracer ion signal, or the isomer if the signal for the tracer ion is saturated, is set as the response ion. Other ions are used for a mass calibration, typically the reagent ion, its clusters and internal calibrants are used as calibrant ions. The strength of the tracer ion response during each step, determines which parameters are optimised. Optimising the resolution enhances the sharpness of peaks within the mass spectrum, facilitating

peak identification. Maximising the sensitivity increases the response of the instrument to the concentration of the compound. Within each step the level of importance given to tuning for optimising resolution or sensitivity is determined by the weight attributed to each. It is not possible to achieve maximum resolution while simultaneously attaining maximum sensitivity, and the configuration that corresponds to the best response for both parameters is selected.

2.2 Filter Inlet for Gas and AEROsols (FIGAERO)

Replacement of the gas-phase inlet on the ToF-CIMS with the FIGAERO (Filter Inlet for Gas and AEROsols, Aerodyne) allows collection and analysis of compounds in the particle-phase[111]. The FIGAERO works by sampling atmospheric gases while particles are simultaneously collected onto a 25 mm PTFE filter (pore size 1 µm, Zefon International Inc, USA). Once sufficient material has been collected onto the filter, repositioning of the linear actuator aligns the filter with the inlet of the ToF-CIMS and the particles on the filter can be thermally desorbed and analysed in the same manner as the gas-phase.

2.2.1 FIGAERO Overview

The FIGAERO consists of a Teflon manifold enclosed in a stainless steel casing[112]. A schematic of the FIGAERO is shown in Figure 2.2. The FIGAERO is mounted onto the ToF-CIMS in place of the gas-phase inlet, such that it is vertical. The FIGAERO has three ports drilled into the Teflon manifold which facilitate continuous gas-phase and particle-phase sampling[113], along with a Teflon linear actuator and a heating block. The use of the linear actuator allows independent sampling of the gas-phase and particle-phase, preventing contamination between them[114].

The FIGAERO can be operated in sampling mode or in desorption mode. When in sampling mode (Figure 2.2, B), gas-phase VOCs pass directly into the ToF-CIMS, through the gas-phase inlet which has a direct connection with the IMR[111]. Simultaneously particles are collected onto a PTFE filter which is held in the linear actuator. Particles are sampled onto the filter at a rate of 2.5 L min^{-1}. The middle port is blocked when in sampling mode.

In order to switch to desorption mode the linear actuator shifts vertically upwards. This blocks the gas-phase sampling port at the top and positions the filter in front of the second port (Figure 2.2, C). In order to desorb the particles, a 2 L min^{-1} N_2 flow is heated and passed over the filter, and desorbed compounds are carried into the IMR.

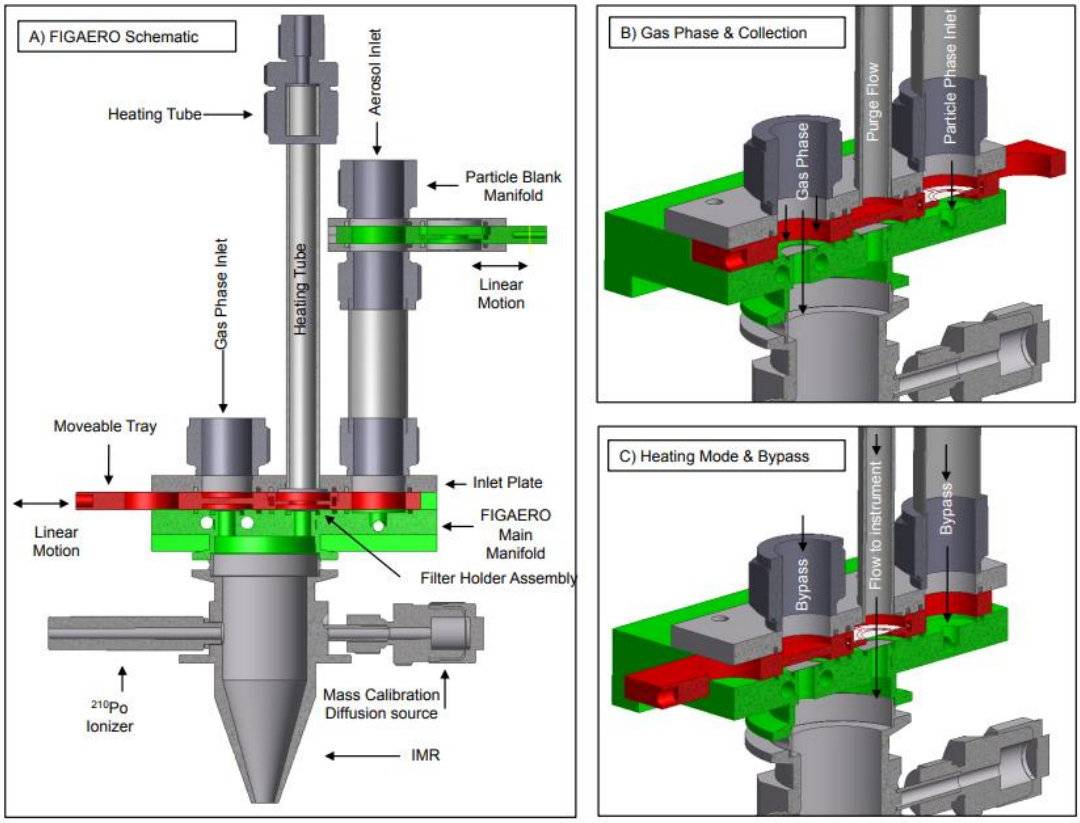

Figure 2.2 *Schematic of the FIGAERO (A) and its two operational modes, sampling (B) and desorption (C), adapted from Lopez-Hilfiker et al. (2014)*[111].

2.2.2 Desorption Cycle

Operation of the FIGAERO is controlled with the EyeOn control box and software. EyeOn can be used to perform a single desorption or can be programmed to run a sequence of sampling and desorption cycles.

For all analysis in this work, a single 35-minute desorption cycle was used. The desorption cycle consisted of three phases; a temperature ramp, a soak and a cooling. Prior to commencing the desorption cycle, the loaded PTFE filter was aligned with the IMR and a 2 L min^{-1} flow of N_2 was passed over it. During the 15-minute temperature ramp the temperature of N_2 passing over the loaded PTFE filter was increased from ambient (typically 21 °C) at 10 °C min^{-1}, to 200 °C. This linearly increased the temperature of the filter to ~ 180 °C, and was followed by a 20-minute soak period at 200 °C[112]. The purpose of the soak is to ensure all organic material has

desorbed from the PTFE filter allowing it to be re-used, without contamination concerns. Following the soak, the temperature of the PTFE filter was cooled to facilitate further sample collection. The heating block was cooled with the use of an in-built fan, and ambient temperature N_2 was passed over the filter for 5 minutes[115].

2.3 Other Instrumentation

2.3.1 Scanning Mobility Particle Sizer

A Scanning Mobility Particle Sizer (SMPS) (TSI model 3938) was used during oxidation experiments to monitor the formation and growth of particles. The SMPS measures the size distribution and concentration of particles in real time, based on the electrical mobility of a charged particle in an electric field[116]. The SMPS consists of three parts; electrostatic classifier (TSI model 3082), differential mobility analyser (DMA) (TSI model 3081), and condensation particle counter (CPC) (TSI model 3750).

Polydisperse aerosol is sampled at a flow rate of 1 L min^{-1} through a 0.071 cm orifice impactor into the electrostatic classifier of the SMPS. The purpose of the impactor is to remove particles above a certain aerodynamic diameter from the sample flow. This reduces interference from multiply charged particles[117]. The particles then pass through a Krypton-85 bipolar neutraliser, which applies a known charge distribution to the aerosol.

After charging, the particles are admitted into the DMA where they are separated according to electrical mobility. The DMA consists of an inner and outer electrode, to which voltages are applied to generate an electric field. The strength of the electric field is varied by scanning the voltage[116]. At a certain electric field strength only particles with a specific electrical mobility will pass through the exit slit of the DMA, producing a monodisperse aerosol. Electrical mobility is proportional to charge and particle size, so assuming the particles are uniformly charged prior to entering the DMA, the electrical mobility can be used to determine the particle size.

Following sizing, the particles are counted with the CPC. In the CPC the particles pass through a saturator, where the aerosol flow becomes saturated with n-butanol vapour. The flow then passes through a condenser, in which the aerosol is cooled and the butanol vapour condenses onto the particles, growing them to a detectable size. The condensed particles pass in front of a laser diode to be counted[118].

2.3.2 NO_x Analyser

A NO_x analyser (Enviro Technology Services, T200 NO_x Analyser) was used to measure the concentrations of $NO^{\bullet}$, NO_2 and NO_x (sum of $NO^{\bullet}$ and NO_2) during oxidation experiments at a 1 minute time resolution. The measurement is based on the chemiluminescence of NO_2 produced from the reaction of $NO^{\bullet}$ in the sampled air with O_3. The NO_2 has excess energy that is released in the form of infrared light, which is detected and converted to a concentration. Some of the sample air is passed over heated molybdenum, which converts NO_2 to $NO^{\bullet}$. The concentration of $NO^{\bullet}$ in the NO_2 converted sample is measured in the same manner, with the concentration corresponding to NO_x. The measurement switches between incoming sample air and the NO_2 converted sample and the difference is calculated to give an NO_2 concentration[119].

2.3.3 O_3 Analyser

An O_3 analyser (Enviro Technology Services, T400 O_3 Analyser) was used during oxidation experiments to measure O_3 concentrations at a 1 minute time resolution. The instrument provides an O_3 concentration based on the difference in the absorption of UV light at 254 nm between the sample and the sample air scrubbed of O_3. The amount of absorbed UV is proportional to the amount of O_3 in the sample[120].

2.4 Atmospheric Simulation Chambers

2.4.1 Environmental Research Institute

The atmospheric simulation chamber at the Environmental Research Institute (ERI) (Figure 2.3) is a 2.2 m^3 cylinder made of 0.1 mm thick fluorinated ethylene propylene (FEP) Teflon foil[121], which is chemically inert and permits transmittance of UV and visible radiation. The chamber is housed in a reflective aluminium casing to maximise light penetration into the chamber, which is equipped with a series of UV lamps (Philips) which lie along the floor: five TL05 40 W lamps that emit in the UVA range with an emission maximum at 370 nm; five TLD08 18 W BLB lamps that emit in the UVA range with an emission maximum at 360 nm; and six TUV T8 15 W lamps which emit in the UVC range with an emission maximum at 253.7 nm. The chamber is equipped with a small fan to facilitate homogenisation of the chamber contents following injection.

Figure 2.3 *Photograph of the atmospheric simulation chamber at the ERI.*

The compressed air that supplies the chamber is filtered by passing it through an air purification system (Zander KA-MT-6) to minimise contamination from VOCs and NO_x. The ends of the cylindrical chamber have several ports each, of varying sizes for sampling instrumentation and reagent injection. A Vaisala relative humidity and

temperature probe (dewpoint probe DMP74A, Viasala, Finland) is located inside the chamber. The chamber could be humidified to 60% by bubbling compressed air through Milli-Q water over night.

When not in use the chamber was continually flushed at 120 L min^{-1}. When in operation the chamber was supplied with a 5 L min^{-1} to 10 L min^{-1} flow, to compensate the volume removed due to instrument sampling and to mitigate chamber shrinkage. This also ensured the chamber was continually over pressurised and prevented inward penetration of laboratory air.

Background concentrations of the measured parameters in the clean chamber are approximately; particle number concentration < 20 cm^{-3}, O_3 = 0.5 ppb, $NO^{\bullet}$ = 0 ppb, NO_2 = 0.5 ppb, relative humidity = 0.17%.

2.4.2 Irish Atmospheric Simulation Chamber (IASC)

IASC is a 27 m^3 cuboid (4.4 m x 3 m x 2 m) chamber made of 0.125 mm thick FEP Teflon foil attached to an aluminium support frame (Figure 2.4). The structure of the chamber is supported 30 cm above the ground with aluminium profiles. The two side walls of the chamber are each equipped with two mounting plates each with various sized ports for reagent admission into the chamber and instrumentation sampling. The mounting plates are approximately 1 m above the base of the chamber, with tubing extending approximately 30 cm into the chamber. The two end walls of the chamber are equipped with ten spectroscopic cavities, also 1 m above the chamber floor. The spectroscopic cavities are designated for the in-situ detection of various gases including NO_2, $NO_3^{\bullet}$ and HONO.

Figure 2.4 *Photograph of inside (left) and outside (right) of IASC.*

The chamber and support frame are situated inside a housing, which is equipped with a built-in ventilation system that allows control of the air temperature within the range 15 °C to 25 °C. The two longer side walls of the housing are fitted with seven panels consisting of ten lamps each, 140 lamps in total. Each panel has seven actinic black light UVA lamps (Phillips TL 40W/10 SLV/25) and three UVB broadband lamps (Phillips TL 40W/12 RS SLV/25) for photolysis of compounds and radical precursors. The internal surface of the chamber housing is covered in a highly reflective foil to maximise light transmission into the chamber.

The chamber is supplied with cleaned air generated by a compressor (Atlas CopCo, air compressor model ZT22) equipped with a drier, two charcoal filters and two HEPA filters to remove humidity, VOCs, NO_x and particles, respectively, prior to admission into the chamber. The chamber is operated at a slight overpressure, which is regulated by a control system through KNX software. While flushing the differential pressure is held at +3 Pa, and during experiments it is maintained at +10 Pa. A fan located on the chamber floor, is briefly turned on following the addition of reactants to achieve rapid mixing.

The chamber is fitted with two PT-1000 thermocouples (Sontay, Flying Lead Temperature Sensor), positioned at opposite corners inside the chamber, to check for uniform temperature throughout the chamber. The chamber is also fitted with a combined relative humidity, temperature and pressure transmitter (Vaisala PTU303), a precision CO_2 diffusion transmitter (Vaisala GMP343) and a precision differential pressure transmitter (Vaisala PDT102). These instruments are constantly connected to the chamber, with the NO_x analyser, O_3 analyser and SMPS also routinely connected.

Background concentrations of the measured parameters in the clean chamber are approximately; particle number concentration < 20 cm^{-3}, O_3 = 0.5 ppb, $NO^{\bullet}$ = 0.5 ppb, NO_2 = 0 ppb, relative humidity = 0.1% and CO_2 = 400 ppm.

Chapter 3 Emissions Characterisation

3.1 Introduction

Each different plant species emits a unique mixture of BVOCs. Once emitted the BVOCs can take part in multiple atmospheric oxidation reactions, the products of which have impacts on the local air quality and climate. Therefore it is important to determine the BVOC emission profile of a plant species prior to establishing large scale plantations.

3.1.1 Biogenic Processes

Photosynthesis is the process by which the photosynthetic apparatus in the chloroplasts of plants convert CO_2, water and sunlight into carbohydrates. There is a strong positive correlation between the assimilation of CO_2 and photosynthetic photon flux density[122] (PPFD), with CO_2 assimilation also having a positive correlation with temperature[123]. Plants also undergo respiratory processes, where CO_2 is released back into the atmosphere. In the dark, mitochondrial respiration causes a positive CO_2 flux, whereas in the light photorespiration reduces net CO_2 assimilation[124], resulting in an overall negative CO_2 flux. This implies that CO_2 assimilation from photosynthetic activity, is greater than CO_2 emission from photorespiration, and is an indication of plant growth[125].

Another indicator of plant growth and health is chlorophyll fluorescence. When chlorophyll absorbs light three processes can occur; photosynthesis, re-emission of the absorbed energy as heat, or re-emission of the absorbed energy as light (fluorescence)[126]. Under conditions where photosynthesis and heat emission are negligible, the only possible outcome is fluorescence. Photosynthetic efficiency can be derived from chlorophyll fluorescence measurements, with maximum photosynthetic efficiency after dark acclimation calculated as F_v/F_m, which is the ratio of chlorophyll that undergoes fluorescence to all chlorophyll. A higher F_v/F_m ratio indicates efficient operation of the photosynthetic apparatus in the plant, particularly a high proportion of functional photosystem II, suggesting the plant is

healthy. A lower ratio is an indication that not all chlorophyll is contributing to photosynthetic function and the plant may be suffering stress[126, 127].

Some of the assimilated CO_2 is converted within the plant and released as BVOCs[8]. BVOCs can be emitted through either a biosynthetic or a pooled emission process. Biosynthetic BVOC emissions, such as isoprene, are synthesised within the chloroplasts of the plant and are emitted immediately[128]. Biosynthetic synthesis pathways only operate under illumination, and are strongly influenced by photosynthetically active radiation (PAR)[129]. PAR specifically refers to light within the visible region, 400 nm to 700 nm, which drives photosynthesis. PAR is commonly measured as PPFD in µmol m^{-2} s^{-1}, which describes the amount of PAR falling on a surface per unit time. In the absence of PAR, biosynthetic pathways cease to operate and BVOC emission stops. For many plant species there is a positive relationship between PPFD and BVOC emission flux, until a saturation point is reached[71]. The point of saturation depends on the plant species and the environmental conditions. Biosynthetic emissions are also influenced by temperature, with many BVOCs experiencing an increase in emission flux up to a saturation temperature. The saturation temperature is commonly around 40 °C, and marks the temperature of maximum enzyme activity for the plant species, above which the synthesis and subsequent emission of BVOCs reduces[130].

Alternatively, BVOCs can originate from pooled emission sources. The BVOCs are synthesised, deposited in storage pools and released later. Typically, monoterpenes are emitted via this pathway[130]. The BVOCs emitted from pooled emission sources have already been synthesised, thus the emission process is not dependent on PAR and occurs under both light and dark conditions. BVOC emissions from pooled sources have a strong relationship with temperature[131]. The BVOCs are assumed to diffuse out of the storage pools, with the rate of diffusion related to the vapour pressure of the particular BVOC[132].

PPFD and temperature are the main drivers for BVOC emissions, although many other environmental conditions and parameters also contribute. Meteorological

events, such as changes in cloud cover or precipitation can affect emission fluxes. Shading is a particularly important factor for biosynthetic BVOC emissions[133]. On a longer timescale, BVOC emissions have been shown to be seasonal, with changes in the emission flux and compositional profile observed[134]. For many plant species the average emission flux, accounting for seasonal differences in PPFD, temperature and biomass, is much larger in the summer than during the winter[135]. This difference is likely due to internal processes within the plant that are season dependent. For instance, the emissions from rye and grape were found to be elevated during blossoming[69]. The composition of the emitted BVOC mixture also changes with the season. The emission of 2-methyl-3-buten-2-ol from Scots pine was observed to decrease across the period April to October, while monoterpene emissions peaked in June and July[71]. The reason for this is unclear, but it is possibly related to a connection between different growth stages and season[136]. The BVOC emissions are also related to the age of the plant. For example, the composition of the BVOC emissions from Downy birch were found to differ with age, with older trees having a higher sesquiterpene emission flux than younger trees[137]. A similar phenomenon has also been observed for resin, which for Sitka spruce was found to have a higher content of oxygenated compounds as it aged[86]. The composition of Sitka spruce resin was also found to vary slightly with height[87]. Neighbouring trees in the same stand, subject to the same conditions have been found to produce different emission profiles[87]. Location can also impact the composition of the BVOC emissions[134]. Sitka spruce in the UK has a high contribution from β-phellandrene, while in the USA it has not been detected in Sitka spruce emissions[138]. Stress has a considerable impact on BVOC emissions. The most common types of stress include herbivory attack, wounding and pollutant exposure. Upon exposure to stress the BVOC emission profile changes, usually with green leaf volatiles (GLVs)[139] and sesquiterpenes[68] contributing significantly to the emission profile. Physical stressors, such as herbivory or wounding, often result in damage to the bark and the exposure of resin ducts, which releases large quantities of pooled emissions[140]. These factors all play a role in the BVOC emissions from plants.

3.1.2 BVOC Measurements

Numerous studies have been conducted both in a field environment and in a laboratory setting to determine the composition of BVOC emissions, and probe the factors that lead to their production. Field measurements involve sampling BVOC emissions from plants, including trees that are in their natural environment. This method has the benefit of the plant growing and adapting to its surroundings in a natural manner and also permits sampling of a range of differently aged plants. However field measurements can present challenges, particularly as external environmental factors cannot be controlled and may lead to changes in the composition of BVOCs released or emission flux strengths. Laboratory measurements involve analysis of the plant in a controlled environment. The ability to control environmental parameters permits an assessment of the influence these have on the BVOC emissions. There is uncertainty as to how representative laboratory BVOC studies are of the natural environment[141]. In many cases the plants are grown outdoors for several years, and are then relocated inside the laboratory, which may alter the emission profile. Due to size limitations within laboratories the types and ages of plant species that can be sampled are restricted, with the majority of laboratory studies involving young plants. The conditions employed in laboratory studies are often not representative of the natural environment and can lead to false assumptions about the emissions from a plant species[141].

All BVOC studies involve the use of an enclosure, to isolate the leaves or branches of interest of the plant from the environment. Several types of enclosure have been developed, although all have the same basic properties. All enclosures are constructed from an inert and transparent material[142], usually Teflon[62] or glass[143]. This prevents adsorption of BVOCs to the walls and allows PAR to pass through. Dynamic enclosures have an inlet port, supplied with either purified oxidant free air[136] or a synthetic air mixture[142], and an outlet port connected to the sampling instrumentation[144]. The enclosures are over pressurised to prevent an inward flux of ambient air[68]. The concentrations of BVOCs are measured before the inlet port and after the outlet port[145], or an empty enclosure is used to account for background

measurents[146]. Open enclosures have a door which periodically switches between being open and closed, while BVOCs are continually sampled[147]. The size of the enclosure depends on the amount of foliage under investigation. Leaf cuvettes are the smallest systems, which encompass a single leaf, or portion of a conifer branch. These systems quickly acclimatise to changes in environmental conditions and can be oriented to maximise PAR adsorption[148]. Teflon or glass enclosures typically encompass a whole branch or small tree[148], which can lead to shading within branch enclosures, preventing all foliage from receiving the same PPFD[148]. Changes in environmental conditions such as temperature, PPFD, relative humidity and CO_2[6, 131], can alter BVOC emissions and should be measured[149]. The placement of the enclosures around the foliage changes the environment and can temporarily obscure the emission profile while the tree or plant acclimatises[142]. Enclosures are regularly placed around the foliage for several hours[68] or days[144] prior to emission sampling to counteract this.

Both online and offline instrumentation are used in the analysis of BVOCs. Adsorbent cartridges[150] or gas canisters[151] have been traditionally used for the collection of BVOCs, which are subsequently analysed by chromatographic techniques. This method is effective for determining the molecular composition of BVOC emissions, although it has poor time resolution. Samples are often collected over a time scale of hours[152], with large passages of time between successive samplings[153]. This hinders the ability to monitor short term changes in BVOC emission fluxes. The use of on-line instrumentation, including PTR-MS and ToF-CIMS, allows continuous monitoring, providing temporal profiles which enables the detection of changes due to alterations in environmental conditions[154]. These techniques provide highly time resolved data, but have limited capacity to identify the specific BVOCs involved, beyond providing a chemical formula.

The emission of BVOCs depends on multiple environmental factors, which can be monitored or controlled during emissions sampling. Some studies, particularly those in a laboratory setting apply a controlled CO_2 concentration to the plants under investigation[145], while other studies use ambient CO_2 and measure the

concentration[132]. Temperature is often measured from inside the enclosure[153], which is assumed to be the same as the leaf temperature. Studies employing the use of leaf cuvettes usually report leaf temperature[145]. PPFD is frequently measured from just above the enclosure[144]. Other measured parameters include relative humidity[145, 151], soil moisture[51] and stomatal conductance[6, 155].

3.1.3 BVOC Standardisation

BVOC emission studies are conducted over a range of environmental conditions. This leads to significant variation between BVOC emission fluxes, especially when measurements are taken at different temperature and PPFD conditions. To facilitate comparison between studies, BVOC emission fluxes are reported at standard conditions of 30 °C and 1000 µmol m^{-2} s^{-1}. For studies that do not have measurements at these conditions a standardisation procedure is applied, and the data is extrapolated to standard conditions. Several methods of standardisation exist, with the basis for the preferred method depending on whether the BVOC emission originates from a biosynthetic or pooled emission pathway.

In work carried out by Tingey et al. (1979 and 1980)[129, 156] and further studied by Guenther et al. (1991 and 1993)[128, 130] it was established that the emission of isoprene was solely biosynthetic, while the emission of monoterpenes was attributed to emission from storage pools only. Following experiments using eucalyptus, aspen, sweet gum and velvet bean at different PPFD and temperatures, equations were developed to describe the emission of isoprene and monoterpenes from plants. The emission fluxes are based on the emission flux at standard conditions and can be used to calculate the emission at any PPFD and temperature. The equation for isoprene emission is as follows:

$$E_{\text{isoprene}} = E_{\text{isoprene}}^{\text{standard}} \times C_{\text{L}} \times C_{\text{T}} \qquad \textbf{\textit{Equation 3.1}}$$

Where: E_{isoprene} is isoprene emission flux at the measured temperature and PPFD in μg h^{-1} g^{-1}; $E_{\text{isoprene}}^{\text{standard}}$ is the isoprene emission flux in μg h^{-1} g^{-1} at standard conditions of 30 °C and 1000 μmol m^{-2} s^{-1}; C_L and C_T are factors to account for the PPFD and temperature dependence of the emissions respectively. C_L is described by:

$$C_{\text{L}} = \frac{\alpha \times c_{\text{L1}} \times L}{\sqrt{1 + (\alpha^2 \times L^2)}} \qquad \textbf{\textit{Equation 3.2}}$$

Where: α and c_{L1} are empirical constants with values 0.0027 and 1.066 respectively; and L is the PPFD in μmol m^{-2} s^{-1}. The temperature dependence of biosynthetic emissions is described by Equation 3.3:

$$C_{\text{T}} = \frac{\exp\left(\frac{c_{\text{T2}} \times (T - T_{\text{S}})}{R \times T \times T_{\text{S}}}\right)}{1 + \exp\left(\frac{c_{\text{T3}} \times (T - T_{\text{M}})}{R \times T \times T_{\text{S}}}\right)} \qquad \textbf{\textit{Equation 3.3}}$$

Where: c_{T2} is an empirical constant of value 95,000 J mol^{-1}; T is the measured temperature in K; T_S is standard temperature, 303 K; R is the universal gas constant, 8.314 J K^{-1} mol^{-1}; c_{T3} is an empirical constant of value 230,000 J mol^{-1}; and T_M is the temperature of maximum enzyme activity in K. These equations have been used in multiple studies to standardise isoprene emissions[72, 143].

The emission of monoterpenes is solely temperature dependent, and is described by Equation 3.4:

$$M = M_{\text{S}} \times \exp\left(\beta \times (T - T_s)\right) \qquad \textbf{\textit{Equation 3.4}}$$

Where: M is the measured monoterpene emission flux in μg h^{-1} g^{-1}; M_S is the monoterpene emission flux in μg h^{-1} g^{-1} at standard temperature, β is an empirical coefficient of value 0.09 K^{-1}, T is the measured temperature in K; and T_S is standard temperature, 303 K. This equation has also been used to standardise the emission of sesquiterpenes[123, 157], with the value of β varying between 0.9 and 0.12 K^{-1}.

Studies by Schuh et al. (1997)[132] on sunflower and beech found BVOC emissions to originate from a combined biosynthetic and pooled emission pathway. A combined equation was developed under the assumption that both emission pathways are completely independent, and the total emission flux is the sum of the emission flux from each pathway, Equation 3.5.

$$E_{\text{combined}} = E_{\text{pooled}} + E_{\text{biosynthsis}} \qquad \textbf{\textit{Equation 3.5}}$$

Where: E_{combined} is the total emission flux in μg h^{-1} g^{-1}, E_{pooled} is the temperature only dependent emission flux from storage pools in μg h^{-1} g^{-1}, using the monoterpene emission equation *M* developed by Guenther et al. (1991); and $E_{\text{biosynthesis}}$ is the biosynthetic emission flux, using the isoprene emission equation E_{isoprene} developed by Guenther et al. (1991). The coefficients in each equation were derived using the measurement data from sunflower and beech.

3.1.4 Aims

There were three aims for the work presented in this chapter on the BVOC emissions from Sitka spruce, the main plantation tree species in Ireland.

The first aim was to identify the main BVOCs emitted from Sitka spruce trees in a laboratory setting. A ToF-CIMS was used to monitor the emissions in real time and provide emission flux data. Samples were also collected onto adsorbent tubes and analysed offline via TD-GC/MS.

The second aim was to investigate the impacts of temperature and PPFD on the BVOC emissions and to determine the emission pathway for each BVOC. The BVOC emissions were then standardised for comparison with previous literature studies.

The third aim was to provide an annual emission flux for the three dominant BVOCs emitted from Sitka spruce in Ireland.

3.2 Experimental Methods and Analysis

3.2.1 Set-up for Emissions Sampling

The overall set-up for emissions sampling is shown schematically in Figure 3.1. Filtered outdoor air was passed over three Sitka spruce trees housed in individual enclosures inside a plant growth chamber. The BVOC emissions were carried into a ToF-CIMS for online analysis and were also collected using sorbent tubes for offline chemical analysis.

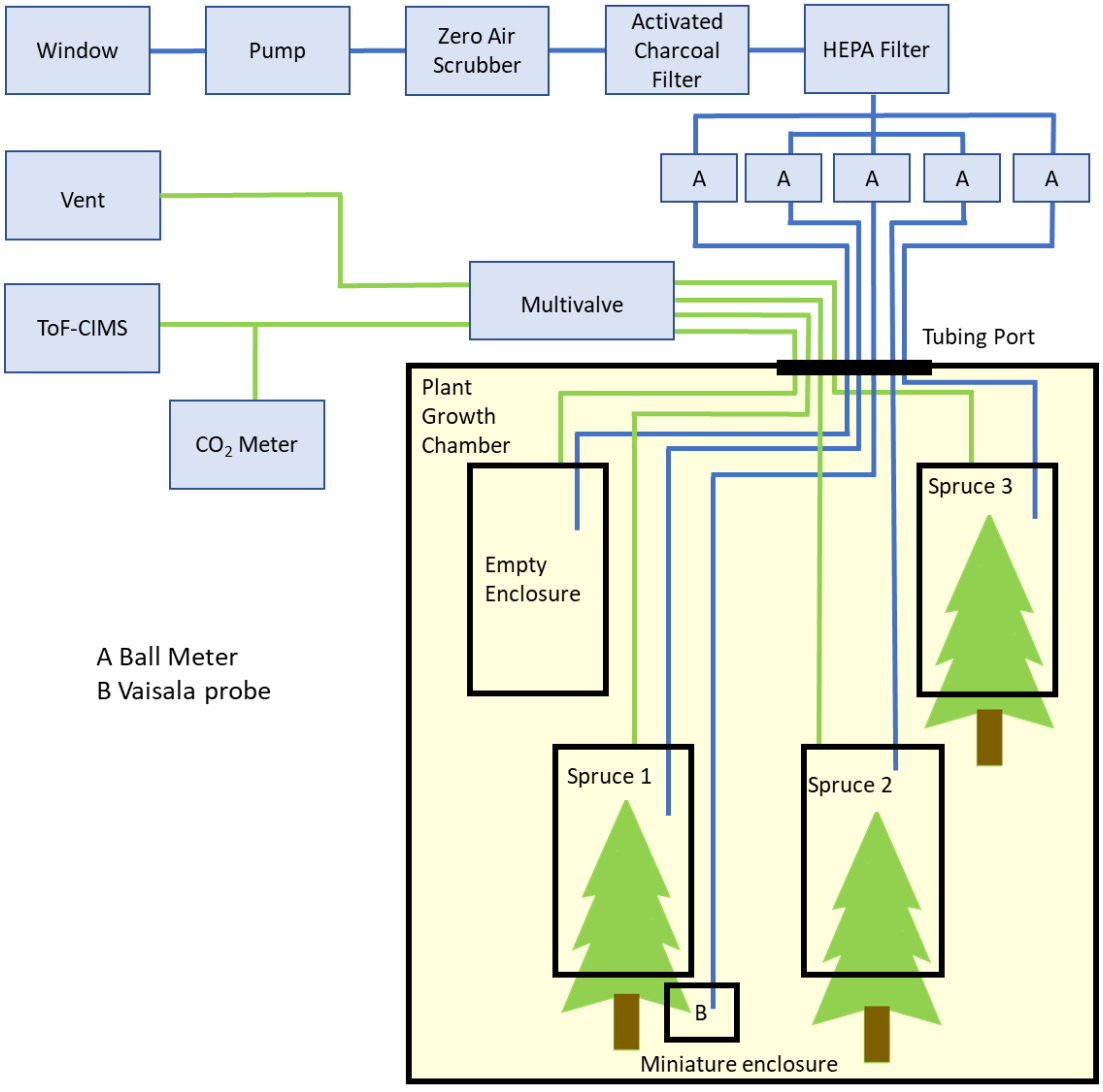

Figure 3.1 *Schematic of emissions sampling set-up.*

3.2.1.1 Air Supply

Filtered outdoor air was used to supply the enclosures. Outdoor air was chosen rather than ambient laboratory air or synthetic air, to provide the trees with conditions (humidity, CO_2, etc.) as close to ambient as possible. The air was sampled through an open window, at 32 L min^{-1} with a pump (Becker VT4.4). The air was passed through a zero air scrubber (OPT 86C, Teledyne) and a home-made activated charcoal filter (Hatchwells granulated charcoal) to remove atmospheric oxidants and VOCs, as well as a HEPA filter (TSI) to remove any particles present. The cleaned air was subsequently split into five separate flows, each regulated with a volumetric ball meter and connected to an enclosure. The flow into each enclosure was set to a value between 4.5 L min^{-1} and 7 L min^{-1}, depending on the degree of sealing of the enclosure.

On several occasions, very high concentrations of an unknown interferant was detected in the outdoor air, which distorted the ToF-CIMS measurements. When the presence of the interferent was suspected, the sample line was temporarily moved indoors and allowed to sample humidified compressed air, until the interference passed. As the sampled air was always characterised by the ToF-CIMS the temporary switch to humidified compressed air did not impact the BVOC emission measurements.

3.2.1.2 Trees

The emissions from three four-year old Sitka spruce trees were analysed in this study, Figure 3.2. For identification purposes the trees were named; Spruce 1, Spruce 2 and Spruce 3. The trees were grown from seed since spring 2017, at Fermoy Woodland Nursery, Co. Cork. In January 2020 they were placed in cold storage for six months, where they took on a state of dormancy. The trees were removed from cold storage in July 2020, planted in individual 5 L pots containing a peat soil, and immediately placed inside a plant growth chamber in a laboratory at the ERI, UCC. The trees were removed from the plant growth chamber in November 2020 for two months and placed in front of a south-facing window.

Figure 3.2 *The three Sitka spruce trees used in this work: Spruce 1 (left), Spruce 2 (middle) and Spruce 3 (right).*

Prior to reinstallation in the plant growth chamber in January 2021, all trees had dark green needles, with Spruce 1 having the largest amount of foliage and Spruce 3 the least. Spruce 1 and Spruce 3 had visible resin deposits on their tree trunks, Figure 3.3. A month prior to emissions sampling Spruce 1 produced new shoots, the majority of which were outside the enclosure. Emissions sampling began in November 2021, when the trees were approximately four years old, and ranged in height from 60 cm to 75 cm. The trees were watered twice a week with 350 mL of tap water each, and did not receive any fertiliser treatment.

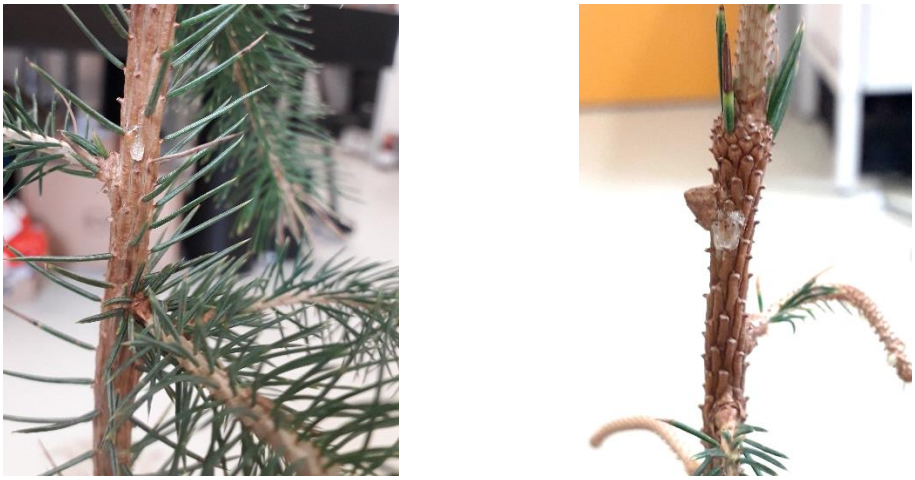

Figure 3.3 *Resin deposits on Spruce 1 (left) and Spruce 3 (right).*

3.2.1.3 Enclosures

Individual cylindrical Teflon enclosures were made for each spruce tree, using clear 0.1 mm thick Teflon FEP foil[148], Figure 3.4. The enclosures were designed to encompass all except the bottom few branches of the trees, and to minimise contact between the contained branches and the interior wall of the enclosure[72, 148]. Plastic box lids, lined with Teflon FEP foil, were used to seal the enclosures at the top. To seal the bottom of the enclosures, the trunk of the tree was wrapped with tissue paper and then aluminium foil, and the enclosure was secured around the aluminium foil with cable ties. The tops of the enclosures were fitted with a ¼" inlet port and a ½" outlet port. A length of ¼" Teflon tubing extended 20 cm from the inlet port into the enclosure to ensure homogenisation[142]. The enclosures were sealed around the trees a week before emissions sampling was commenced.

A separate, Empty enclosure, was made for background measurements[83], Figure 3.4. The top of the enclosure consisted of a piece of FEP Teflon foil attached to a plastic ring. The bottom of the Empty enclosure was sealed around the bottom of a laboratory glass bottle with Teflon tape and cable ties.

Figure 3.4 *Enclosure around Spruce 3 (left), and Empty enclosure (right).*

A miniature enclosure was made to facilitate temperature and relative humidity measurements. Measurements were taken from inside the enclosure to account for any changes in conditions due to the presence of the enclosure[143], which was supplied with the same filtered air. The miniature enclosure was sealed around a temperature and relative humidity probe (dewpoint probe DMP74A, Viasala, Finland), and one of the lower branches of Spruce 1. Temperature and relative humidity measurements were recorded manually every 30 minutes during working hours only.

3.2.1.4 Plant Growth Chamber

The Sitka spruce trees were housed in a plant growth chamber (Panasonic MLR-352) throughout the emissions sampling period, Figure 3.5, which was capable of accommodating up to four small trees. A port in the roof of the plant growth chamber was used to supply tubing to and from the enclosures. The two interior side walls and door of the plant growth chamber were each equipped with five photosynthetically activating lamps. The lamps extended from the floor to the ceiling and provided a PPFD range from 0 µmol m^{-2} s^{-1} (no lamps illuminated) to 250 µmol m^{-2} s^{-1} (all lamps

illuminated when empty). The temperature was adjustable between 5 °C and 40 °C. The plant growth chamber settings for PPFD and temperature could be programmed and saved as a cycle[158].

Figure 3.5 *Plant growth chamber exterior (left)[159], and interior with Spruce trees inside (right).*

3.2.1.5 Multivalve

The use of a flow-through multivalve (Multiposition Actuator EMTMA-CE, Vici Valco) allowed rapid and controlled sample switching between the various enclosures, Figure 3.6.

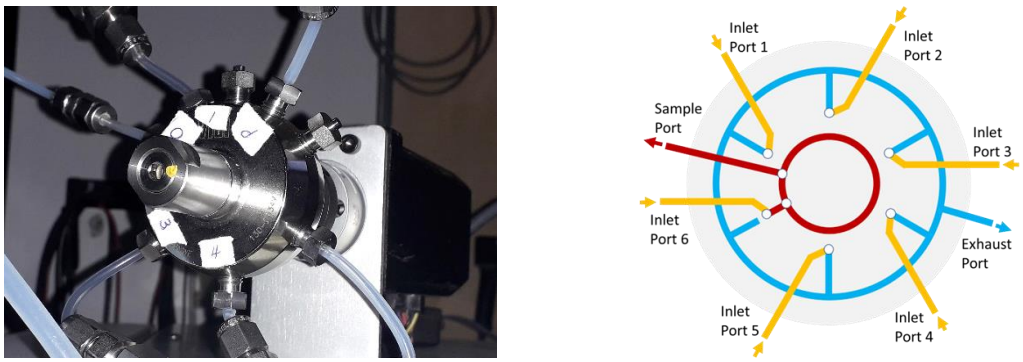

Figure 3.6 *Multivalve with connections to enclosures (left), and internal operation (right).*

The multivalve consisted of a rotatable valve with six inlet ports, a sample port and an exhaust port. At any time a single inlet port was connected to the sample port which supplied the ToF-CIMS, while the remaining inlet ports were connected to the exhaust port which was externally pumped to ensure that all lines were continually flushed preventing dead volume effects. Switching the connection between the inlet port and various sample ports was programmed and controlled with VCom software. VCom allows the user to generate switching cycles, which controls the duration of the connection between the inlet port and the sample port, and the order in which inlet ports are connected.

3.2.1.6 ToF-CIMS

The ToF-CIMS was used to monitor the BVOC emissions from the Sitka spruce trees in real time. The basic operation of the ToF-CIMS used in this work is described in Chapter 2. Benzene was selected as the reagent ion for these measurements because of its ability to ionise compounds with a low oxygen content and hydrocarbons such as monoterpenes, which are typical of biogenic emissions[106]. The voltages and pressures applied to the ToF-CIMS were controlled via TOFWERK TPS Settings and were based on the optimised configuration determined during instrument tuning on 08/07/2021. Trichlorobenzene ($C_6H_3Cl_3$) (Sigma Aldrich, 99%), was used as an internal mass calibrant, by allowing it to diffuse into the inlet of the instrument.

3.2.1.7 CO_2 Meter

A CO_2 meter (K30 ELG 10,000 ppm CO_2 Data Logging Sensor) was used to monitor photosynthetic activity. The operation of the CO_2 meter is based on near infra-red absorption and was controlled with GasLab software, which recorded a measurement every 10 s.

3.2.2 Experimental Procedures

3.2.2.1 PPFD and Temperature

A Light meter (LI-250, LI-COR Light Meter) was used to measure PPFD in the centre of the plant growth chamber with all three Sitka spruce trees and enclosures present. The measurements were taken before and after the emissions sampling cycles. The plant growth chamber door remained closed during PPFD measurements.

The average PPFD values recorded at the three light settings were 21 µmol m^{-2} s^{-1}, (one lamp on), 44 µmol m^{-2} s^{-1} (two lamps on) and 164 µmol m^{-2} s^{-1} (three lamps on). These values are much lower than those reported for natural sunlight, which can exceed 1,600 µmol m^{-2} s^{-1} under clear sky conditions[152, 160]. In Ireland PPFD is usually much lower than this due to the high prevalence of cloud cover. PPFD measurements recorded in Co. Cork were found to reach maximum values of 350 µmol m^{-2} s^{-1} in the winter and up to 1000 µmol m^{-2} s^{-1} in the summer[161, 162].

Temperature measurements were recorded from inside the miniature enclosure, to account for temperature increases due to the greenhouse effect from the enclosure surrounding the spruce trees[143]. The temperatures applied to the plant growth chamber were representative of the Irish summer, which have day and night mean temperatures of 18 °C and 11 °C respectively.

3.2.2.2 Plant Growth Chamber Cycles

Three different plant growth cycles were used to assess the impact of temperature and PPFD on the BVOC emissions from the Sitka spruce trees. Each cycle was 24 hours long and was applied to the plant growth chamber for at least a week. Prior to BVOC emissions sampling an acclimation period of two to three days was applied to allow the trees sufficient time to adapt to the new conditions.

Daily Cycle

The *Daily Cycle* was the first cycle applied to the plant growth chamber. For the *Daily Cycle* the trees were subject to conditions as similar as possible to Irish summer

conditions, in which temperature and PPFD increase simultaneously to a maximum and decrease. The purpose of the *Daily Cycle* was to determine the BVOC and CO_2 emissions from the Sitka spruce trees, and to assess variations in BVOC emissions and photosynthesis in response to changes in PPFD and temperature. Figure 3.7 shows the PPFD and temperature variation during the *Daily Cycle*.

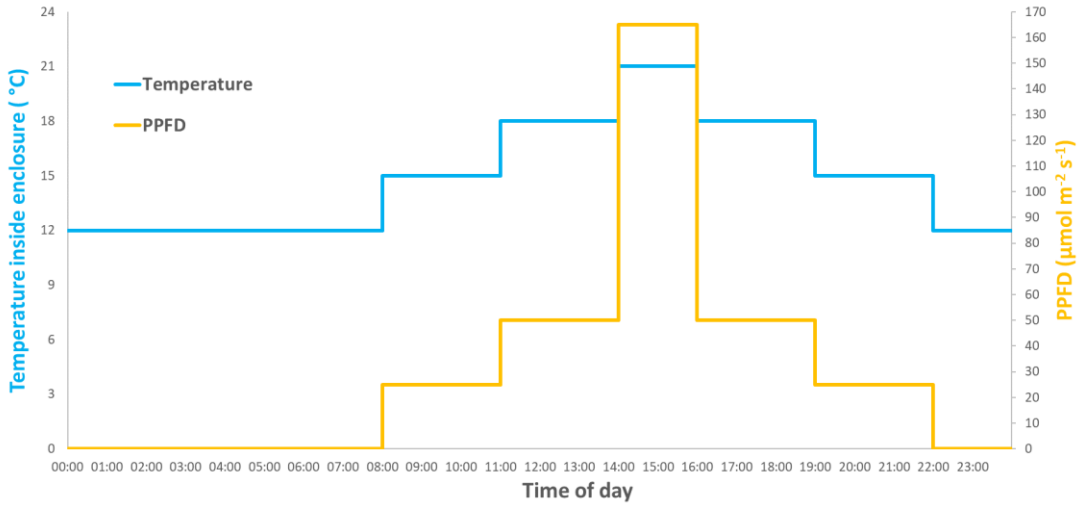

Figure 3.7 *Temperature and PPFD variation during the Daily Cycle.*

The conditions for the *Daily Cycle* were a repeating 24 hour cycle of: 10 hours of darkness at 12 °C; 3 hours at 21 µmol m^{-2} s^{-1} and 15 °C; 3 hours at 44 µmol m^{-2} s^{-1} and 18 °C; 2 hours at 164 µmol m^{-2} s^{-1} and 21 °C; 3 hours at 44 µmol m^{-2} s^{-1} and 18 °C; and 3 hours at 21 µmol m^{-2} s^{-1} and 15 °C. The trees were subject to these conditions for three days prior to sampling emissions. The *Daily Cycle* commenced on 04/11/2021 and ran until 12/11/2021.

Temperature Cycle

The purpose of the *Temperature Cycle* was to determine the effect of temperature alone on BVOC emissions and photosynthesis. During the hours of illumination a constant PPFD of 44 µmol m^{-2} s^{-1} was applied[132], Figure 3.8.

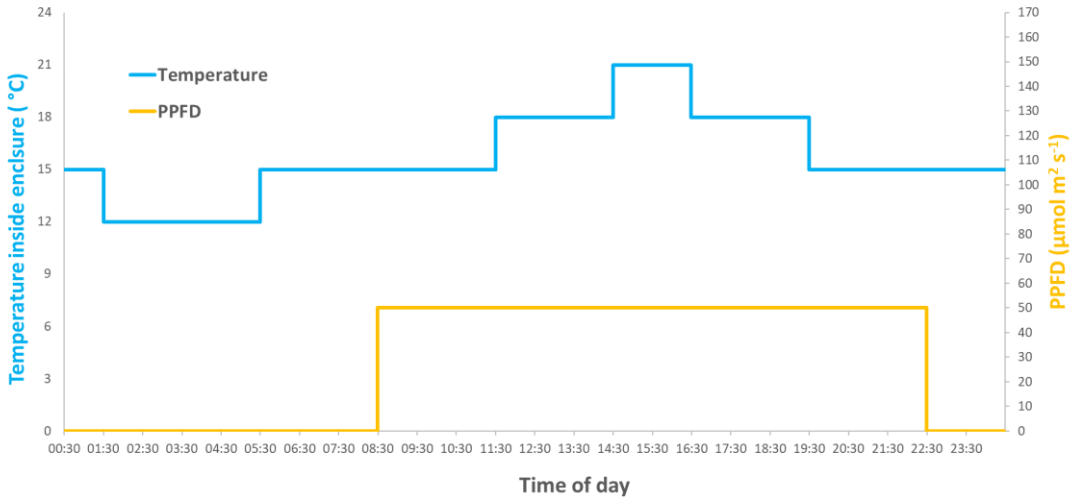

Figure 3.8 *Temperature and PPFD variation during the Temperature Cycle.*

The conditions for the *Temperature Cycle* were: 4 hours of darkness at 12 °C; 3 hours of darkness at 15 °C; 3 hours of illumination at 15 °C; 3 hours of illumination at 18 °C; 2 hours of illumination at 21 °C; 3 hours of illumination at 18°C; 3 hours of illumination at 15 °C; and 3 hours of darkness at 15 °C. The *Temperature Cycle* was operated from 15/11/2021 to 24/11/2021.

Light Cycle

The final cycle applied to the plant growth chamber was the *Light Cycle*. The purpose of the *Light Cycle* was to identify changes in BVOC emissions and photosynthesis resulting from variations in PPFD only. A constant temperature of 18 °C was applied for the duration of the *Light Cycle*, Figure 3.9[132].

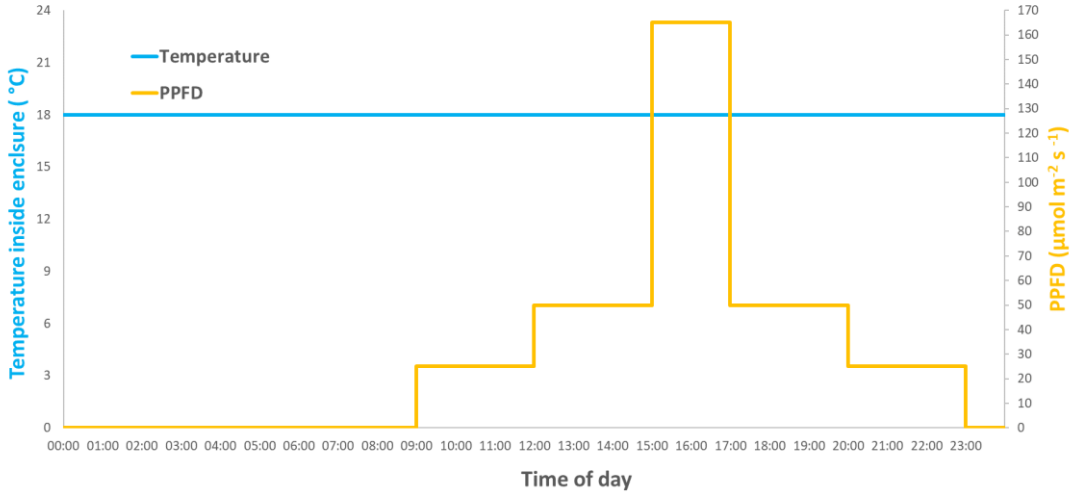

Figure 3.9 *Temperature and PPFD variation during the Light Cycle.*

During the *Light Cycle* PPFD was varied according to: 10 hours of darkness; 3 hours at 21 µmol m^{-2} s^{-1}; 3 hours at 44 µmol m^{-2} s^{-1}; 2 hours at 164 µmol m^{-2} s^{-1}; 3 hours at 44 µmol m^{-2} s^{-1}; and 3 hours at 21 µmol m^{-2} s^{-1}. The trees were subject to the conditions for the *Light Cycle* for two days before sampling was commenced. Emission sampling for the *Light Cycle* started 26/11/2021 and stopped 03/12/2021.

3.2.2.3 Emission Sampling

On-line Sampling

The outflows from the three Spruce enclosures and the Empty enclosure were each connected to an inlet port on the multivalve. The remaining two inlet ports were not used and remained sealed. The multivalve was programmed to connect the sample port with each inlet port for 7.5 minutes, in the following order: Empty enclosure, Spruce 2, Spruce 1, Spruce 3. This 30-minute cycle was continuously repeated. The other end of the sample port was connected to the ToF-CIMS and CO_2 meter.

Off-line Sampling

After completion of the three plant growth cycles, emissions were collected onto Tenax tubes (Markes Tenax TA, C1-CAXX-5003). To account for any potential residue remaining on the Tenax tubes from previous use, two tubes were unopened. Four Tenax tubes were used to simultaneously collect samples from the four enclosures

with conditions in the plant growth chamber set to 44 µmol m^{-2} s^{-1} and 18 °C and another four were collected with conditions set to 164 µmol m^{-2} s^{-1} and 24 °C.

Sampling onto the Tenax tubes did not commence until an hour after the conditions in the plant growth chamber had been set[81]. The samples were collected at a flow rate of 200 mL min^{-1} for 2 hours[152]. Following collection the Tenax tubes were sealed, individually wrapped in aluminium foil, placed into separate zip lock bags, and stored in a refrigerator[163] until analysis could be performed.

3.2.2.3 Measured Parameters

Chlorophyll Fluorescence

A chlorophyll fluorescence meter (Hansatech FMS2) was used to monitor the degree of chlorophyll fluorescence in the Sitka spruce needles. Chlorophyll fluorescence measurements were recorded twice a day, three days per sampling cycle. One measurement was taken 30 minutes prior to illumination and a further measurement was taken 90 minutes into the maximum PPFD and temperature setting.

Three branches on each tree were selected for measurements. Clips were placed over the needles for dark adaptation for 30 minutes before a measurement. Measurements were taken by fitting the head of the chlorophyll fluorescence meter to the clip and opening the clip window. The needles were exposed to a weak modulated red light source to determine the minimum fluorescence (F_0). A saturating pulse of white light was then applied to determine the maximum fluorescence (F_m). The variable fluorescence (F_v) was determined as F_m - F_0, and the maximum photosystem II efficiency determined as F_v/F_m[126].

Biomass

Following all measurements the Sitka spruce trees were cut, and all biomass contained within the enclosures was removed. The needles and branches from each tree were dried at 60 °C for 72 hours[83] using incubators (Memmert IN110 Incubator). When drying was completed a mass balance (Explorer OHAUS, E02140) was used to

determine the mass of the needles only, as well as the mass of the needles plus branches for each tree. The results are presented in Table 3.1.

Table 3.1 *Dried biomass measurements for each spruce tree.*

	Dried Needle Mass **g**	**Dried Needle and Branch Mass** **g**
Spruce 1	8.03	18.50
Spruce 2	9.80	19.56
Spruce 3	3.77	11.33

3.2.3 Analysis

3.2.3.1 CO_2

Calibration

The CO_2 meter was zero calibrated by allowing it to sample N_2 (BOC, oxygen free), and the reading set to 0 ppm using the GasLab software. The CO_2 meter was subsequently connected to the chamber at the ERI and CO_2 from a gas cylinder (BOC, 99.8%) was added to the chamber in aliquots of either 100 ppm or 200 ppm. A calibration curve was generated and used to determine the calibration coefficient.

Data Analysis

CO_2 data was recorded with GasLab software. Any data points recorded while the CO_2 meter was disconnected from the sample tubing were removed. CO_2 data for each measurement cycle was analysed using R Studio 4.0.2. All data was corrected using the CO_2 calibration factor. The last 2 minutes of the 7.5 minute sampling period for each of the four enclosures were used to generate 30 minute averages. The CO_2 flux was calculated for each spruce tree according to Equation 3.6:

$$CO_2\ Flux = \frac{(Spruce_{CO_2} - Empty_{CO_2}) \times Flow \times Factor_{CO_2}}{N_A \times Biomass} \qquad \textbf{\textit{Equation 3.6}}$$

Where: *CO_2 Flux* is the flux of CO_2 in nmol s^{-1} g^{-1}; *Spruce* $_{CO_2}$ is the CO_2 concentration from the spruce enclosure in ppm; *Empty*$_{CO_2}$ is the CO_2 concentration from the Empty

enclosure in ppm; *Flow* is the flow through the Spruce enclosure in m^3 h^{-1}; N_A is Avogadro's number in mol^{-1}; *Biomass* is the mass of the needles in g; and $Factor_{CO_2}$ is a constant in h ppm^{-1} m^{-3} s^{-1}, which accounts for unit conversions.

3.2.3.2 ToF-CIMS

VOC Calibrations

To quantify BVOC emissions from the Sitka spruce trees, calibration coefficients were applied to the ToF-CIMS measurements. Calibration coefficients were determined for δ-3-carene, β-myrcene, camphor (Sigma Aldrich, purity 90%, 75% and 98%, respectively) and piperitone (Santa Cruz Biotechnology, purity > 94%).

Calibrations were carried out by connecting the ToF-CIMS to the atmospheric simulation chamber at the ERI. N_2 was flowed through a glass impinger containing a measured volume of the BVOC, and admitted into the chamber[164]. Upon reaching a stable concentration measured by the ToF-CIMS, further additions of the BVOC were performed. Calibration curves were generated from the calculated mixing ratios of the standards and the CIMS response, and were subsequently used to determine calibration coefficients for each BVOC.

Due to the size of the chamber, and the difficulty in injecting very small volumes of BVOC to achieve low concentrations, the measurements from the Sitka spruce trees were below the range of the calibration curves. As a result, it was assumed that the ToF-CIMS had a linear response over the full range of concentrations measured during BVOC emissions sampling and calibrations. The calibration coefficients for the four BVOCs were applied to various ions detected with the ToF-CIMS according to the composition and manner in which the particular BVOCs were ionised.

ToF-CIMS Data Analysis

Data collected by the ToF-CIMS were analysed with Tofware 3.2.0, operated through IGOR Pro 7.08. Firstly, 1 Hz data were averaged to a 10 s time resolution. Following this, a mass calibration was performed using $C_6H_6^+$ (*m/z* 78.05), $C_6H_3Cl_3^+$ (*m/z* 179.93),

$C_{12}H_{23}N_2O_2^+$ (*m/z* 227.18), $C_{12}H_{22}N_2O_4^+$ (*m/z* 258.16) and $C_{18}H_{27}N_2O_2^+$ (*m/z* 303.21). The nitrogen containing calibrants are benzene clusters of an interferant originating from the N_2 supply, $C_6H_{11}NO$. The remaining data analysis steps included correction of the baseline position, peak shape and peak resolution. Chemical formulae were then assigned to peaks within the calibrated mass range. Only formulae containing the elements C, H, O, N and Cl were assigned. If an appropriate formula could not be determined, the peak was left unassigned, and excluded from further analysis.

After completing peak assignment, all data was exported from Tofware, and data points recorded during periods of interference were removed. Two separate types of interference events occurred during the *Daily Cycle*. On two occasions the CO_2 meter became disconnected, which caused contamination of the ToF-CIMS sample line with laboratory air. The second type of interference was due to a sudden spike in the abundance of $C_{10}H_{15}^+$, *m/z* 135, which appeared occasionally during all measurement cycles. Due to difficulties in identifying the source, which originated from outside of the laboratory, it was decided to remove the data during the affected time periods.

Scripts for the analysis of the ToF-CIMS data were written using R Studio 4.0.2. Initially all signals were normalised to the reagent ion signal, $C_6H_6^+$. The data from the last 2 minutes of the measurement period for each sample (Spruce 1, Spruce 2, Spruce 3 and Empty enclosure) were taken as the average for that 30 minute sampling cycle. This approach was adopted to allow sufficient time for the emission fluxes to stabilise following the switching of samples.

A Welch T-test was performed on the data from the *Daily Cycle* to remove background signals. Only spruce ions with a P-value of less than 0.05 when compared with three times the ion concentration from the Empty enclosure, at a PPFD greater than 40 µmol m^{-2} s^{-1}, were identified as statistically significant emissions. Further filtering was carried out to remove clusters and fragments. Only ions identified in the *Daily Cycle* were analysed for the *Temperature Cycle* and *Light Cycle*.

The ion concentrations for each spruce tree were then converted to emission fluxes using Equation 3.7:

$$Emission\ Flux_{\mathrm{BVOC}} = \frac{(Spruce_{\mathrm{BVOC}} - Empty_{\mathrm{BVOC}}) \times Flow \times Mw_{\mathrm{BVOC}} \times Factor}{N_{\mathrm{A}} \times Biomass} \qquad \textbf{Equation 3.7}$$

Where: *Emission Flux*$_{\mathrm{BVOC}}$ is the flux of that BVOC from that spruce tree in µg h^{-1} g^{-1}; *Spruce*$_{\mathrm{BVOC}}$ is the concentration of the ion as measured by the ToF-CIMS for the spruce tree in ions s^{-1}; *Empty*$_{\mathrm{BVOC}}$ is the concentration of the ion as measured by the ToF-CIMS from the Empty enclosure in ions s^{-1}; *Flow* is the flow through the Sitka spruce enclosure in m^3 h^{-1}; *Mw*$_{\mathrm{BVOC}}$ is the molecular weight of the BVOC in g mol^{-1}; *Biomass* is the mass of the dried needles and branches in g; and *Factor* is a constant to account for unit conversions[83] in $ions^{-1}$ s^{-1} m^{-3}.

The emission fluxes were standardised to a PPFD of 1000 µmol m^{-2} s^{-1}, and a temperature of 30 °C according to Equations 3.1, 3.4 and 3.5 in Section 3.1.3, developed by Guenther et al. (1993)[130] and adapted by Schuh et al. (1997)[132].

3.2.3.3 TD-GC/MS

VOC Identification

The presence of specific BVOCs in the Sitka spruce emissions was confirmed using TD-GC/MS with the use of standards. The experimental work and analysis was carried out by Iwona Skibinska at the Teagasc Food Research Centre, Moorepark, Fermoy, Co. Cork, Ireland. The presence of isoprene, α-pinene, β-pinene, myrcene, camphene, camphor (Sigma Aldrich, purities 99%, 98%, 99%, 75%, > 96% and 98%, respectively) and piperitone (Santa Cruz Biotechnology, purity 94%) were verified in this manner.

Standard solutions were prepared according to standard procedures employed at the Teagasc Laboratory. Stock solutions were made by diluting the standards in methanol, these were diluted to 1 ppm working solutions with deionised water. The working solutions were then injected into Tenax tubes in 10 µl volumes.

The Tenax tubes were dried for 2 minutes using a 1:20 split with N_2, before undergoing a 5-minute thermal desorption (Unity 2 Thermal Desorption Unit, Markes International Ltd) at 150 °C, this was followed by a secondary desorption at 280 °C for 5 minutes. During the desorption BVOCs were collected onto a materials emissions trap. A 2-minute fire purge was applied to the trap with a 1:50 split, the BVOCs on the trap were then desorbed with a temperature ramp of 24 °C min^{-1} with a 1:10 split for 5 minutes[165].

Following desorption, BVOCs were admitted into a Gas Chromatograph-Mass Spectrometer (Agilent 7890A GC and Agilent 5977B MSD) fitted with a 60 m capillary column (Agilent Technologies Ltd, DB 624 UI). The BVOCs were injected onto the column using a 250 °C injector. The column temperature was initially held at 40 °C for 5 minutes, and then increased at a rate of 5 °C min^{-1} to 230 °C where it remained for 35 minutes. The BVOCs were detected using a quadrupole MS detector[165].

The Tenax tubes were analysed in conjunction with a standard solution, consisting of 1-butanol, dimethyl sulfide, butyl acetate and cyclohexanone. Standard tubes were run at the start and at the end of the sample set, and empty tubes were run between different samples.

TD-GC/MS Data Analysis

The chromatograms generated from each tube were analysed with MassHunter Qualitative Analysis Navigator (B.08.00, 2016). BVOC identification was verified using retention indices and fragmentation patterns according to an in-house spectral library and the NIST 2014 mass spectral library with the assistance of the AMDIS software package (2.72, June 2014).

3.3 Results and Discussion

3.3.1 Composition

In total seventy-four BVOCs were detected in the emissions from all three Sitka spruce trees using the ToF-CIMS and TD-GC/MS, Table 3.2. While there was some variation between the trees, there was also a degree of consistency, with each tree emitting the same twenty-one BVOCs.

Table 3.2 *BVOC emissions from all Sitka spruce trees detected with ToF-CIMS and TD-GC/MS.*

Formula	Mw	Name	Spruce 1		Spruce 2		Spruce 3	
	g mol^{-1}		ToF-CIMS	TD-CG/MS	ToF-CIMS	TD-GC/MS	ToF-CIMS	TD-CG/MS
C_3H_9N	59.11		✓					
$C_2H_4O_2$	60.05	Acetic acid				✓		
C_5H_8	68.12	Isoprene	✓	✓		✓		✓
C_4H_6O	70.09	Methacrolein				✓		
$C_3H_6O_2$	74.08	Propanoic acid		✓		✓		✓
$C_4H_{10}O$	74.12	1-Butanol				✓		✓
C_6H_8	80.13				✓			
C_5H_6O	82.10	2-Methyl-furan		✓		✓		✓
C_5H_8O	84.12	E-3-Penten-2-one				✓		
$C_5H_{10}O$	86.13	2-Methyl-3-buten-2-ol		✓				✓
		2-Pentanone		✓		✓		✓
		Pentanal				✓		
$C_4H_8O_2$	88.11	Butanoic acid				✓		
$C_3H_8N_2O$	88.11		✓					
$C_5H_{12}O$	88.15	3-Methyl-1-butanol		✓		✓		✓
C_7H_8	92.14		✓		✓			
C_6H_6O	94.11	Phenol				✓		
C_6H_8O	96.13				✓*			
$C_6H_{10}O$	98.15	E-2-Hexenal			✓	✓		
$C_5H_8O_2$	100.13		✓					
$C_6H_{12}O$	100.16	Hexanal				✓		
		2-Hexanone				✓		
C_7H_{16}	100.20	Heptane		✓		✓		✓
$C_6H_{14}O$	102.18	1-Hexanol		✓		✓		✓
C_7H_8O	108.14		✓		✓			
C_8H_{12}	108.18		✓		✓			
$C_7H_{10}O$	110.15				✓			
$C_5H_{10}NO_2$	117.15		✓					

C_8H_8O	120.15	Acetophenone				✓		
C_9H_{12}	120.19		✓		✓			
$C_7H_{12}N_2$	124.18		✓					
$C_8H_{12}O$	124.18				✓			
$C_8H_{16}O$	128.21	1-Octen-3-ol				✓		
$C_{10}H_{10}$	130.19		✓					
$C_8H_{18}O$	130.23	2-ethyl-1-hexanol				✓		
$C_{10}H_{14}$	134.22	o-Cymene		✓		✓		✓
C_9H_8O	132.16	(E)-Cinnamaldehyde	✓	✓	✓	✓		✓
$C_6H_{14}O_3$	134.18		✓					
$C_8H_8O_2$	136.15	Methyl benzoate		✓		✓		✓
$C_9H_{12}O$	136.19				✓			
$C_{10}H_{16}$	136.24	Monoterpene	✓		✓*			
		Myrcene		✓		✓		✓
		β-Phellandrene		✓		✓		✓
		δ-Limonene		✓		✓		✓
		a-Pinene		✓		✓		✓
		Camphene		✓		✓		✓
$C_8H_{12}O_2$	140.18				✓			
$C_9H_{10}O_2$	150.17				✓			
C_3H_9N	150.22		✓					
$C_7H_4O_4$	152.10		✓					
$C_8H_8O_3$	152.14	Methyl salicylate		✓	✓	✓		✓
$C_{10}H_{16}O$	152.23	Piperitone	✓	✓	✓	✓		✓
		Camphor	✓	✓	✓	✓		✓
$C_{10}H_{18}O$	154.25	Eucalptol		✓	✓	✓		✓
$C_{12}H_{16}$	160.25		✓					
$C_{11}H_{14}O$	162.23		✓					
$C_5H_{10}O_6$	166.13		✓					
$C_{10}H_{14}O_2$	166.22		✓		✓*			
$C_{10}H_{16}O_2$	168.24		✓					
$C_{10}H_{20}O_2$	172.26	Isopentyl isovalerate	✓	✓		✓		✓
$C_{12}H_{16}O$	176.26				✓			
$C_{12}H_{20}O$	180.29		✓					
$C_{10}H_{16}O_3$	184.23				✓			
$C_{13}H_{12}O$	184.24		✓					
$C_{14}H_{16}O$	200.28		✓		✓			
$C_{10}H_{18}O_4$	202.25		✓		✓			
$C_{15}H_{24}$	204.36	E-Farnesene			✓	✓		
$C_{10}H_{14}O_5$	214.22		✓					
$C_{17}H_{26}O$	246.39		✓		✓			
$C_{20}H_{24}$	264.40		✓		✓			
$C_{13}H_{30}O_5$	266.37		✓		✓			

$C_{18}H_{34}O$	266.46		✓		✓			
$C_{20}H_{24}O_2$	296.40		✓		✓			

** Isomers with different temporal trends detected by ToF-CIMS as different ions. Counted as two distinct BVOCs.*

The BVOCs detected in the TD-GC/MS analysis from all three spruce trees were quite similar. All twenty-one BVOCs detected in the emissions from Spruce 1 were also detected in the emissions from the other trees. One additional BVOC (1-butanol) was present in the emissions from Spruce 2, which was also detected in the emissions from Spruce 3. The BVOC emissions from Spruce 2 were the most unique, consisting of twelve compounds that were not detected in the emissions of either of the other two trees. The ToF-CIMS detected sixteen BVOCs common to the emissions of both Spruce 1 and Spruce 2. These results indicate that it is possible for similarly aged Sitka spruce trees in the same environment to have different BVOC emission profiles, as observed for other plant species[68].

The majority, 70%, of the BVOCs detected from all three spruce trees were oxygenated compounds. This observation is somewhat different from reports in the literature, which typically identify isoprene[166], monoterpenes[167] and sesquiterpenes[168] as the dominant biogenic emissions. The contribution from oxygenated BVOCs is usually quite low, and the reporting is typically restricted to specific groups: small compounds such as acetone[26] and methanol[15], GLVs[169] and the $C_{10}H_{18}O$ isomers, including linalool[70] and eucalyptol[71]. Few studies have reported oxygenated BVOCs that fall outside these groups[62, 144]. The high proportion of oxygenated BVOCs detected in this study is potentially due to the capabilities of the instrumentation used. In particular, $C_6H_6^+$ ToF-CIMS is suited to the detection of hydrocarbons and certain oxygenated compounds[93]. In contrast, GC-MS and PTR-MS which are traditionally used in the analysis of BVOCs, tend to focus on the detection of hydrocarbons and small oxygenated compounds[19, 81].

3.3.1.1 Spruce 1

In total forty-nine different BVOCs were detected in the emissions from Spruce 1, as shown in Table 3.2. TD-GC/MS analysis identified twenty-one different BVOCs, which included eight hydrocarbons and thirteen oxygenated compounds, with nine of these containing only one oxygen atom in their molecular formula. The carbon content of the BVOCs ranged from C_3 to C_{10}, with ten C_{10} compounds and five C_5 compounds. Three sets of isomeric structures were also identified. Two BVOCs were identified as $C_{10}H_{16}O$, piperitone and camphor. Five were detected as monoterpenes ($C_{10}H_{16}$). Two compounds were found to have the chemical formula $C_5H_{10}O$, isoprenyl alcohol and 2-pentanone.

ToF-CIMS analysis enabled the detection of thirty-four BVOCs in the emissions from Spruce 1. Note that the ToF-CIMS is not capable of providing structural information, only a chemical formula is attained. Eight of the BVOCs detected by the ToF-CIMS were hydrocarbons. Four were found to contain nitrogen in the chemical formula, two CHN compounds and two CHON compounds. The detection of nitrogen containing compounds in BVOC emissions in not frequently reported in the literature. The remaining twenty-two BVOC emissions were oxygen containing. The oxygen content of the BVOCs varied between O_0 and O_6, with twelve O_1 compounds and six O_2 compounds. The carbon content of the BVOCs ranged from C_3 to C_{20}, with ten being C_{10} compounds.

Chemical structures for six of the BVOCs detected by the ToF-CIMS were confirmed from the TD-GC/MS analysis. Five of the compounds identified were in the top ten emissions; piperitone, isoprene, sum of monoterpenes, cinnamaldehyde (C_9H_8O), and camphor. Due to different ionisation mechanisms in the ToF-CIMS piperitone and camphor were detected as different ions. Isopentyl isovalerate ($C_{10}H_{20}O_2$) was also identified with both analysis methods.

An oxygenated monoterpene, piperitone ($C_{10}H_{16}O$) was the main BVOC emitted from Spruce 1 and was also detected in the emissions of both other trees. Piperitone has

been identified as a BVOC emission in previous studies, but never as the main emitted BVOC. Piperitone was identified as a minor emission from damaged Sitka spruce branches, with the sum of the concentration of the isomers piperitone and camphor found to be over an order of magnitude lower than the sum of monoterpene concentration[82]. The elevated piperitone concentration in this work may be related to differences in environmental conditions between this work and other studies, or due to different chemotypes, as has previously been reported for Scots pine[68]. Piperitone has also been detected as a BVOC emitted by Norway spruce[170] and Ponderosa pine[67]. Several studies on the needle oil[86-88] and cortical resin[87] of Sitka spruce found it to be composed mainly of myrcene ($C_{10}H_{16}$), and the $C_{10}H_{16}O$ isomers, piperitone and camphor. In all studies, the proportion of piperitone in the leaf oil and cortical resin was always greater than for camphor. The detection of camphor in the BVOC emissions of Sitka spruce[79, 82], is more common than for piperitone, implying that in the emissions camphor is the dominant isomer. In this work, the ratio of piperitone to camphor in the emissions was quite high for all trees, and was similar to what has been reported in the literature for resin. Resin deposits were visible on the trunks of Spruce 1 and Spruce 3 and may also have been present on Spruce 2. The high piperitone to camphor ratio observed in this study indicates that evaporation from the resin deposits may have contributed to the BVOC emissions detected from the Sitka spruce trees.

The second highest emission from Spruce 1 was isoprene, which was also detected in the emissions of Spruce 3, with minimal amounts in the emissions of Spruce 2. Isoprene has been detected in the emissions of various spruce species, including Sitka spruce[79, 81, 171], Norway spruce[155, 172], and several others[131, 149]. Isoprene has been reported as a minor emission for other coniferous species including Scots pine[72], although is it more commonly found in the emissions from deciduous species such as Holm oak[173] and willow[151].

The sum of monoterpene emissions were detected as the third highest emission from Spruce 1. In Table 3.2 the monoterpenes are ordered according to decreasing concentration, which were inferred from TD-GC/MS chromatogram peak areas. Five

monoterpenes were detected, myrcene, β-phellandrene, α-pinene, δ-limonene and camphene. Myrcene was identified as the dominant monoterpene from all three Sitka spruce trees. This observation is in agreement with previous studies which identified myrcene as the main BVOC emitted by Sitka spruce[81, 138, 166]. The emission of β-phellandrene as the next dominant monoterpene is consistent with previous Sitka spruce studies[81, 138]. This compound has also been detected in the emissions of other spruce species[79, 138]. The contributions from α-pinene [63, 79, 166], δ-limonene[63, 166] and camphene[63, 79, 166] were quite low, all of them have been detected in the emissions of Sitka spruce previously. Some studies have reported β-pinene[79, 81, 82] as a major emission from Sitka spruce, but it was not identified by TD-GC/MS in this work.

The remaining emissions contributed very little to the total BVOC flux of Spruce 1. The majority of the remaining hydrocarbon emissions have not been identified in previous studies. o-Cymene ($C_{10}H_{14}$) has been detected in the emissions from Blue spruce, Douglas-fir and Bristlecone pine[67]. Heptane (C_7H_{16}) has been detected in the air in a Sitka spruce forest in north England[12]. The BVOC emission detected as C_7H_8 in the ToF-CIMS analysis is likely toluene, but since this was also detected in quite high concentrations in the Empty enclosure and unopened Tenax tubes, it was deemed to be a background artefact and was not assigned as an emission. Toluene has not been detected in the emissions of Sitka spruce previously, although it has been reported as an emission from birch species[174, 175].

Of the less intense oxygenated BVOC emissions, several have been reported previously. Camphor has been detected in the emissions of Sitka spruce[82] and some other spruce species[67, 138], and it was found to be the dominant emission from sage[176]. Eucalyptol ($C_{10}H_{18}O$) has also been previously reported as an emission from Sitka spruce[166] , Scots pine[152], and as a substantial emission from artemisia[176]. MBO (2-methyl-3-buten-2-ol, $C_5H_{10}O$) is a common emission from pine species[62, 152], but has not previously been reported for Sitka spruce. Methyl salicylate ($C_8H_8O_3$) has been detected in the emissions of Norway spruce previously[177].

3.3.1.2 Spruce 2

Fifty-eight BVOCs were detected in the emissions of Spruce 2, Table 3.2. TD-GC/MS analysis identified thirty-four of these compounds which consisted of nine hydrocarbons and twenty-five oxygenated compounds. The carbon content of the emissions ranged from C_2 to C_{15}, with five C_6, six C_5 and ten C_{10} compounds. Nineteen BVOCs were identified as O_1 compounds, five as O_2 and one O_3. Four sets of isomers were identified, in addition to the three identified in the Spruce 1 emissions, hexanal and 2-hexanone ($C_6H_{12}O$) were also present.

The ToF-CIMS detected thirty-two BVOCs in the emissions from Spruce 2. Eight BVOCs were hydrocarbons and the remaining twenty-four were oxygenated. The carbon content of the emissions ranged from C_6 to C_{20}, with twenty of the BVOCs having ten or fewer carbon atoms. The oxygen content of the emissions varied between O_1 and O_5, with fifteen O_1 compounds.

The chemical structures of eight of the BVOCs detected by the ToF-CIMS were identified by TD-GC/MS analysis. Six of these were in the top ten emissions; sum of monoterpenes, piperitone, cinnamaldehyde, E-2-hexenal ($C_6H_{10}O$), E-farnesene ($C_{15}H_{14}$) and camphor. Methyl salicylate and eucalyptol were also identified by both analysis methods.

The main BVOCs emitted by Spruce 2 were monoterpenes. The same isomers detected in the Spruce 1 emissions were present, although the relative contributions were slightly different. In agreement with Spruce 1 and previous studies[82, 138], myrcene was the main emission, followed by β-phellandrene. δ-Limonene also made a substantial contribution to the monoterpene emissions from Spruce 2; this is in contrast to the monoterpene mixture emitted from Spruce 1 which had higher amounts of α-pinene than δ-limonene. The concentrations of α-pinene and camphene were the lowest of all monoterpene emissions from Spruce 2.

The second highest emission from Spruce 2 was piperitone, which was emitted in much lower amounts than for Spruce 1. While isoprene was the second highest emission for Spruce 1, it was not present in the ToF-CIMS analysis for Spruce 2 and was only detected at trace levels in the TD-GC/MS analysis. A similar phenomenon has been observed for Scots pine, in which δ-carene was a dominant emission from one chemotype, and not emitted from the other[68]. This further supports the idea that trees of the same species can have different emission profiles.

The third highest emission from Spruce 2, C_6H_8O, was not detected in the emissions of Spruce 1 or Spruce 3 and a structure was not confirmed by TD-GC/MS. In total, six of the emissions that are unique to Spruce 2 are C_6 compounds, some of which are known to be GLVs[169], such as E-2-hexenal[178]. GLVs are emitted from plants in response to stress, such as wounding[179, 180], infestation[178] or drought[181]. The C_6H_8O compound may also be a GLV, emitted by Sitka spruce in response to stress. In addition a sesquiterpene, E-farnesene, was detected in the Spruce 2 emissions. Elevated levels of sesquiterpenes have been observed in the emissions of ozone stressed plants[157, 182]. In other studies, the emission of farnesenes from Norway spruce[170] and Scots pine[68] were found to be elevated due to infestation. Although all trees in this work were exposed to the same conditions, the presence of C_6 GLVs and E-farnesene indicate that Spruce 2 may have been stressed.

3.3.1.3 Spruce 3

No BVOCs were detected in the ToF-CIMS analysis of the emissions from Spruce 3. The BVOC emission fluxes were similar in magnitude to those from the empty enclosure, and were deemed negligible.

Twenty-two BVOCs were detected in the TD-GC/MS analysis of the Spruce 3 emissions, Table 3.2. The emissions from Spruce 3 consisted of eight hydrocarbons and fourteen oxygenated compounds. The carbon content of the BVOCs ranged from C_3 to C_{10}, with four C_5 and five C_{10} compounds. The oxygen content of the emissions varied between O_0 and O_3, with ten of the compounds containing one oxygen atom.

Three sets of isomers were detected, the same as for Spruce 1. The emissions from Spruce 3 were quite similar to the emissions from Spruce 1, and did not contain any of the stress related compounds associated with Spruce 2.

3.3.2 Daily Cycle

A month before sampling commenced Spruce 1 produced new shoots. The new shoots were a bright green colour, while the needles were soft, and mainly on the lower part of the trunk outside the enclosure. At the time of sampling the needles had darkened to almost the same dark green colour as the older needles. Spruce 2 had less foliage than Spruce 1, and all needles were dark green. Spruce 3 had the least amount of foliage, and some of the needles had a brownish hue. No ToF-CIMS data is available for Spruce 3 because the concentrations of the measured BVOCs were not statistically significant compared to the Empty enclosure. It seems likely that Spruce 3 was suffering from some stress that lowered the emissions and resulted in no BVOCs registering above the statistical threshold for reliable detection by the ToF-CIMS.

3.3.2.1 BVOC Emissions

The ToF-CIMS results obtained during the *Daily Cycle* show that all BVOC emissions responded to the simultaneous changes in temperature and PPFD as expected. The BVOC emission fluxes were at their highest when temperature and PPFD peaked and were at their lowest during the hours of darkness at the lowest temperature. All BVOC emissions responded in the same manner to a particular change in environmental conditions, but the magnitude of the response was dependent on the specific BVOC and tree. Figure 3.10 shows the time series profile for the emission of piperitone from Spruce 1 during the *Daily Cycle*. The time series for most other BVOCs emitted from Spruce 1 follow a similar pattern.

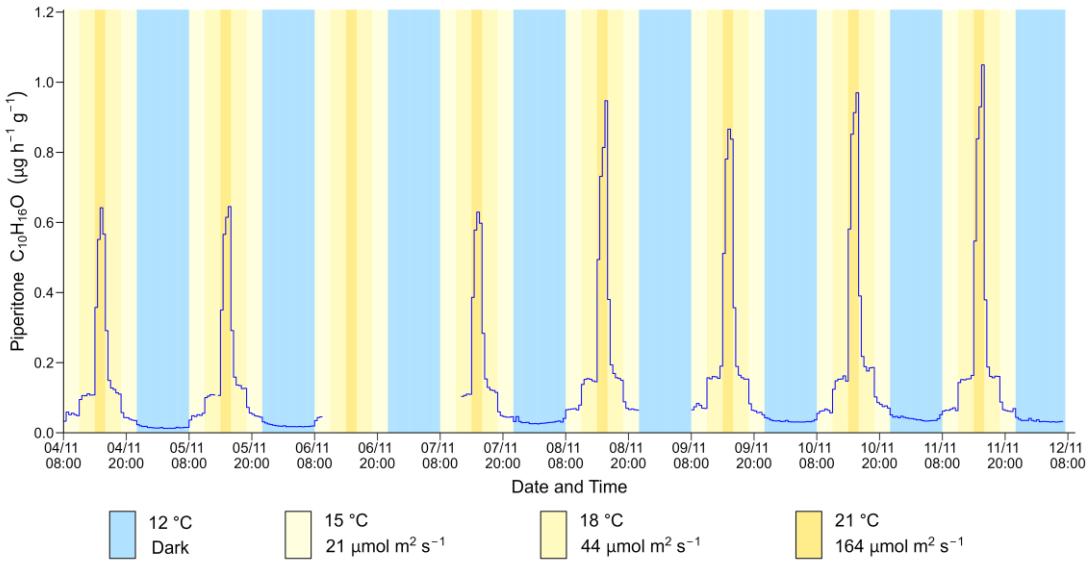

Figure 3.10 *Time series of the piperitone emission flux from Spruce 1 during the Daily Cycle.*

The emission of piperitone from Spruce 1 was lowest during the hours of darkness at 12 °C. Upon illumination of the plant growth chamber to 21 µmol m^{-2} s^{-1} (one lamp on) and temperature increase to 15 °C, the emission of piperitone increased immediately and reached a new steady state. The emission increased with a further 3 °C increase in temperature and doubling of the PPFD (three lamps on). A sharp increase in emission was observed following the transition to the most intense conditions of 21°C and 164 µmol m^{-2} s^{-1} (five lamps on). The emission flux took longer to stabilise at these settings, likely due to the significant increase in PPFD. As the conditions were cycled back to darkness the BVOC emission fluxes decreased accordingly. For a given temperature and PPFD the emission flux attained a certain value, irrespective of short-term history. The magnitude of the change in flux at the different conditions depended on the specific BVOC, with some species showing a pronounced increase in emission upon illumination, and others having a more muted response. The relationship between BVOC emission fluxes and light and temperature has been reported for many tree and plant species[6, 81]. In the field BVOC emissions have been reported to be at their lowest at night, and highest during the day when temperature and PPFD reach a maximum[155], as observed in this work.

The time series profile shown in Figure 3.10 is representative of the emission profile for twenty-eight of the thirty-four BVOCs detected by ToF-CIMS in the Spruce 1 emissions. While the remaining six BVOCs - isoprene, $C_5H_8O_2$, $C_{11}H_{14}O$, $C_{10}H_{10}$, $C_{12}H_{16}$ and $C_{12}H_{20}O$ - all show a similar profile under illumination, they also show a different pattern in the dark, Figure 3.11.

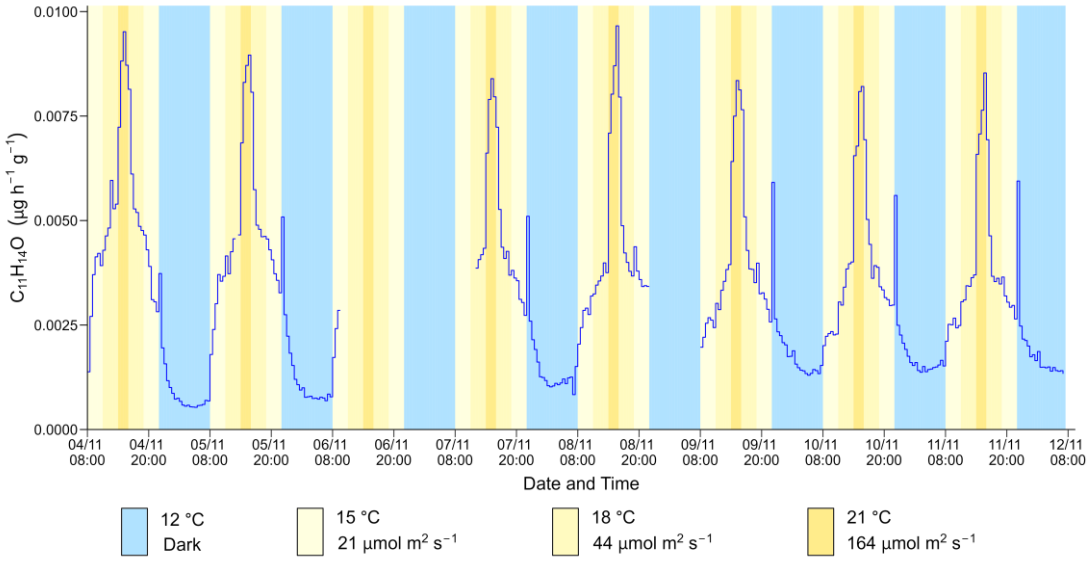

Figure 3.11 *Time series of the $C_{11}H_{14}O$ emission flux from Spruce 1 during the Daily Cycle.*

The time series for $C_{11}H_{14}O$, Figure 3.11, shows a large spike in emission immediately after the lights in the plant growth chamber were turned off. This was observed for all light to dark transitions. A similar phenomenon was observed for the other five BVOCs, although the spike in emissions was not as intense. This observation suggests that these six BVOCs are emitted via similar mechanisms. An analogous event has been observed for the emission of isoprene from Sitka spruce previously. Following sudden darkening the emission of isoprene underwent an immediate decrease, followed by a re-increase 20 minutes later, and maximised after 10 minutes, to about 70% of its value prior to darkening. This was accompanied by a spike in acetaldehyde emission[83]. In this work sampling was switched between the trees every 7.5 minutes, which prevents identification of the exact timing of the spike. The burst was only observed during a single measurement, indicating that it was a short event and had a time frame similar to that measured by Hayward et al. (2004)[83]. Acetaldehyde was

not measured in this work, and Hayward et al. (2004)[83], did not measure the other BVOCs detected in this work that exhibited similar trends. Similar observations have been made for other tree species including oak and poplar[183]. Post-illumination acetaldehyde bursts are proposed to originate from a biological process in which acetaldehyde is produced from an excess of pyruvate via a pyruvate overflow mechanism[83].

The emission profiles of all detected BVOCs from Spruce 1 were quite reproducible across the duration of the *Daily Cycle*, with slight variations exhibited over time. For some BVOCs such as $C_{11}H_{14}O$, the magnitude of the emission flux was very similar each day, Figure 3.11. For other BVOCs, such as piperitone, the emission flux increased slightly as the *Daily Cycle* progressed, Figure 3.10, while for a minority of the BVOCs, the emission flux decreased over the course of the *Daily Cycle*. The reason for these differences in the magnitude of the fluxes across the week is not clear. However, this kind of variation across days for tree and plant species in a laboratory has also been observed for other species including eucalyptus[128].

The BVOC emission patterns from Spruce 2 during the *Daily Cycle*, shown for the sum of monoterpenes in Figure 3.12, were not as well defined as for Spruce 1. Across a 24-hour period the BVOC emission trend was similar to that from Spruce 1, with fluxes lowest in the dark, and peaking under the highest temperature and light conditions. For the intermediate conditions there was little difference observed in the emission fluxes. In addition the fluxes did not always stabilise after a change in conditions, often showing an increasing or decreasing trend. Due to the emissions not having a distinct pattern, the reproducibility across the week was quite poor.

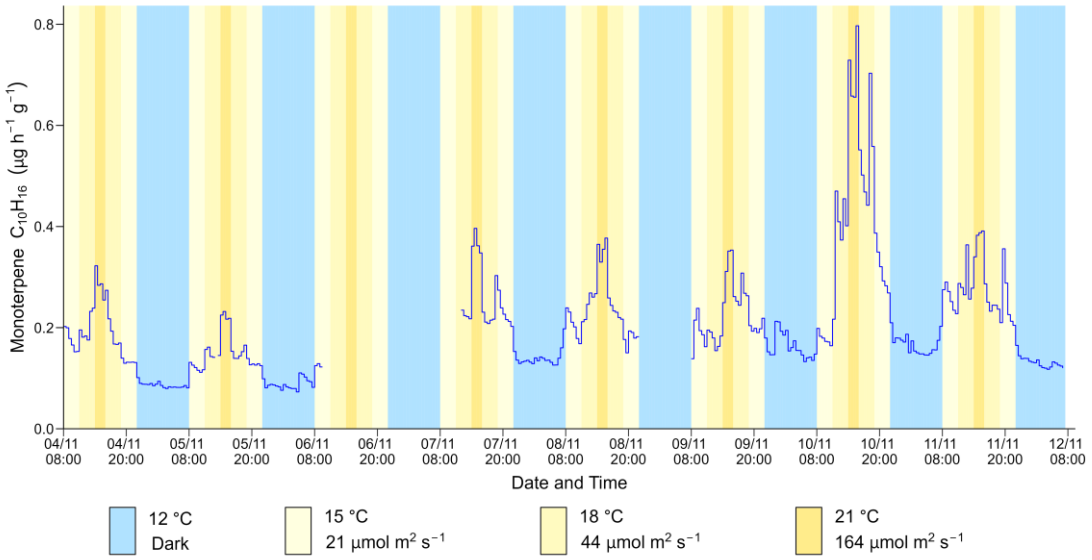

Figure 3.12 *Time series of the sum of monoterpenes emission flux from Spruce 2 during the Daily Cycle.*

The emission fluxes for the sum of monoterpenes and eight other BVOCs spiked on 10/11/2021, the reason for this is unknown. The conditions were exactly the same as the other days of the *Daily cycle* and this was not observed for any of the emissions from Spruce 1. For the majority of the BVOC emissions the magnitude of the flux increased as the Daily Cycle progressed and for a small number of BVOCs it decreased. The variation in emission fluxes from stressed Norway spruce under controlled environmental conditions[184], was similar to that observed in this study for Spruce 2. This further indicates that Spruce 2 may have been suffering from some unknown stress during emissions sampling. None of the Spruce 1 BVOCs that exhibited post-illumination spikes were emitted from Spruce 2. As the phenomenon is likely related to the biological activity of the tree, this could be a further indication that Spruce 2 was stressed and the biological activity of the tree was not operating at maximum capacity.

3.3.2.2 CO_2 Flux

The CO_2 data was used to analyse the extent of photosynthesis and respiration over the course of the *Daily Cycle*, Figure 3.13.

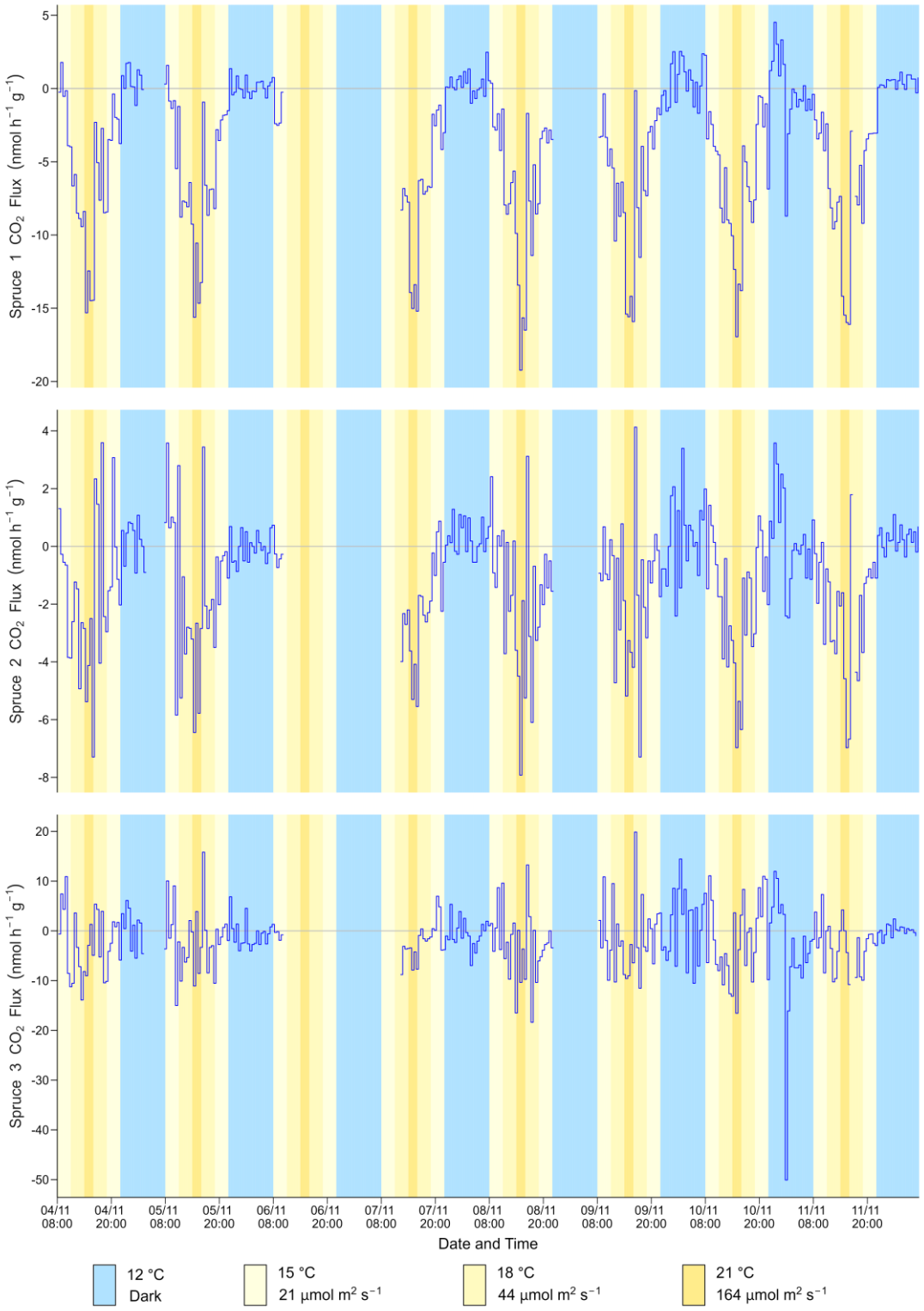

Figure 3.13 *Time series of CO_2 flux for Spruce 1 (top), Spruce 2 (middle) and Spruce 3 (bottom) during the Daily Cycle.*

For Spruce 1 (Figure 3.13, top) the response of the CO_2 flux to changes in the PPFD was not as well defined as the BVOC emission flux. In general the CO_2 flux followed

the expected trend and was highest in the dark, when photosynthesis and CO_2 uptake are not expected to occur, and mitochondrial respiration takes place. A negative CO_2 flux was observed upon illumination, which became larger as the PPFD increased. This is an indication of photosynthetic activity and plant growth[125]. For Spruce 1 the flux in the dark varied between 0 nmol s^{-1} g^{-1} and 5 nmol s^{-1} g^{-1}, similar to that previously observed for oak in the dark[122]. At the highest PPFD (164 µmol m^{-2} s^{-1}) and temperature (21 °C) the CO_2 flux was approximately 15 nmol s^{-1} g^{-1}, which is comparable to the value of 20 nmol s^{-1} g^{-1} measured for Norway Spruce[172] at 23 °C and 200 µmol m^{-2} s^{-1}. For Sitka spruce in the field[185] CO_2 fluxes were approximately 80 nmol s^{-1} g^{-1} at a minimum PPFD of 700 µmol m^{-2} s^{-1}.

The CO_2 flux for Spruce 2 (Figure 3.13, middle) was quite scattered with spikes occurring regularly throughout the *Daily Cycle*. The trend was similar to that observed for Spruce 1, although the magnitude of the CO_2 flux was much lower. A lower CO_2 flux may imply that a tree is stressed, this may be a further indication that Spruce 2 was suffering stress. For example, when subject to heat stress the CO_2 flux for Norway spruce decreased to a third of its original value over a 12 °C temperature increase[172].

For Spruce 3 (Figure 3.13, bottom) the data was highly scattered, and there was no correlation between illumination and CO_2 flux. This suggests that Spruce 3 may not have been undergoing photosynthesis effectively and could be linked to the reason why no BVOCs were detected in the ToF-CIMS analysis.

3.3.2.3 Carbon Balance

Net ecosystem carbon balance is an assessment of all inward and outward fluxes of carbon associated with an ecosystem[186]. The Spruce 1 BVOC emission and CO_2 data for the *Daily Cycle* were used to calculate the carbon balance for Sitka spruce, to determine the contribution that BVOC emissions make to the overall carbon flux, Table 3.3.

Table 3.3 *Contribution of CO_2 uptake, respiration and BVOC emissions to the carbon balance for Spruce 1.*

Carbon Balance	Carbon Flux mg C day^{-1} g^{-1}	Respiration %	BVOC Emission %
Absolute Uptake	- 4.0716	6.99	0.21
Respiration	0.2848	-	-
BVOC Emission	0.0086	-	-
Net Uptake	- 3.7782	7.54	0.23

The absolute daily carbon uptake was calculated to be -4.07 mg C day^{-1} g^{-1}, with an outward flux of CO_2 due to respiration of 0.28 mg C day^{-1} g^{-1}, and a BVOC emission flux of 0.0086 mg C day^{-1} g^{-1}. Resulting in a net carbon uptake of -3.78 mg C day^{-1} g^{-1}. The carbon loss due to BVOC emissions in terms of carbon units, was calculated to be approximately 0.2% of carbon taken in as CO_2. This is quite low and indicates that the contribution of BVOC emissions to the carbon balance for Sitka spruce is negligible. For comparison, the emission of monoterpenes and isoprene were found to account for 0.93% of the net carbon flux from a Japanese larch plantation on an annual basis[187]. In another study the annual carbon loss from a Ponderosa pine forest due to BVOC emissions was calculated to be 0.6% on an absolute carbon scale, and 4% on a net carbon scale[186]. BVOC emissions from a poplar plantation accounted for 0.63% of carbon uptake, on a net carbon scale. The value calculated in this work is lower than that determined from these field studies. However the field studies were conducted over timescales of at least a year and over a range of environmental conditions, and tree ages, both of which are expected to impact carbon uptake and BVOC emissions[186, 188]. The carbon balance for Sitka spruce determined here was calculated using Spruce 1 *Daily Cycle* data, and does not account for annual changes in environmental conditions or tree ages. Based on the values determined from field measurements for other tree species, the exact contribution of BVOC emissions to the overall carbon balance for Sitka spruce is expected to be greater under real-world conditions.

3.3.2.4 Chlorophyll Fluorescence

Maximum photosystem II efficiency (F_v/F_m) was determined by measuring chlorophyll fluorescence. F_v/F_m reflects the ability of photosystem II to reduce its electron acceptors in the photosynthetic electron transport chain and it is used to infer plant health[126]. The chlorophyll fluorescence was measured on three days during the *Daily Cycle*, Table 3.4.

Table 3.4 *Chlorophyll fluorescence measurements for Spruce 1, Spruce 2 and Spruce 3 during the Daily Cycle. Each value is the average of three measurements taken from three branches on the same tree.*

Date	PPFD µmol m^{-2} s^{-1}	Temperature °C	Spruce 1	Spruce 2	Spruce 3
04/11/2021	0	12	0.848	0.831	0.754
04/11/2021	164	21	0.624	0.552	0.599
08/11/2021	0	12	0.794	0.804	0.831
08/11/2021	164	21	0.766	0.718	0.794
11/11/2021	0	12	0.814	0.791	0.824
11/11/2021	164	21	0.713	0.765	0.789

Chlorophyll fluorescence was measured in the dark and at the highest temperature and PPFD settings. Dark adaptation clips were placed on the branches for 30 minutes prior to all measurements. The F_v/F_m values in the dark were similar for all three trees and centred around 0.81 (unitless). Values below 0.8 indicate photoinhibition, likely due to stress. An optimum F_v/F_m value of 0.83 indicates the plant is not suffering any stress and there is no damage to components along the photosynthetic pathways[126]. Almost all measurements were quite close to the optimum, indicating that all trees were healthy. This is surprising for Spruce 2 and Spruce 3, as BVOC and CO_2 measurements indicate that these trees may have been suffering from stress. One possible explanation is that BVOC and CO_2 measurements are more sensitive to low levels of stress compared to F_v/F_m measurements.

Almost all measurements taken in the dark were greater than the measurements taken during illumination. Lower F_v/F_m ratios indicate that all chlorophyll is not taking part in photosynthesis, which could be due to damage, and implies the plant is

stressed[189]. It is unlikely the trees were suffering from stress, as the temperatures used in this study are representative of the natural environment, and the PPFD was an order of magnitude lower than that measured for the ambient atmosphere. F_v/F_m has been shown to decrease with increasing PPFD[126], it is likely the slight decrease in F_v/F_m is due to this trend, rather than in response to stress.

Due to the absence of ToF-CIMS data and the highly scattered CO_2 data, the data recorded from Spruce 3 was excluded from any further analysis.

3.3.3 Temperature Cycle

The *Temperature Cycle* commenced three days after the *Daily Cycle* finished. For the *Temperature Cycle* PPFD was held constant during the hours of illumination and temperature was varied. The purpose of this cycle was to assess the contribution that temperature made to the emission flux, elucidating the importance of pooled BVOC emissions. At the start of the *Temperature Cycle* the appearance of Spruce 1 was the same as for the Daily Cycle, while the needles of Spruce 2 started to turn brown.

3.3.3.1 BVOC Emissions

All BVOCs responded to changes in temperature, with the lowest fluxes measured at the lowest temperature in the dark, and the highest fluxes measured at 21 °C under illumination.

The emission of piperitone from Spruce 1 during the *Temperature Cycle* (Figure 3.14, top) is representative of almost all BVOC emissions from Spruce 1. Increasing the temperature from 12 °C to 15 °C in the dark caused a slight increase in the emission flux, indicating that the emissions were temperature dependent, and possibly originated from storage pools. The time series for isoprene (Figure 3.14, bottom) is representative of $C_5H_8O_2$, $C_{10}H_{10}$, $C_{12}H_{16}$ and $C_{12}H_{21}O$. In the dark these BVOCs have a very low emission flux and do not show any variation with temperature indicating that they are unlikely to originate from storage pools. As with the *Daily Cycle* there

was a spike in emission of these BVOCs following darkening and there was also a spike in the emission of $C_{11}H_{14}O$, although its emission profile had more similarities with that of piperitone.

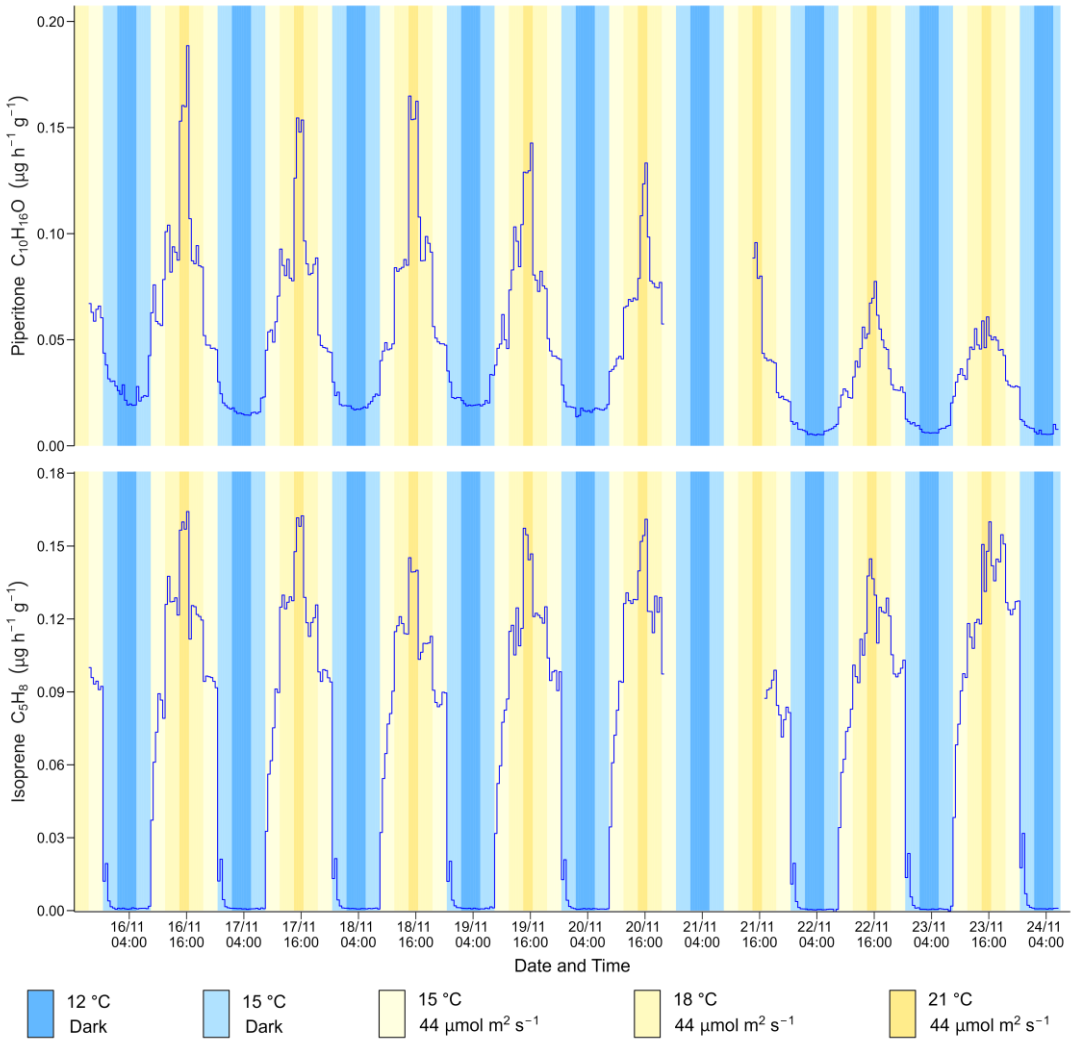

Figure 3.14 *Time series of the emission fluxes of piperitone (top) and isoprene (bottom) from Spruce 1 during the Temperature Cycle.*

The time series for all Spruce 1 BVOCs show a significant increase in emission when the lamps were turned on, although the temperature was maintained at 15 °C, indicating light also plays a role in the emission of all BVOCs from Spruce 1. As the temperature was increased during illumination the emission flux of all BVOCs also increased, showing that the emissions were also temperature dependent. A temperature dependence has been observed for the emission of isoprene and

monoterpenes from Sitka spruce previously[81, 83]. A correlation between oxygenated BVOCs and temperature has also been reported for sunflower[132] and aspen[190]. For the majority of the BVOCs the change in emission flux with temperature was similar to that for piperitone, with the flux stabilising at each temperature setting. Other BVOCs, such as isoprene, experienced a continual increase in emission flux upon illumination even though the temperature was maintained at 15 °C for three hours before and after illumination. This may be due to the emission of these BVOCs being closely linked to biosynthesis and the continual increase in emission is a result of the initiation of biosynthesis until it reaches optimum efficiency. The emission of isoprene is assumed to occur immediately following biosynthesis[131].

The emission flux of all BVOCs emitted from Spruce 1 flux gradually decreased over the course of the *Temperature Cycle* and was much lower in magnitude than for the *Daily Cycle*. If part of the emission flux originated from the resin deposits visible on the tree, it may be an indication that these were becoming depleted.

For Spruce 2 the emission profile for the *Temperature Cycle* was similar to that of Spruce 1, with the emissions peaking at the highest temperature setting and the lowest flux recorded at the lowest temperature setting in the dark. The time series for the sum of monoterpenes from Spruce 2 is shown in Figure 3.15, and is representative of all BVOC emissions from Spruce 2.

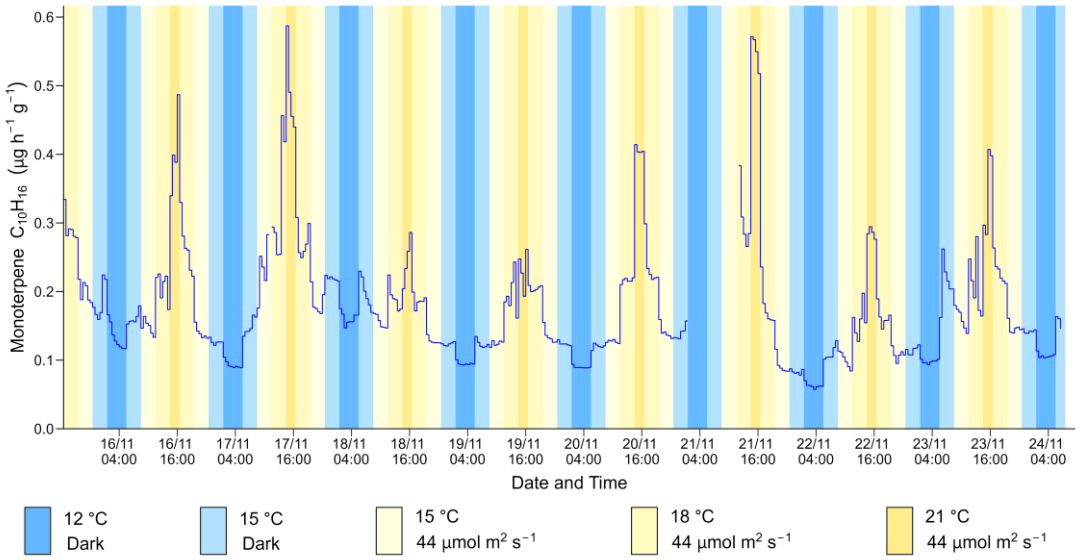

Figure 3.15 *Time series of sum of monoterpenes from Spruce 2 during the Temperature Cycle.*

In contrast to Spruce 1, the BVOCs emitted from Spruce 2 had a much stronger response to changes in temperature, especially in the dark. Upon illumination there was a minimal change in the emission flux for all BVOCs. This is quite different to what was observed for Spruce 1, and indicates that the Spruce 2 BVOC emissions were much more closely linked to temperature than those from Spruce 1. As observed for the *Daily Cycle* the data from Spruce 2 is quite scattered, and 20/11/2021 was the only day with a clear BVOC emission profile. The BVOC emissions showed a pronounced response to changes in temperature and reached a stable emission flux immediately after each change. This indicates that the Spruce 2 BVOC emissions had a strong temperature dependence, and likely originated from storage pools[131]. The magnitude of the BVOC emission flux from Spruce 2 during the *Temperature Cycle* was lower than during the *Daily Cycle*. This may have been a result of Spruce 2 suffering from some stress, that caused a reduction in the emission flux. It also indicates that the BVOC emissions from Spruce 2 were largely due to emission from storage pools and the emission via the biosynthetic pathway was largely reduced due to stress.

3.3.3.2 CO_2 Flux

The CO_2 flux during the *Temperature Cycle* is shown in Figure 3.16 for Spruce 1 (top) and Spruce 2 (bottom).

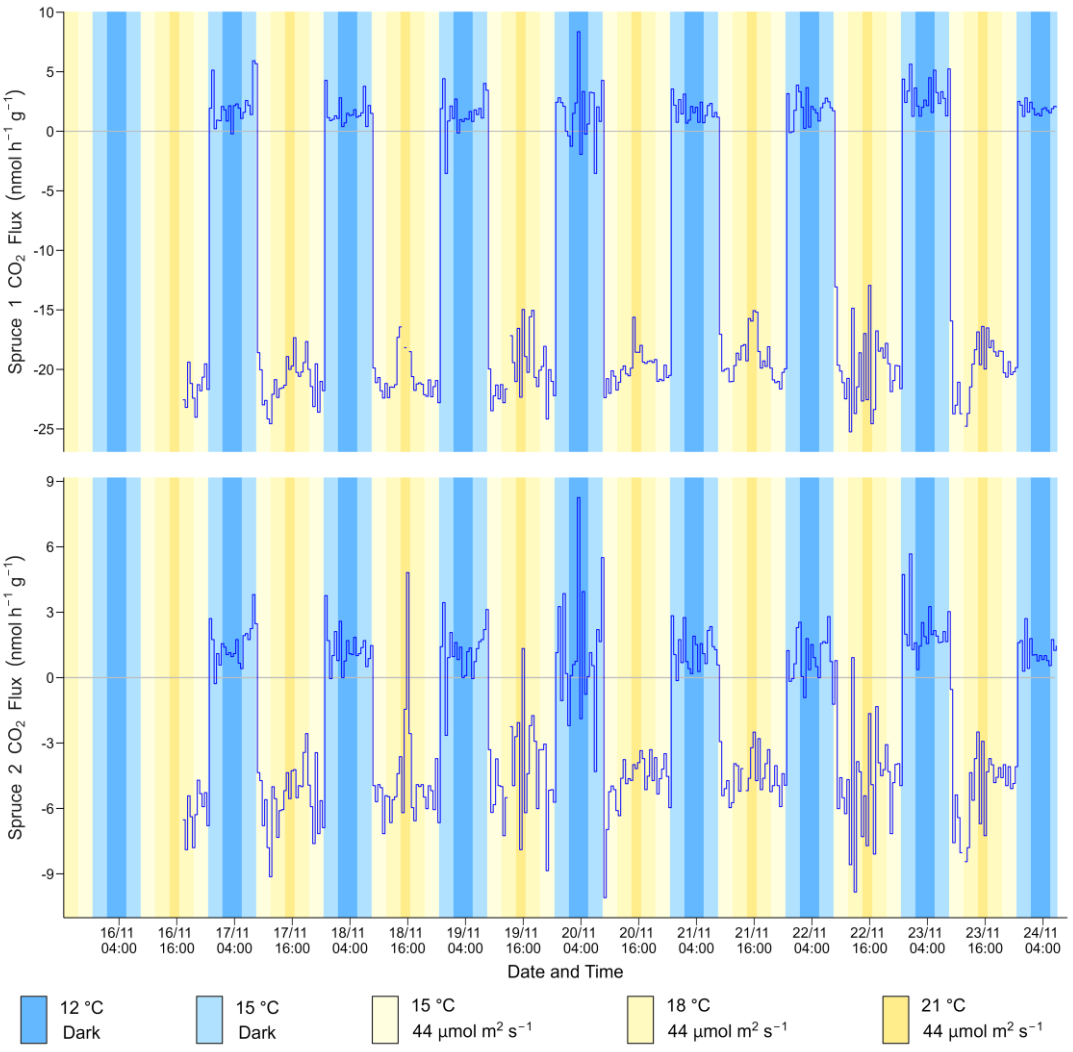

Figure 3.16 *Time series of the CO_2 flux for Spruce 1 (top) and Spruce 2 (middle) during the Temperature Cycle.*

The CO_2 flux showed little variation with temperature. The temperature variation in the dark did not have any impact on the mitochondrial respiration for either tree. Upon illumination a significant decrease was observed, due to CO_2 uptake as a result of photosynthesis. For Spruce 1, there was a slight decrease in the CO_2 flux with increasing temperature, suggesting photosynthetic activity was decreasing. An inverse relationship between photosynthesis and temperature has been observed

for Sitka spruce previously[191]. This was not observed for Spruce 2, possibly due to the scatter of the data and the magnitude of the flux being quite low. The magnitude of the Spruce 1 CO_2 flux was 20 nmol s^{-1} g^{-1}, which is larger than was measured for the *Daily Cycle*, but is still in agreement with previously reported values[185]. In contrast with the BVOC emissions which gradually decreased as the *Temperature Cycle* progressed, the CO_2 flux was quite reproducible throughout.

3.3.3.3 Chlorophyll Fluorescence

The F_v/F_m values obtained for Spruce 1 and Spruce 2 during the *Temperature Cycle* are listed in Table 3.5. The values in the dark were centred around 0.8 and were similar to those observed during the *Daily Cycle*.

Table 3.5 *Chlorophyll fluorescence measurements for Spruce 1 and Spruce 2 during the Temperature Cycle. Each value is the average of three measurements taken from three branches on the same tree.*

Date	Light Intensity µmol m^{-2} s^{-1}	Temperature °C	Spruce 1	Spruce 2
16/11/2021	0	12	0.815	0.810
16/11/2021	44	18	0.762	0.773
19/11/2021	0	12	0.821	0.831
19/11/2021	44	18	0.820	0.785
22/11/2021	0	12	0.815	0.760
22/11/2021	44	18	0.785	0.805

As with the *Daily Cycle* dark adaptation clips were placed on the branches 30 minutes prior to all measurements. There was little variation across the measurements for Spruce 1. The increase in temperature had no effect on F_v/F_m. Temperature extremes, either high or low, have been found to cause photoinhibitory damage and lead to a reduction in F_v/F_m[189]. The temperature range used in the study was too low to elicit a change in chlorophyll fluorescence. One of the branches of Spruce 2 had a lower F_v/F_m measurement for half of the measurements taken. This may be another indication that Spruce 2 was stressed.

3.3.4 Light Cycle

The final cycle applied to the plant growth chamber was the *Light Cycle*. During the *Light Cycle* the temperature was maintained at 18 °C, and the PPFD was varied. The purpose of the *Light Cycle* was to determine the impact of PPFD on the Sitka spruce emissions, and to evaluate the importance of the biosynthetic BVOC emission pathway. At the start of the *Light Cycle* the appearance of Spruce 1 was the same as during the *Daily Cycle* and *Temperature Cycle*, while all needles on Spruce 2 had turned brown.

3.3.4.1 BVOC Emissions

Figure 3.17 shows the time series of piperitone emitted from Spruce 1 during the *Light Cycle*. All BVOC emission fluxes from Spruce 1 increased with PPFD during the *Light Cycle*. The variation in emission flux depended on the BVOC, with piperitone showing a marked change in emission flux at each PPFD setting, Figure 3.17, while other emissions, such as $C_{10}H_{12}O_2$, only showed a significant increase in emission flux at 164 µmol m^{-2} s^{-1}. The emission of isoprene from Sitka spruce has previously been shown to be PPFD dependent, with the emissions of monoterpenes from Sitka spruce reported to be PPFD independent[79, 83]. This is in contrast to the results obtained here, where the sum of monoterpene emissions from Spruce 1 showed a clear response to PPFD changes. Monoterpene emissions are traditionally assumed to be temperature dependent only[156], although monoterpene emissions from Norway spruce[192] and oak[122] have been found to also have a PPFD dependence. As with the previous cycles, a spike in emission following darkness was observed for isoprene, $C_5H_8O_2$, $C_{11}H_{14}O$, $C_{10}H_{10}$, $C_{12}H_{16}$ and $C_{12}H_{21}O$.

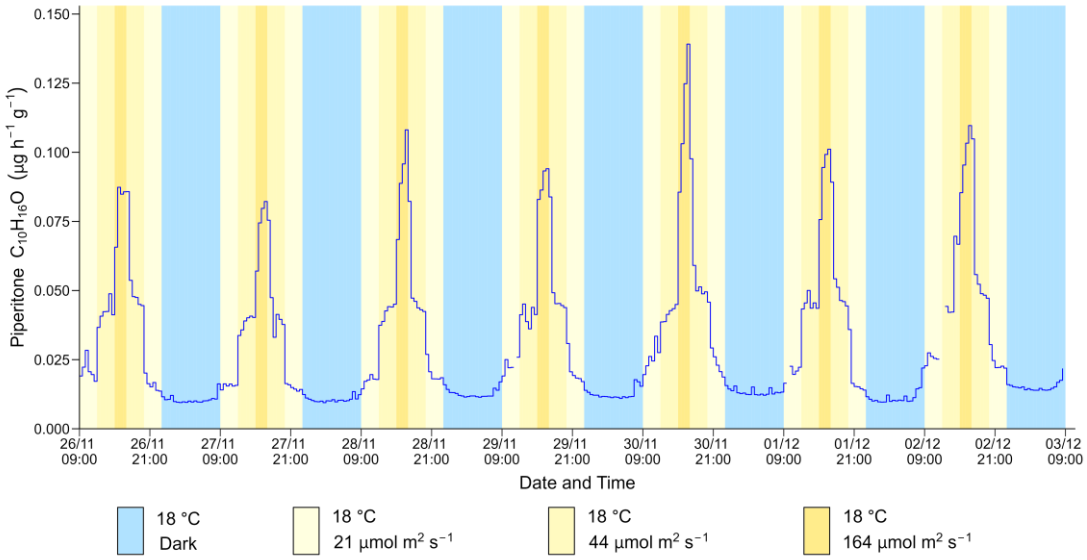

Figure 3.17 *Time series profile of piperitone flux from Spruce 1 during the Light Cycle.*

The time series profiles for all Spruce 1 BVOCs were quite reproducible across the duration of the *Light Cycle*, with the emission fluxes reaching roughly the same values each day. This is in contrast to the previous cycles where clear increasing or decreasing trends were observed as the cycles progressed. The magnitude of the emission flux was much lower for the *Light Cycle* than for the *Daily Cycle*. This is likely due to a portion of the emissions originating from storage pools that are temperature rather than PPFD dependent.

In contrast to Spruce 1, the emissions from Spruce 2 did not show a strong PPFD dependence. Figure 3.18 (top) shows the time series profile for the sum of monoterpene signal during the *Light Cycle*, which is representative of most Spruce 2 emissions. There was no correlation between PPFD and the majority of the BVOCs emitted from Spruce 2. It may be the case that Spruce 2 was not sensitive to PPFD. The emission of monoterpenes[18], methanol and acetaldehyde[45] from Sitka spruce were found to be PPFD independent from 0 µmol m^2 s^{-1} to 1000 µmol m^2 s^{-1}. Most BVOCs did not follow any emission pattern, with the flux in the dark exceeding that under illumination on several occasions. It may be the case that the emission flux was quite low and near the limit of detection of the instrument, and the recorded measurements are more representative of noise than actual emission fluxes. It is also

possible that the stress Spruce 2 had been suffering from was stronger during the *Light Cycle*, and obscured the emission pattern.

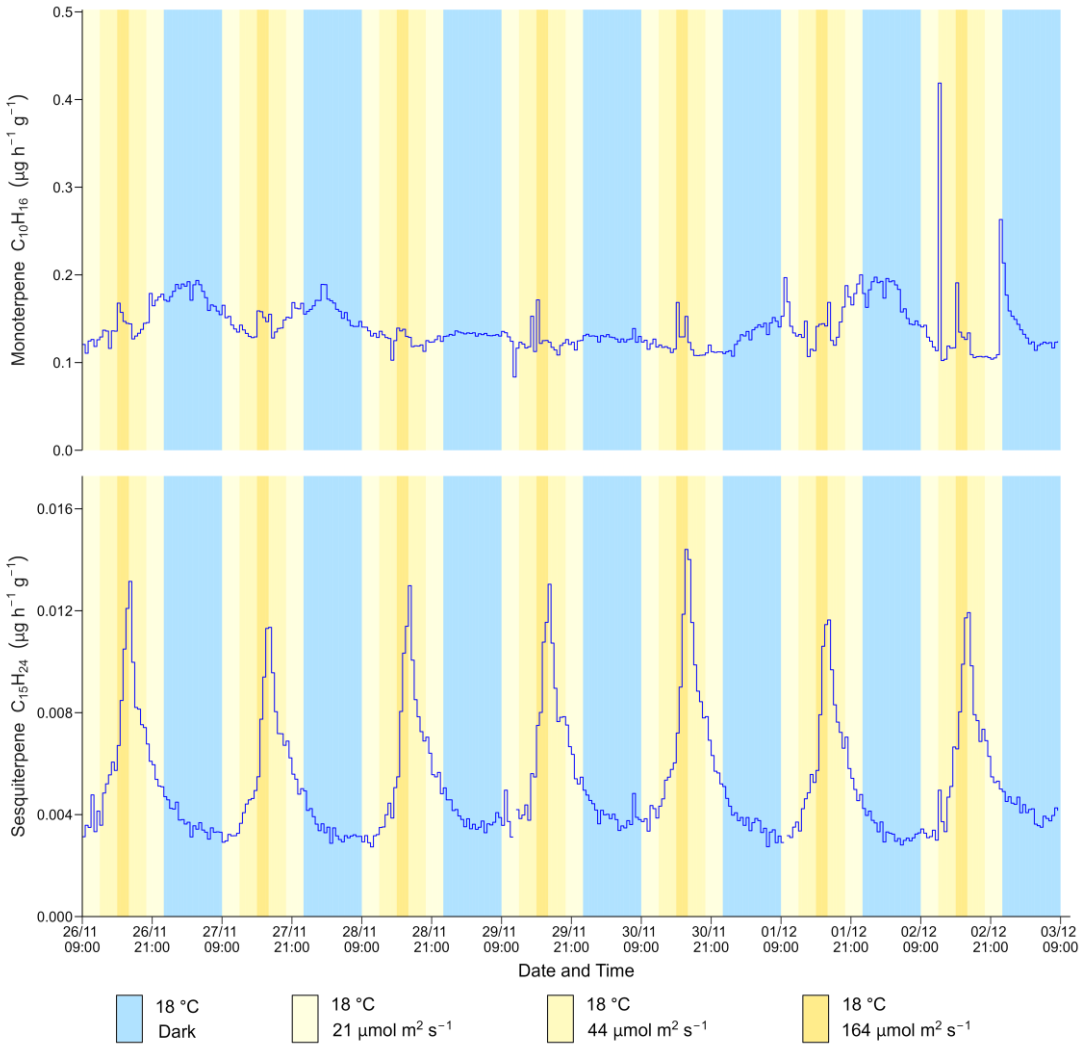

Figure 3.18 *Time series for the sum of monoterpene fluxes (top) and sum of sesquiterpene fluxes (bottom) from Spruce 2 during the Light Cycle.*

A light dependence was observed for a few select emissions, including E-farnesene (Figure 3.18, bottom) and camphor. E-farnesene showed the strongest PPFD dependence. This was unexpected as sesquiterpene emissions from Norway spruce were found to be PPFD independent[157]. The change in E-farnesene flux was not very well correlated with the changes in PPFD, and did not stabilise at set values, but continually increased. There was also a time lag between the changes in light intensity and emission flux, with the maximum flux often being recorded slightly after

the light intensity had begun to decrease, and the increase occurring about an hour after illumination. The reason for the time delay is not clear and it was not observed for any other BVOCs. The other light dependent Spruce 2 emissions only showed a small response to changes in PPFD, with most only responding at the highest PPFD of 164 µmol m^{-2} s^{-1}.

While the BVOC emission from Spruce 2 showed a strong temperature dependence in the *Temperature Cycle*, the results obtained here for the *Light Cycle*, show that the emission fluxes were barely affected by light. This is in contrast to the BVOC emissions from Spruce 1, which showed clear light and temperature dependences.

3.3.4.2 CO_2 Flux

Figure 3.19 shows the CO_2 fluxes for Spruce 1 (top) and Spruce 2 (bottom). The pattern of the CO_2 flux during the *Light Cycle* was the same as that observed during the *Daily Cycle*, with a clear change in response to PPFD variations for both trees. The magnitude of the CO_2 flux during the *Light Cycle* was larger than for the *Daily Cycle*. This is somewhat surprising as the PPFD was the same for both cycles, therefore the fluxes would be expected to be similar.

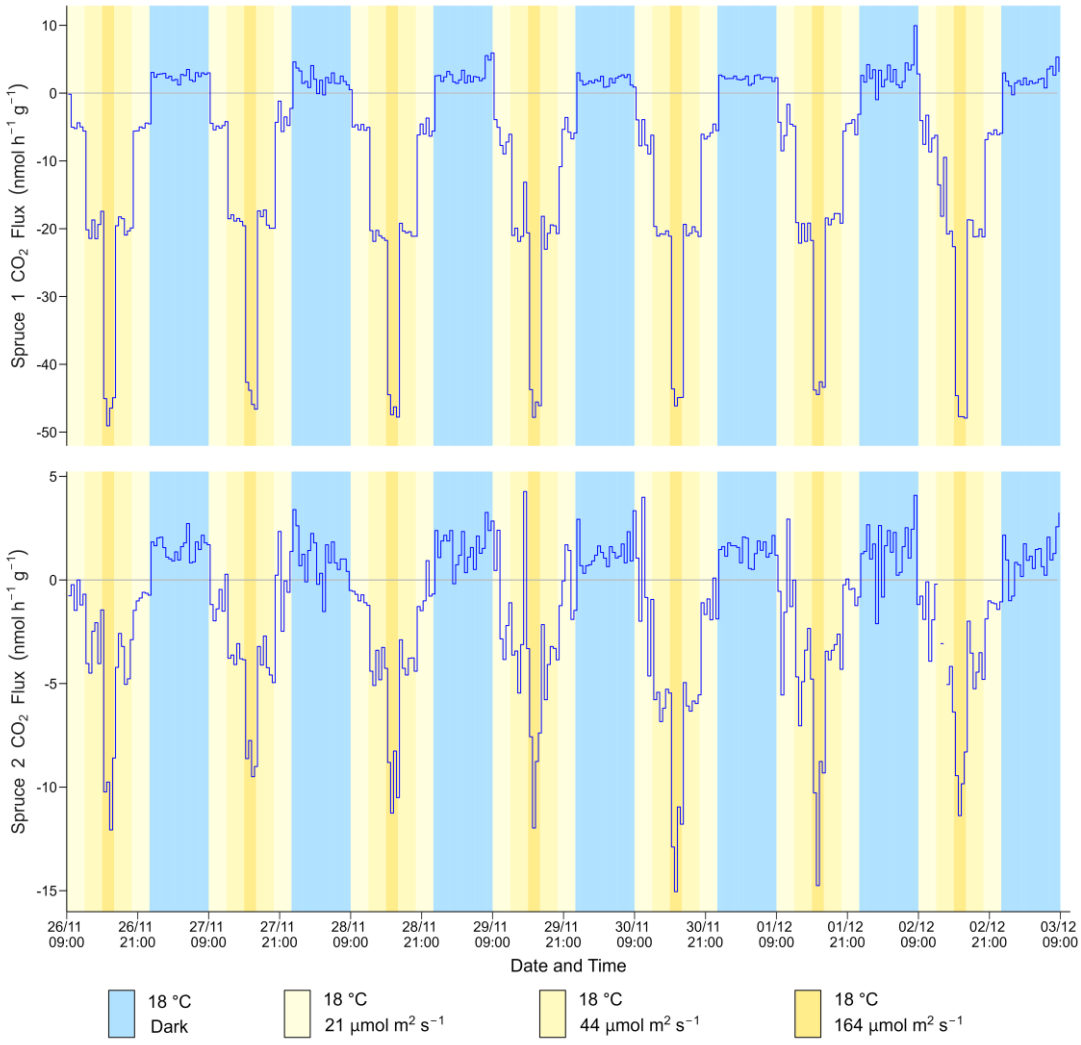

Figure 3.19 *Time series of CO_2 flux for Spruce 1 (top) and Spruce 2 (bottom) during the Light Cycle.*

The Spruce 1 CO_2 flux was approximately five times higher than that for Spruce 2. This is a further indication that Spruce 2 was suffering stress. Although, unlike for the *Daily Cycle* the CO_2 flux for Spruce 2 was quite regular, and much less scattered. The BVOC emission profiles from Spruce 2 during the *Light Cycle*, indicated that the stress experienced by Spruce 2 was stronger during the *Light Cycle*, and was affecting the physiology of the tree. This is not the case for the CO_2 measurements, which show CO_2 uptake by Spruce 2, indicating that some biological processes were still functional. It is possible that physiological processes relating to biosynthetic BVOC emission are more sensitive to the stress experienced by Spruce 2 than photosynthetic processes are.

3.3.4.3 Chlorophyll Fluorescence

The chlorophyll fluorescence measurements for both trees were used to indicate that the trees were healthy during the *Light Cycle*, Table 3.6.

Table 3.6 *Chlorophyll fluorescence measurements for Spruce 1 and Spruce 2 during the Light Cycle. Each value is the average of three measurements taken from three branches on the same tree.*

Date	Light Intensity µmol m^{-2} s^{-1}	Temperature °C	Spruce 1	Spruce 2
28/11/2022	0	18	0.804	0.828
28/11/2022	164	18	0.653	0.742
30/11/2021	0	18	0.694	0.768
30/11/2021	164	18	0.718	0.751
02/12/2021	0	18	0.726	0.769
02/12/2021	164	18	0.750	0.724

The F_v/F_m values recorded during the *Light Cycle* for Spruce 1 and Spruce 2 were slightly lower than those measured during the other cycles. The measurements recorded after 10 hours of darkness were centred around 0.75 and were more scattered. Three of the branches from Spruce 1 recorded values below 0.66. Most of the other measurements for Spruce 1 were above 0.75, therefore it is unlikely that Spruce 1 was stressed. The F_v/F_m measurements for Spruce 2 during the *Light Cycle* were similar to those measured for the other cycles. This indicates that although Spruce 2 was stressed, there was no additional stress during the *Light Cycle*.

3.3.5 BVOC Emission Standardisation

BVOC emissions were standardised to a PPFD of 1000 µmol m^{-2} s^{-1}, and a temperature of 30 °C, in line with recommendations[130]. All BVOC emissions were subject to three standardisation procedures; pooled standardisation, biosynthetic standardisation and combined standardisation. For each BVOC emitted from Spruce 1 and Spruce 2,

the method that best reproduced the emission profile for the *Daily Cycle* was selected and used to determine the standardised emission flux.

3.3.5.1 Standardisation Procedures

Pooled Model

Pooled BVOC emissions are those that are assumed to originate solely from storage pools within plants, have no correlation with physiological processes, and have fluxes that are dependent on temperature only. Equation 3.4 initially developed by Guenther et al. (1993)[130], has been widely used to describe monoterpene emissions from plants[62, 166]. The term β (0.09 K^{-1} for monoterpenes)[130], is used to describe the temperature dependence. In this work, initially the original value of β was applied to the data, and pooled standardised emission fluxes were calculated. The equation was then used to model the measurement data for the *Daily Cycle*. The model data did not match the measured data for any BVOCs, including for the sum of monoterpenes. In order to improve the model a unique β value was calculated for each BVOC emitted by each Stika spruce. These unique β values were then used to calculate $BVOC_S$, the pool standardised emission flux for the BVOC at 30 °C. The values for $BVOC_S$ and β for each BVOC were used to model the measured data for the *Daily Cycle* for both Spruce 1 and Spruce 2, Figure 3.20 and Figure 3.21.

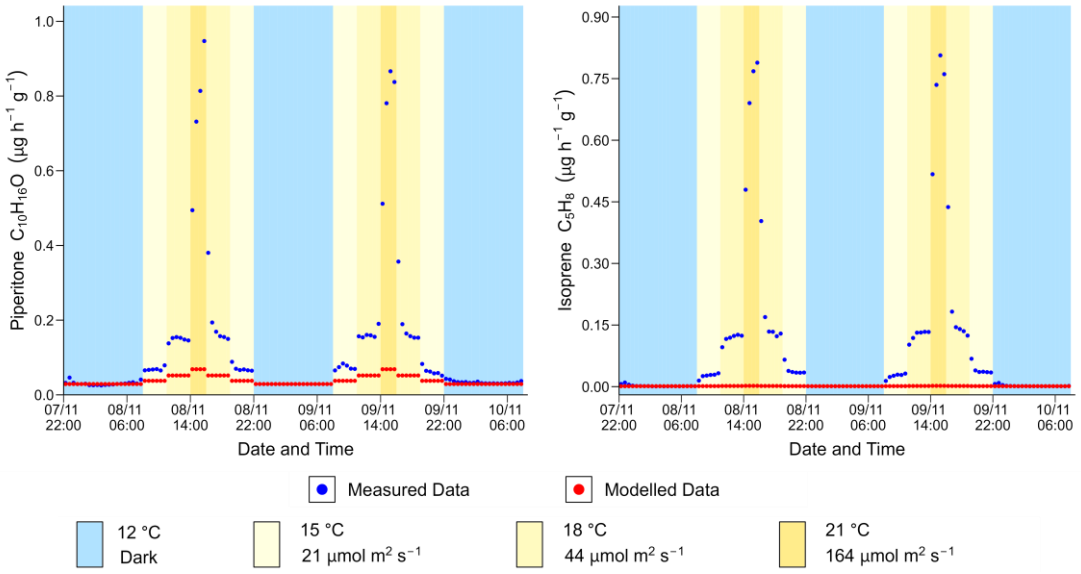

Figure 3.20 *Measured data (blue) and pooled model data (red) for the emission of piperitone (left) and isoprene (right) from Spruce 1 during the Daily cycle.*

For Spruce 1 the model was only capable of reproducing measurements recorded in the dark. Data acquired under illumination were significantly underestimated by the model for all BVOCs, particularly at the highest PPFD setting. This was unexpected, especially for monoterpenes which are assumed to be emitted solely from storage pools[26] and thus entirely temperature dependent. Previous studies have found Sitka spruce monoterpene emissions to be PPFD independent, with a strong temperature dependence[83]. The emission of isoprene from Stika spruce has been shown to be temperature and PPFD dependent[79], as it is emitted via a biosynthetic pathway, and therefore was not expected to be reproduced with the pooled model. The inability of the model to replicate the *Daily Cycle* measurements indicates that for all BVOCs emitted by Spruce 1 biosynthetic pathways play a role in the emission process.

The results from the *Temperature Cycle* showed that the influence of temperature on the BVOCs emitted from Spruce 2 was much stronger than for Spruce 1. As a result, there was closer agreement between the pooled emissions model and measurement data for Spruce 2 than there was for Spruce 1, Figure 3.21.

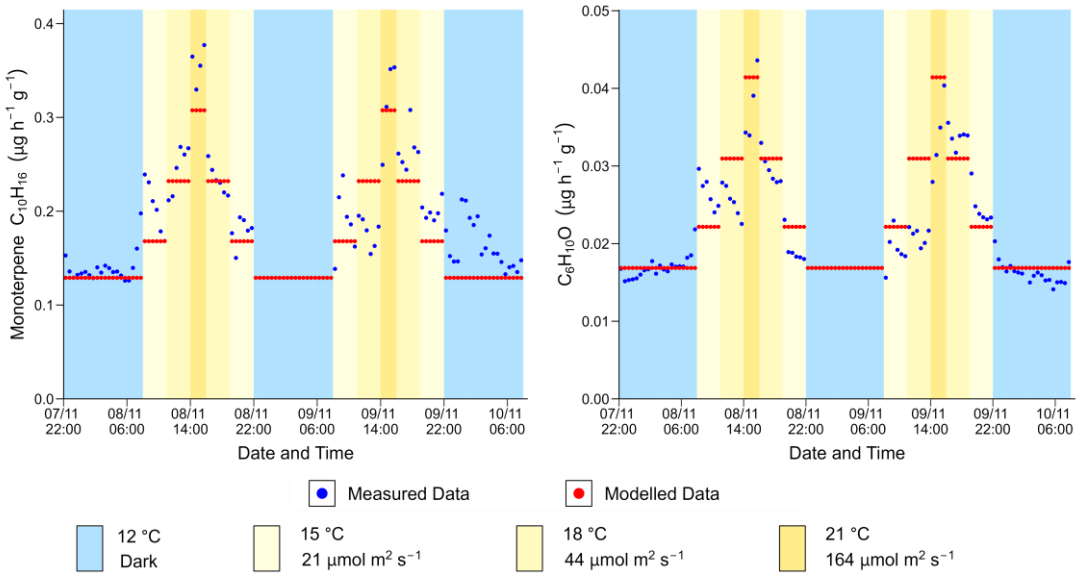

Figure 3.21 *Measured data (blue) and pooled model data (red) for the emission of the sum of monoterpenes (left) and $C_6H_{10}O$ (right) from Spruce 2 during the Daily cycle.*

The emission profiles of six Spruce 2 BVOCs including, $C_6H_{10}O$ and $C_{20}H_{24}$, were completely described by the pooled emission model (Figure 3.21). For the remaining BVOCs, the model was unable to completely reproduce the measured data, indicating that biosynthetic pathways contributed to the emissions from Spruce 2 also. Of the sixteen BVOCs common to the emissions of Spruce 1 and Spruce 2, there was a large discrepancy between the extent to which the pooled emission model could reproduce the measured data, and depended on the specific BVOC. For piperitone, 35% of the total emission flux from Spruce 1 could be reproduced using the pooled emission model, while for Spruce 2 it accounted for 83% of the piperitone emission flux.

Biosynthetic Model

Biosynthetic BVOC emissions are released immediately after synthesis, there are no storage reservoirs for these BVOCs. The emission of biosynthetic BVOCs depends on the rate of synthesis, which in turn, depends on both temperature, which is linked to enzymatic activity, and PPFD, which is linked to photosynthesis. Equation 3.1 developed by Guenther et al. (1993)[130] to describe the biosynthetic emission of isoprene was used to calculate biosynthetic standardised emission fluxes. In order to test the accuracy of the standardised emission fluxes, the equation was then used to

model the measured data for the *Daily Cycle*. As an initial approach the coefficients in the original equation by Guenther et al. (1993)[130] were used to calculate biosynthetic standardised emission fluxes and to model the *Daily Cycle* data. Those coefficients could not accurately reproduce the measurement data, and unique coefficients were calculated for each BVOC emitted from Spruce 1 and Spruce 2. The temperature-dependent term of the biosynthesis equation was simplified with the removal of the denominator, as described previously by Schuh et al. (1997)[132], Equation 3.5. It relies on T_M, the temperature of maximum enzyme activity, which was unknown for the Sitka spruce used in this study, but is expected to be close to 40 °C. Due to the large temperature difference anticipated between T_M and the temperatures employed in this study, the denominator can be approximated to one. The unique coefficients for each BVOC were used to model Spruce 1 and Spruce 2 *Daily Cycle* data, Figure 3.22 and Figure 3.23, respectively.

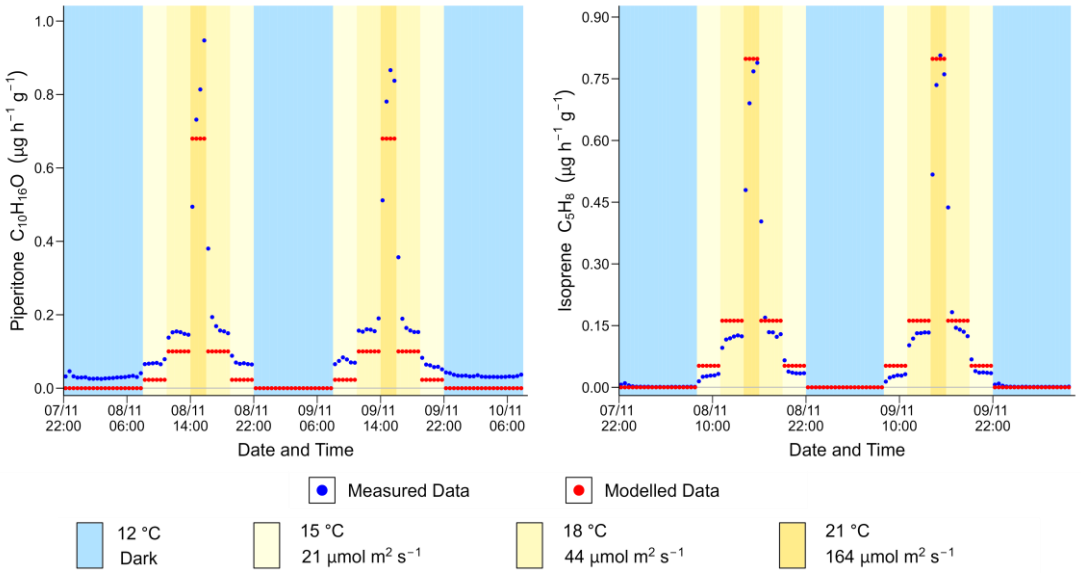

Figure 3.22 *Measured data (blue) and biosynthetic model data (red) for the emission of piperitone (left) and isoprene (right) from Spruce 1 during the Daily cycle.*

Comparison between the measured data from the *Daily Cycle* with the biosynthetic model for Spruce 1 showed better agreement than the pooled emission model. The biosynthetic model more accurately described the BVOC emissions under illumination, reflecting the large increase in emissions that was observed when the trees were exposed to higher PPFD conditions. As expected, the emission of isoprene

was accurately described by the biosynthetic model. The coefficients used in the Spruce 1 model for isoprene (α = 0.0019, c_L = 1.127 and c_{T1} = 79,194 J mol^{-1}) were similar to those originally derived from sweet gum, aspen, eucalyptus and velvet bean (α = 0.0027, c_L = 1.066, c_{T1} = 95,000 J mol^{-1})[130]. The calculated values are quite close to the original values, which indicates the emission of isoprene from Sitka spruce is similar to that from other plant species. The biosynthetic model was able to reproduce the *Daily Cycle* emission profiles of eleven BVOCs emitted by Spruce 1. These included five of the six BVOCs that underwent post-illumination spikes. As the post-illumination burst is related to PPFD exposure, it was expected that these BVOCs would have a strong PPFD dependence. For the remaining BVOCs emitted by Spruce 1 the biosynthetic model was not capable of completely describing the *Daily Cycle* emission profile, indicating that these BVOCs were also originating from storage pools.

The biosynthetic emission model largely under represented all the Spruce 2 BVOC emissions, Figure 3.23. The high correlation of the pooled emission model with Spruce 2 indicated that the contribution from the biosynthetic emission pathway would be low. It is possible that the stress experienced by Spruce 2 led to an inhibition of the biosynthetic emission pathways. This may explain why isoprene, which is produced via a biosynthetic pathway was not detected in the emissions from Spruce 2. Six of the BVOCs emitted from Spruce 2 were completely replicated by the pooled emission model and were not described by the biosynthetic emission model. The sum of monoterpene signal did show a correlation with the biosynthetic emission model, although it could not fully explain the emission flux. Previous studies involving Sitka spruce have not reported a biosynthetic factor in monoterpene emissions[83], but it has been observed for beech[132] and holm oak[173] previously.

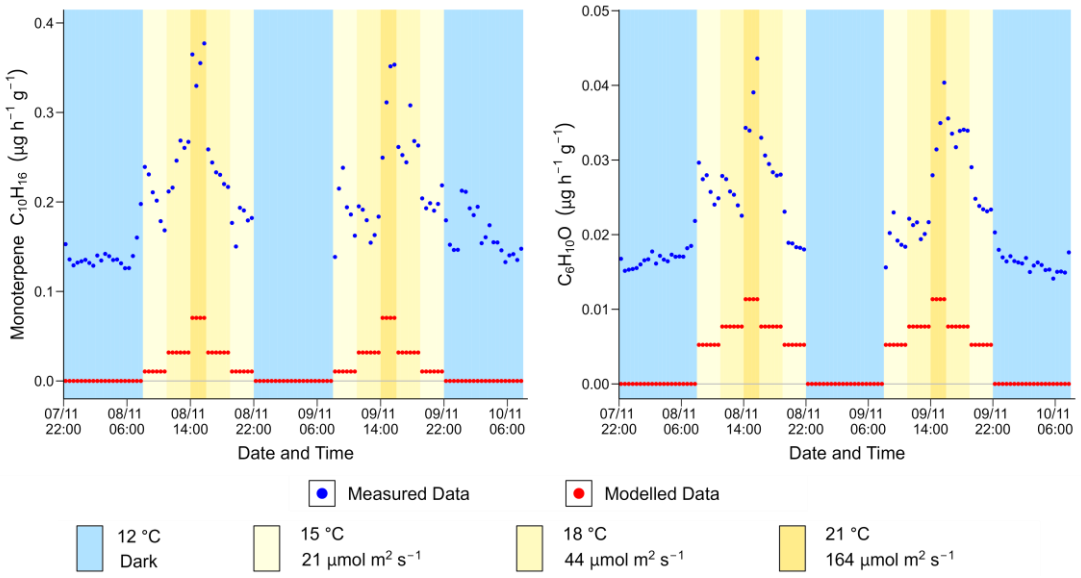

Figure 3.23 *Measured data (blue) and biosynthetic model data (red) for the emission of the sum of monoterpenes (left) and $C_6H_{10}O$ (right) from Spruce 2 during the Daily cycle.*

Combined Emission Model

The emission fluxes of eleven BVOCs from Spruce 1 and six BVOCs from Spruce 2 could be reproduced using either the pooled emission model or the biosynthetic emission model. All other BVOCs displayed contributions from both emission pathways. A combined biosynthesis and pooled emission standardisation equation developed by Schuh et al. (1997)[132] was used to standardise and model the emissions. The combined emission equation sums the biosynthetic and pooled emission equations used previously, with the assumption that the two emission methods are completely independent. The previously calculated coefficients were used to derive combined standardised emission fluxes and to model the data for comparison with the *Daily Cycle* measurement data, Figure 3.24 and Figure 3.25.

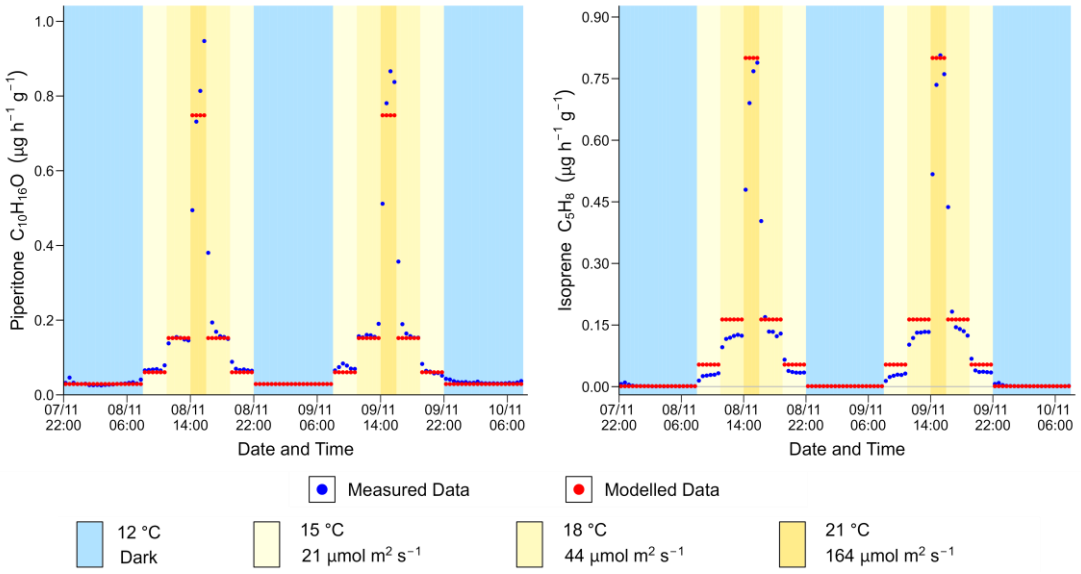

Figure 3.24 *Measured data (blue) and combined model data (red) for the emission of piperitone (left) and isoprene (right) from Spruce 1 during the Daily cycle.*

The emission fluxes for twenty-three BVOCs emitted from Spruce 1, that were not reproduced by the biosynthesis emission model, were replicated by the combined emission model. The contribution each method made to the total emission was BVOC dependent, although for all BVOCs the contribution from the biosynthetic pathway was larger. The isoprene emission flux was overestimated by the combined emission model, indicating it is a biosynthetic emission only. The combined emission model was able to accurately describe the remaining twenty-six BVOC emissions from Spruce 2, such as the sum of monoterpenes, however for pooled emissions including $C_6H_{10}O$, the emission flux was overestimated, Figure 3.25.

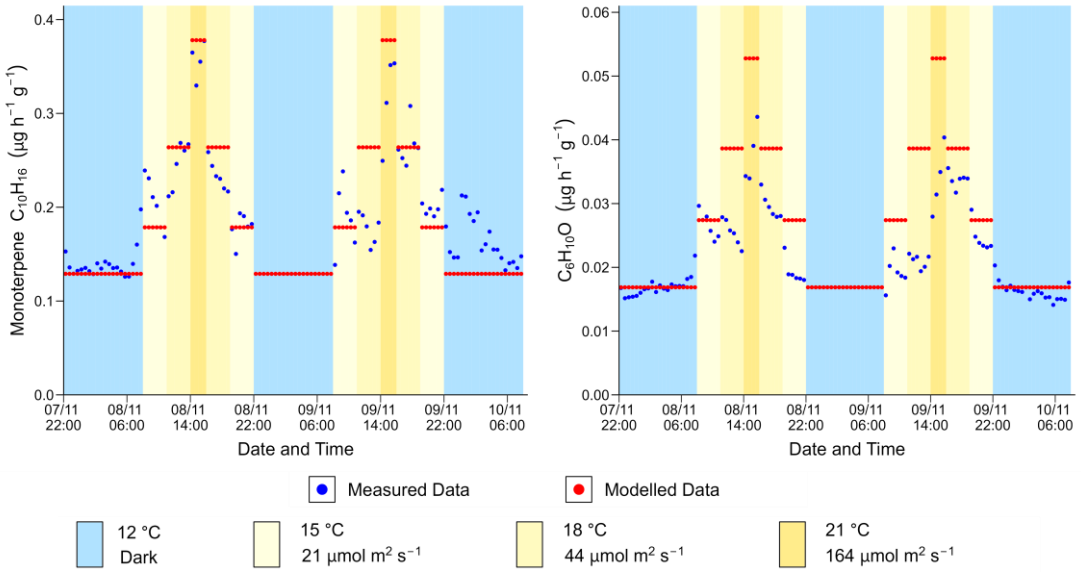

Figure 3.25 *Measured data (blue) and combined model data (red) for the emission of the sum of monoterpenes (left) and $C_6H_{10}O$ (right) from Spruce 2 during the Daily cycle.*

In contrast to Spruce 1, the dominant emission pathway for all Spruce 2 emissions was the pooled emission pathway, this further supports the theory that the biosynthetic pathways were not functioning to optimum capacity for Spruce 2 due to stress. The combined emission pathway has been used previously to describe the emissions from sunflower and beech[132]. The emissions from Norway spruce have been shown to originate from both pooled and biosynthetic emission pathways simultaneously[193]. The combined emission pathway has not been used to standardise the emissions of Sitka spruce previously, for monoterpenes only the pooled emission equation[83] has been used, and for isoprene the biosynthetic emission equation has been used[81].

Thirteen of the sixteen emissions common to both spruce trees were standardised using the combined emission equation. The remaining three BVOCs: C_9H_8O, $C_{10}H_{14}O_2$ and $C_{20}H_{24}$, originated from different pathways from each tree. The emission of C_9H_8O, identified as E-cinnamaldehyde, from Spruce 1 originated from a biosynthetic pathway, while from Spruce 2 it appeared as a pooled emission. For $C_{10}H_{14}O_2$ and $C_{20}H_{24}$ the emission from Spruce 1 was via both pathways, while for Spruce 2 the emission was via the pooled pathway only. The latter two emissions may be indicative of BVOCs that when emitted from a healthy tree, Spruce 1, proceed mainly

via a biosynthetic pathway, and when a tree suffers stress, Spruce 2, the biosynthetic pathway ceases as an emission route and the only available emission pathway is diffusion from storage pools.

3.3.5.2 Standardisation Application

Sitka Spruce

The modelling approach which best replicated the *Daily Cycle* BVOC emission profile for each Sitka spruce tree was used to provide the standardised emission flux at a PPFD of 1000 µmol m^{-2} s^{-1} and temperature of 30 °C. For the majority of the BVOCs emitted from both trees the combined emission model was used to calculate the standardised emission flux, with the remaining BVOCs from Spruce 1 using the biosynthetic emission model (Table 3.7) and the remaining BVOCs from Spruce 2 using the pooled emission model (Table 3.9).

Table 3.7 *BVOC emission fluxes from Spruce 1 standardised to 1000 µmol m^{-1} s^{-1} and 30°C in µg h^{-1} g^{-1}. BVOC emissions ordered in order of decreasing standardised emission flux.*

Formula	BVOC	Standardisation Method	Standardised Emission Flux µg h^{-1} g^{-1}
$C_{10}H_{16}O$	Piperitone	Combined	17.290
C_5H_8	Isoprene	Biosynthesis	6.306
$C_{10}H_{16}$	Monoterpene	Combined	0.925
$C_{10}H_{14}O$		Combined	0.859
$C_5H_8O_2$		Biosynthesis	0.467
$C_{10}H_{16}O_2$		Combined	0.455
C_9H_8O	(E)-Cinnamaldehyde	Biosynthesis	0.334
$C_{13}H_{30}O_5$		Combined	0.276
$C_{12}H_{20}O$		Biosynthesis	0.271
$C_{10}H_{16}O$	Camphor	Combined	0.199
$C_5H_{10}O_6$		Biosynthesis	0.196
$C_{20}H_{24}$		Combined	0.177
$C_{10}H_{14}O_2$		Combined	0.166
$C_{10}H_{10}$		Biosynthesis	0.155
$C_{10}H_{20}O_2$	Isopentyl isovalerate	Biosynthesis	0.148
C_8H_{12}		Combined	0.147

$C_{14}H_{16}O$		Combined	0.138
$C_7H_{12}N_2$		Biosynthesis	0.127
$C_3H_8N_2O$		Biosynthesis	0.082
$C_6H_{14}O_3$		Combined	0.082
$C_{12}H_{16}$		Biosynthesis	0.081
$C_{11}H_{14}O$		Combined	0.077
$C_{20}H_{24}O_2$		Combined	0.074
$C_7H_4O_4$		Combined	0.067
C_7H_8O		Combined	0.052
$C_{17}H_{26}O$		Combined	0.046
C_7H_8		Combined	0.040
C_9H_{12}		Combined	0.030
$C_{13}H_{12}O$		Biosynthesis	0.025
$C_{10}H_{18}O_4$		Combined	0.020
$C_{10}H_{14}O_5$		Combined	0.016
$C_5H_{10}NO_2$		Combined	0.015
$C_{18}H_{34}O$		Combined	0.014
C_3H_9N		Combined	0.012

Apart from the three dominant BVOCs emitted by Spruce 1, the standardised emission flux of all other BVOCs was below 0.9 μg h^{-1} g^{-1}. Piperitone was the dominant BVOC emitted by Spruce 1, with a standardised emission flux of 17.29 μg h^{-1} g^{-1}. Piperitone has been detected in the emissions of Sitka spruce previously, although an emission flux was not provided. The standardised emission flux of piperitone was reported to be 0.37 μg h^{-1} g^{-1} from Ponderosa pine[67]. Comparison of the standardised emission flux of piperitone is difficult as most previous studies do not report oxygenated BVOCs. Table 3.8 provides a comparison of the previously reported isoprene and monoterpene emission fluxes from Sitka spruce.

Table 3.8 *Reported emission fluxes for isoprene and monoterpenes from Sitka spruce.*

Isoprene	Monoterpene	Temperature	PPFD	Reference
µg h^{-1} s^{-1}	µg h^{-1} s^{-1}	°C	µmol m^{-1} s^{-1}	
3.06	0.95	28	1000	Evans et al. (1982)
5.21	2.30	38	1000	Evans et al. (1985)
0.05	1.50	16	360	Street et al. (1993)
1 - 5	0.001 - 0.025	21 - 36	not reported	Street et al. (1996)
14 - 17	-	28	230	Hayward et al. (2002)
13.4	2.97	30	1000	Hayward et al. (2004)
6.30	6.30	30	1000	This work

** Emission fluxes standardised, otherwise reported at measured conditions.*

The standardised emission flux of isoprene from Spruce 1 was 6.3 µg h^{-1} g^{-1}. In a study by Evans et al. (1982)[78] the reported isoprene emission flux from Sitka spruce was roughly half the standardised value determined in this work. The isoprene emission flux from Sitka spruce in another study by Evans et al. (1985)[79] was quite similar to the standardised value in this work, although there is an 8 °C temperature difference between the study conditions and the standardisation temperature of 30 °C. The conditions employed in this work were similar to the conditions in a study conducted by Street et al. (1993)[141], although the isoprene emission flux reported in that study was much lower. In another study by Street et al. (1996)[81] the range of isoprene emission fluxes that was reported is similar to the 0.8 µg h^{-1} g^{-1} observed in this work at 21 °C and 164 µmol m^{-2} s^{-1}, however PPFD was not reported, which hinders the comparison. The highest Sitka spruce isoprene emission fluxes were reported by Hayward et al. (2002)[171]. This may be due to an alteration in the emission composition as the tree aged, as suggested by Hakola et al. (2001)[137] for the emissions from birch, or due to environmental factors[83]. The isoprene standardised emission flux from nine-year old Sitka spruce determined by Hayward et al. (2004)[83], was roughly double the standardised value determined in this work. Overall, the isoprene emission flux found in this work is in a similar range to previously reported values.

The standardised emission flux for the sum of monoterpenes from Spruce 1 was calculated to be 0.93 µg h^{-1} g^{-1}. The study by Evans et al. (1982)[78], reported an

emission flux for five monoterpenes very similar to the value observed in this work, despite the composition of the monoterpene emissions being slightly different. The other study by Evans et al. (1985)[79] reported a much higher monoterpene emission flux from Sitka spruce, this may be due to differing temperature conditions or a different monoterpene composition. The total monoterpene emission flux reported by Street et al. (1993)[141], is similar to the standardised emission flux reported in this work. The range reported for the monoterpene emission flux by Street et al. (1996)[81] is much lower than all other studies. The standardised total monoterpene emission flux provided by Hayward et al. (2004)[83] is over three times the standardised emission flux determined in this work. Hayward et al. (2004)[83] also reported higher isoprene emission fluxes, which indicates their elevated emission fluxes may be related to environmental factors. The standardised monoterpene emission flux calculated in this work is in line with that reported in previous studies.

The standardised emission fluxes of most BVOCs emitted by Spruce 2 were lower than those for Spruce 1, Table 3.9. This is likely due to Spruce 2 suffering from some unknown stress which reduced the effectiveness of the biosynthetic pathway and led to a reduction in the emission fluxes.

Table 3.9 *BVOC emission fluxes from Spruce 2 standardised to 1000 µmol m^{-1} s^{-1} and 30°C in µg $h^{-1}s^{-1}$. BVOC emissions ordered in order of decreasing standardised emission flux.*

Formula	BVOC	Standardisation Method	Standardised Emission Flux µg h^{-1} g^{-1}
$C_{10}H_{16}$	Monoterpene	Combined	1.226
$C_{10}H_{16}O$	Piperitone	Combined	1.029
C_6H_8O		Pooled	0.192
$C_{20}H_{24}$		Pooled	0.134
C_9H_8O	(E)-Cinnamaldehyde	Combined	0.120
$C_6H_{10}O$	E-2-Hexenal	Pooled	0.104
$C_{15}H_{24}$	E-Farnesene	Combined	0.097
$C_8H_{12}O$		Combined	0.073
$C_{14}H_{16}O$		Combined	0.071
$C_{10}H_{14}O_2$		Pooled	0.066

$C_{10}H_{16}O$	Camphor	Combined	0.061
C_7H_8O		Combined	0.056
$C_{13}H_{30}O_5$		Combined	0.055
C_8H_{12}		Combined	0.051
$C_9H_{12}O$		Combined	0.046
C_9H_{12}		Combined	0.035
$C_8H_8O_3$	Methyl salicylate	Combined	0.033
$C_{20}H_{24}O_2$		Combined	0.033
C_7H_8		Combined	0.031
$C_{10}H_{16}$		Pooled	0.029
$C_{10}H_{18}O_4$		Combined	0.025
C_6H_8		Combined	0.023
$C_{10}H_{18}O$	Eucalyptol	Combined	0.022
$C_{17}H_{26}O$		Combined	0.018
$C_9H_{10}O_2$		Combined	0.018
$C_{12}H_{16}O$		Combined	0.012
$C_7H_{10}O$		Combined	0.009
$C_{10}H_{16}O_3$		Combined	0.008
C_8H_{12}		Combined	0.007
C_6H_8O		Combined	0.007
$C_{10}H_{14}O_2$		Pooled	0.006
$C_{18}H_{34}O$		Combined	0.003

The standardised total monoterpene emission flux from Spruce 2 was 1.2 μg h^{-1} g^{-1}, higher than from Spruce 1. The emission of monoterpenes from several spruce species have been observed to increase upon exposure to stress. Monoterpene emissions from blue spruce experienced an increase under stressed conditions[194], although the standardised emission flux, 23.3 μg h^{-1} g^{-1}, is not comparable to that determined in this work, the process causing increased monoterpene emissions when subject to stress may be similar. A similar phenomenon has been observed for Norway spruce, the monoterpene emission flux was observed to increase when the trees were subject to elevated O_3 concentrations. A standardised monoterpene emission flux of 1.1 μg h^{-1} g^{-1} was reported when exposed to O_3 concentrations above 60 ppb. This is similar to the value obtained in this work. Although the stress experienced by Spruce 2 was unknown, the elevated monoterpene flux compared to

Spruce 1, a healthy Sitka spruce tree, seems to be in line with findings from other spruce species.

Annual Emission Flux

Annual emission fluxes for the three main BVOCs emitted from Spruce 1, piperitone, isoprene and the sum of monoterpenes, were calculated using Equation 3.8.

$$BVOC_{\mathrm{Flux}} = E_{\mathrm{BVOC}} \times LMA \times Area \qquad \textbf{\textit{Equation 3.8}}$$

Here $BVOC_{\mathrm{Flux}}$ is the annual emission of a particular BVOC from all Sitka spruce in Ireland, in tonne year^{-1}; E_{BVOC} is the annual emission flux of a particular BVOC per dried mass of Sitka spruce, in tonne year^{-1} g^{-1}; *LMA* is foliar mass per ground area of Sitka spruce, in g m^{-2}; and *Area* is the total land area of Sitka spruce forests in Ireland, in m^2. E_{BVOC} was calculated for each BVOC using the standardised emission flux equations combined with global solar radiation and temperature data acquired from Met Éireann[162, 195]. An estimate for LMA was derived from assessments of Sitka spruce forests in Ireland[196] and the UK[197-200]. The annual BVOC emission fluxes for piperitone, isoprene and monoterpenes are given in Table 3.10.

Table 3.10 *Table of annual emission fluxes for piperitone, isoprene and monoterpenes from Sitka spruce in Ireland.*

BVOC	**Annual Emission Flux**		
	Tonne year^{-1}	**g C ha^{-1} year^{-1}**	**g C m^{-2} year^{-1}**
Isoprene	13,000	34,000	3.3
Piperitone	8,200	19,000	1.9
Monoterpene	1,600	4,200	0.4
Total	22,800	57,200	5.6

The total annual emission flux for the three main BVOCs emitted from all Sitka spruce in Ireland was calculated to be 22,972 tonne year^{-1}. This figure is proposed as a lower estimate for the true emission flux for several reasons. Firstly, due to limited data availability the calculation does not account for increases in foliage as the trees grow[186], which would lead to an increased emission flux. Secondly, the calculation

only accounts for the three main foliar BVOC emissions and does not include emissions that may originate from the bark of the tree. As previously discussed visible resin deposits were observed on the trees in this study and potentially contributed to the overall emission flux. Finally, the calculation does not take all BVOCs emitted from Sitka spruce into consideration.

The total non-methane VOC emissions produced by anthropogenic sources in Ireland for 2020 was 112,620 tonne $year^{-1}$, as reported by the Environmental Protection Agency[201]. This figure is based on bottom up emissions inventory calculations for air pollutants resulting from human activity, and does not account for BVOC emissions[202]. Accounting for 23.7% of the total, the Food and Beverage Industry was the second highest contributor to this emission category, with 26,730 tonne emitted in 2020[201]. This is comparable to the lower estimate of 22,972 tonne $year^{-1}$ emitted by Sitka spruce, and shows that biogenic sources account for a significant proportion of ambient VOCs.

An annual BVOC emission flux has not been previously calculated for a Sitka spruce forest, although the value calculated in this work falls within the range of previously reported values for other plantation tree species. An annual BVOC emission flux of 19,200 g C ha^{-1} $year^{-1}$ was reported for a poplar plantation in Belgium[203], three times lower than the 56,820 g C ha^{-1} $year^{-1}$ calculated for Sitka spruce in this work. The emissions from the poplar plantation were dominated by isoprene, methanol and acetic acid, all of which have a low carbon content, while in this work piperitone and monoterpenes, both C_{10} BVOCs, made substantial contributions to the emission flux. BVOCs with a higher carbon content will contribute more if the emission is reported in terms of carbon mass, and this may partially explain why the emission flux is higher for Sitka spruce. An annual BVOC emission flux of 9.4 g C m^{-2} $year^{-1}$ was calculated for a Ponderosa pine forest in California[186]. This is higher than the 5.7 g C^{-1} m^{-2} $year^{-1}$ calculated in this work for Sitka spruce. Each tree and plant species emits a unique BVOC profile, which will lead to differing values for annual emission fluxes.

A value of 8,240 tonne year^{-1} was calculated as the annual emission flux of piperitone from all Sitka spruce in Ireland, with 13,115 tonne year^{-1} determined for isoprene and 1,620 tonne year^{-1} for the sum of monoterpenes. The annual emission flux of isoprene is greater than the annual emission flux for piperitone, despite piperitone being identified as the dominant emission in this work, and having a standardised emission flux almost three times that of isoprene. This is due to the relationships between temperature, PPFD and BVOC emission, which are different for piperitone and isoprene, as depicted in Figure 3.26.

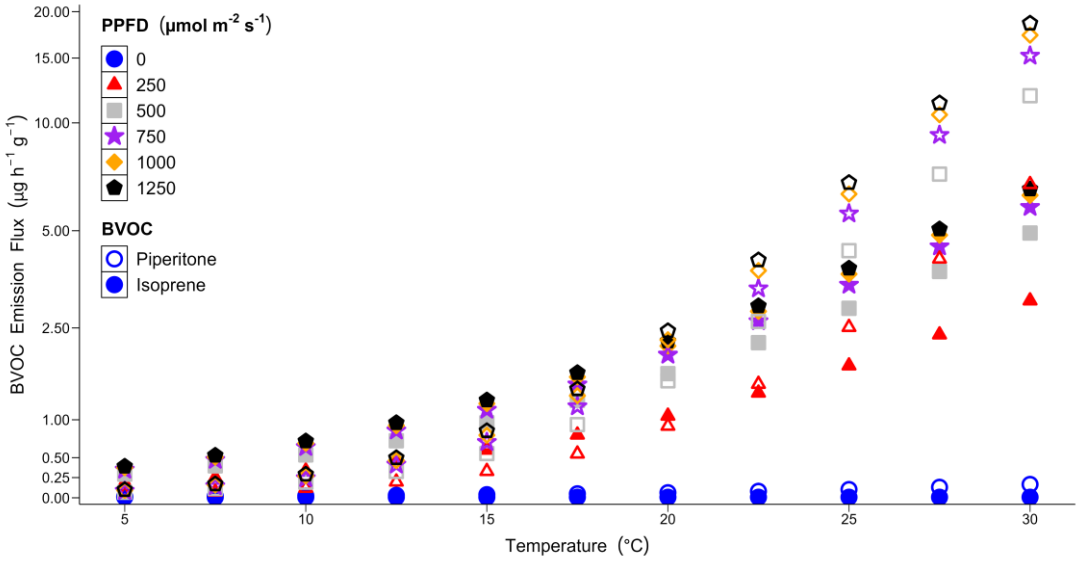

Figure 3.26 *Relationship between piperitone and isoprene emission fluxes and temperature at different PPFDs. Colour and shape indicate different PPFD, empty symbols - piperitone, filled symbols - isoprene.*

BVOC emission fluxes have an exponential relationship with temperature. At a certain temperature there is an inflection point, above which increasing the temperature causes a significant increase in emission flux (Figure 3.26). Piperitone (open symbols) has a strong exponential relationship with temperature, with an inflection point around 15 °C. Below this temperature the piperitone emission flux is quite low and displays little change with temperature. Isoprene (closed symbols) has a much weaker relationship with temperature than piperitone, with an inflection point at around 22.5 °C, although it is not as clearly defined as it is for piperitone.

BVOCs emission fluxes have a logarithmic relationship with PPFD. At a given temperature, the increase in emission flux decreases with fixed successive increases in PPFD, until a saturation point is reached. Below 750 µmol m^2 s^{-1} the piperitone emission flux is strongly PPFD dependent. This relationship weakens as PPFD increases and the emission flux approaches the saturation point. The isoprene emission flux has a stronger relationship at lower PPFD than piperitone, seen in Figure 3.26 through the sharp increase in emission flux between 0 µmol m^2 s^{-1} and 250 µmol m^2 s^{-1}. The saturation point for isoprene is lower than for piperitone, with a minimal increases in the isoprene emission flux above 500 µmol m^2 s^{-1}.

The exponential temperature and logarithmic PPFD relationships operate simultaneously. For both piperitone and isoprene, at lower temperatures the influence of PPFD is stronger than that of temperature. Above the respective inflection points the temperature factor plays a greater role in the emission flux. At lower temperatures the emission flux of piperitone is less than that for isoprene. This is because of the strong exponential relationship between the piperitone emission flux and temperature. Isoprene has a more muted relationship with temperature and the emission flux is not as sensitive to lower temperatures. In the lower temperature regime the emission of isoprene is higher than piperitone, at all PPFD levels.

Typical temperatures for Ireland range between 6 °C and 17 °C. Under these conditions the emission of isoprene is higher than piperitone. The temperature for standardising BVOC emissions is 30 °C. At this temperature the emission of piperitone is higher than isoprene. The conditions employed during the measurement cycles in this work fall between these two extremes and favour the emission of piperitone. Analysis of the temperature and PPFD dependence of the emission of both BVOCs explains why the annual emission flux of isoprene is greater than that for piperitone. A 2 °C increase in surface temperatures due to climate change[204], would be sufficient to alter the piperitone - isoprene emission ratio from Sitka spruce in favour of piperitone. Therefore under current future climate warming projections piperitone would be the dominant BVOC emitted by Sitka spruce.

3.4. Conclusions

The composition of the BVOCs emitted by three Sitka spruce trees was determined using a combination of on-line, $C_6H_6^+$ ToF-CIMS (composition and temporal resolution), and off-line TD-GC/MS (structure) analyses. CO_2 fluxes and chlorophyll fluorescence measurements were also recorded. Three Sitka spruce trees were housed in a plant growth chamber and subjected to three sets of environmental conditions (*Daily cycle*, *Temperature Cycle* and *Light Cycle*) to assess the influence of temperature and PPFD on the emission fluxes.

Seventy-four different BVOCs were found in the Sitka spruce emissions; twenty-one BVOCs were common to the emissions of all three trees. Fifty-two BVOCs were oxygenated, with O_1 BVOCs dominating the emissions. The carbon content of the emissions ranged from C_3 - C_{20}, with C_{10} being the prominent carbon content.

Forty-nine BVOCs were detected in the emissions from Spruce 1. Piperitone $C_{10}H_{16}O$, an oxygenated monoterpene, was the dominant emission, with a standardised emission flux of 17.29 µg h^{-1} g^{-1}. The second highest emission was isoprene, with a standardised emission flux of 6.3 µg h^{-1} g^{-1}. Five monoterpenes were identified; myrcene, β-phellandrene, δ-limonene, α-pinene, and camphene. The standardised emission flux for the sum of monoterpenes was 0.93 µg h^{-1} g^{-1}. Six BVOCs emitted from Spruce 1, including isoprene, experienced a post-illumination burst, which is thought to be related to a pyruvate overflow mechanism. CO_2 uptake increased with increasing PPFD, indicating that for Spruce 1 photosynthesis was active. BVOC emissions from Spruce 1 accounted for approximately 0.2% of carbon uptake.

A total of fifty-eight BVOCs were emitted from Spruce 2, although they had lower BVOC emission fluxes than Spruce 1. The main BVOCs emitted from Spruce 2 were monoterpenes. The same five monoterpenes emitted from Spruce 1 were also emitted from Spruce 2, with a standardised emission flux of 1.3 µg h^{-1} g^{-1}. The second highest emission from Spruce 2 was piperitone, with a standardised emission flux of 1 µg h^{-1} g^{-1}. The emissions from Spruce 2 contained a sesquiterpene and six C_6

oxygenated BVOCs, signifying that Spruce 2 was under some unknown stress. The CO_2 fluxes from Spruce 2 were quite scattered and the magnitude was much lower than for Spruce 1, further indicating that Spruce 2 was stressed.

The TD-GC/MS analysis of Spruce 3 found twenty-two of the BVOCs detected in the emissions of Spruce 1. No BVOCs were detected by the ToF-CIMS from Spruce 3.

All BVOCs monitored by the ToF-CIMS were lowest during the dark and increased upon illumination and temperature increases, with the emission fluxes highest at the highest PPFD and temperature settings. The BVOC emissions were standardised to a temperature of 30 °C and PPFD of 1000 µmol m^{-2} s^{-1}, according to the equations derived by Guenther et al. (1993)[130], and Schuh et al. (1997)[132]. The standardisation approach employed was based on the reproducibility of the emissions using the standardisation model. The majority of the BVOC emission fluxes were standardised using the combined emission model, indicating that the emissions from Sitka spruce originate from both pooled and biosynthetic emission sources simultaneously.

The Spruce 1 standardised emission fluxes for piperitone, isoprene and the sum of monoterpenes were used to calculate annual fluxes for all Sitka spruce plantations in Ireland. The annual emission flux of piperitone was found to be 8,240 tonne $year^{-1}$, 13,114 tonne $year^{-1}$ for isoprene, and 1,618 tonne $year^{-1}$ for the sum of monoterpenes. The isoprene annual emission flux is higher than that for piperitone, due to their temperature and PPFD relationships. This highlights the importance of assessing BVOC emissions at the conditions relevant to the local climate.

The annual BVOC emission flux from Sitka spruce in Ireland was calculated to be 22,972 tonne $year^{-1}$. This contributes substantially to Ireland's total VOC flux, equalling approximately 20% of the total anthropogenic VOC emission flux.

Chapter 4 Kinetics and Products of the $OH^{\bullet}$ Initiated Oxidation of Piperitone

4.1 Introduction

Once emitted into the atmosphere, BVOCs may undergo gas-phase oxidation reactions initiated by the atmospheric oxidants, $OH^{\bullet}$, O_3 and $NO_3^{\bullet}$, and in some cases photolysis by sunlight. The specific chemical functionalities present in the BVOC determine which types of reactions are possible[22, 205]. It is important to determine the reaction rates and oxidation mechanisms of prominent BVOCs in order to assess the impact they have on air quality and climate. Forests are often assumed to be pristine environments, with little influence from anthropogenic sources[25, 206], and therefore reaction with $OH^{\bullet}$ and where possible O_3 and photolysis, are expected to be the dominant loss processes. Piperitone was identified as the main BVOC emitted from Sitka spruce (Chapter 3). However, there have been no previous studies on the atmospheric chemistry of piperitone. wed 20 2.45

4.1.1 Reaction Kinetics

Kinetic studies are used to determine the reactivity of a compound (analyte) with respect to reaction with a particular oxidant. There are several predictive and experimental approaches available for determining rate coefficients. The most widely used prediction method is the structure activity relationship (SAR) developed by Atkinson et al. (1987)[207] and re-evaluated by Kwok and Atkinson et al. (1995)[208]. For reaction with a given oxidant, the method is used to calculate the partial rate coefficient at each reactive site, accounting for the influence of neighbouring functionalities, and sums across all reactive sites to determine the overall rate coefficient. The method assumes that reaction at a particular site is completely independent from reaction at any other site, and that reactivities are additive. This method is widely used for reaction of VOCs with $OH^{\bullet}$, and can also be used for reaction with O_3[209] and $NO_3^{\bullet}$[210]. Other SAR methods have also been developed based on molecular orbital theory[37, 211] and ionisation energy[37, 212], however these are not commonly used.

Rate coefficients can be determined via two experimental methods: absolute rate and relative rate. For both methods the second order bimolecular rate equation is used,

$$-\frac{d[A]}{dt} = k_{\mathrm{A}} \times [A] \times [O] \qquad \textit{Equation 4.1}$$

where: $-\frac{d[A]}{dt}$ is the rate of decay of analyte; k_{A} is the rate coefficient for the reaction; [*A*] is the concentration of analyte; and [*O*] is the concentration of oxidant.

The absolute rate method employs pseudo first order conditions, in which the concentration of either the analyte or oxidant is added in excess and is assumed to be constant, and the decay of the other is monitored with time[44]. For an excess of oxidant, Equation 4.1 can be abbreviated to Equation 4.2, and is used to derive Equation 4.3,

$$-\frac{dA}{dt} = k_{\mathrm{A}}' \times [A] \qquad \textit{Equation 4.2}$$

$$\ln\left(\frac{[A]_0}{[A]_{\mathrm{t}}}\right) = k_{\mathrm{A}}' \times t \qquad \textit{Equation 4.3}$$

where: *t* is time; $[A]_0$ is the concentration of analyte at the start of the reaction; $[A]_{\mathrm{t}}$ is the concentration of analyte at time *t*; and k_{A}' is the pseudo first order rate coefficient, given by $k_{\mathrm{A}}' = k_{\mathrm{A}} \times [O]$. Experiments are conducted several times with varying concentrations of oxidant, and a plot of k_{A}' as a function of [*O*], will yield a straight line, with slope equal to k_{A}[213]. There is a high degree of accuracy associated with absolute rate coefficients, as they are direct measurements[44]. However, the difficulty associated with the absolute method is that accurate measurement of both the analyte and oxidant is required[44].

The relative rate method employs the use of another reactive compound, called the reference compound that has a known rate coefficient for reaction with the oxidant. The decay of the analyte is measured relative to that of the reference compound[214].

Equation 4.3 holds for both the analyte and reference compounds, and as [*O*] and *t* will be the same, combination of the equations gives Equation 4.4,

$$\ln\left(\frac{[A]_0}{[A]_t}\right) = \frac{k_A}{k_R} \times \ln\left(\frac{[R]_0}{[R]_t}\right) \qquad \textit{Equation 4.4}$$

where: k_R is the rate coefficient for the reference compound with the oxidant; $[R]_0$ and $[R]_t$ are the concentrations of the reference compound at the start of the reaction and at time *t*, respectively. The relative decay of analyte with respect to the reference compound is determined from a plot of $\ln\left(\frac{[R]_0}{[R]_t}\right)$ versus $\ln\left(\frac{[A]_0}{[A]_t}\right)$, which will yield a straight line with slope equal to $\frac{k_A}{k_R}$. The relative coefficient is then scaled by k_R to place it on an absolute scale[44, 214].

Relative rate coefficients are easier to measure than absolute rate coefficients, as they do not require precise measurement of the oxidant concentration, only measurements proportional to the analyte and reference compound concentrations are necessary[215]. Relative rate coefficients are not as accurate as absolute rate coefficients, as the error associated with k_R is carried into the value determined for k_A. Care must be taken when selecting a reference compound, as it ideally should have similar reactivity to the reference compound[44], and there should not be interference between the measurements of the analyte and reference compounds[214]. Experiments should be conducted with several reference compounds to ensure accuracy.[215]

For determination of both absolute and relative rate coefficients, care should be taken to ensure that the decay of the analyte is only due to reaction with the oxidant, and not due to photolysis, reaction with other oxidants present in the system[214, 215] or "chamber losses" caused by sampling, dilution or deposition to the chamber walls. Photolysis and chamber losses are first order processes which can be accounted for by monitoring the decay of the compound in the absence of other loss processes[215]. Modification of Equation 4.2 to Equation 4.5 allows calculation of the rate coefficient for a first order loss process,

$$k_{\text{loss}} = \frac{\ln\left(\frac{[A]_0}{[A]_t}\right)}{t} \qquad \textit{Equation 4.5}$$

where: k_{loss} is the rate coefficient (in s^{-1}) for a first order loss process, such as photolysis or chamber losses. Decays due to chamber losses and photolysis can be corrected for using Equation 4.6,

$$[A]_t^{\text{corrected}} = [A]_t^{\text{uncorrected}} + ([A]_0 \times t \times k_{\text{loss}}) \qquad \textit{Equation 4.6}$$

where: $[A]_t^{\text{corrected}}$ is the concentration of the analyte corrected for chamber losses at time *t*; and $[A]_t^{\text{uncorrected}}$ is the instrument measured reagent concentration at time *t*.

4.1.2 Oxidation Mechanisms

The oxidation of atmospheric BVOCs is typically initiated by reaction with $OH^{\bullet}$, O_3, and $NO_3^{\bullet}$. For BVOCs containing a light absorbing functionality or chromophore, such as a carbonyl group, photolysis (photodissociation) by sunlight is also possible. Aldehydes and ketones are known to undergo photolysis via three pathways[216, 217].

$$R_1C(O)R_2 \xrightarrow{h\nu} R_1\dot{C}(O) + \dot{R}_2 \qquad \textit{Reaction 4.1}$$

$$R_1C(O)R_2 \xrightarrow{h\nu} \dot{R}_1 + \dot{C}H(O)R_2 \qquad \textit{Reaction 4.2}$$

$$R_1C(O)R_2 \xrightarrow{h\nu} R_1R_2 + CO \qquad \textit{Reaction 4.3}$$

For aldehydes R_2 is a hydrogen atom. The relative importance of each photolysis pathway depends on the structure of the compound and the wavelength range of the incident light[217, 218]. Some compounds containing unsaturated carbonyls may also undergo photoisomerisation, rather than photodissociation[219, 220].

The reaction of BVOCs with OH• proceeds via two mechanisms; hydrogen abstraction (H-abstraction) from either C-H or O-H bonds, and OH• addition to an unsaturated functionality[214]. Both pathways lead to the formation of a highly reactive radical, which will continue to react leading to the formation of other radicals until a stable molecule is produced. H-abstraction preferentially occurs from the most substituted carbon, which will yield a more substituted alkyl radical[214], Figure 4.1.

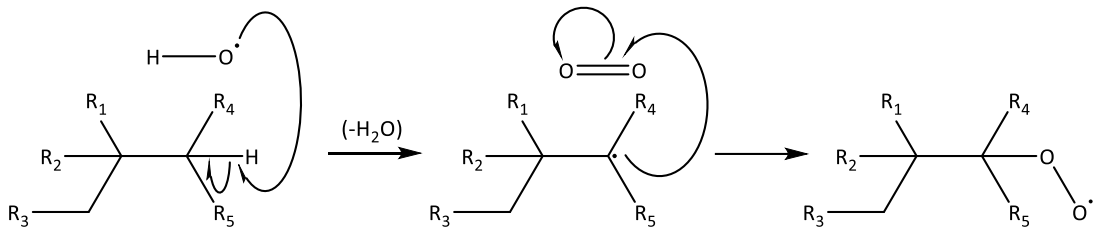

Figure 4.1 *Example of H-abstraction mechanism for the reaction of OH• with an organic compound. R can be alkyl or hydrogen.*

The resulting alkyl radical rapidly adds O_2, to produce a peroxy radical (ROO•)[22, 214]. Several routes are available to the peroxy radical, depending on the environment, Figure 4.2.

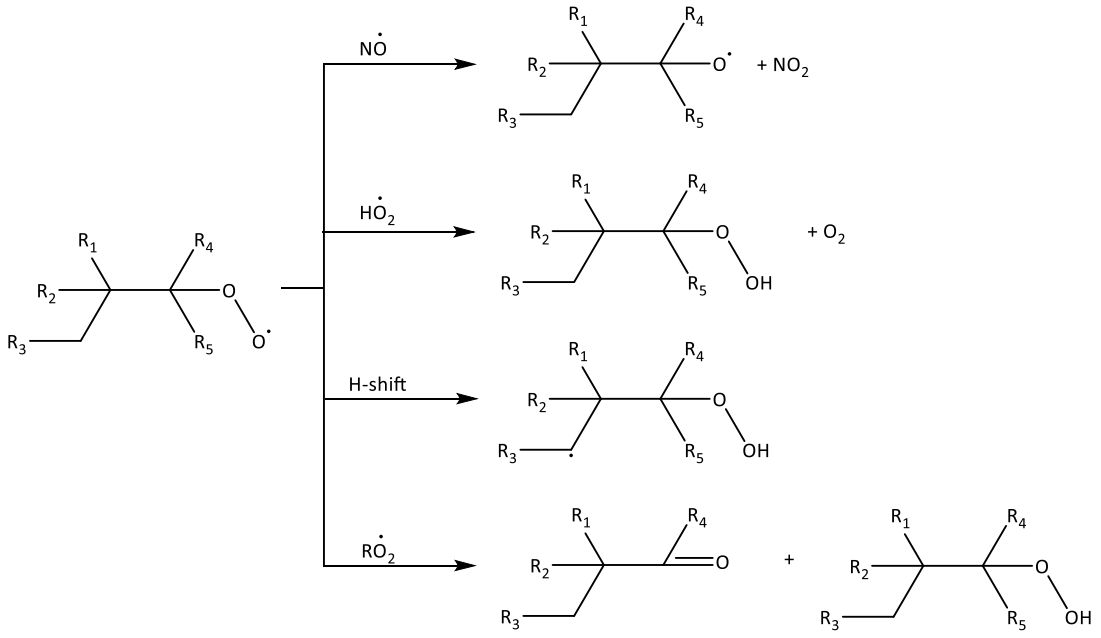

Figure 4.2 *Main reaction pathways for peroxy radicals (RO_2•) in the atmosphere.*

Reaction with $NO^{\bullet}$, will lead to the formation of NO_2 and an alkoxy radical ($RO^{\bullet}$), which can undergo dissociation or isomerisation[22, 36]. However, reaction with $NO^{\bullet}$ is not likely for BVOCs in pristine forest environments where NO_x levels are typically low[25]. Reaction with $HO_2^{\bullet}$ is expected to be a major pathway for peroxy radicals in these conditions, with a stable hydroperoxide and O_2 produced[214, 221]. Several other products are also possible from this reaction[221], although the hydroperoxide is expected to be the dominant product. Peroxy radicals can also undergo hydrogen shifts, with 1,5-shifts and 1,6-shifts being the most likely[222], as they involve stable six membered and seven membered transition states, respectively. These hydrogen shift reactions produce another alkyl radical, which will add O_2 and react in a similar manner[223]. Peroxy radicals can also react with other peroxy radicals, with the main reaction products being a carbonyl and an alcohol, provided R_5 is a hydrogen atom. Other products are also possible[22, 224].

$OH^{\bullet}$ addition only occurs for unsaturated and aromatic hydrocarbons. Upon $OH^{\bullet}$ addition the unsaturated bond is broken and a new bond between the carbon atom and the $OH^{\bullet}$ is formed, producing a radical centre at the other carbon in the C=C bond, giving a β-hydroxyalkyl radical[22, 214], Figure 4.3.

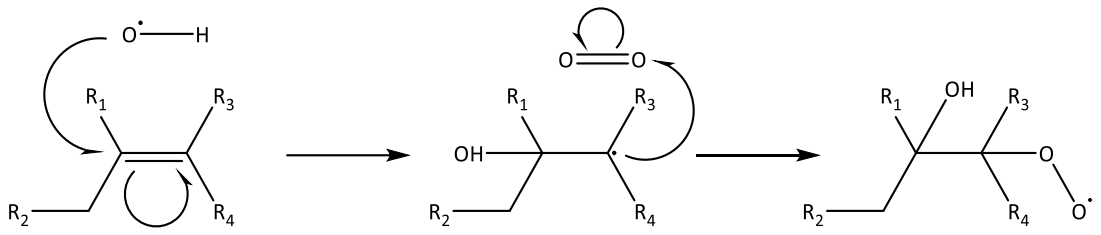

Figure 4.3 *Schematic of mechanism for $OH^{\bullet}$ addition to an alkene. R can be alkyl or hydrogen.*

$OH^{\bullet}$ addition to a C=C bond in an alkene predominantly occurs at the less substituted carbon atom. Sterically this site is more accessible and it will produce a more stable alkyl radical at the other more substituted carbon atom[222]. O_2 rapidly adds to the alkyl radical, producing a β-hydroxyperoxy radical[22, 224]. The fate of β-hydroxyperoxy radicals is the same as for the peroxy radicals produced from the H-abstraction mechanism described above[206, 222], Figure 4.2.

Reaction with O_3 and $NO_3^{\bullet}$ are other loss processes for BVOCs. Ozonolysis only occurs if an alkene or alkyne bond is present, and will add across the unsaturated functionality to produce a primary ozonide, which undergoes rapid decomposition leading to the formation of a Criegee biradical[22, 225]. Reaction with $NO_3^{\bullet}$ proceeds in a similar manner to that for $OH^{\bullet}$[21].

4.1.3 Aims

The overall aim of this chapter was to determine the atmospheric fate of piperitone, the main BVOC emitted from Sitka spruce. This was achieved by focussing on two objectives.

The first objective was to determine the rate coefficients for the reaction of piperitone with the main atmospheric oxidants using a SAR approach, and then to determine the rate coefficient for reaction with $OH^{\bullet}$ experimentally. This allowed atmospheric lifetimes for reaction with various oxidants to be determined.

The second objective was to identify the main oxidation products from the reaction of piperitone with $OH^{\bullet}$ and to propose mechanisms for their formation.

4.2 Prediction of Rate Coefficients using SAR

4.2.1 OH• Rate Coefficient

A rough estimate of the rate coefficient for the reaction of the OH• with piperitone was made by assessing the reactivity of similarly structured compounds. Table 4.1 provides the rate coefficients for the reaction of OH• (k_{OH}) for some alkenes (blue) and their α-ketone conjugated analogues (orange) with similar structures to piperitone. Among the alkenes, the value of k_{OH} increases with increasing substitution around the C=C bond, with cyclic compounds having the highest rate coefficients. The α-ketone conjugated analogues of these alkenes might be expected to have lower k_{OH} values, due to the electron withdrawing effect of the carbonyl group. While this appears to be true for methylvinyl ketone (MVK) and seudenone, the other ketones show similar reactivity to their analogous alkenes. This phenomenon has been observed for other linear alkenes and their α-ketone conjugated analogues, and it has been speculated that the formation of a hydrogen bond between the OH• and the carbonyl facilitates OH• addition to the C=C bond, counteracting the electron withdrawing effect of the carbonyl group[226]. Nevertheless, based on the reactivity patterns shown in Table 4.1 k_{OH}(piperitone) is expected to fall between those of 1-p-menthene[227] and seudenone[44].

Table 4.1. *Experimentally determined values of k_{OH} for a series of alkenes and their α-ketone conjugated analogues at 298 (± 3) K, in units of cm^3 $molecule^{-1}$ s^{-1}.*

Alkene	But-1-ene[228]	Pent-1-ene[228]	2-methylpent-2-ene[229]	1-methylcyclohexene[229]	1-p-menthene[227]
Formula	C_4H_8	C_5H_{10}	C_6H_{12}	C_7H_{12}	$C_{10}H_{18}$
k_{OH}	3.1×10^{-11}	3.1×10^{-11}	8.9×10^{-11}	9.4×10^{-11}	1.2×10^{-10}
Structure	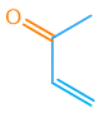	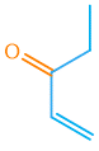	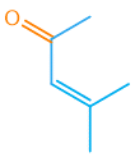	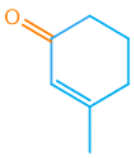	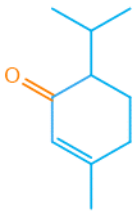
Ketone	MVK[229]	Pent-1-en-3-one[230]	Mesityl oxide[231]	Seudenone[44]	Piperitone
Formula	C_4H_6O	C_5H_8O	$C_6H_{10}O$	$C_7H_{10}O$	$C_{10}H_{16}O$
k_{OH}	2×10^{-11}	3×10^{-11}	1.02×10^{-10}	3.1×10^{-11}	

A value of k_{OH}(piperitone) can be estimated by using the SAR method that was originally developed by Atkinson et al. (1987)[207] and was subsequently updated by Kwok and Atkinson et al. (1995)[208]. The method assumes that for a given reaction, the rate coefficient is equal to the sum of rate coefficients for all individual reactions that can occur. Reactions with OH• include addition to unsaturated functionalities and H-abstraction from the primary, secondary and tertiary carbons and O-H bonds. The partial rate coefficient for the reaction at a particular site (k_{site}) depends on the type of site and the other functionalities in close proximity to it, for which a factor (*F*[X] or *C*[X]) is applied to k_{site}. Figure 4.4 shows the structure of piperitone, with each of the possible reaction sites labelled.

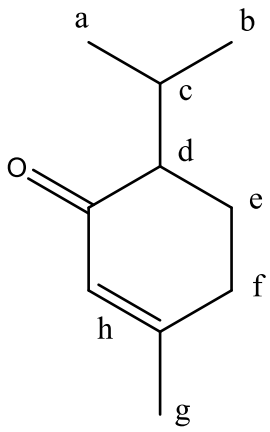

Figure 4.4 *Structure of piperitone, with OH• reaction sites labelled.*

For piperitone the possible reactions with OH• are: H-abstraction from primary carbons (a, b, g); H-abstraction from secondary carbons (e, f); H-abstraction from tertiary carbons (c, d); and OH• addition to the alkene group (h). The values for k_{site} and the factors used in calculating the overall value for k_{OH}(piperitone) were derived from experimentally determined rate coefficients, and are valid at 298 K, Table 4.2.

Table 4.2 *Values for k_{site}, F[X] and C[X] used in the calculation of k_{OH}(piperitone) at 298 K. Adapted from Kwok and Atkinson et al. (1995)[208].*

Symbol	Description	k_{site} cm^3 molecule^{-1} s^{-1}	Factor	Position
$k_{primary}$	H-abstraction from primary carbon	0.136×10^{-12}		c, d
$k_{secondary}$	H-abstraction from secondary carbon	0.934×10^{-12}		e, f
$k_{tertiary}$	H-abstraction from tertiary carbon	1.940×10^{-12}		a, b, g
F[-CH$_3$]	CH_3 substituent		1.00	
F[-CH$_2$-]	CH_2 substituent		1.23	
F [>CH-]	CH substituent		1.23	
F[>C=C<]	alkene substituent		1.00	
F[>C=O]	carbonyl substituent		0.75	
F[-C(O)-CH$_3$]	carbonyl β to site of H-abstraction		3.90	
F_6	part of a six membered ring		1.00	
$k_{C=C}$	OH• addition to alkene	86.90×10^{-12}		h
C[-C(O)-CH$_3$]	carbonyl α to alkene		0.90	

$$k_{OH}(\text{piperitone}) = k_{primary} \times F[\text{>CH-}] \quad \text{(a)}$$
$$+ k_{primary} \times F[\text{>CH-}] \quad \text{(b)}$$
$$+ k_{tertiary} \times F[\text{-C(O)-CH<}] \times F[\text{-CH}_3] \times F[\text{-CH}_3] \quad \text{(c)}$$
$$+ k_{tertiary} \times F[\text{>CO}] \times F[\text{>CH-}] \times F[\text{-CH}_2\text{-}] \times F_6 \quad \text{(d)}$$
$$+ k_{secondary} \times F[\text{-C(O)-CH}_3] \times F[\text{-CH}_2\text{-}] \times F_6 \quad \text{(e)}$$
$$+ k_{secondary} \times F[\text{-CH}_2\text{-}] \times F[\text{>C=C<}] \times F_6 \quad \text{(f)}$$
$$+ k_{primary} \times F[\text{>C=C<}] \quad \text{(g)}$$
$$+ k_{C=C} \times F[\text{-C(O)-CH}_3] \quad \text{(h)}$$

Equation 4.7[208]

$$k_{OH}(\text{piperitone}) = 0.136 \times 10^{-12} (\text{cm}^3 \text{ molecule}^{-1} \text{ s}^{-1}) \times 1.23 \quad \text{(a)}$$
$$+ 0.136 \times 10^{-12} (\text{cm}^3 \text{ molecule}^{-1} \text{ s}^{-1}) \times 1.23 \quad \text{(b)}$$
$$+ 1.94 \times 10^{-12} (\text{cm}^3 \text{ molecule}^{-1} \text{ s}^{-1}) \times 3.9 \times 1 \times 1 \quad \text{(c)}$$
$$+ 1.94 \times 10^{-12} (\text{cm}^3 \text{ molecule}^{-1} \text{ s}^{-1}) \times 0.75 \times 1.23 \times 1.23 \times 1 \quad \text{(d)}$$
$$+ 0.934 \times 10^{-12} (\text{cm}^3 \text{ molecule}^{-1} \text{ s}^{-1}) \times 3.9 \times 1.23 \times 1 \quad \text{(e)}$$
$$+ 0.934 \times 10^{-12} (\text{cm}^3 \text{ molecule}^{-1} \text{ s}^{-1}) \times 1.23 \times 1 \times 1 \quad \text{(f)}$$
$$+ 0.136 \times 10^{-12} (\text{cm}^3 \text{ molecule}^{-1} \text{ s}^{-1}) \times 1 \quad \text{(g)}$$
$$+ 86.9 \times 10^{-12} (\text{cm}^3 \text{ molecule}^{-1} \text{ s}^{-1}) \times 0.9 \quad \text{(h)}$$

Calculation 4.1

k_{OH}(piperitone) = 9.41 × 10^{-11} cm^3 $molecule^{-1}$ s^{-1}

A value of 9.41 × 10^{-11} cm^3 $molecule^{-1}$ s^{-1} was calculated for k_{OH}(piperitone) using the SAR method, Calculation 4.1. H-abstraction was assumed to occur for all C-H bonds, except for the C-H bond that is part of the alkene functionality. H-abstraction is known to be extremely unlikely from this site[232], and there is no k_{site} available[207, 208]. It should be noted that this method does not provide an exact substituent factor for the cyclic α-keto-alkene system present in piperitone, and in the calculations the substituent factor *F*[-C(O)-CH_3] was used instead[207, 208]. While it is not known how accurately this factor represents this part of the chemical system in piperitone, excluding the term from the calculations causes k_{OH}(piperitone) to increase by 10%. Being part of a six membered ring has a negligible impact on alkene reactivity[208], and it is assumed here that this is also true for cyclic α-keto-alkenes[233].

Calculation of the rate coefficient using the SAR method also allows identification of the dominant reaction sites in piperitone. From the calculations presented above, it is estimated that almost 85% of piperitone reactivity proceeds via OH• addition to the alkene. This estimate is consistent with observations for other alkene-containing compounds[207], such as isoprene[24]. H-abstraction from site c and site e account for over 7% and 4% of piperitone reactivity, respectively. Both sites are β to the carbonyl, which facilitates H-abstraction[224, 233, 234]. Reactivity at all other sites is predicted to be negligible.

4.2.2 O_3 Rate Coefficient

A rough estimate of the rate coefficient for the reaction of O_3 with piperitone can be made by assessing the reactivity of similarly structured compounds. Table 4.3 lists k_{O_3} for some compounds with similar structures to piperitone. Note that these are not the same compounds listed above for the OH• reactions, as there is no experimental data available for 1-p-menthene, the alkene analogue of piperitone.

Table 4.3 *Experimentally determined values of k_{O_3} for a series of alkenes and their α-ketone conjugated analogues at 298 (± 3) K, in units of cm^3 $molecule^{-1}$ s^{-1}.*

Alkene	but-1-ene[44]	pent-1-ene[44]	2-methylpent-2-ene[44]	cyclohexene[229]	1-methylcyclohexene[235]
Formula	C_4H_8	C_5H_{10}	C_6H_{12}	C_6H_{12}	C_7H_{12}
k_{O_3}	1×10^{-17}	1.1×10^{-17}	4.5×10^{-16}	8.1×10^{-17}	1.5×10^{-16}
Structure	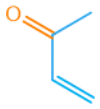		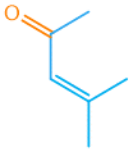	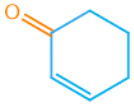	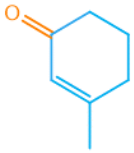
Ketone	MVK[44]	pent-1-en-3-one[44]	mesityl oxide[44]	cyclohex-2-enone[236]	seudenone
Formula	C_4H_6O	C_5H_8O	$C_6H_{10}O$	C_6H_8O	$C_7H_{10}O$
k_{O_3}	5.2×10^{-18}	6×10^{-18}	8.1×10^{-18}	1.2×10^{-18}	

The k_{O_3} values listed in Table 4.3 exhibit similar trends to their OH• counterparts. k_{O_3} increases with increasing substitution around the alkene. This has been observed for other compounds[237], and is likely due to the increased stability of the ozonide produced. For all compounds in Table 4.3, k_{O_3} is lower for the oxygenate than the hydrocarbon analogue, indicating that the presence of a ketone in the α position to an alkene reduces k_{O_3}. This is due to the electron withdrawing effect of the carbonyl, which lowers the electrophilicity of the C=C bond, hindering reaction with O_3[237]. As with the alkene analogues, an increase in substitution around the α-keto-alkene increases k_{O_3}. The impact of the carbonyl on k_{O_3} is much greater than the impact of substitution, therefore k_{O_3}(piperitone) is expected to be close to that of mesityl oxide.

The value of k_{O_3}(piperitone) can be estimated using the SAR approach developed by Jenkin et al. (2020)[238], which is similar to the SAR for predicting OH• rate coefficients[37]. The only available reaction pathway for O_3 is via addition to an unsaturated functionality and the rate coefficient depends on the type of unsaturation (k_{site}) and the substituents surrounding it ($F_\alpha[X]$)[209]. Figure 4.5 shows the structure of piperitone, with the reaction site and influential substituent labelled.

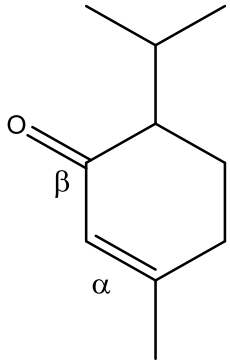

Figure 4.5 *Structure of piperitone, with labels for site of O_3 attack, α, and the substituent affecting reactivity,* β.

The values for k_{site} and $F_\alpha[X]$ used to calculate k_{O_3}(piperitone) were derived from experimentally determined rate coefficients, and are valid at 298 K, Table 4.4[238].

Table 4.4 *Values for k_{site} and $F_\alpha[X]$ used in the calculation of k_{O_3}(piperitone) at 298 K. Adapted from Jenkin et al. (2020)[238].*

Symbol	Description	k_{site} cm^3 molecule^{-1} s^{-1}	Factor	Position
$k_{CHR=CR_2}$	O_3 addition to alkene	4.7×10^{-16}		α
F_α[-C(O)-]	carbonyl α to alkene in a ring		0.02	β
F_6	part of a six membered ring		0.52	

$$k_{O_3}(\text{piperitone}) = k_{CHR=CR_2} \times F_\alpha[\text{-C(O)-}] \times F_6 \qquad \textbf{Equation 4.8}^{238}$$

(α) (β)

$$k_{O_3}(\text{piperitone}) = 4.7 \times 10^{-16}\ (\text{cm}^3\ \text{molecule}^{-1}\ \text{s}^{-1}) \times 0.02 \times 0.52 \qquad \textbf{Calculation 4.2}$$

(α) (β)

$$k_{O_3}(\text{piperitone}) = 4.89 \times 10^{-18}\ \text{cm}^3\ \text{molecule}^{-1}\ \text{s}^{-1}$$

A value of 4.89×10^{-18} cm^3 molecule^{-1} s^{-1} was calculated for k_{O_3}(piperitone) using the SAR Equation 4.8. There is some uncertainty associated with the coefficients used in this calculation. Due to limited kinetic data for α-keto-alkenes and other alkene

oxygenate conjugates systems, the SAR does not have coefficients for these functionalities and it was recommended a generic coefficient of 0.02 be applied[238].

As explained above, k_{O_3}(piperitone) is expected to be similar to that for mesityl oxide. The value of k_{O_3}(piperitone) calculated using this SAR method is approximately 1.5 times that of mesityl oxide. While k_{O_3}(piperitone) is within the expected range, experimental determination is required.

4.2.3 $NO_3^\bullet$ Rate Coefficient

Reaction with $NO_3^\bullet$ is an important loss process for VOCs in the dark, when NO_x and O_3 are present and react to generate $NO_3^\bullet$. As the emission of piperitone from Sitka spruce was observed under darkness (Chapter 3), night-time reaction with $NO_3^\bullet$ may occur in polluted areas. Reaction with $NO_3^\bullet$ proceeds via similar mechanisms to that of $OH^\bullet$; H-abstraction from C-H bonds, and addition to unsaturated functionalities.

k_{NO_3} for some compounds with similar structures to piperitone are given in Table 4.5. As was observed for $OH^\bullet$ and O_3, the rate coefficient for reaction with $NO_3^\bullet$ increases with increasing substitution around the alkene. A reduction in k_{NO_3} is observed for the α-keto analogues of the alkenes. However, there are no reported rate coefficients for cyclic alkenes similar to piperitone. Considering all of the available data, k_{NO_3}(piperitone) is predicted to be similar to that of mesityl oxide.

Table 4.5 *Experimentally determined values of k_{NO_3} for a series of alkenes and their α-ketone conjugated analogues at 298 (± 3) K, in units of cm^3 $molecule^{-1}$ s^{-1}.*

Alkene	But-1-ene[44]	Pent-1-ene[44]	Hex-2-ene[44]	2-methylpent-2-ene
Formula	C_4H_8	C_5H_{10}	C_6H_{12}	C_6H_{12}
k_{NO_3}	1×10^{-14}	6.8×10^{-14}	4×10^{-13}	
Structure	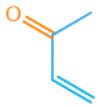	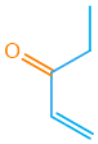	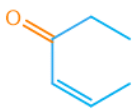	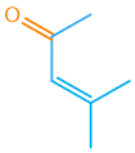
Ketone	MVK[44]	Pent-1-en-3-one[44]	Hex-4-en-3-one	Mesityl oxide[44]
Formula	C_4H_6O	C_5H_8O	$C_6H_{10}O$	$C_6H_{10}O$
k_{NO_3}	$< 6 \times 10^{-16}$	9.9×10^{-17}		1.4×10^{-13}

The SAR approach developed by Kerdouci et al. (2010 and 2014)[210, 239] was used to calculate k_{NO_3}(piperitone). It uses a similar method to that developed for OH•[208] and O_3[238] to determine the reactivity of specific sites in the VOC towards NO_3. Figure 4.6 shows the structure of piperitone, with each of the possible reaction sites labelled.

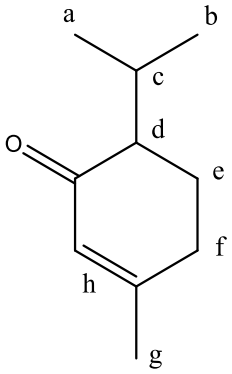

Figure 4.6 *Structure of piperitone, with $NO_3^•$ reaction sites labelled.*

The values for k_{site}, F[X] and G[X] used to calculate k_{NO_3}(piperitone) were derived from experimentally determined rate coefficients, and are valid at 298 K[210], Table 4.6.

Table 4.6 *Values for k_{site}, F[X] and G[X] used in the calculation of k_{NO_3}(piperitone) at 298 K. Adapted from Kerdouci et al. (2014)[210].*

Symbol	Description	k_{site} cm^3 molecule^{-1} s^{-1}	Factor	Position
$k_{primary}$	H-abstraction from primary carbon	0.1×10^{-17}		c, d
$k_{secondary}$	H-abstraction from secondary carbon	2.56×10^{-17}		e, f
$k_{tertiary}$	H-abstraction from tertiary carbon	10.5×10^{-17}		a, b, g
F[-CH$_3$]	CH$_3$ substituent		1	
F[-CH$_2$-]	CH$_2$ substituent		1.02	
F [>CH-]	CH substituent		1.61	
F[>C=C<]	alkene substituent		1	
F[>C=O]	carbonyl substituent		0.64	
$k_{C=C}$	OH addition to alkene (1 H)	8.35×10^{-12}		h
G[-CH$_3$]	CH$_3$ substituent on alkene		1	
G[-CH$_2$-]	CH$_2$ substituent on alkene		1.15	
G[-C(O)-R]	carbonyl α to alkene		0.02	
G_6	part of a six membered ring		0.93	

$$k_{NO_3}(\text{piperitone}) = k_{primary} \times F[\text{>CH-}] \quad \text{(a)}$$
$$+ k_{primary} \times F\,[\text{>CH-}] \quad \text{(b)}$$
$$+ k_{tertiary} \times F\,[\text{>CH-}] \times F\,[\text{-CH}_3] \times F\,[\text{-CH}_3] \quad \text{(c)}$$
$$+ k_{tertiary} \times F\,[\text{>CO}] \times F\,[\text{>CH-}] \times F\,[\text{-CH}_2\text{-}] \quad \text{(d)}$$
$$+ k_{secondary} \times F\,[\text{>CH-}] \times F\,[\text{-CH}_2\text{-}] \times F\,[\text{-CH}_2\text{-}] \quad \text{(e)}$$
$$+ k_{secondary} \times F\,[\text{-CH}_2\text{-}] \times F\,[\text{>C=C<}] \quad \text{(f)}$$
$$+ k_{primary} \times F[\text{>C=C<}] \quad \text{(g)}$$
$$+ k_{C=C} \times G[\text{-C(O)-R}] \times G[\text{-CH}_2\text{-}] \times G[\text{-CH}_3] \times G_6 \quad \text{(h)}$$

Equation 4.9[210]

$$k_{NO_3}(\text{piperitone}) = 0.1 \times 10^{-17}\ (\text{cm}^3\ \text{molecule}^{-1}\ \text{s}^{-1}) \times 1 \quad \text{(a)}$$
$$+ 0.1 \times 10^{-17}\ (\text{cm}^3\ \text{molecule}^{-1}\ \text{s}^{-1}) \times 1 \quad \text{(b)}$$
$$+ 10.5 \times 10^{-17}\ (\text{cm}^3\ \text{molecule}^{-1}\ \text{s}^{-1}) \times 1.61 \times 1 \times 1 \quad \text{(c)}$$
$$+ 10.5 \times 10^{-17}\ (\text{cm}^3\ \text{molecule}^{-1}\ \text{s}^{-1}) \times 0.64 \times 1.61 \times 1.02 \times 1 \quad \text{(d)}$$
$$+ 2.56 \times 10^{-17}\ (\text{cm}^3\ \text{molecule}^{-1}\ \text{s}^{-1}) \times 1.61 \times 1.02 \times 1 \quad \text{(e)}$$
$$+ 2.56 \times 10^{-17}\ (\text{cm}^3\ \text{molecule}^{-1}\ \text{s}^{-1}) \times 1.02 \times 1 \times 1 \quad \text{(f)}$$
$$+ 0.1 \times 10^{-17}\ (\text{cm}^3\ \text{molecule}^{-1}\ \text{s}^{-1}) \times 1 \times 1 \quad \text{(g)}$$
$$+ 8.35 \times 10^{-12}\ (\text{cm}^3\ \text{molecule}^{-1}\ \text{s}^{-1}) \times 0.02 \times 1.15 \times 1 \times 0.93 \quad \text{(h)}$$

Calculation 4.3

k_{NO_3}(piperitone) = 1.79×10^{-13} cm^3 molecule^{-1} s^{-1}

A value of 1.79×10^{-13} cm^3 molecule^{-1} s^{-1} was calculated for k_{NO_3}(piperitone) using the SAR, Calculation 4.3. The dominant reaction site is the alkene functionality, which accounts for 99% of the total reactivity.

As explained above, k_{NO_3}(piperitone) is expected to be similar to that for mesityl oxide. The value calculated using the SAR method is in fact very close to that for mesityl oxide, suggesting that k_{NO_3}(piperitone) is likely in this range. However, experimental measurements are still required to accurately determine k_{NO_3}(piperitone).

4.3 Experimental Methods and Analysis

4.3.1 Kinetic Studies

4.3.1.1 Procedure

Experiments to determine k_{OH}(piperitone) were carried out in the IASC facility described in detail in Chapter 2. The chamber was flushed at 1000 L min^{-1} for a minimum of 2 hours prior to each experiment, until the concentrations of VOCs and particles had returned to background levels. During an experiment the differential pressure inside the chamber was maintained at 10 Pa above the external pressure, and the temperature was set to 298 K. The temperature inside the chamber increased by approximately 0.5 K following 1 hour of illumination. All lamps (98 UVA and 42 UVB) were used for irradiating the chamber contents.

The decay of reactants was monitored with the ToF-CIMS (Chapter 2) utilising $C_6H_6^+$ as the reagent ion, generated from the liquid system. The voltages and pressures applied to the ToF-CIMS were controlled via TOFWERK and were chosen based on tuning performed on 20/02/2023. The ToF-CIMS was connected to the chamber via a 1.5 m length of PFA ½" outer diameter tubing. Prior to the experiments, tests were carried out to identify the primary ion and fragment ions for each compound.

Other instruments connected to the chamber during the kinetics experiments include an SMPS, NO_x monitor, O_3 monitor, CO_2 monitor and relative humidity and temperature probe.

Photolysis Experiments

The background levels of gases and particles in the chamber were measured for a minimum of 10 minutes. Following background measurement, piperitone (10 µL) and cyclohexane (5 ml) were added to the chamber individually by injecting liquid into a small glass vessel, and passing dry compressed air over it. The glassware was gently heated to assist evaporation. Cyclohexane was added in excess to act as an $OH^{\bullet}$ scavenger[9], ensuring that any chemical loss of piperitone was solely due to

photolysis. Following addition of the reagents, the fan was turned on for a maximum of 5 minutes to ensure homogenisation throughout the chamber[38]. In order to account for chamber losses, reagent concentrations were measured in the dark over 30 minutes, before turning on all of the lamps for 1 hour. Photolysis experiments were repeated three times. A blank photolysis experiment was also carried out, using the same procedure except piperitone and cyclohexane were not added to the chamber.

$OH^{\bullet}$ Relative Rate Experiments

The background levels of gases and particles in the chamber were measured for a minimum of 10 minutes, followed by addition of each VOC (1 - 3 µL) and hydrogen peroxide (500 µL). Experiments were performed with piperitone and each reference compound (isoprene, 1-methyl cyclohexane (1-MCH) and 1,3,5-trimethylbenzene, (1,3,5-TMB)) individually, and then as combinations. Isoprene and 1-MCH were not run as a combination as their ToF-CIMS signals were found to interfere with each other. Following complete reagent addition, the fan was turned on for a maximum of 5 minutes to ensure complete mixing[38], after which the reagent concentrations were measured in the dark for 30 minutes to evaluate chamber losses. All of the lamps were then turned on and reagent decay was monitored for 30 minutes. Eleven piperitone relative rate experiments were conducted, five with 1,3,5-TMB as the reference compound, three with isoprene and three with 1-MCH. A blank $OH^{\bullet}$ experiment was also performed, using the same procedure except only hydrogen peroxide was added to the chamber.

4.3.1.2 Data Analysis

Data collected by the ToF-CIMS was analysed with Tofware 3.2.0, operated through IGOR Pro 7.08. Firstly 1 Hz data were averaged to 30 s time resolution. A mass calibration was then performed using the ion signals for $C_6H_6^+$ (*m/z* 78.04), $C_6H_6O^+$ (*m/z* 94.04), $C_6H_{12}NO^+$ (*m/z* 114.09), and $C_{12}H_{12}^+$ (*m/z* 156.09). C_6H_6O was produced from the liquid benzene system, $C_6H_{11}NO$ was a contaminant present in the N_2 used to supply the ToF-CIMS and $C_{12}H_{12}$ was a benzene dimer. The other data analysis

steps included correction of the baseline position, peak shape and peak resolution. Chemical formulae were then assigned to peaks within the calibrated mass range. Only formulae containing the elements C, H, O and N were assigned. If an appropriate formula could not be elucidated, the peak was left unassigned.

Further analysis involved only the primary ToF-CIMS signals for piperitone and the reference compounds, and was performed using Microsoft Excel. The data was normalised to the $C_6H_6^+$ reagent ion signal.

The decay of the compounds during the 30 minutes of darkness in each experiment were used to determine a unique chamber losses rate coefficient for each reagent using Equation 4.5, where k_{loss} is $k_{chamber\ losses}$. The time series profiles for each reagent were then corrected for these chamber losses according to Equation 4.6. The error associated with $k_{chamber\ losses}$ was calculated as twice the standard deviation of the data.

Determination of Photolysis Rate Coefficient

The loss of piperitone due to photolysis was calculated according to Equation 4.5, using chamber loss corrected data during illumination, where k_{loss} is $J_{Piperitone}$, the rate coefficient (s^{-1}) for the photolysis of piperitone using all lamps in the chamber. An overall value for $J_{Piperitone}$ was determined as the average of the values calculated from the three photolysis experiments. The error associated with $J_{Piperitone}$ was calculated as a combination of twice the standard deviation of the data and chamber loss error in a weighted root mean square (RMS) approach.

Determination of $OH^\bullet$ Rate Coefficient

The chamber loss corrected piperitone data was further corrected for photolysis using Equation 4.6, to ensure the decay in the piperitone signal during illumination was only due to reaction with $OH^\bullet$. The reference compounds 1,3,5-TMB, isoprene and 1-MCH do not undergo photolysis and their data was only corrected for chamber losses. Following all corrections, a unique k_{OH}(piperitone) value was determined for each experiment using Equation 4.4. An average of all eleven rate coefficients was

taken to be the reported value. The error associated with k_{OH}(piperitone) was calculated as a combination of errors in a weighted RMS approach scaled by k_{OH}(piperitone), with errors for the reference compounds taken from literature.

4.3.2 Product Studies

4.3.2.1 Procedure

Experiments to identify the products of the $OH^{\bullet}$ initiated oxidation of piperitone were carried out in the IASC facility described in Chapter 2. The chamber was operated in the same manner as for the kinetics experiments. Following flushing at 1000 L min^{-1} for 2 hours, the background levels of gases and particles in the chamber were measured for a minimum of 15 minutes. Piperitone (1.5 µL) and hydrogen peroxide (1 ml) were added to the chamber. Due to the sticky nature of piperitone and the long injection time the full volume was not added to the chamber. After reagent addition, the fan in the chamber was turned on for a maximum of 5 minutes to facilitate rapid homogenisation. Following a 30 minute stabilisation period, all lamps were turned on to initiate hydrogen peroxide photolysis to produce $OH^{\bullet}$.

The decay of piperitone and formation of oxidised products and SOA were monitored for 3 hours. Experiments were performed with the ToF-CIMS operated in two separate modes. $C_6H_6^+$ was used as the ToF-CIMS reagent ion for monitoring the decay of piperitone and formation of oxidation products with a low oxygen content. The ToF-CIMS was operated in the same manner as for the piperitone kinetics experiments. In addition, trichlorobenzene was used as an internal mass calibrant, by allowing it to diffuse into the inlet of the instrument.

The experiments were repeated with I^- as the ToF-CIMS reagent ion, generated via the GC oven heating method. Using I^- allowed for the detection of highly oxygenated gas-phase oxidation products. The voltages and pressures applied to the ToF-CIMS were controlled via TOFWERK and were chosen based on tuning performed on 17/07/2022. Perfluoroheptanoic acid ($C_7HF_{13}O_2$) and perfluorooctanoic acid

($C_8HF_{15}O_2$) were used as internal mass calibrants. An amount of each solid was placed in a glass vessel and allowed to diffuse into the inlet of the instrument with the sample flow.

In total, six piperitone $OH^{\bullet}$ initiated oxidation experiments were performed, three with the ToF-CIMS in $C_6H_6^+$ mode, and three with ToF-CIMS in I^- mode. Four blank experiments were also carried out, two with the ToF-CIMS in each mode. The procedure was the same except only hydrogen peroxide was added to the chamber.

An SMPS (Chapter 2) was used to monitor the formation and growth of particles during the reactions. The SMPS was operated with a sheath flow of 10 L min^{-1} and a sample flow of 1 L min^{-1}. The voltage was scanned twice per sample over 50 s with a 10 s purge between scans, measuring particles in the range 7.7 nm to 283.9 nm. The two scans were averaged to give a single sample measurement every 2.5 minutes. The SMPS was connected to the chamber with a 1.5 m length of stainless steel tubing (¼" outer diameter).

Other instruments connected to the chamber during the piperitone oxidation experiments included a NO_x monitor, O_3 monitor, CO_2 sensor and relative humidity and temperature probe.

4.3.2.3 Data Analysis

TOF-CIMS Data Analysis

ToF-CIMS data was analysed with Tofware 3.2.0, operated through IGOR Pro 7.08. Initially 1 Hz data was averaged to 10 s time resolution. Following this, a mass calibration was performed. For the experiments performed with the ToF-CIMS in $C_6H_6^+$ mode; the ion signals for $C_6H_6^+$ (*m/z* 78.04), $C_6H_{12}NO^+$ (*m/z* 114.04), $C_6H_3Cl_3^+$ (*m/z* 179.93) and $C_{18}H_{18}^+$ (*m/z* 234.14) were used. $C_6H_3Cl_3$ was the trichlorobenzene internal mass calibrant, and $C_{18}H_{18}$ was a benzene trimer. For experiments performed with the ToF-CIMS in I^- mode the ion signals for NO_3^- (*m/z* 61.99) I^-, (*m/z* 126.91), I_2^- (*m/z* 253.81), I_3^- (*m/z* 38.071), $I.C_7HF_{13}O_2^-$ (*m/z* 491.88) and $I.C_7HF_{13}O_2^-$ (*m/z* 541.88)

were used. The other data analysis steps included correction of the baseline position, peak shape and peak resolution. Following these steps, chemical formulae were assigned to peaks within the calibrated mass range. Only formulae containing the elements C, H, O and N (and Cl in $C_6H_6^+$ mode, and I and F in I^- mode) were assigned. If an appropriate formula could not be assigned, the peak was left unassigned.

After completing peak assignment, the remaining data analysis was performed using R Studio 4.0.2. Initially all signals were normalised to the reagent ion signal, $C_6H_6^+$ or I^-. The data were then filtered to isolate only signals corresponding to products. Filtering involved the removal of unassigned and calibrant signals. A Welch T-test was performed comparing the concentrations during the stable period and after illumination. The stable period was scaled by 1.5, and only signals with a P-value below 0.00005 were retained. A further Welch T-test was carried out to compare the concentrations during illumination between piperitone oxidation experiments and blank experiments. Signals with a P-value less than 0.00005 when compared with two times the ion concentration of the blank experiments were retained. To remove signals with a high degree of scatter, the deviation of each data point from a smoothed trace was calculated. Ions with a mean deviation greater than 6% were filtered out and the remaining ions were identified as statistically significant oxidation products.

The estimated steady state $OH^\bullet$ concentration during the experiments was calculated from the decay of piperitone under illumination after correction for chamber losses. A plot was generated using Equation 4.3, with the ratio of the slope to k_{OH}(piperitone) (Section 4.4.1.2) determining the steady state $OH^\bullet$ concentration in molecule cm^{-3}.

SMPS Data Analysis

The SMPS number concentration data were corrected for multiple charge losses and diffusion losses which occur within the SMPS, following this, the data was then corrected for chamber losses using Equation 4.6, with size bin specific loss coefficients. The size bin specific coefficients were determined from chamber losses experiments performed in the chamber using ammonium sulfate seed, assuming that

chemical composition has a negligible impact on particle deposition. After correction for chamber losses, the particle number was used to calculate particle mass using a density[68] of 1.3 g cm^{-3}.

4.3.3 Materials

The materials used in these experiments were: piperitone, 1-MCH (Santa Cruz Biotechnology, purities 94%, 98% respectively), cyclohexane, 1,3,5-TMB, isoprene, trichlorobenzene, perfluoroheptanoic acid, perfluorooctanoic acid (Sigma Aldrich, purities 99.5, 98%, 99%, 99%, 97%, and 98%, respectively), and hydrogen peroxide (Sigma Aldrich, 50% aqueous solution).

4.4 Results and Discussion

4.4.1 Piperitone Kinetics

4.4.1.1 Photolysis Rate Coefficient

Piperitone photolysis was investigated using all available lamps (UVA and UVB). A typical time series of piperitone obtained during a photolysis experiment is shown in Figure 4.7.

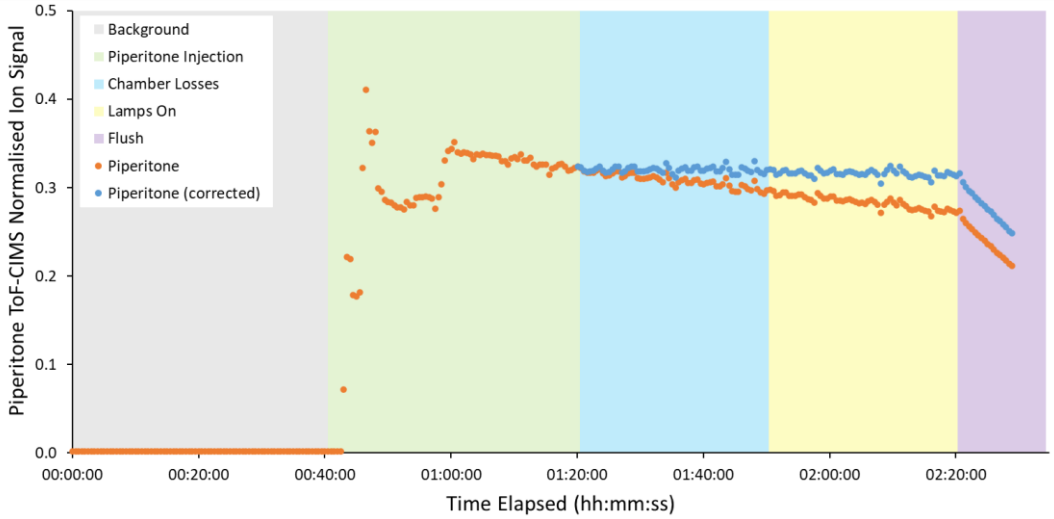

Figure 4.7 *Time series of piperitone during a photolysis experiment.*

A background of the chamber was measured (grey shading), following this piperitone and an excess of cyclohexane were added to the chamber (green shading), and the fan was temporarily turned on ensure homogenisation. The decay of piperitone due to chamber losses was then measured (blue shading). The orange data points show the piperitone signal as measured by the ToF-CIMS, and the blue data points show the piperitone signal corrected for chamber losses. The slight decay in piperitone signal (blue data points) during illumination (yellow shading) is due to photolysis only.

The data, corrected for chamber losses, obtained during illumination was used to determine the piperitone photolysis rate coefficient ($J_{piperitone}$) during each of the three experiments, Figure 4.8 and Table 4.7.

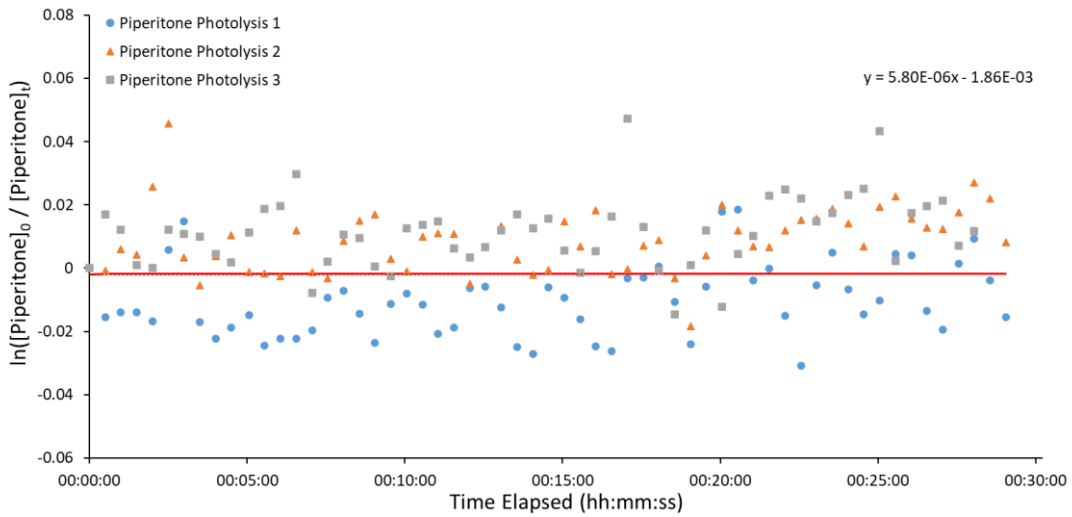

Figure 4.8 *Plot showing data used to calculate the piperitone photolysis rate coefficient from all experiments. Data have been corrected for chamber losses.*

There was good agreement between the three photolysis experiments, Figure 4.8 and Table 4.7. For each experiment a plot of $\ln\left(\frac{[Piperitone]_0}{[Piperitone]_t}\right)$ against time followed a straight line, with near zero intercept, in agreement with Equation 4.5. The trend line and equation in Figure 4.8 are the average of all experiments. The average value for the piperitone photolysis coefficient was $J_{piperitone}$ = 5.8 (± 0.21) x 10^{-6} s^{-1}, almost an order of magnitude slower than the chamber losses coefficient.

Table 4.7. *Table of piperitone photolysis coefficients.*

Experiment	Chamber Losses[A] s^{-1}	Photolysis Rate Coefficient[B] s^{-1}
Piperitone Photolysis 1	4.61 (± 0.79) × 10^{-5}	5.74 (± 0.21) × 10^{-6}
Piperitone Photolysis 2	4.35 (± 0.92) × 10^{-5}	5.64 (± 0.20) × 10^{-6}
Piperitone Photolysis 3	4.26 (± 0.56) × 10^{-5}	6.01 (± 0.22) × 10^{-6}
Average	4.41 (± 0.76) × 10^{-5}	5.80 (± 0.21) × 10^{-6}

[A] *Error calculated as twice the standard deviation of the data.*

[B] *Error calculated as a combination of twice the standard deviation of the data and chamber loss error in weighted RMS approach.*

4.4.1.2 OH• Rate Coefficient

A series of relative rate experiments were conducted to determine k_{OH}(piperitone). Three reference compounds were selected; 1,3,5-TMB, isoprene and 1-MCH. These compounds were selected as they have k_{OH} similar to that determined for piperitone using the SAR method, and do not undergo photolysis with UVA and UVB lamps. The recommended k_{OH} values for the reference compounds at 298 K in molecule cm^{-3} s^{-1} are: 5.86 (± 0.88) × 10^{-11} for 1,3,5-TMB[44]; 1.00 (± 0.15) × 10^{-10} for isoprene[44]; and 9.40 (± 2.82) × 10^{-11} for 1-MCH[44]. Relative rate experiments were conducted with reference compounds individually, and then as combinations. Combinations were run as 1,3,5-TMB with either isoprene or 1-MCH. Due to interference of the ToF-CIMS signals isoprene and 1-MCH were not run together as a combination. Figure 4.9 shows the time series of piperitone (circles) and 1-MCH (triangles) during a relative rate experiment, and is typical of all relative rate experiments.

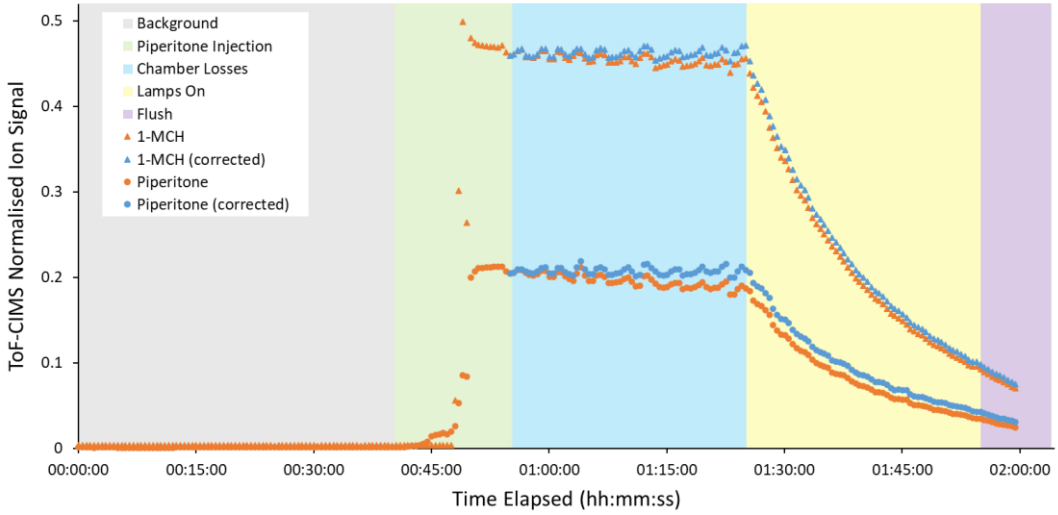

Figure 4.9 *Time series of piperitone (circles) and 1-MCH (triangles) during a relative rate experiment. ToF-CIMS measured data points (blue) and corrected data points (orange). Corrections made: 1-MCH chamber losses; piperitone chamber losses and photolysis.*

A background of the chamber was measured (grey shading). Piperitone, 1-MCH and H_2O_2 (not shown) were added to the chamber (orange data points, green shading) and the fan was temporarily turned on to ensure homogenisation. The decays of piperitone and 1-MCH due to chamber losses were then measured (blue shading).

The data during this period were used to calculate a unique chamber losses coefficient, using Equation 4.5, for each compound in each experiment. Equation 4.6 was used to correct the data for chamber losses. The lamps were turned on for approximately 30 minutes to continuously generate OH• and the decay in piperitone and 1-MCH were observed (yellow shading). For piperitone, the photolysis rate coefficient was used to correct the data recorded during illumination.

The chamber losses corrected decays of piperitone and reference compound during the first 20 minutes of illumination were used with Equation 4.4 to calculate k_{OH}(piperitone) during each experiment. The time period of 20 minutes was chosen to prevent interference of the ToF-CIMS signals from oxidation products.

Figure 4.10 is a relative rate plot of $\ln\left(\frac{[piperitone]_0}{[piperitone]_t}\right)$ as a function of $\ln\left(\frac{[reference]_0}{[reference]_t}\right)$ for all relative rate experiments.

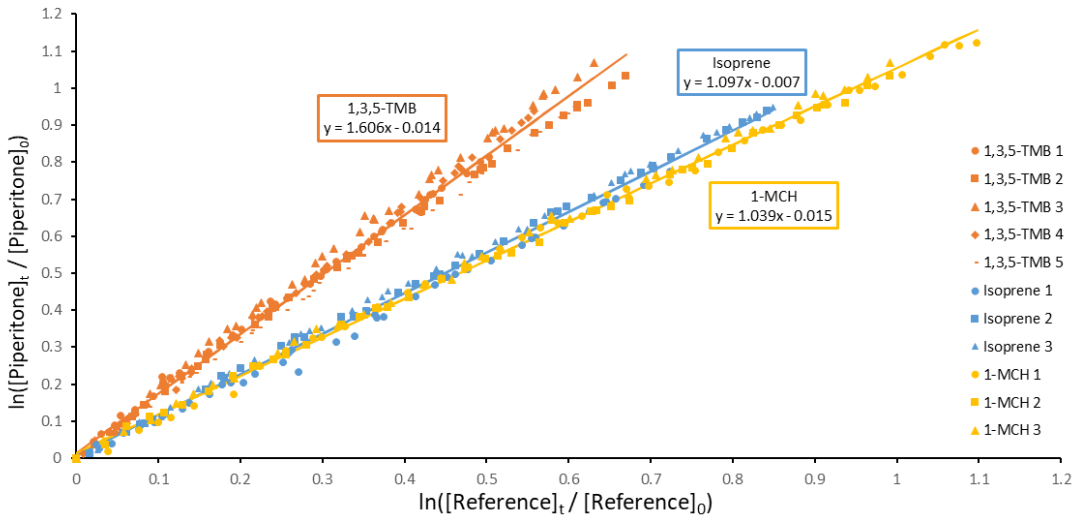

Figure 4.10 *Relative rate plot for the reaction of piperitone with OH•, using 1,3,5-TMB (orange), isoprene (blue) and 1-MCH (yellow) as reference compounds.*

For each reference compound a straight line plot is obtained, with near zero intercepts, as expected from Equation 4.4. The linear equations shown are averages of all experiments with that particular reference compound, with slope

$\frac{k_{\mathrm{OH}}(piperitone)}{k_{\mathrm{OH}}(reference)}$. The data from each relative rate experiment were used to derive a unique value for k_{OH}(piperitone), Table 4.8.

Table 4.8 *Results for kinetics experiments on the reaction of piperitone with OH•, using reference compounds 1,3,5-TMB, isoprene and 1-MCH, at 298 K.*

Experiment	Reference Chamber Losses[A]	Piperitone Chamber Losses[A]	Piperitone Photolysis Coefficient	$k_{reference}$[B]	$k_{piperitone}/k_{reference}$[A]	$k_{piperitone}$[C]
	s^{-1}	s^{-1}	s^{-1}	cm^3 $molecule^{-1}$ s^{-1}		cm^3 $molecule^{-1}$ s^{-1}
1,3,5-TMB 1	1.95 (± 0.38) × 10^{-5}	6.55 (± 0.69) × 10^{-5}	5.80 (± 0.21) × 10^{-6}	5.86 ± (0.88) × 10^{-11}	1.59 ± (0.02)	9.30 (± 1.05) × 10^{-11}
1,3,5-TMB 2	3.44 (± 0.69) × 10^{-5}	6.67 (± 1.06) × 10^{-5}	5.80 (± 0.21) × 10^{-6}	5.86 ± (0.88) × 10^{-11}	1.53 ± (0.02)	8.69 (± 1.03) × 10^{-11}
1,3,5-TMB 3	2.22 (± 0.61) × 10^{-5}	6.53 (± 1.03) × 10^{-5}	5.80 (± 0.21) × 10^{-6}	5.86 ± (0.88) × 10^{-11}	1.68 ± (0.02)	9.83 (± 1.15) × 10^{-11}
1,3,5-TMB 4	3.40 (± 0.65) × 10^{-5}	7.00 (± 1.06) × 10^{-5}	5.80 (± 0.21) × 10^{-6}	5.86 ± (0.88) × 10^{-11}	1.68 ± (0.02)	9.82 (± 1.13) × 10^{-11}
1,3,5-TMB 5	2.59 (± 0.80) × 10^{-5}	6.00 (± 1.26) × 10^{-5}	5.80 (± 0.21) × 10^{-6}	5.86 ± (0.88) × 10^{-11}	1.26 ± (0.01)	9.14 (± 1.14) × 10^{-11}
Isoprene 1	2.22 (± 0.73) × 10^{-5}	4.43 (± 1.23) × 10^{-5}	5.80 (± 0.21) × 10^{-6}	1.00 ± (0.15) × 10^{-10}	1.07 ± (0.02)	1.07 (± 0.13) × 10^{-10}
Isoprene 2	3.19 (± 0.61) × 10^{-5}	7.00 (± 1.06) × 10^{-5}	5.80 (± 0.21) × 10^{-6}	1.00 ± (0.15) × 10^{-10}	1.11 ± (0.01)	1.11 (± 0.13) × 10^{-10}
Isoprene 3	3.37 (± 0.77) ×10^{-5}	6.00 (± 1.26) × 10^{-5}	5.80 (± 0.21) × 10^{-6}	1.00 ± (0.15) × 10^{-10}	1.11 ± (0.01)	1.11 (± 0.13) × 10^{-10}
1-MCH 1	1.81 (± 0.47) × 10^{-5}	6.43 (± 1.03) × 10^{-5}	5.80 (± 0.21) × 10^{-6}	9.84 ± (2.82) × 10^{-11}	1.04 ± (0.02)	9.76 (± 2.10) × 10^{-11}
1-MCH 2	3.05 (± 0.61) × 10^{-5}	6.67 (± 1.06) × 10^{-5}	5.80 (± 0.21) × 10^{-6}	9.84 ± (2.82) × 10^{-11}	1.03 ± (0.01)	9.65 (± 2.06) × 10^{-11}
1-MCH 3	1.46 (± 0.57) × 10^{-5}	6.53 (± 1.03) × 10^{-5}	5.80 (± 0.21) × 10^{-6}	9.84 ± (2.82) × 10^{-11}	1.05 ± (0.01)	9.87 (± 2.14) × 10^{-11}
Average						9.93 (± 1.43) ×10^{-11}

[A] Errors calculated as twice the standard deviation of the least squares fit of the data.

[B] Recommended reference rate coefficients and errors are taken from the literature[44].

[C] Errors were calculated using previously stated errors in a weighted RMS approach, scaled by k_{OH}(piperitone).

All coefficients involved in calculating k_{OH}(piperitone) are provided in Table 4.8. Chamber losses were individually calculated for each compound in each experiment. Piperitone chamber losses were much higher than the chamber losses for any of the reference compounds, and is likely due to piperitone undergoing higher wall deposition as a result of it having lower volatility. The piperitone photolysis rate coefficient was taken from the results obtained in Section 4.4.1.1. There is good agreement between the eleven determinations of k_{OH}(piperitone), with all values within the error limits of the average, 9.93 (± 1.43) × 10^{-11} molecule cm^{-3} s^{-1}.

Comparison

k_{OH}(piperitone) values determined from the SAR (9.41 × 10^{-11} molecule cm^{-3} s^{-1}) and the relative rate method agree to within 6%. This high level of agreement validates the accuracy of the SAR approach for piperitone. Since this is the first determination of k_{OH}(piperitone), it is interesting to compare the reactivity of piperitone with some common BVOCs, Table 4.9.

Table 4.9 *Recommended OH• rate coefficients at 298 K for a series of BVOCs*[44].

Compound	Formula	k_{OH}	# C=C	# C=O
		molecule cm^{-3} s^{-1}		
Fenchone	$C_{10}H_{16}O$	0.4 × 10^{-11}		1
Camphor	$C_{10}H_{16}O$	0.4 × 10^{-11}		1
Seudenone	$C_7H_{10}O$	3.0 × 10^{-11}	1	1
α-Pinene	$C_{10}H_{16}$	5.3 × 10^{-11}	1	
δ-Carene	$C_{10}H_{16}$	8.5 × 10^{-11}	1	
Piperitone*	$C_{10}H_{16}O$	9.9 × 10^{-11}	1	1
Isoprene	C_5H_8	10.0 × 10^{-11}	2	
Limonene	$C_{10}H_{16}$	16.5 × 10^{-11}	2	
β-Phellandrene	$C_{10}H_{16}$	16.6 × 10^{-11}	2	

** k_{OH}(piperitone) determined in this work.*

Fenchone and camphor both contain ketone functionalities like piperitone, although they do not have any C=C bonds. The much higher k_{OH} for piperitone relative to that of fenchone and camphor, further signifies dominant contribution of the C=C bond to the total piperitone reactivity. Seudenone has a cyclic α-keto-alkene system,

similar to piperitone, although its k_{OH} is over three times lower than that for piperitone. The reason for this is unclear, although it could be related to the absence of substituent groups around the cyclic α-keto-alkene system in seudenone.

The mono-alkene monoterpenes α-pinene and δ-carene, have similar structures to piperitone, with a single C=C bond internal to a C_6 ring. Interestingly, piperitone is the most reactive of these three compounds[44], while the k_{OH} for isoprene, a linear unsubstituted di-alkene[240], is very similar to that of piperitone. The di-alkene monoterpenes, limonene and β-phellandrene, each of which possess an internal C=C bond in a C_6 ring, have larger k_{OH} values than piperitone[44]. The higher reactivity is due to the secondary alkene in these compounds.

In summary, k_{OH}(piperitone) is much larger than those of compounds containing only a ketone functionality, and falls between those of similarly structured mono-alkene and di-alkene monoterpenes, and is quite similar to that of isoprene[44]. The presence of the ketone functionality in piperitone causes an enhancement in the rate coefficient relative to mono-alkene monoterpenes, giving it similar reactivity to an unsubstituted di-alkene[240].

4.4.1.3 Piperitone Lifetime

The lifetime of a compound in the atmosphere due to reaction with an oxidant can be determined using Equation 4.10.

$$\tau_{\text{oxidant}} = \frac{1}{k * [oxidant]} \qquad \textit{Equation 4.10}$$

Where: $\tau_{oxidant}$ is the lifetime of the compound due to reaction with a particular oxidant, in s; k is the rate coefficient for the reaction between the compound and the particular oxidant, in cm^3 $molecule^{-1}$ s^{-1}; and [*oxidant*] is the oxidant concentration, in molecules cm^{-3}.

The following oxidant concentrations were used to calculate the piperitone atmospheric lifetime: 1.6×10^6 molecules cm^{-3} as an average $OH^\bullet$ concentration over 12 hours; 7×10^{11} molecules cm^{-3} as an average O_3 concentration over 24 hours; and 5×10^8 molecules cm^{-3} as an average $NO_3^\bullet$ concentration over 12 hours[27]. Table 4.10 gives the lifetimes of piperitone due to reaction with $OH^\bullet$, O_3 and $NO_3^\bullet$, calculated using Equation 4.10. For reaction with $OH^\bullet$ the experimentally determined value for k_{OH}(piperitone) was used, while for O_3 and $NO_3^\bullet$ the k(piperitone) values predicted by the SAR approach were used.

Table 4.10 *Calculated atmospheric lifetimes for piperitone due to reaction with $OH^\bullet$, O_3 and $NO_3^\bullet$.*

Oxidant	**k(piperitone)** cm^3 $molecule^{-1}$ s^{-1}	**[Oxidant]** molecules cm^{-3}	**Lifetime** hours
$OH^\bullet$	9.93×10^{-11}	1.6×10^6	1.7
O_3	4.89×10^{-18}	7.0×10^{11}	81.1
$NO_3^\bullet$	1.79×10^{-13}	5.0×10^8	3.1

The lifetime of piperitone due to reaction with $OH^\bullet$ is quite short, less than 2 hours. Reaction with O_3 is also quite fast, with a lifetime of just over than 81 hours, although there is some uncertainty regarding the SAR method for predicting k_{O_3}(piperitone). During the day, reaction with $OH^\bullet$ is expected to be the dominant removal process for piperitone in the atmosphere. Piperitone photolysis is also a potential loss process during the day, however it is expected to be minor considering the low value for $J_{piperitone}$ measured in the chamber. The lifetime of piperitone due to reaction with $NO_3^\bullet$ is about 3 hours. As Sitka spruce monocultures are mainly found in pristine or very low NO_x environments, reaction with $NO_3^\bullet$ is expected to be minimal. The short atmospheric lifetime of piperitone with respect to reaction with $OH^\bullet$ indicates that piperitone will be rapidly oxidised in the atmosphere, and impact on the oxidising capacity and composition of the atmosphere fairly close to its emission sources.

4.4.2 Piperitone Oxidation Products

Three $OH^{\bullet}$ initiated piperitone oxidation experiments were performed with $C_6H_6^+$ as the ToF-CIMS reagent ion. The steady state $OH^{\bullet}$ concentration in the chamber was approximately 6 x 10^6 molecules cm^{-3} in each experiment, determined from the decay of piperitone. For experiments conducted with the ToF-CIMS in I^- mode, piperitone could not be detected and therefore the steady state $OH^{\bullet}$ concentration could not be estimated. However as the initial reaction conditions were the same, it is assumed that the steady state $OH^{\bullet}$ concentration was similar to that for the experiments conducted with the ToF-CIMS in $C_6H_6^+$ mode. Since piperitone photolysis accounted for less than 1% of the total piperitone reactivity, it is assumed the primary oxidation products observed are solely due to the reaction of piperitone with $OH^{\bullet}$.

For the experiments conducted with the ToF-CIMS in $C_6H_6^+$ mode, five oxidation products were identified; $C_8H_{14}O_2$, $C_9H_{14}O_2$, $C_5H_8O_3$, $C_9H_{16}O_3$ and $C_9H_{14}O_4$. Since the time series were near identical in all three experiments, one single experiment was selected to represent all the experiments analysed with the ToF-CIMS in $C_6H_6^+$ mode. The same procedure was applied to the experiments performed with the ToF-CIMS in I^- mode, which identified twenty-eight oxidation products. The results from both ion detection modes were combined, to give a total of thirty-three piperitone oxidation products, Table 4.11 and Figure 4.11.

Table 4.11 *Oxidation products identified from the reaction of $OH^{\bullet}$ with piperitone. The products are grouped by both oxygen number (rows) and carbon number (columns).*

	C_5	**C_6**	**C_7**	**C_8**	**C_9**	**C_{10}**	**C_{14}**
O_2				$C_8H_{14}O_2$	$C_9H_{14}O_2$		
O_3	$C_5H_8O_3$				$C_9H_{16}O_3$	$C_{10}H_{16}O_3$	$C_{14}H_{24}O_3$
O_3					$C_9H_{16}O_3$		
O_4	$C_5H_8O_4$	$C_6H_8O_4$	$C_7H_8O_4$	$C_8H_{12}O_4$	$C_9H_{14}O_4$	$C_{10}H_{14}O_4$	
O_4		$C_6H_{10}O_4$	$C_7H_{10}O_4$		$C_9H_{14}O_4$	$C_{10}H_{16}O_4$	
O_4			$C_7H_{12}O_4$		$C_9H_{16}O_4$	$C_{10}H_{18}O_4$	
O_4			$C_7H_{14}O_4$				
O_5			$C_7H_{12}O_5$	$C_8H_{12}O_5$	$C_9H_{14}O_5$	$C_{10}H_{14}O_5$	
O_5					$C_9H_{16}O_5$	$C_{10}H_{16}O_5$	
O_5						$C_{10}H_{18}O_5$	
O_6					$C_9H_{14}O_6$	$C_{10}H_{14}O_6$	
O_6						$C_{10}H_{16}O_6$	
O_6						$C_{10}H_{18}O_6$	
O_7						$C_{10}H_{16}O_7$	

Products with chemical formulae $C_9H_{16}O_3$ and $C_9H_{14}O_4$ are listed twice in Table 4.11, and represented twice in Figure 4.11, as they were detected with the ToF-CIMS in both modes. Discrepancies between the time series of the ions associated with the products in both ToF-CIMS modes confirmed they were not the same product, but isomers formed at different rates.

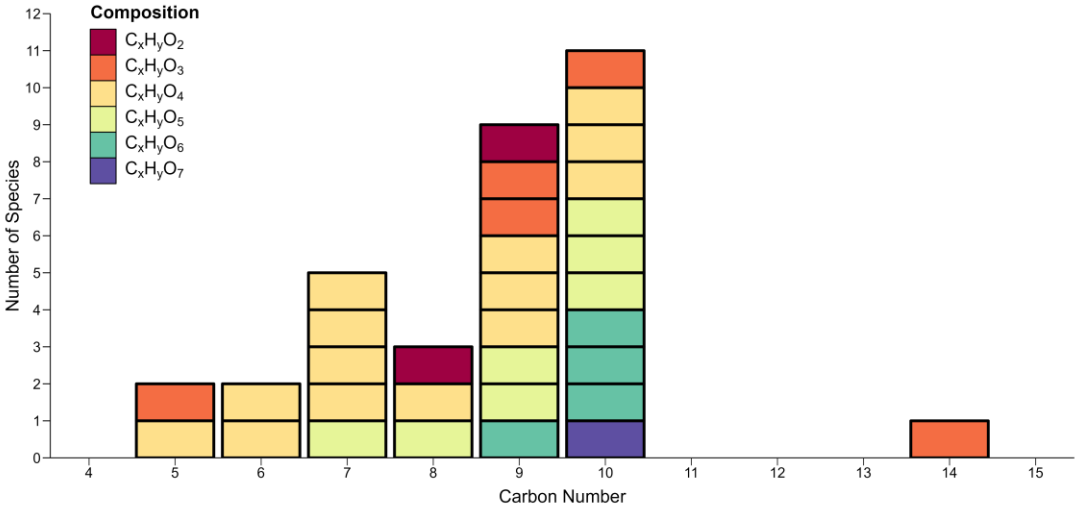

Figure 4.11 *Composition of all piperitone oxidation products by number of species per carbon number. Colour corresponds to oxygen number.*

The carbon content of the oxidation products ranged from C_5 to C_{14}. The dominant products were C_{10} compounds, accounting for 33% of all products. Compounds retaining the original carbon skeleton have also been found to dominate the products observed for the $OH^{\bullet}$ initiated oxidation of limonene[241] and α-pinene[242] under low NO_x conditions. The smallest products detected were C_5 compounds. It is highly likely that smaller compounds, such as formaldehyde (C_1) and acetone (C_3) were also formed, as has been observed for the $OH^{\bullet}$ initiated oxidation of several monoterpenes[243]. The detection of these compounds is at the limit of the ToF-CIMS used in this work, which was operated to focus between *m*/*z* 50 and 500, and may explain their absence.

$C_{14}H_{24}O_3$ was the only product with a carbon number above ten, suggesting radical combination reactions were not prevalent. This is in contrast to the product distribution observed for many other BVOCs, where dimers and oligomers are commonly identified as oxidation products[244]. It is possible that dimers and oligomers were formed during piperitone oxidation, but were not detected or underwent fragmentation during the ToF-CMS ionisation process. Another possibility is that due to the low concentrations of piperitone used in the experiment, the probability of combination reactions occurring was low, and as dimer products are expected to have a low vapour pressure and exist mainly in the particle-phase, the gas-phase concentrations were below the limit of detection of the ToF-CIMS.

The lowest oxygen content of the oxidation products detected was O_2, while the most abundant oxygen number was O_4, accounting for fourteen products. A single compound, $C_{10}H_{16}O_7$, was the highest oxygen containing product detected. It is possible further oxidised products were formed, however due to the reduction in volatility with increasing extent of oxidation, these compounds would likely rapidly partition into the particle-phase, and therefore are not expected to be detected in the gas-phase[244]. Also, the detection capabilities of I^- ToF-CIMS reduces as the oxygen content exceeds O_7[105].

The evolution of oxidation products can be investigated using a Kroll diagram, which depicts the carbon number of a compound as a function of the mean oxidation state of carbon in the molecule, Equation 4.11.

$$\overline{OS}_C = 2\left(\frac{O}{C}\right) - \frac{H}{C} \qquad \textit{Equation 4.11}$$

Where for compounds containing only C, H and O: $\overline{OS}_C$ is the mean oxidation state of carbon in the molecule; $\frac{O}{C}$ is the oxygen to carbon ratio in the molecule; and $\frac{H}{C}$ is the hydrogen to carbon ratio in the molecule[245]. Figure 4.12 shows the Kroll diagrams of the piperitone oxidation products during each hour of the experiment.

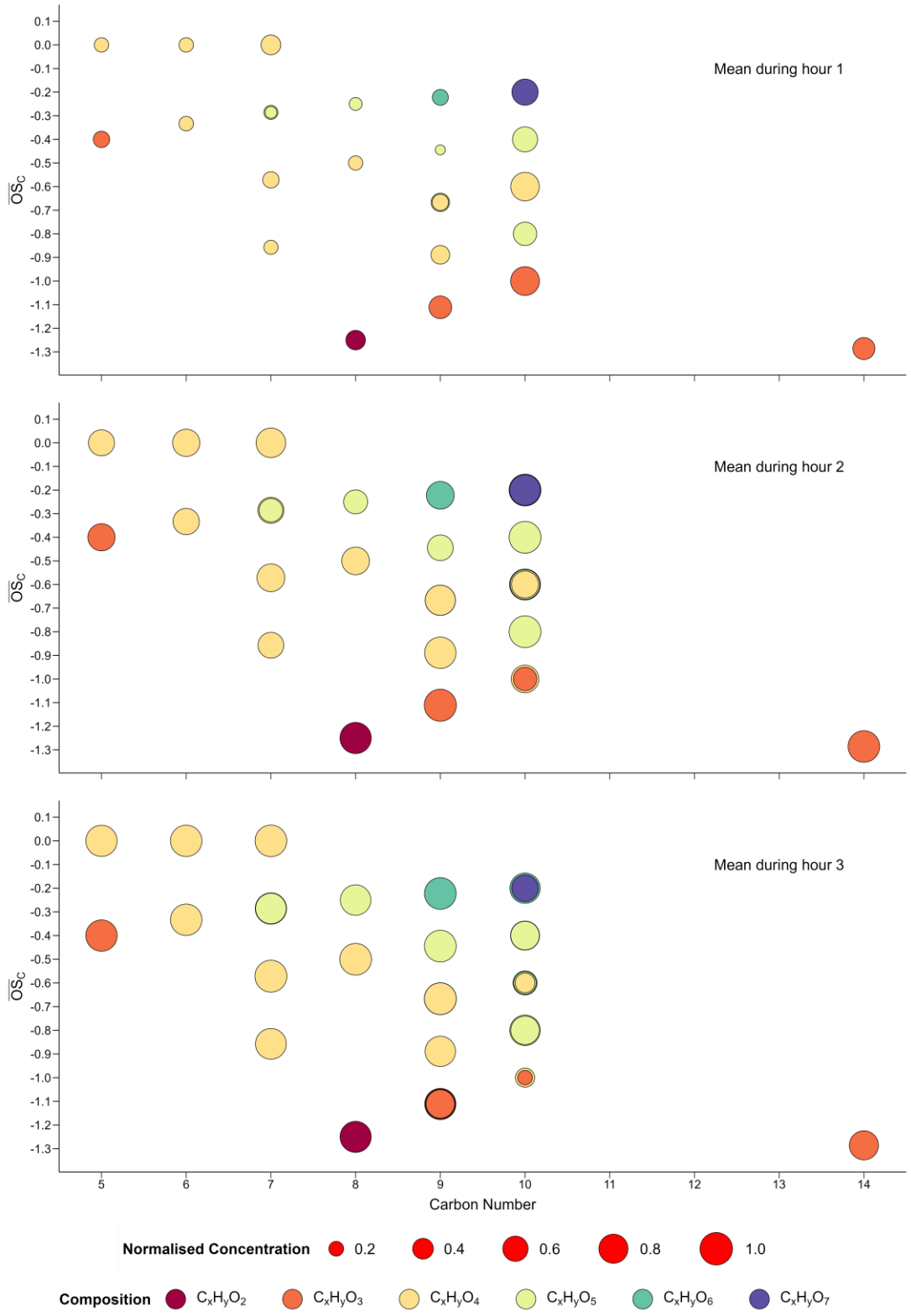

Figure 4.12 *Kroll diagrams for the products of the OH• initiated oxidation of piperitone. Each plot is the mean signal over an hour of the experiment. Colour refers to oxygen number, and size is proportional to ToF-CIMS signal normalised to one.*

Not all products are visible on the plots, as compounds with the same carbon number and $\overline{OS}_C$ appear at the same position on the Kroll diagram[245]. For most piperitone oxidation products, those with a lower carbon number have a higher $\overline{OS}_C$. During the first hour the composition of the products was mainly C_{10} and C_9 compounds with an $\overline{OS}_C$ below -0.5. As the reaction progressed to the last hour, the importance of these compounds diminished, and compounds with a carbon content below C_9, and $\overline{OS}_C$ above -0.5 became dominant. This is in line with expectations, as a compound is further oxidised, the position of its products on a Kroll diagram will approach that of CO_2 (carbon number 1, $\overline{OS}_C$ +4)[245].

Figure 4.13 shows Van Krevelen diagrams for each hour of the experiment. The location of a compound on a Van Krevelen diagram depends on its O:C and H:C ratios. The primary piperitone oxidation products ($C_xH_yO_3$ and $C_xH_yO_4$ compounds) have a lower oxygen content and higher H:C ratio relative to the later oxidation products. Similar to the Kroll diagrams, comparison of the three Van Krevelan diagrams shows the importance of the various oxidation products at different stages of the reaction, and can be used to determine reaction progression. An increase in symbol size between successive diagrams indicates the compound was still being produced, while a decrease corresponds to the compound undergoing oxidation, leading to the formation of secondary products.

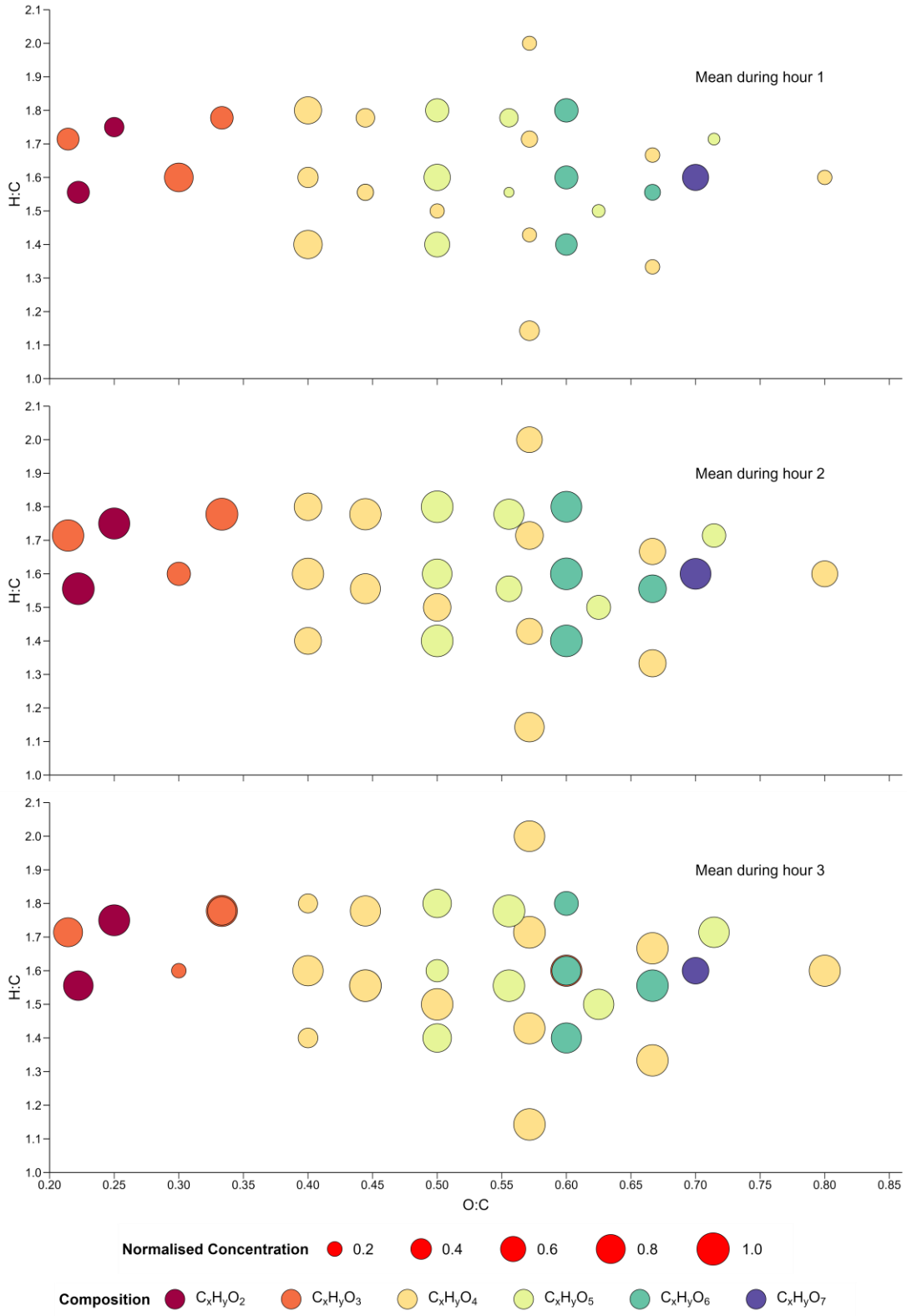

Figure 4.13 *Van Krevelen diagrams for the products $OH^{\bullet}$ initiated oxidation of piperitone. Each plot is the mean signal over an hour of the experiment. Colour refers to oxygen number, and size is proportional to ToF-CIMS signal normalised to one.*

4.4.3 Piperitone Oxidation Mechanisms

Figure 4.14 shows the order in which oxidation products attained their maximum intensity during the experiment. The first products to appear and maximise were C_{10} compounds, $C_{10}H_{16}O_3$ (01:00:00), followed by $C_{10}H_{14}O_4$ (01:07:00) and $C_{10}H_{18}O_4$ (01:12:00). The remaining C_{10} compounds peaked later and had a higher oxygen content, indicating they could be secondary products, generated through the oxidation of these primary products.

The C_9 products peaked later than the initial C_{10} products, indicating they are secondary or possibly tertiary products. The C_5 to C_8 products peaked close to the end of the experiment, it is likely these compounds have many formation pathways, generated through the fragmentation of multiple oxidation products.

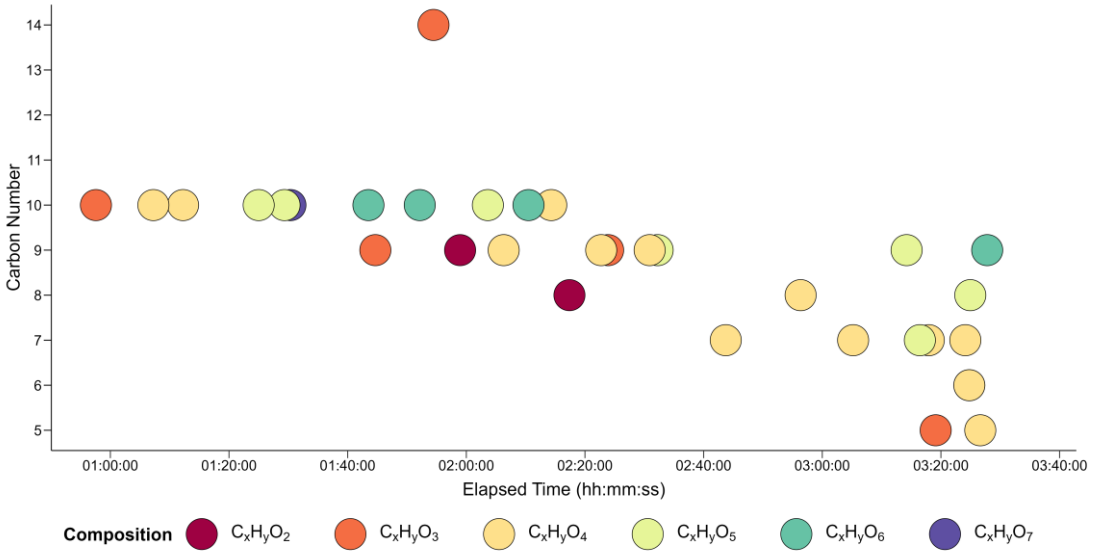

Figure 4.14 *Reaction progression plot for the products of the OH• initiated oxidation of piperitone. The position of a compound on the x-axis indicates the time after illumination at which the product reached its maximum intensity and the y-axis is carbon number. Colour refers to oxygen content.*

Possible oxidation mechanisms for the formation of the observed products have been derived from the expected oxidation processes following initial OH• attack at the main reactive sites on piperitone identified by the SAR (Section 4.2.1). Based on

this approach plausible oxidation product structures are proposed, although structural confirmation is not possible. The analysis showed that several of the main oxidation products could have been explained through the same initial reaction pathways. These products were allocated to a group according to the identified formation pathways; $C_{10}H_{16}O_x$, $C_{10}H_{14}O_x$, $C_{10}H_{18}O_x$, $C_9H_{16}O_x$, $C_9H_{14}O_x$ and others.

4.4.3.1 $C_{10}H_{16}O_x$ Products

The $C_{10}H_{16}O_x$ mechanistic pathway accounts for the formation of five oxidation products: $C_{10}H_{16}O_3$, $C_{10}H_{16}O_5$, $C_{10}H_{16}O_7$, $C_{10}H_{16}O_6$, and $C_{10}H_{16}O_4$. The time series profiles for each of these compounds is shown in Figure 4.15.

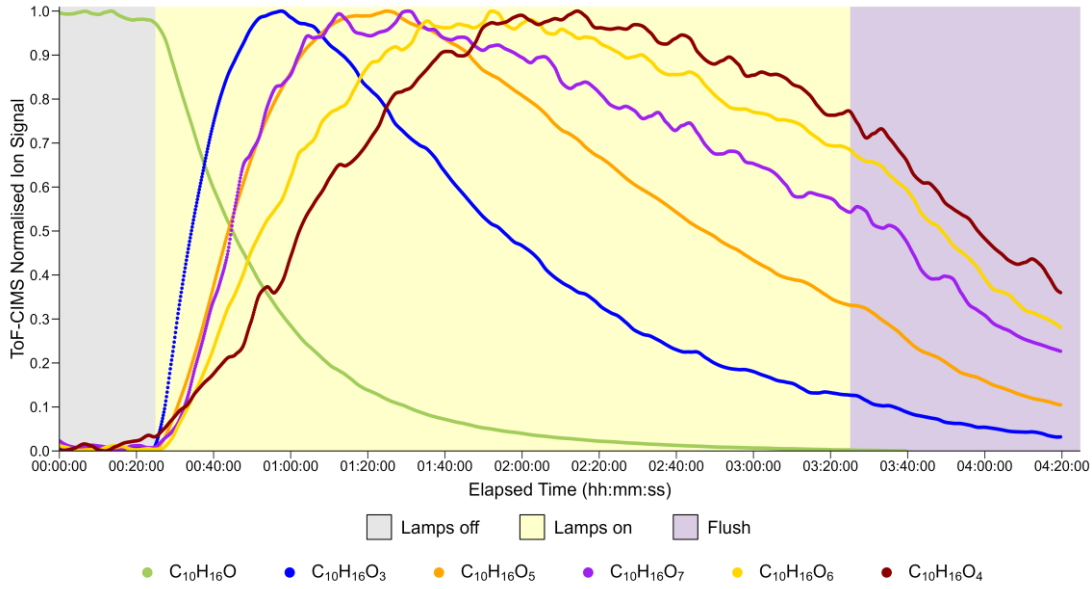

Figure 4.15 *Time series of $C_{10}H_{16}O_x$ products, resulting from the $OH^{\bullet}$ initiated oxidation of piperitone. Due to large differences in signal intensity between different products, each signal is normalised to one. Data not corrected for chamber losses.*

$C_{10}H_{16}O_3$ was the first piperitone oxidation product to form. It was produced immediately after illumination (Figure 4.15), and also exhibited a rapid decay due to oxidation. $C_{10}H_{16}O_5$ and $C_{10}H_{16}O_7$ were produced next, with near similar formation rates. The appearance of $C_{10}H_{16}O_6$ and $C_{10}H_{16}O_4$ occurred much later, suggesting these were secondary products. Figure 4.16 shows the proposed mechanism for the formation of the $C_{10}H_{16}O_x$ products from the oxidation of piperitone.

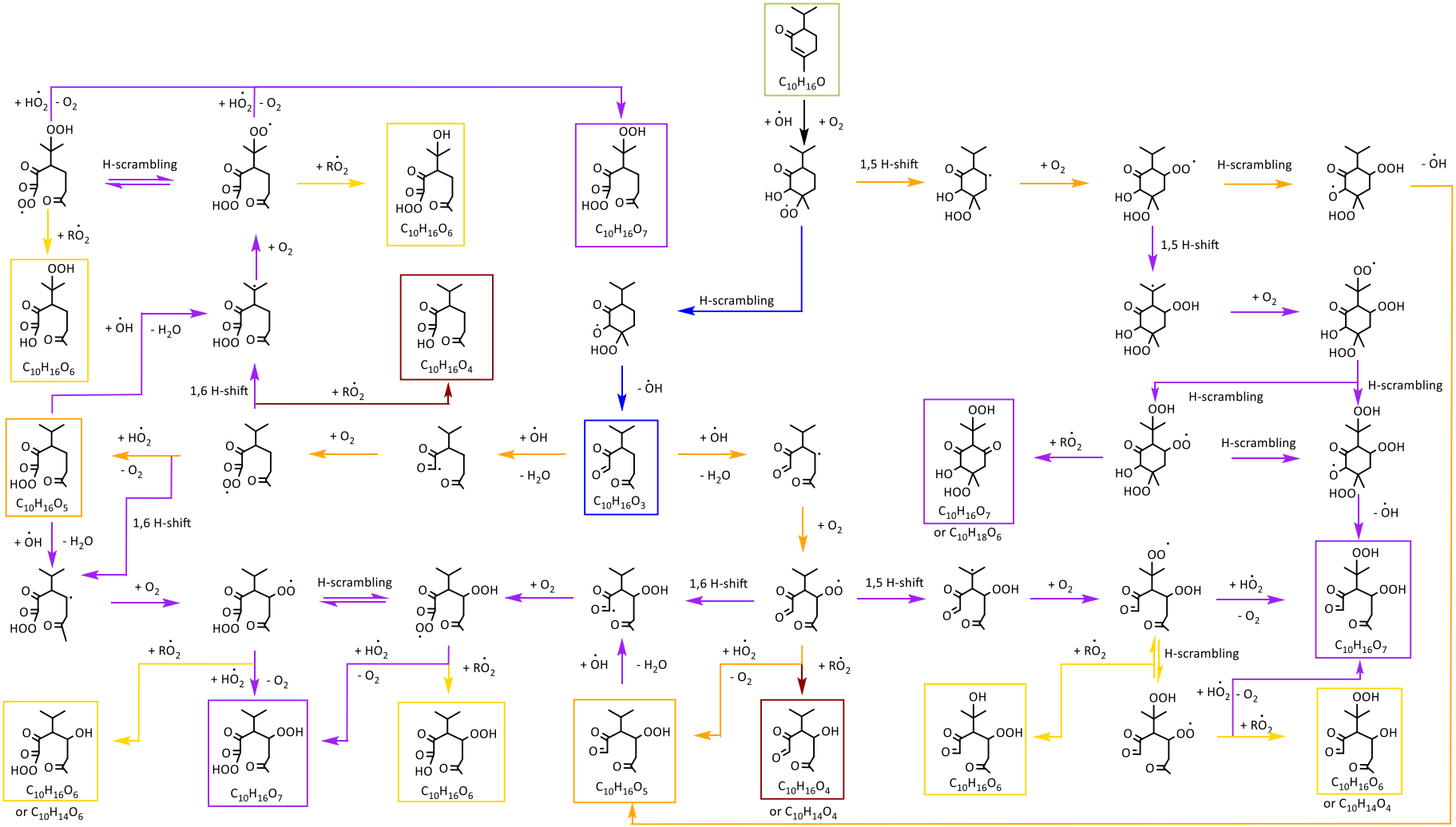

Figure 4.16 *Proposed mechanism for the formation of $C_{10}H_{16}O_x$ products resulting from the $OH^{\bullet}$ initiated oxidation of piperitone.*

Plausible mechanisms for the formation of all $C_{10}H_{16}O_x$ products can be proposed following initial addition of OH• to the alkene functionality in piperitone, which is identified as the dominant reaction pathway by SAR (Section 4.2.1). This reactive site in piperitone is similar to that in the α,β-unsaturated ketone shown in Figure 4.17, where OH• addition is expected to mostly occur on the carbon adjacent to the ketone (α position). The oxygen of the ketone can form a hydrogen bond with the hydrogen of the OH•, which coordinates the oxygen towards the α carbon[38, 224, 233, 246]. This will produce a tertiary alkyl radical[38] that is more stable than the secondary alkyl radical that would be formed if OH• addition occurred at the other carbon (β position). Also in the case of piperitone, addition to the β carbon is likely sterically hindered[38].

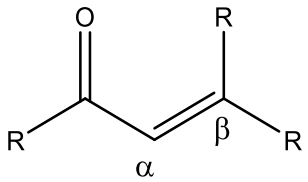

Figure 4.17 *Structure of an α,β-unsaturated ketone.*

The mechanism for piperitone oxidation shows OH• addition to the α carbon only, however addition to the β carbon would yield the same products. Following OH• addition to piperitone, O_2 rapidly adds to the alkyl radical, (Figure 4.16, black arrow) leading to the formation of an initial hydroxyl peroxy radical. Two major routes are available for the hydroxyl peroxy radical within the $C_{10}H_{16}O_x$ mechanism: hydrogen atom transfer between the adjacent hydroxyl and peroxy groups called hydrogen scrambling (H-scrambling)[247] (Figure 4.16, blue arrow), and hydrogen atom transfer across the ring (1,5-hydrogen shift) (Figure 4.16 orange arrow).

$C_{10}H_{16}O_3$

The most likely pathway (Figure 4.16, blue arrow) for the initial hydroxy peroxy radical is H-scrambling between the adjacent hydroxyl and peroxy groups to produce an alkoxy radical at the α carbon and a hydroperoxyl (-OOH) group at the β carbon. Decomposition of this alkoxy radical leads to ring opening, and the formation of an

aldehyde at the α carbon and an alkyl radical at the β carbon with the hydroperoxyl group. Rapid elimination of $OH^{\bullet}$ occurs to produce a ketone, giving a stable oxidation product $C_{10}H_{16}O_3$. H-scrambling in a hydroxyl peroxy radical and subsequent carbonyl formation via $OH^{\bullet}$ elimination has been observed in the formation of MACR and MVK from isoprene under low NO_x conditions[206, 222], as well as for limonene[241].

Due to the rapid decay of $C_{10}H_{16}O_3$, kinetic SAR analysis was performed to identify the most reactive sites towards $OH^{\bullet}$. The approach was the same as that employed in the SAR determination of k_{OH}(piperitone). The coefficients in Table 4.2 were used with F[=O] = 8.7 also[208].

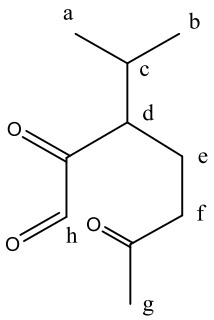

Figure 4.18 *Structure of $C_{10}H_{16}O_3$, with $OH^{\bullet}$ reaction sites labelled.*

$$
\begin{aligned}
k_{OH}(C_{10}H_{16}O_3) = {} & k_{primary} \times F[\text{>CH-}] && \text{(a)}\\
& + k_{primary} \times F[\text{>CH-}] && \text{(b)}\\
& + k_{tertiary} \times F[\text{-C(O)-CH<}] \times F[\text{-CH}_3] \times F[\text{-CH}_3] && \text{(c)}\\
& + k_{tertiary} \times F[\text{>CO}] \times F[\text{>CH-}] \times F[\text{-CH}_2\text{-}] && \text{(d)}\\
& + k_{secondary} \times F[\text{-C(O)-CH}_3] \times F[\text{-C(O)-CH}_3] && \text{(e)}\\
& + k_{secondary} \times F[\text{-CH}_2\text{-}] \times F[\text{>CO}] && \text{(f)}\\
& + k_{primary} \times F[\text{>C=C<}] && \text{(g)}\\
& + k_{secondary} \times F[\text{=O}] \times F[\text{>CO}] && \text{(h)}
\end{aligned}
$$

Equation 4.12[208]

$k_{OH}(C_{10}H_{16}O_3) = 0.136 \times 10^{-12}$ (cm^3 $molecule^{-1}$ s^{-1}) × 1.23 (a)

+ 0.136 × 10^{-12} (cm^3 $molecule^{-1}$ s^{-1}) × 1.23 (b)

+ 1.94 × 10^{-12} (cm^3 $molecule^{-1}$ s^{-1}) × 3.9 × 1 × 1 (c)

+ 1.94 × 10^{-12} (cm^3 $molecule^{-1}$ s^{-1}) × 0.75 × 1.23 × 1.23 (d)

+ 0.934 × 10^{-12} (cm^3 $molecule^{-1}$ s^{-1}) × 3.9 × 3.9 (e)

+ 0.934 × 10^{-12} (cm^3 $molecule^{-1}$ s^{-1}) × 1.23 × 0.75 (f)

+ 0.136 × 10^{-12} (cm^3 $molecule^{-1}$ s^{-1}) × 0.75 (g)

+ 1.94 × 10^{-12} (cm^3 $molecule^{-1}$ s^{-1}) × 8.7 × 0.75 (h)

Calculation 4.4

$k_{OH}(C_{10}H_{16}O_3) = 3.79 \times 10^{-11}$ cm^3 $molecule^{-1}$ s^{-1}

From the SAR calculation, site e, β to two ketones, is the most reactive site accounting for 37.5% of reactivity, followed by site h, aldehydic hydrogen abstraction (33.4%), and site c hydrogen abstraction from the isopropyl group (9.6%).

$C_{10}H_{16}O_5$

There are two possible $C_{10}H_{16}O_5$ isomers that can be formed from the oxidation of piperitone through three pathways. One isomer can be produced either as a primary piperitone oxidation product, or as a secondary piperitone product from the oxidation of $C_{10}H_{16}O_3$. The other $C_{10}H_{16}O_5$ isomer can only be produced as a secondary piperitone product from the oxidation of $C_{10}H_{16}O_3$. It is likely all mechanisms occur.

The alternate fate of the initial hydroxyl peroxy radical is an autoxidation process, initiated by a 1,5-hydrogen shift from the β carbon (Figure 4.4, site e) to the peroxy radical[248] (Figure 4.16, orange arrow). The 1,5-hydrogen shift proposed in Figure 4.16 seems the most plausible, as it involves a favourable six membered transition state. Due to steric strain a hydrogen shift from another site is unlikely[244]. Following the 1,5-hydrogen shift, a peroxy group and an alkyl radical are produced. The alkyl radical rapidly adds O_2, to form a peroxy radical. H-scrambling occurs between the peroxy radical and other oxygenated functionalities[35, 241, 249], which eventually leads to the formation of an alkoxy radical and two -OOH groups. The alkoxy radical undergoes

decomposition leading to ring opening and the formation of two carbonyls and an $OH^{\bullet}$[206, 222], in the same manner as was described for the formation of $C_{10}H_{16}O_3$.

$C_{10}H_{16}O_5$ can also be formed through reaction of $OH^{\bullet}$ with $C_{10}H_{16}O_3$ (Figure 4.16, orange arrows) via H-abstraction from either the di-β-ketone carbon or from the aldehyde (Figure 4.18, site e and site h, respectively). The addition of O_2 to the resulting alkyl radical leads to the formation of a peroxy radical, which can react with $HO_2^{\bullet}$ leading to the formation of a stable $C_{10}H_{16}O_5$ oxidation product and O_2[22].

$C_{10}H_{16}O_5$ can also be produced through peroxy radical reactions involving $C_{10}H_{17}O_6^{\bullet}$ peroxy radicals from the $C_{10}H_{18}O_x$ mechanism (Section 4.4.3.3). The reaction can produce a ketone, $C_{10}H_{16}O_5$ or an alcohol, $C_{10}H_{18}O_5$.

Thus, $C_{10}H_{16}O_5$ is likely formed as a primary product from the direct oxidation of piperitone and also as a secondary product from the oxidation of $C_{10}H_{16}O_3$. The formation of $C_{10}H_{16}O_5$ as a primary product would be expected to dominate at the start of the reaction, when the piperitone concentration was greatest. As the reaction progressed the formation pathway for $C_{10}H_{16}O_5$ is expected to shift towards the secondary product mechanism, as the concentration of piperitone decreased and the concentration of $C_{10}H_{16}O_3$ increased. As shown in Figure 4.15, the time series for $C_{10}H_{16}O_5$ increases rapidly, and exhibits a slower decay than $C_{10}H_{16}O_3$, which is indicative of a competition between its continued formation as a secondary product and loss by reaction with $OH^{\bullet}$.

$C_{10}H_{16}O_7$

Four separate $C_{10}H_{16}O_7$ isomers can be formed from the oxidation of piperitone. One isomer can be produced as a primary piperitone oxidation product only. Another isomer has two formation routes, it can be produced as a primary piperitone oxidation product or as a secondary piperitone product from the oxidation of $C_{10}H_{16}O_3$. The remaining two isomers can be produced as secondary piperitone products through the oxidation of $C_{10}H_{16}O_3$, or tertiary piperitone products through the oxidation of $C_{10}H_{16}O_5$.

The formation of $C_{10}H_{16}O_7$ directly from piperitone (Figure 4.16, purple arrows) proceeds via an autoxidation mechanism involving two 1,5-hydrogen shifts and O_2 additions to give a peroxy radical. This is followed by H-scrambling between the peroxy and hydroxy groups until an alkoxy radical is produced. Alkoxy radical decomposition leads to ring opening producing a di-carbonyl and $OH^{\bullet}$[206, 222], as observed in the mechanisms for $C_{10}H_{16}O_3$ and $C_{10}H_{16}O_5$. Alternatively H-scrambling can result in a peroxy radical on the β-ketone carbon, which can react with another peroxy radical in a radical termination reaction producing a ketone on the β-ketone carbon[22], giving $C_{10}H_{16}O_7$.

The initial steps in the mechanism for the formation of $C_{10}H_{16}O_7$ as a secondary piperitone product from the oxidation of $C_{10}H_{16}O_3$ are the same as the initial steps for the formation of $C_{10}H_{16}O_5$, until the peroxy radical is formed. The peroxy radical undergoes a hydrogen shift producing an alkyl radical (Figure 4.16, purple arrows). For the aldehydic peroxy radical two 1,6-hydrogen shifts are possible; either from the di-β-ketone carbon, or from the tertiary isopropyl carbon. For the peroxy radical at the di-β-ketone carbon a 1,6-hydrogen shift from the aldehyde, or 1,5-hydrogen shift from the tertiary isopropyl carbon can occur. The resulting alkyl radical adds O_2 giving a peroxy radical which reacts with $HO_2^{\bullet}$ to give a stable $C_{10}H_{16}O_7$ product and O_2.

$C_{10}H_{16}O_7$ can produced as a tertiary piperitone product through the oxidation of either of the $C_{10}H_{16}O_5$ isomers. H-abstraction by $OH^{\bullet}$ leads to the formation of an alkyl radical and H_2O. For the aldehydic $C_{10}H_{16}O_5$ isomer H-abstraction most likely occurs from the aldehyde. For the peroxy acid $C_{10}H_{16}O_5$ isomer H-abstraction can occur from either the tertiary isopropyl carbon or the di-β-ketone carbon. The resulting alkyl radical adds O_2 giving a peroxy radical which reacts with $HO_2^{\bullet}$ to give a stable $C_{10}H_{16}O_7$ product and O_2.

The rate of formation of $C_{10}H_{16}O_7$ is the same as for $C_{10}H_{16}O_5$ (Figure 4.15) which indicates both are initially formed via the direct and rapid piperitone autoxidation mechanism, involving hydrogen shifts. The decay of $C_{10}H_{16}O_7$ is much more

prolonged than for $C_{10}H_{16}O_3$ or $C_{10}H_{16}O_5$. This is likely due to $C_{10}H_{16}O_7$ being produced as secondary and tertiary oxidation products, which as they require successive $OH^{\bullet}$ reactions are expected to occur later in the overall oxidation process.

$C_{10}H_{16}O_6$

$C_{10}H_{16}O_6$ reaches a maximum much later than the other initial $C_{10}H_{16}O_x$ products, Figure 4.15. The proposed mechanism shows that $C_{10}H_{16}O_6$ can be formed as a secondary or tertiary piperitone product from the oxidation of $C_{10}H_{16}O_3$ or $C_{10}H_{16}O_5$ (Figure 4.16), which explains its late appearance in the oxidation process. In total six $C_{10}H_{16}O_6$ isomers can be formed from the oxidation of piperitone.

The formation mechanism for $C_{10}H_{16}O_6$ proceeds via the secondary or tertiary $C_{10}H_{16}O_7$ formation mechanism until the final peroxy radical is formed (Figure 4.16, yellow arrows). The interaction of a peroxy radical with another peroxy radical is a termination reaction that will lead to the formation of a carbonyl or an alcohol[22]. Six possible alcohols can be formed from the six potential peroxy radicals to give $C_{10}H_{16}O_6$, as well as two $C_{10}H_{14}O_6$ ketones (Section 4.4.3.2). The likelihood of peroxy termination reactions occurring at the start of the experiment is quite low, as there would not be a sufficient peroxy radical concentration for the reaction to compete effectively with $HO_2^{\bullet}$ reactions[50]. The appearance of $C_{10}H_{16}O_6$ later in the reaction (Figure 4.15) supports this formation mechanism.

$C_{10}H_{16}O_4$

$C_{10}H_{16}O_4$ is the last member of the $C_{10}H_{16}O_x$ group to reach its peak (Figure 4.15), and its rate of formation is much slower than for the other $C_{10}H_{16}O_x$ oxidation products. Two $C_{10}H_{16}O_4$ isomers can be produced as secondary piperitone products from the oxidation of $C_{10}H_{16}O_3$. As with $C_{10}H_{16}O_6$, $C_{10}H_{16}O_4$ can not be formed directly from piperitone.

$C_{10}H_{16}O_4$ is formed through the same initial mechanism as the $C_{10}H_{16}O_5$ products from the oxidation of $C_{10}H_{16}O_3$ until the final peroxy radical is produced (Figure 4.16, burgundy arrows). Reaction of the peroxy radical with another peroxy radical will

produce $C_{10}H_{16}O_4$ alcohols, or $C_{10}H_{14}O_4$ ketones (Section 4.4.3.2). As with $C_{10}H_{16}O_6$, the likelihood of peroxy termination reactions occurring at the start of the experiment is quite low. In order for $C_{10}H_{14}O_4$ to be produced peroxy radical termination reactions must outcompete hydrogen shifts[22] and $HO_2^{\bullet}$ reactions[50], which is unlikely at the start of the experiment when peroxy radical concentrations are low. This may explain the later appearance of $C_{10}H_{14}O_4$ in the reaction.

4.4.3.2 $C_{10}H_{14}O_x$ Products

Figure 4.19 shows the time series profiles for the three oxidation products, $C_{10}H_{14}O_4$, $C_{10}H_{14}O_5$ and $C_{10}H_{14}O_6$ in the $C_{10}H_{14}O_x$ group. $C_{10}H_{14}O_4$ was the second primary piperitone oxidation product to be formed, after $C_{10}H_{16}O_3$. It was the first oxidation product in the $C_{10}H_{14}O_x$ group to maximise. $C_{10}H_{14}O_5$ was the second $C_{10}H_{14}O_x$ product to be formed and can only be produced as a secondary piperitone product through the oxidation of $C_{10}H_{14}O_4$. $C_{10}H_{14}O_6$ was the final $C_{10}H_{14}O_x$ product to appear, and can be formed as either a primary piperitone oxidation product, or as a secondary piperitone product from the oxidation of $C_{10}H_{14}O_4$. Figure 4.20 shows the proposed formation mechanisms for the products in the $C_{10}H_{14}O_x$ group.

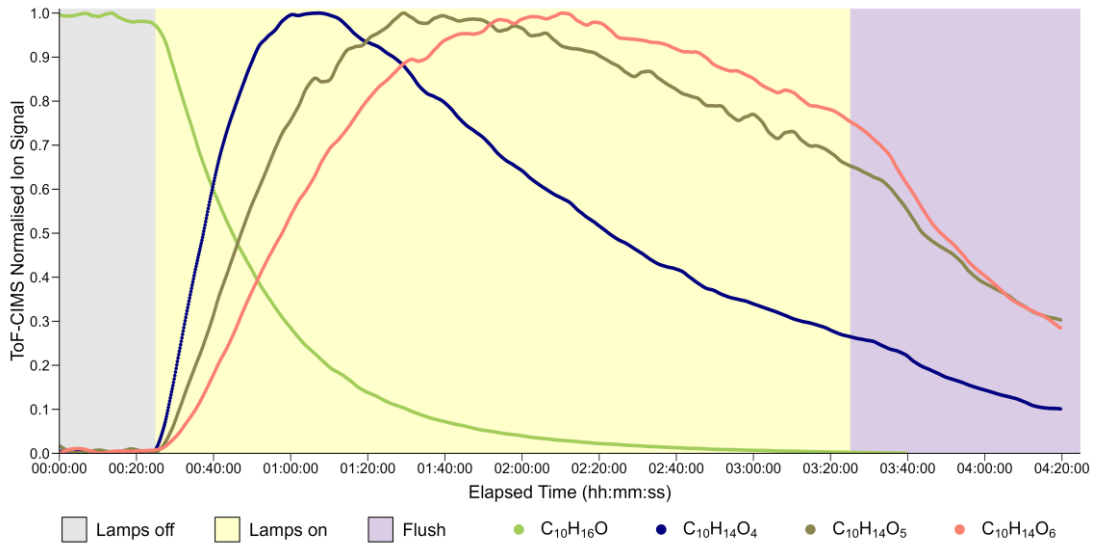

Figure 4.19 *Time series of $C_{10}H_{14}O_x$ products, resulting from the $OH^{\bullet}$ initiated oxidation of piperitone. Due to large differences in signal intensity between different products, each signal is normalised to one. Data not corrected for chamber losses.*

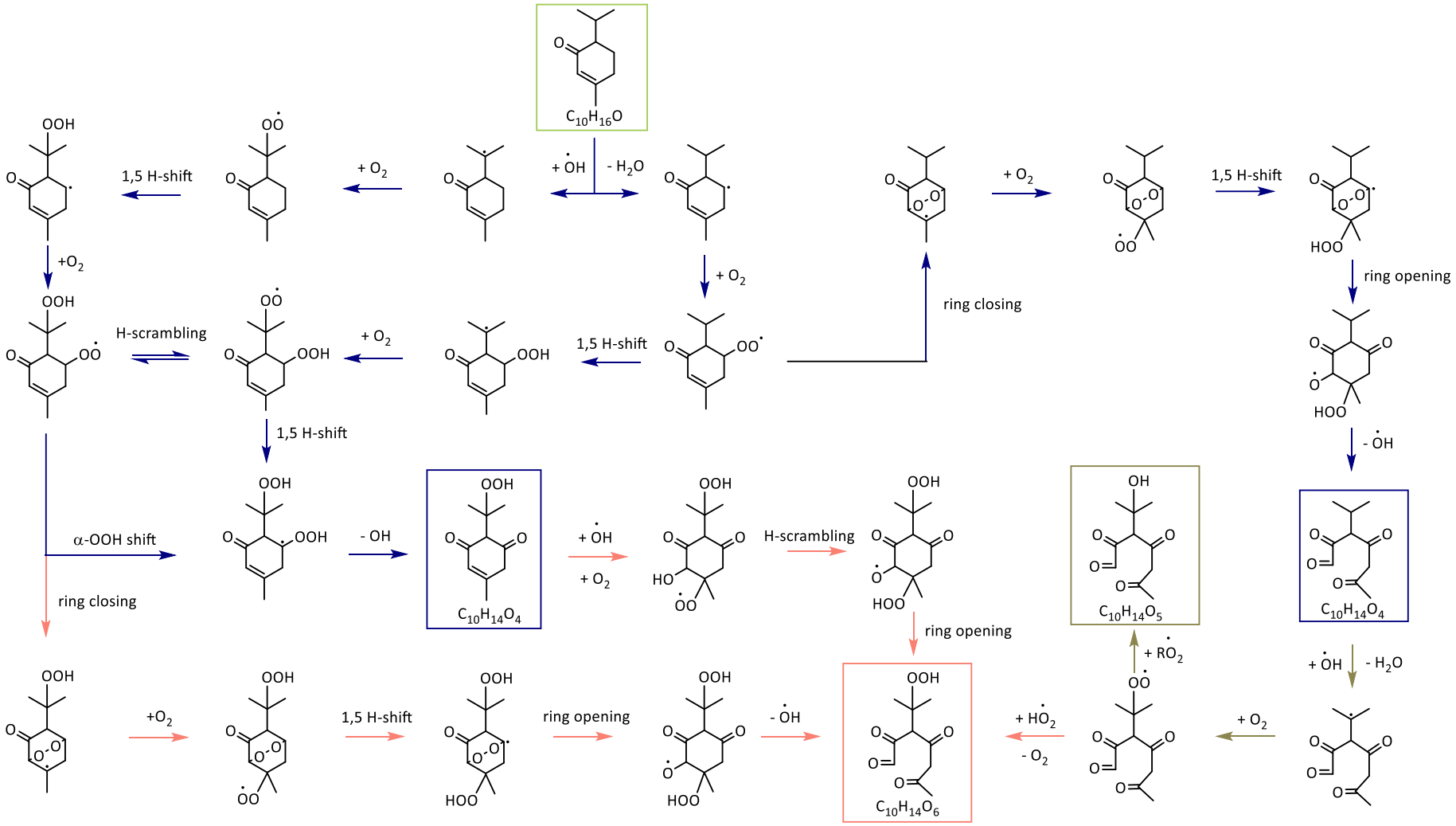

Figure 4.20 *Proposed mechanism for the formation of $C_{10}H_{14}O_x$ products resulting from the $OH^{\bullet}$ initiated oxidation of piperitone.*

Analysis of the possible reaction pathways indicates that the formation of the $C_{10}H_{14}O_x$ products can only occur following H-abstraction from piperitone. The SAR method predicted that H-abstraction accounts for 15% of piperitone reactivity (Section 4.2.1), with the most likely site for attack being the tertiary isopropyl carbon (Figure 4.4, site c), followed by the β-ketone carbon (Figure 4.4, site e), accounting for 7% and 4% of total piperitone reactivity, respectively. H-abstraction by $OH^{\bullet}$ has been observed to occur to a significant extent during the $OH^{\bullet}$ initiated oxidation of several monoterpenes[250], including α-pinene[251] and limonene[241].

$C_{10}H_{14}O_4$

Two $C_{10}H_{14}O_4$ isomers can be produced from the oxidation of piperitone, through two pathways (Figure 4.20, navy blue arrows). One of the pathways proceeds via an autoxidation mechanism, while the other pathway involves a peroxy radical ring closure step.

The most likely site for H-abstraction from piperitone is from the isopropyl carbon (Figure 4.4, site c). This site is β to a ketone, which can coordinate $OH^{\bullet}$, and because it is bonded to three alkyl groups it will produce a stable alkyl radical[38, 224, 233, 246]. Addition of O_2 leads to the formation of a peroxy radical. A 1,5-hydrogen shift occurs between the peroxy radical and β-ketone carbon (Figure 4.4, site e), giving an alkyl radical at the β-ketone carbon and a peroxy group at the isopropyl carbon. The addition of O_2 produces a peroxy radical. H-scrambling between the peroxy functionalities is likely, giving two peroxy radical isomers.

The same peroxy radical isomers can be produced through the same mechanistic steps following H-abstraction from the β-ketone carbon on piperitone. Both of the peroxy radical isomers can react to produce $C_{10}H_{14}O_4$. The isomer with the peroxy radical at the β-ketone carbon has the possibility to undergo an α-OOH hydrogen shift, producing $^{\bullet}COOH$ at the β-ketone carbon[241]. The isomer with the peroxy radical at the tertiary isopropyl carbon can undergo a 1,5-hydrogen shift with the hydrogen remaining on the β-ketone carbon[252]. In both cases the same $^{\bullet}COOH$ intermediate is

formed, which could undergo rapid $OH^{\bullet}$ elimination to produce a ketone[42, 241], $C_{10}H_{14}O_4$.

The formation pathway for the other $C_{10}H_{14}O_4$ isomer proceeds via $OH^{\bullet}$ H-abstraction from the β-ketone carbon on piperitone (Figure 4.4, site e). This produces an alkyl radical that will add O_2 to produce a peroxy radical. The peroxy radical has the possibility to undergo ring closure by adding across the C=C bond, which has been observed in the $OH^{\bullet}$ initiated oxidation of several monoterpenes[241, 253]. The electron withdrawing nature of the carbonyl likely enhances 1,6-ring closure[254], and will produce a tertiary alkyl radical that is more stable than the secondary radical that would be formed from 1,5-ring closure[254]. The alkyl radical rapidly adds O_2, producing a peroxy radical. A 1,5-hydrogen shift from the β-ketone carbon to the peroxy radical leads to the formation of a peroxy group and an alkyl radical[254] at the β-ketone carbon. This causes rapid peroxy ring opening, producing a ketone at the β-ketone carbon, and an alkoxy radical[253, 254] α to the peroxy group. The alkoxy radical can then undergo decomposition in the same manner as was proposed for the $C_{10}H_{16}O_x$ products, producing an $OH^{\bullet}$ and two carbonyls[206, 222, 241], giving $C_{10}H_{14}O_4$.

$C_{10}H_{14}O_4$ can also be produced through the $C_{10}H_{16}O_x$ mechanism, via peroxy radical reactions involving $C_{10}H_{15}O_5^{\bullet}$, resulting in the formation of a $C_{10}H_{14}O_4$ ketone and a $C_{10}H_{16}O_4$ alcohol.

$C_{10}H_{14}O_5$

$C_{10}H_{14}O_5$ can be produced as a secondary piperitone product through the oxidation of the ring-opened $C_{10}H_{14}O_4$ isomer. H-abstraction by $OH^{\bullet}$ from the isopropyl carbon (Figure 4.20, brown arrows) produces an alkyl radical which adds O_2 to give a peroxy radical. A peroxy termination reaction results in the formation of an alcohol, $C_{10}H_{14}O_5$.

$C_{10}H_{14}O_6$

$C_{10}H_{14}O_6$ can be formed from the oxidation of piperitone through three pathways (Figure 4.20, orange arrows). Direct formation from piperitone proceeds via the same

steps as the ring retaining $C_{10}H_{14}O_4$ product described above, until the two peroxy radical isomers are formed. The isomer with the peroxy radical at the β-ketone carbon can undergo 1,6-ring closure, with the C=C bond, producing a six membered peroxy ring and a tertiary radical, which adds O_2 to give a tertiary peroxy radical. It is possible for 1,5-ring closure to occur, but is less likely as previously explained[254]. The tertiary peroxy radical can abstract the remaining hydrogen from the β-ketone carbon, leading to peroxy ring decomposition, and the formation of a ketone, and an alkoxy radical. The alkoxy radical will then undergo ring opening and $OH^{\bullet}$ elimination[206, 222, 241] to produce $C_{10}H_{14}O_6$.

$C_{10}H_{14}O_6$ can also be produced as a secondary product via the oxidation of either of the $C_{10}H_{14}O_4$ isomers. For the ring retaining $C_{10}H_{14}O_4$ isomer, $OH^{\bullet}$ can add across the C=C bond, followed by O_2 addition, leading to the formation of an alcohol and peroxy radical. H-scrambling can occur until an alkoxy radical is formed which undergoes ring opening eliminating $OH^{\bullet}$, giving $C_{10}H_{14}O_6$. Reaction of the ring opened $C_{10}H_{14}O_4$ isomer with $OH^{\bullet}$ most likely occurs via H-abstraction from the tertiary isopropyl carbon, which is β to two ketones. An alkyl radical is produced which adds O_2 to form a peroxy radical, which upon reaction with $HO_2^{\bullet}$ produces O_2, and the stable $C_{10}H_{14}O_6$ oxidation product.

$C_{10}H_{14}O_6$ can also be produced through the $OH^{\bullet}$ addition ($C_{10}H_{16}O_x$) mechanism (Section 4.4.3.1), via peroxy radical reactions involving $C_{10}H_{15}O_7^{\bullet}$, resulting in the formation a ketone, $C_{10}H_{14}O_6$ or an alcohol, $C_{10}H_{16}O_6$.

4.4.3.3 $C_{10}H_{18}O_x$ Products

There are three oxidation products in the $C_{10}H_{18}O_x$ group; $C_{10}H_{18}O_4$, $C_{10}H_{18}O_6$ and $C_{10}H_{18}O_5$. $C_{10}H_{18}O_4$ was the third primary piperitone oxidation product to form, and the first product in the $C_{10}H_{18}O_x$ group to appear, followed by $C_{10}H_{18}O_6$ and $C_{10}H_{18}O_5$. Figure 4.21 shows the time series of the oxidation products in the $C_{10}H_{18}O_x$ group.

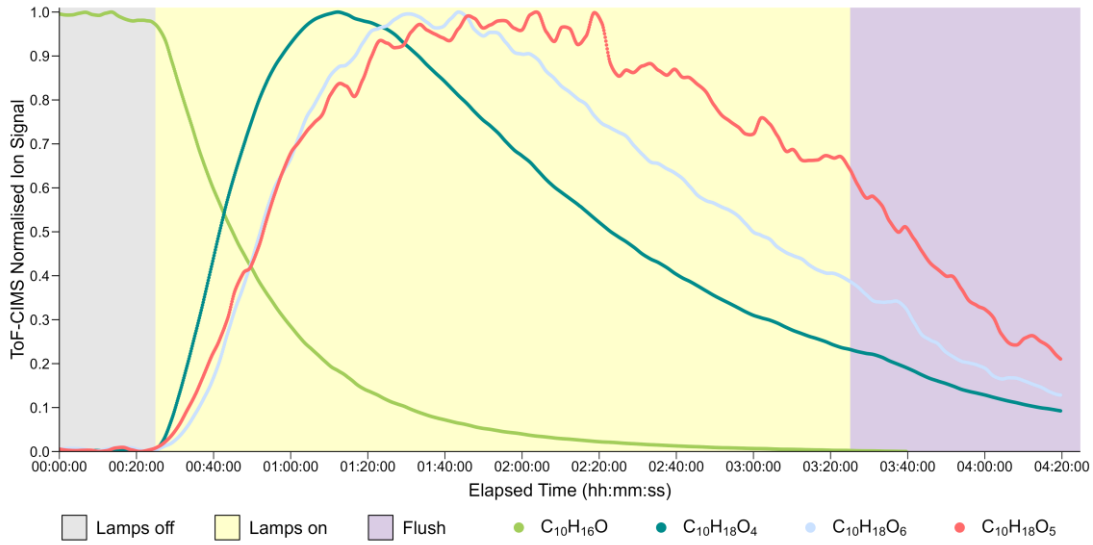

Figure 4.21 *Time series of $C_{10}H_{18}O_x$ products, resulting from the $OH^{\bullet}$ initiated oxidation of piperitone. Due to large differences in signal intensity between different products, each signal is normalised to one. Data not corrected for chamber losses.*

The compounds in the $C_{10}H_{18}O_x$ group have two more hydrogen atoms than piperitone, which indicates a degree of unsaturation was lost during the oxidation process. Figure 4.22 shows the proposed formation mechanisms for the products in the $C_{10}H_{18}O_x$ group. All thee products can be formed directly from the oxidation of piperitone, while $C_{10}H_{18}O_6$ and $C_{10}H_{18}O_5$ can also be formed as secondary products through the oxidation of $C_{10}H_{18}O_4$.

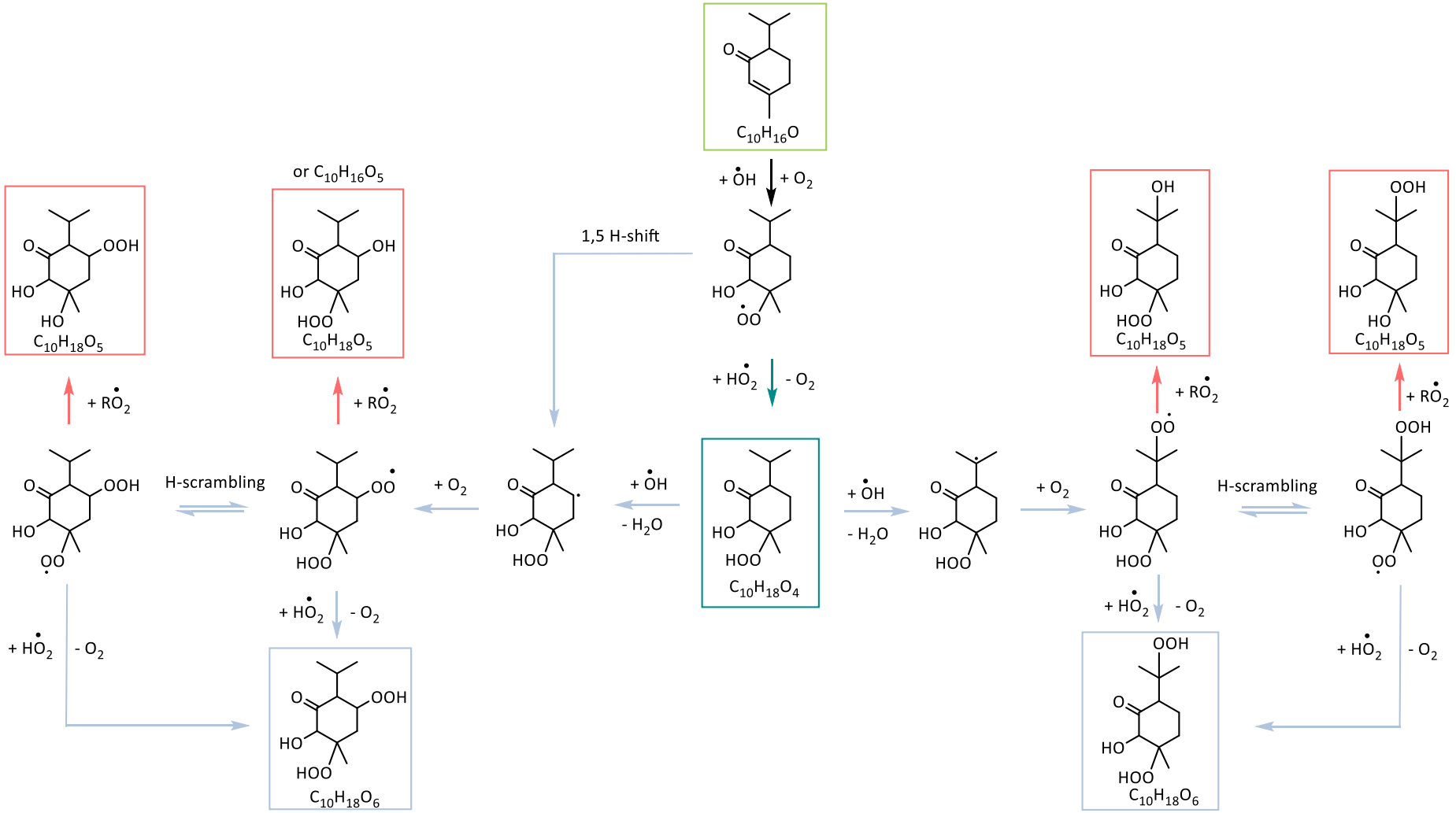

Figure 4.22 *Proposed mechanism for the formation of $C_{10}H_{18}O_x$ products resulting from the $OH^{\bullet}$ initiated oxidation of piperitone.*

The proposed mechanisms for the formation of all $C_{10}H_{18}O_x$ products proceed following initial $OH^\bullet$ addition to the alkene in piperitone (Figure 4.22, black arrow). As with the $C_{10}H_{16}O_x$ products, $OH^\bullet$ preferentially adds to the α carbon, producing an alkyl radical at the β carbon[38, 224, 246]. Only addition to the α carbon is shown, although addition to the β carbon would yield different isomeric products. Addition of O_2 to the alkyl radical leads to the formation of a peroxy radical.

$C_{10}H_{18}O_4$

Reaction of the peroxy radical with $HO_2^\bullet$ (Figure 4.22, turquoise arrow) will form O_2 and a hydroperoxide[22] with the formula $C_{10}H_{18}O_4$. The formation of this product is in competition with the formation of $C_{10}H_{16}O_3$, the first piperitone oxidation product, as they both pass through the same peroxy radical intermediate. The later appearance of $C_{10}H_{18}O_4$ relative to $C_{10}H_{16}O_3$ is likely due to the limited amount of $HO_2^\bullet$ present at the start of the reaction and the faster rate of unimolecular decomposition relative to bimolecular reaction with $HO_2^\bullet$. As the reaction progressed an increase in $HO_2^\bullet$ concentration would have shifted the equilibrium in favour of the formation of $C_{10}H_{18}O_4$, explaining why it peaks later into the reaction, Figure 4.14.

$C_{10}H_{18}O_6$

Two isomers of $C_{10}H_{18}O_6$ can be formed from the oxidation of piperitone through three pathways (Figure 4.22, grey arrows). The formation of $C_{10}H_{18}O_6$ as a primary piperitone product can occur via an autoxidation process involving a 1,5-hydrogen shift from the β-ketone carbon, followed by O_2 addition. H-scrambling between the oxygenated functionalities in the peroxy radical[249] yields two peroxy radical isomers which can subsequently react with $HO_2^\bullet$ leading to the formation of a hydroperoxide with the formula $C_{10}H_{18}O_6$ and O_2.

$C_{10}H_{18}O_6$ can also be produced as a secondary piperitone product through the oxidation of $C_{10}H_{18}O_4$ (Figure 4.22, grey arrows). H-abstraction by $OH^\bullet$ can occur from either the isopropyl carbon or the β-ketone carbon to give an alkyl radical, which

adds O_2 to give a peroxy radical which reacts in the same manner as the peroxy radical described in the $C_{10}H_{18}O_6$ formation mechanism above.

$C_{10}H_{18}O_5$

Four $C_{10}H_{18}O_5$ isomers can be produced via the oxidation of piperitone through three pathways (Figure 4.22, orange arrows). The formation of $C_{10}H_{18}O_5$ as either a primary or secondary piperitone product proceeds through the same steps as for the formation of $C_{10}H_{18}O_6$, until the peroxy radical isomers are formed. A radical termination reaction between of any of the peroxy radical isomers with another peroxy radical (Figure 4.22, orange arrows) will produce an alcohol with formula $C_{10}H_{18}O_5$, or for one of the peroxy radical isomers a ketone with formula $C_{10}H_{16}O_5$ (Section 4.4.3.1) could be produced. The later appearance of $C_{10}H_{18}O_5$ relative to $C_{10}H_{18}O_6$ is possibly due to the competition between the peroxy termination reactions and reaction with $HO_2^{\bullet}$, as was explained for the later appearance of $C_{10}H_{16}O_6$ and $C_{10}H_{16}O_4$ relative to the other $C_{10}H_{16}O_x$ products (Section 4.4.3.1).

4.4.3.4 $C_9H_{16}O_x$ Products

The oxidation products in the $C_9H_{16}O_x$ group include; $C_9H_{16}O_3$, $C_9H_{16}O_4$, and $C_9H_{16}O_5$. The C_9 oxidation products peak much later in the reaction than initial C_{10} products, suggesting that they are not primary piperitone oxidation products, Figure 4.23. The $C_9H_{16}O_x$ products appear in the order $C_9H_{16}O_3$ followed by $C_9H_{16}O_4$ and $C_9H_{16}O_5$, Figure 4.23. It is proposed that the $C_9H_{16}O_x$ products are formed following photolysis of $C_{10}H_{16}O_3$, with some possible mechanisms shown in Figure 4.24.

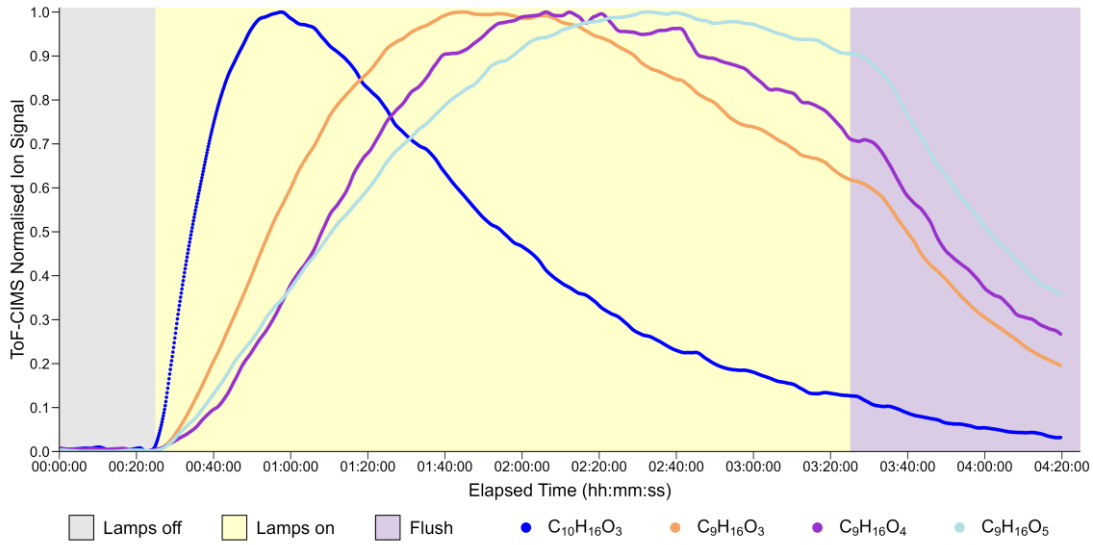

Figure 4.23 *Time series of $C_9H_{16}O_x$ products, resulting from the $OH^{\bullet}$ initiated oxidation of piperitone. Due to large differences in signal intensity between different products, each signal is normalised to one. Data not corrected for chamber losses.*

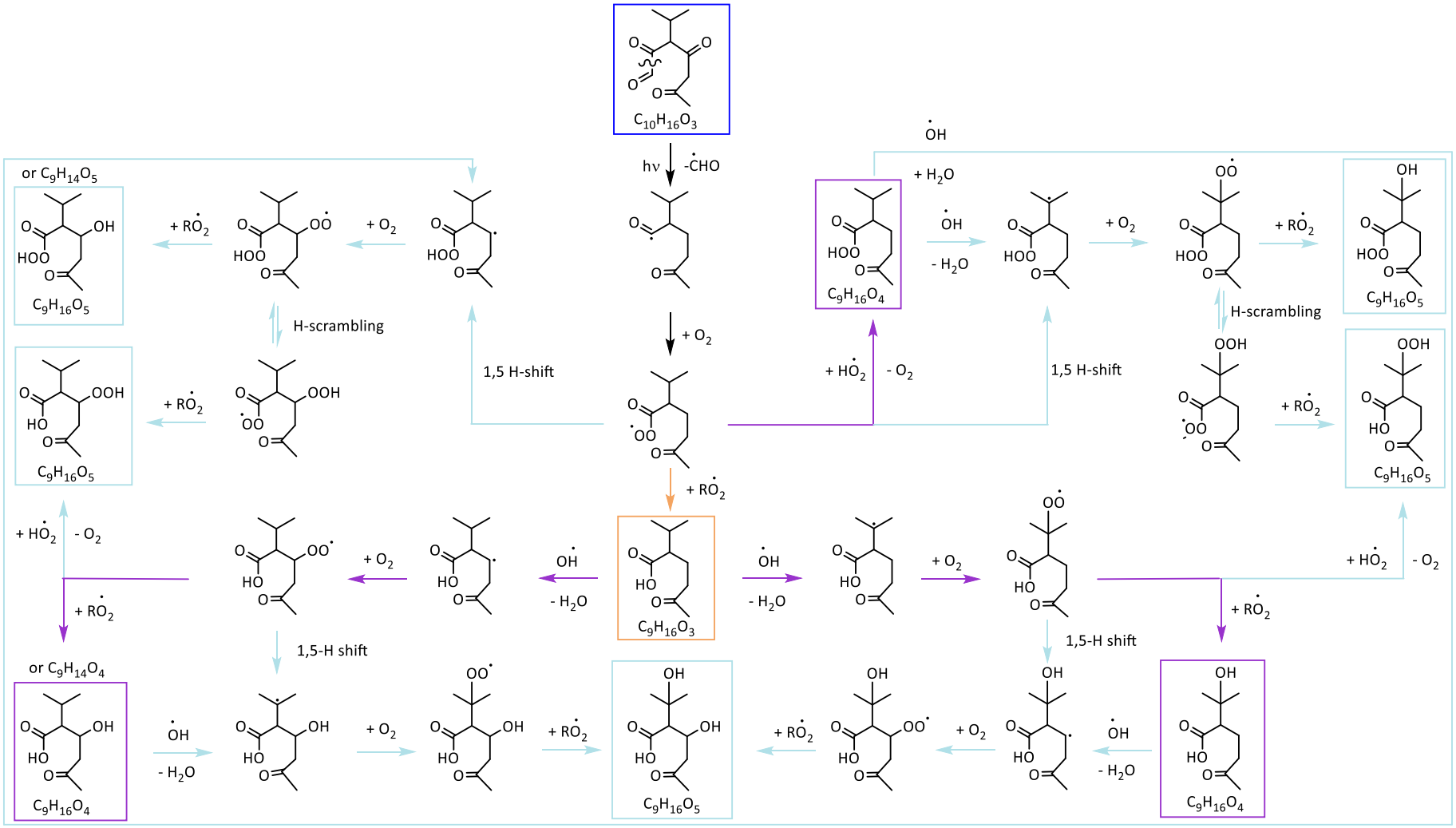

Figure 4.24 *Proposed mechanism for the formation of $C_9H_{16}O_x$ products resulting from the $OH^{\bullet}$ initiated oxidation of piperitone.*

The $C_9H_{16}O_x$ oxidation products are believed to be formed through photolysis of the keto-aldehyde $C_{10}H_{16}O_3$ primary oxidation product. Carbonyls are known to undergo photolysis[217], with aldehydes exhibiting a higher propensity to photolyse than ketones[216]. Similar to glyoxal and methyl glyoxal, the $C_{10}H_{16}O_3$ piperitone oxidation product contains an α,β-dicarbonyl group. The C-C bond between these two carbonyls is the weakest bond in the molecule, and it is the most likely to dissociate upon photolysis[255, 256]. There are several wavelength dependent photolysis pathways available[255, 257]. For glyoxal the dominant process is dissociation of the α,β-dicarbonyl bond leading to the formation of two formyl radicals ($HCO^{\bullet}$)[257]. For methyl glyoxal the main photolysis products are a formyl radical and an acetyl radical[255, 258]. The $C_{10}H_{16}O_3$ piperitone oxidation product is therefore expected to undergo photolysis in a similar manner with direct cleavage of the keto-aldehyde bond producing a formyl radical and the remaining C_9 alkyl radical (Figure 4.24, black arrow). Rapid addition of O_2 to the C_9 alkyl radical leads the formation of a C_9 peroxy radical.

$C_9H_{16}O_3$

$C_9H_{16}O_3$ was the first product $C_9H_{16}O_x$ group to peak. This product can be formed by reaction of the C_9 peroxy radical with another peroxy radical, to make a carboxylic acid, $C_9H_{16}O_3$ (Figure 4.24, orange arrow). In contrast to the $C_{10}H_yO_z$ mechanisms described above, reaction with another peroxy radical appears to be the main reaction pathway for the C_9 peroxy radical. This is likely due to the increase in peroxy radical concentration as the reaction progresses. The C_9 products appear later in the reaction, along the same timescale as $C_{10}H_{16}O_6$, $C_{10}H_{16}O_4$, $C_{10}H_{14}O_5$ and $C_{10}H_{18}O_5$ all of which are produced from peroxy radical termination reactions.

$C_9H_{16}O_4$

Three $C_9H_{16}O_4$ isomers can be produced from photolysis and subsequent oxidation of $C_{10}H_{16}O_3$, through three pathways (Figure 4.24, purple arrows). $C_9H_{16}O_4$ can be formed as a primary $C_{10}H_{16}O_3$ photolysis product via reaction of the initial C_9 peroxy radical with $HO_2^{\bullet}$ to yield O_2 and a peroxy acid with formula $C_9H_{16}O_4$.

Two $C_9H_{16}O_4$ isomers can also be formed via the oxidation of $C_9H_{16}O_3$ (Figure 4.24, purple arrows). The most likely sites for H-abstraction on $C_9H_{16}O_3$ are the di-β-ketone carbon followed by the isopropyl functionality. Following H-abstraction an alkyl radical is formed which adds O_2 to give a peroxy radical. Reaction of the peroxy radical with another peroxy radical gives an alcohol $C_9H_{16}O_4$ or in one case a ketone $C_9H_{14}O_4$ (Section 4.4.3.5) can be produced.

$C_9H_{16}O_5$

Five $C_9H_{16}O_5$ isomers can be formed as primary, secondary or tertiary $C_9H_{16}O_3$ photolysis products (Figure 4.24, light blue arrows). The formation of $C_9H_{16}O_5$ as a primary product requires the C_9 peroxy radical to undergo a 1,5-hydrogen shift from either the di-β-ketone carbon or isopropyl carbon (Figure 4.24, light blue arrows) producing an alkyl radical which contains a peroxy acid functionality. Addition of O_2 leads to the formation of a peroxy radical, which can undergo H-scrambling, and a peroxy radical termination reaction of any of the peroxy radicals yields and alcohol $C_9H_{16}O_5$, or in one case a ketone $C_9H_{14}O_5$ (Section 4.4.3.5) can be formed. While this pathway accounts for the formation of four of the $C_9H_{16}O_5$ isomers it is the least likely as the 1,5-hydrogen shift is in competition with reaction with $HO_2^\bullet$ and peroxy radical termination reactions, both of which are expected to be more prevalent later in the reaction. $C_9H_{16}O_5$ can also be produced through the same oxidation steps outlined above following H-abstraction from either $C_9H_{16}O_3$ or $C_9H_{16}O_4$.

The results suggest that the main fate of C_9 peroxy radicals is reaction with another peroxy radical. This is in contrast to the C_{10} peroxy radicals for which hydrogen shift, or reaction with $HO_2^\bullet$ were the dominant processes. The $C_9H_{16}O_x$ products are formed much later in the reaction than the C_{10} products; $C_9H_{16}O_3$, the first C_9 product peaks an hour after $C_{10}H_{16}O_3$, the first C_{10} product (Figure 4.14). At this stage into the reaction it is expected there would be a higher concentration of peroxy radicals, which makes peroxy radical termination reactions more likely, and reduces the possibility of H-abstraction or reaction with $HO_2^\bullet$.

4.4.3.5 $C_9H_{14}O_x$ Products

The oxidation products in the $C_9H_{14}O_x$ group include; $C_9H_{14}O_4$, $C_9H_{14}O_6$ and $C_9H_{14}O_5$. These products are thought to be produced via the photolysis of $C_{10}H_{14}O_4$, similar to the $C_9H_{16}O_x$ products from $C_{10}H_{16}O_3$. Figure 4.25 shows the time series of the oxidation products in the $C_9H_{14}O_x$ group, and Figure 4.26 shows their proposed formation mechanisms.

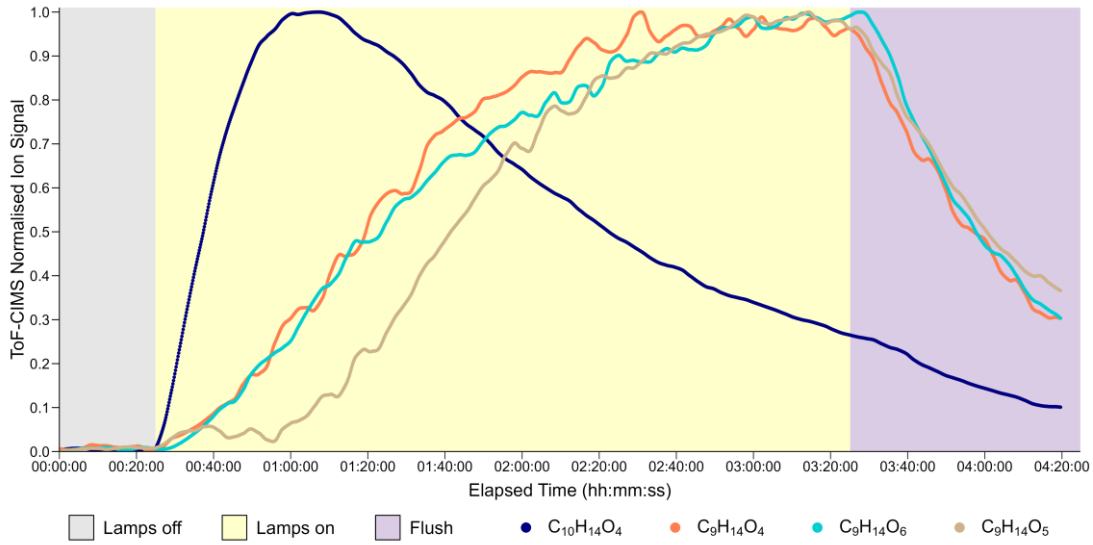

Figure 4.25 *Time series of $C_9H_{14}O_x$ products, resulting from the $OH^{\bullet}$ initiated oxidation of piperitone. Due to large differences in signal intensity between different products, each signal is normalised to one. Data not corrected for chamber losses.*

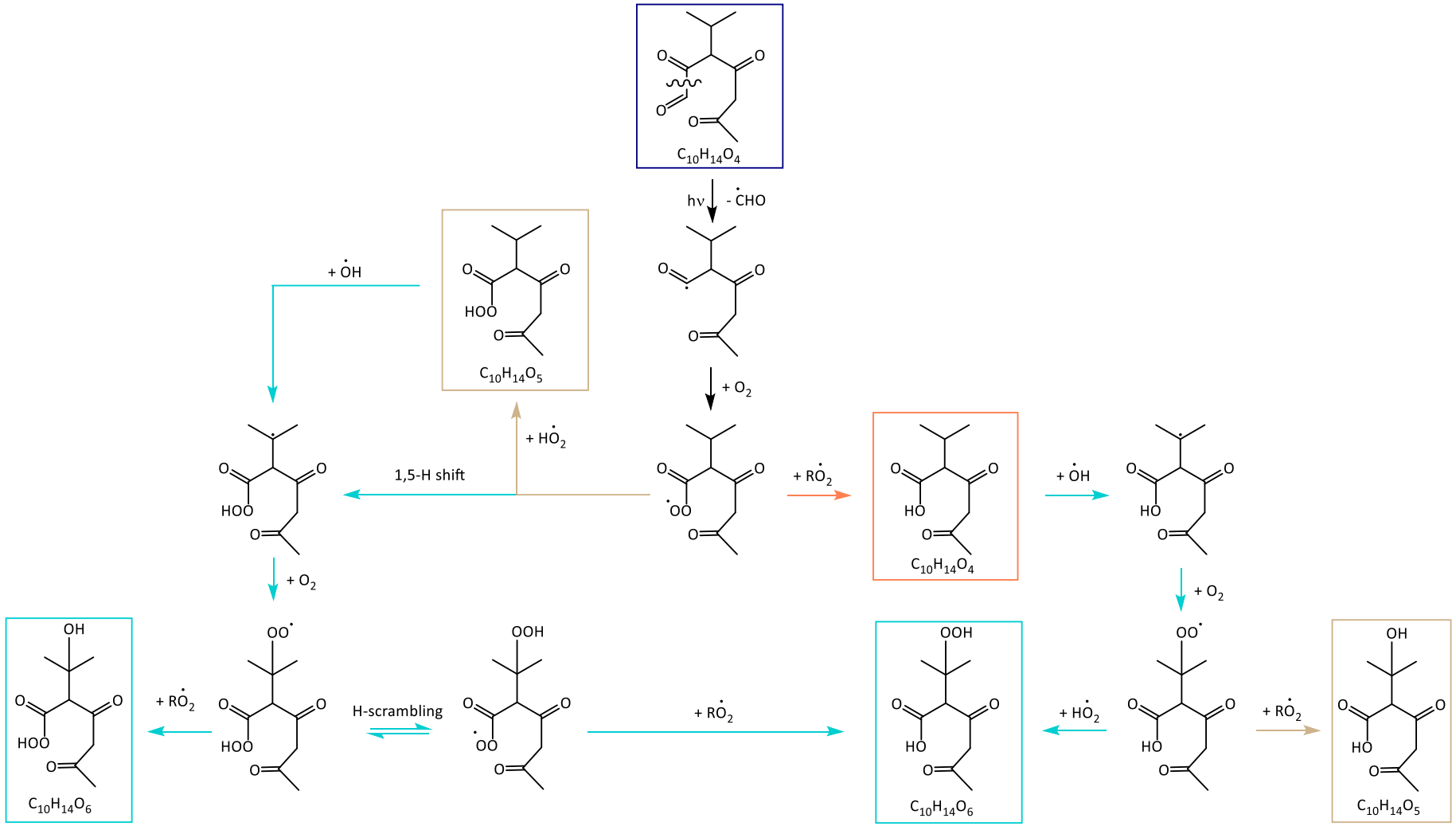

Figure 4.26 *Proposed mechanism for the formation of $C_9H_{14}O_x$ products resulting from the $OH^{\bullet}$ initiated oxidation of piperitone.*

The $C_9H_{14}O_x$ products appear quite late into the reaction (Figure 4.14) and their proposed mechanism proceeds via photolysis of the keto-aldehyde[255, 256] bond in $C_{10}H_{14}O_4$, which produces an alkyl radical (Figure 4.25, black arrow). Addition of O_2 produces a peroxy radical, which can then participate in a peroxy radical termination reaction (Figure 4.25, orange arrow), react with $HO_2^\bullet$ (Figure 4.25, beige arrow) or undergo a 1,5-hydrogen shift (Figure 4.25, turquoise arrow).

$C_9H_{14}O_4$

$C_9H_{14}O_4$ is the first product in the $C_9H_{14}O_x$ group to appear. The formation of $C_9H_{14}O_4$ (Figure 4.25, orange arrows) is via a peroxy radical termination reaction, which is expected to be more competitive than the other available pathways, due to an increase in peroxy radical concentration as the reaction progresses.

$C_9H_{14}O_6$

$C_9H_{14}O_6$ is the second product in the $C_9H_{14}O_x$ group to appear. The mechanism shows the formation pathways for two $C_9H_{14}O_6$ isomers through three pathways. $C_9H_{14}O_6$ can be formed through an autoxidation mechanism following the photolysis of $C_{10}H_{14}O_4$ (Figure 4.26, turquoise arrows), although this pathway involves a hydrogen shift which makes this formation route unlikely. The later appearance of the $C_9H_{14}O_x$ products in the reaction suggests that the fate of the peroxy radicals in this mechanism is reaction with $HO_2^\bullet$ or $RO_2^\bullet$ rather than hydrogen shift. $C_9H_{14}O_6$ can also be formed from the oxidation of either $C_9H_{14}O_4$ or $C_9H_{14}O_5$.

$C_9H_{14}O_5$

The last product in the $C_9H_{14}O_x$ group to appear is $C_9H_{14}O_5$. Figure 4.26 (beige arrows) shows the mechanisms for the formation of two $C_9H_{14}O_5$ isomers, formed either directly from the photolysis of $C_9H_{14}O_6$ or following the oxidation of $C_9H_{14}O_4$. The reason for the later appearance of $C_9H_{14}O_5$ is unclear, especially as this product can also be formed through peroxy radical reactions from the $C_9H_{16}O_x$ mechanism.

4.4.3.6 Other Products

The majority of the remaining sixteen piperitone oxidation products have a carbon content less than C_{10}. With the exception of $C_8H_{14}O_2$ and $C_7H_8O_4$, these products steadily increase over the course of the reaction, implying they are produced through multiple fragmentation reactions of piperitone and its reactive oxidation products. $C_8H_{14}O_2$ and $C_7H_8O_4$ can be produced through the same reaction mechanism, involving H-abstraction by $OH^{\bullet}$ from the tertiary carbon α to the keto-aldehyde functionality on $C_{10}H_{16}O_3$. Following the addition of O_2, reaction with a peroxy radical produces an alkoxy radical. Decomposition producing a carbonyl will cause fragmentation, resulting in the formation of $C_8H_{14}O_2$ and a glyoxoyl radical, or $C_7H_8O_4$ and an alkyl radical. The single C_{14} oxidation product is likely formed through the dimerisation of two peroxy radicals.

4.4.4 Particle Formation

The SMPS was connected to the chamber during the $OH^{\bullet}$ initiated piperitone oxidation experiments to monitor the formation and growth of particles. Particle number and mass concentrations varied between the six experiments: particle number ranged from 3,800 cm^{-3} to 5,500 cm^{-3}, and particle mass number ranged from 3.6 µg m^{-3} to 5.3 µg m^{-3}. This variation is likely due to uncertainties regarding the complete transfer of piperitone into the chamber. This was deemed to have little consequence as the time series profiles were near identical across all experiments. The data shown in Figure 4.27 is from one experiment, which is at the maximum of the particle number and mass ranges, and is representative of all experiments. The data has been corrected for chamber losses.

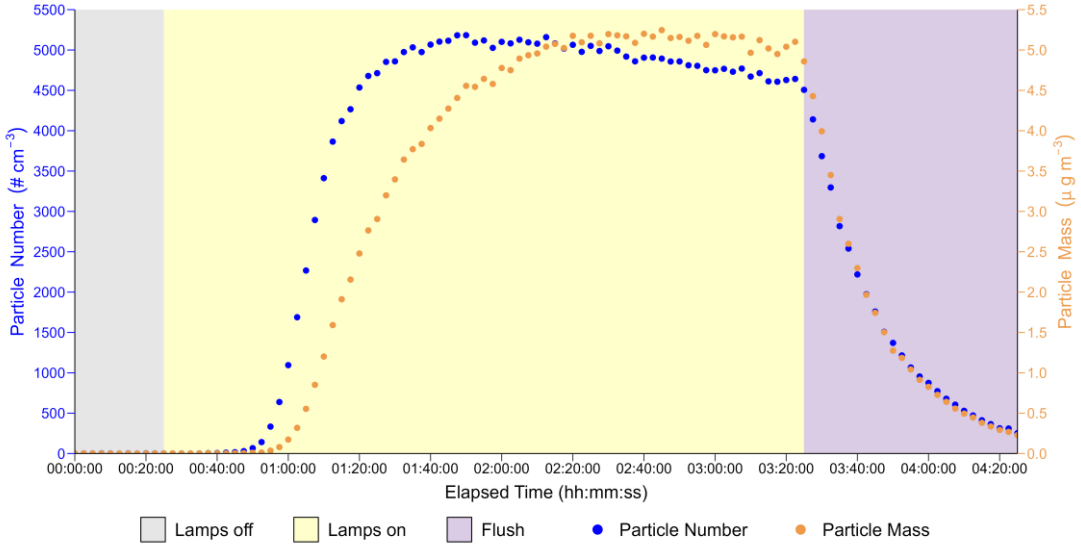

Figure 4.27 *Number and mass concentration time series profiles during an OH• initiated piperitone oxidation experiment. Data corrected for chamber losses.*

For all experiments particle formation commenced approximately 30 minutes after the start of the reaction (Figure 4.27). The particle number concentration increased rapidly, due to partitioning of low volatility piperitone oxidation products from the gas-phase to the particle-phase, leading to new particle formation[259]. This continued for around 50 minutes, reaching a maximum number concentration of 5,500 cm^{-3}. At this point there appeared to be a sufficient number of particles for condensation onto pre-existing particles[259] to outcompete new particle formation. This in combination with coagulation led to a decrease in particle number concentration for the remainder of the reaction.

The mass concentration exhibited a slower increase than the number concentration (Figure 4.27). For the initial 40 minutes there was a near linear increase in particle mass, after which the rate of increase slowed. This is likely due to the nature of the condensing species. In order for new particle formation to occur, the volatility of the condensing compound needs to be quite low[150, 259]. Once a sufficient particle concentration is present, condensation onto a pre-existing surface becomes competitive[150]. The volatility required for condensation onto a pre-existing surface, is higher than that for new particle formation to occur[259]. This results in less volatile compounds starting to condense onto the particles. These compounds are less

oxidised and therefore have a lower mass than the initial new particle forming compounds. The lower increase in mass from condensation, relative to new particle formation is what causes the slower overall increase in particle mass concentration. The continued increase in mass following the decrease in number concentration is due to particle coagulation and condensation of any newly formed low volatility products. Particle mass concentration reached a maximum of 5 µg m^{-3} approximately 100 minutes after reaction initiation, and remained stable thereafter.

Figure 4.28 shows the particle growth during the experiment. During the first few minutes of particle formation, several hundred particles were formed with a diameter of approximately 40 nm to 50 nm. As the reaction progressed condensation onto smaller particles and coagulation led to particle growth. The median particle diameter grew to a maximum of approximately 100 nm, after 90 minutes of growth.

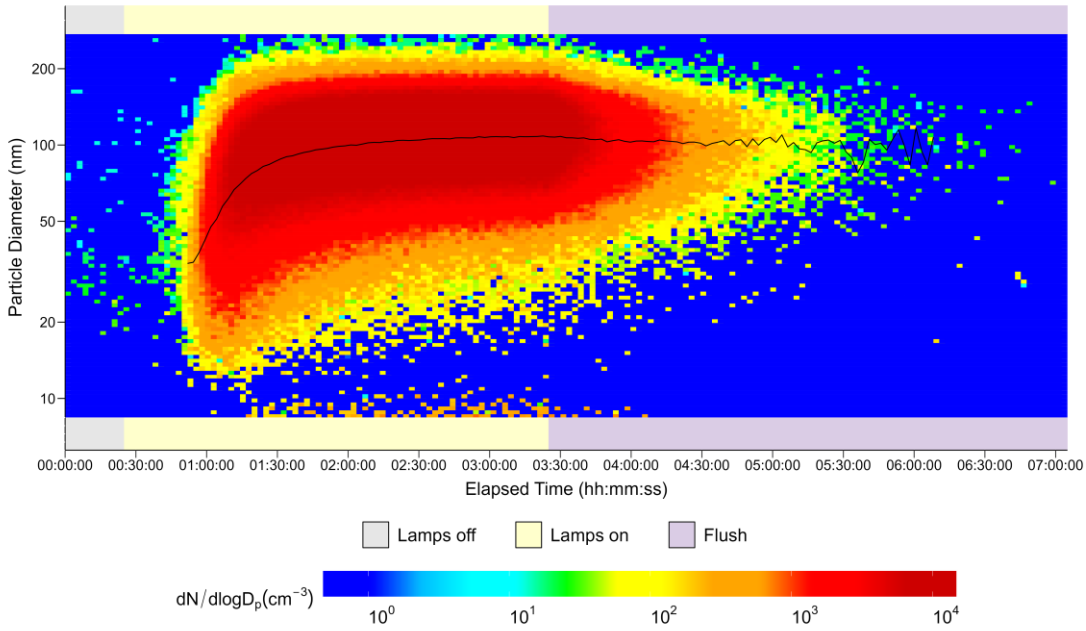

Figure 4.28 *Banana plot showing particle growth during an $OH^{\bullet}$ initiated piperitone oxidation experiment. Black line represents median diameter. Data corrected for chamber losses.*

Compositional analysis of the particle-phase was not possible to due difficulties in operating the FIGAERO.

4.5 Conclusions

A series of simulation chamber experiments have been conducted to evaluate the kinetics, products and mechanisms for the $OH^{\bullet}$ initiated oxidation of piperitone. A mean value of k_{OH}(piperitone) = 9.93 ($\pm$ 1.24) $\times$ 10^{-11} cm^3 $molecule^{-1}$ s^{-1} was obtained using the relative rate method with three reference compounds, 1,3,5-TMB, isoprene and 1-MCH. Since this is the first determination of the rate coefficient, comparison with literature is not possible, however, there is very close agreement (within 6%) with the value calculated using the SAR approach[207, 208]. SAR methods were also used to determine the values k_{O_3}(piperitone)[209] = 1.4 $\times$ 10^{-16} cm^3 $molecule^{-1}$ s^{-1} and k_{NO_3}(piperitone)[210, 239] = 1.79 $\times$ 10^{-13} cm^3 $molecule^{-1}$ s^{-1}. Using standard average concentrations for each of the three oxidants, the piperitone tropospheric lifetimes for reaction with $OH^{\bullet}$, O_3 and $NO_3^{\bullet}$ were estimated to be 1.7 hours, 81.1 hours and 3.1 hours, respectively. This suggests that $OH^{\bullet}$ and $NO_3^{\bullet}$ could contribute to the chemical removal of piperitone from the troposphere, however experimental determination of k_{O_3}(piperitone) and k_{NO_3}(piperitone) are necessary to confirm this. Furthermore, while reaction with $NO_3^{\bullet}$ could be important in polluted air masses containing NO_x, it is unlikely to occur to a large extent in remote forest environments[260].

Experiments performed in the chamber indicated that piperitone was slowly photolysed with a value of J(piperitone) = 5.8 ($\pm$ 0.21) $\times$ 10^{-6} s^{-1}obtained using all the UVA and UVB lamps. It is not possible to accurately extrapolate these results to determine accurately the value of J(piperitone) under real atmospheric conditions and further work e.g. to measure the gas-phase UV absorption spectrum and perform chamber experiments using real sunlight[220], could be useful in assessing the importance of this degradation pathway.

Thirty-three oxidation products were identified in a series of chamber experiments to identify the main oxidation products from the reaction of piperitone with $OH^{\bullet}$ in the absence of NO_x. The carbon number of the products ranged from C_5 to C_{14}, with the majority being C_9 and C_{10} compounds. The oxygen content of the products varied

between O_2 and O_7, with O_4 products dominating. Oxidation mechanisms were derived for seventeen products which were allocated to groups such that all products in a group shared the same initial formation steps.

The SAR method identified $OH^{\bullet}$ addition to the alkene functionality on piperitone as being the dominant initiating step in the oxidation process, with H-abstraction from the isopropyl carbon and β-ketone carbon as minor pathways.

The first oxidation product produced from the $OH^{\bullet}$ reaction with piperitone was $C_{10}H_{16}O_3$. The proposed formation mechanism is $OH^{\bullet}$ addition to the alkene functionality on piperitone, followed by O_2 addition, and decomposition. The four other products, $C_{10}H_{16}O_5$, $C_{10}H_{16}O_7$, $C_{10}H_{16}O_6$ and $C_{10}H_{16}O_4$ that make up the $C_{10}H_{16}O_x$ group, are also formed via the same initial reaction pathway, followed by hydrogen shifts and termination reactions with $HO_2^{\bullet}$ and $RO_2^{\bullet}$.

The second product to be identified from the $OH^{\bullet}$ initiated oxidation of piperitone was $C_{10}H_{14}O_4$. The proposed mechanisms for the formation of this product involved H-abstraction from the isopropyl carbon or β-ketone carbon, followed by a range of possible oxidation, isomerisation and radical termination reactions. The other products in the $C_{10}H_{14}O_x$ group, $C_{10}H_{14}O_6$ and $C_{10}H_{14}O_5$ are also formed from the same initial pathways.

The final primary piperitone oxidation product to appear during the reaction was $C_{10}H_{18}O_4$. This was the first product in the $C_{10}H_{18}O_x$ group to appear, followed by $C_{10}H_{16}O_6$ and $C_{10}H_{18}O_5$. The formation mechanism for the products in the $C_{10}H_{18}O_x$ group is also $OH^{\bullet}$ addition to the C=C bond, but involves reaction with $HO_2^{\bullet}$. All $C_{10}H_{18}O_x$ products retain the C_6 ring.

Two groups of C_9 oxidation products were identified, $C_9H_{16}O_x$ and $C_9H_{14}O_x$. These products cannot be formed directly from the oxidation of piperitone, and it is proposed that they are produced through the photolysis of $C_{10}H_{16}O_3$ and $C_{10}H_{14}O_4$

primary piperitone oxidation products, both of which possess an α,β-keto-aldehyde functionality, that is highly susceptible to photolysis.

SOA formation was observed in all of the experiments on the $OH^{\bullet}$ initiated oxidation of piperitone. Particle formation commenced approximately 30 minutes after reaction initiation. The particle number increased quickly, reaching a maximum of between 3,800 cm^{-3} and 5,000 cm^{-3} after 50 minutes. Particle mass increased at a slower rate, reaching a maximum, of between 3.6 $\mu g\ m^{-3}$ and 5 $\mu g\ m^{-3}$, 100 minutes after the onset of oxidation. Initially high concentrations of small particles, with diameters less than 50 nm were formed, which grew to have a final diameter of around 100 nm. Future work for the particle-phase includes repetition of the experiments with the use of the FIGAERO, to enable characterisation of the compounds in the particle-phase.

Chapter 5: Spruce 1 Emissions Oxidation

5.1 Introduction

Globally it is estimated that a total of 0.5×10^{15} g C year^{-1} to 1×10^{15} g C year^{-1} are emitted into the atmosphere as BVOCs[26, 261, 262]. These estimates are likely lower limits as they only account for the emissions of traditional BVOCs including isoprene, monoterpenes, sesquiterpenes and well-characterised oxygenated BVOCs such as GLVs (Green Leaf Volatiles). Once emitted into the atmosphere BVOCs can undergo gas-phase reactions producing a range of oxidation products, some of which can lead to the formation of SOA, and can influence local climate[263]. The composition of the SOA and thus the climate impacts are determined by the nature of the emitted BVOCs[176]. Multiple experimental approaches have been employed to assess BVOC atmospheric reactivity and to determine their SOA formation potential.

5.1.1 BVOC Oxidation Experiments

The simplest type of BVOC oxidation experiments involve the oxidation of a single model compound with a single oxidant using atmospheric simulation chambers or flow tube reactors. These types of experiments have been conducted for the majority of the main BVOCs including isoprene[96], monoterpenes[264], sesquiterpenes[265], as well as some BVOC oxidation products[242, 266]. Single component experiments are useful for determining the specific products generated from the oxidation of a single BVOC, as well as the potential for SOA formation and associated impacts on climate. While single component BVOC oxidation experiments are the simplest to perform, the results may lead to inaccurate conclusions regarding natural atmospheric processing[60, 184], as the atmosphere is a complex mixture of BVOCs and oxidants, with different reactivities and physiochemical properties leading to the production of various oxidation products which are likely to interact.

Multicomponent oxidation experiments are better able to replicate ambient atmospheric oxidation. The most common type involves the use of multiple oxidants[267, 268], particularly $OH^{\bullet}$ and O_3. Experiments have also been carried out using multiple BVOC reactants[267, 269]. Studies assessing multicomponent oxidation reactions find that the oxidation product distribution can vary significantly from that

of the single component system, and lead to an enhancement or reduction in SOA formation[269, 270]. For example, the SOA produced from the oxidation of α-pinene by $OH^{\bullet}$ is greatly suppressed in the presence of isoprene. This is due to several factors: the competition between α-pinene and isoprene for reaction with $OH^{\bullet}$, which leads to a reduction in the extent of α-pinene oxidation; and α-pinene peroxy radicals undergoing termination reactions with isoprene peroxy radicals, producing C_{11} to C_{15} oligomers and hindering the formation of less volatile C_{16} to C_{20} α-pinene dimers[267]. The findings from multicomponent reactions are likely to have greater similarities with ambient oxidation than their single component counterparts. Despite this, the simultaneous oxidation of two or three BVOCs is unlikely to accurately replicate atmospheric processing of naturally emitted BVOCs, as many plants emit numerous BVOCs in significant concentrations[151, 271].

Several BVOC oxidation experiments have been carried out using the emissions from real trees. In most cases this involves transferral of the BVOC emissions into an atmospheric simulation chamber[145, 272] over several hours, or collection of BVOCs onto adsorbent tubes, which are then desorbed into a reactor[184]. Real BVOC emissions oxidation experiments are difficult to perform as several factors must be considered. The plant under investigation must be kept under controlled temperature and PPFD conditions for the duration of the experiments, to limit changes in the BVOC emission profile[6, 26]. The foliage used to supply the BVOC emissions for the oxidation experiments must be isolated and supplied with pure air[145, 273]. Where possible the BVOC emission profile should be monitored regularly to identify any changes in the composition or fluxes[73, 145]. Consideration should also be given to the number and type of plants under investigation. Experiments involving the use of multiple plant species[181] should aim to use plants that are found in the same environments. Different plant combinations have been observed to result in significantly different oxidation product distributions, leading to changes in the overall SOA produced[45].

Experiments designed to investigate the atmospheric oxidation of BVOC emissions from plants should aim to replicate the naturally-occurring processes as closely

possible, however this is not always the case. There is concern regarding the placement of enclosures around plants altering the natural emission profile[148], and whether laboratory plants behave the same as plants in their natural environment[69]. Despite this, experiments conducted on real BVOC emissions are more representative of ambient oxidation than either single component or multicomponent oxidation experiments.

Comparison between the gas-phase products and SOA generated from the oxidation of model compounds and real plant emissions is essential for understanding how well the oxidation of model compounds represents ambient oxidation of real plant emissions. This is of particular importance for modelling studies, as it provides guidance regarding the number of VOCs that should be taken into consideration to accurately account for VOC oxidation and SOA formation in the atmosphere.

5.1.2 SOA Volatility

Volatility is a key parameter in determining whether an oxidised compound will remain in the gas-phase or partition into the particle-phase, leading to the formation of SOA. Thermal desorption techniques are used to determine the saturation vapour pressure of a compound[274]. Saturation vapour pressure is often used to indicate the volatility at which a compound partitions to the particle-phase however, measurement is challenging, with significant differences between values obtained using different methods[113].

In SOA studies involving the use of a FIGAERO coupled to a ToF-CIMS, it is possible to determine the volatility of the compounds in the particle-phase. During a desorption cycle, heated N_2 is passed over the filter to thermally desorb the particles[111]. The temperature range over which a compound desorbs from the filter is related to its chemical and physical properties[111]. The temperature of maximum desorption (T_{max}) is the temperature at which the desorption signal is maximised, and can be used to infer the volatility[68, 113], chemical or physical state[275] and the enthalpy of

sublimination[111] of the compound. Determining the volatility of compounds in the particle-phase is of particular interest as it can be used to indicate the point at which gas-to-particle partitioning occurs[274], and allows compounds to be grouped according to volatility class[68, 276].

The saturation vapour concentration, C° in μg m^{-3}, is the saturation concentration of a vapour over a pure liquid, and C^{*} is the saturation vapour concentration over a mixture[277], and is temperature dependent. Volatility can be described by grouping C^{*} into so-called volatility bins, which correspond to C^{*} values over a single order of magnitude. The sequential arrangement of volatility bins generates a volatility basis set (VBS)[277]. The assignment of a compound to a volatility bin facilitates in the determination of its atmospheric fate.

5.1.3 Aims

The aims of the work in this chapter were to investigate the atmospheric reactivity of Sitka spruce BVOC emissions with $OH^{\bullet}$.

The first aim was to determine the bulk properties of all oxidation products in both the gas-phase and particle-phase, and to estimate the volatility of the particle-phase products.

The second aim was to identify the main gas-phase and particle-phase oxidation products from the reaction of Sitka spruce BVOC emissions with $OH^{\bullet}$ and to compare them with literature and the results reported in Chapter 4, to identify their precursor BVOCs.

The third aim was to assess the particle formation and growth from the oxidation of Sitka spruce emissions and to determine the SOA yield.

5.2 Experimental Methods and Analysis

5.2.1 Materials and Instrumentation

Experiments on the $OH^{\bullet}$ initiated oxidation of Sitka spruce emissions were performed using the atmospheric simulation chamber at the ERI (Chapter 2). During an oxidation experiment the chamber was operated in batch mode[18], with a continuous inflow of 10 L min^{-1} to compensate for instrument sampling.

The BVOC emissions from Spruce 1 (Chapter 3) were used for all emissions oxidation experiments. H_2O_2 (Sigma Aldrich, 50% aqueous solution) was used to generate $OH^{\bullet}$ under low NO_x conditions.

Spruce 1 was housed in a plant growth chamber (Chapter 3) for the duration of the oxidation experiments, with the top portion of the tree surrounded by an enclosure made of FEP Teflon foil (Chapter 3). Spruce 2 and Spruce 3 were also in the plant growth chamber, but their emissions were not used in the oxidation experiments. The Empty enclosure was also present, and was used for blank experiments. The plant growth chamber settings were a repeating 24-hour cycle of 14 hours at PPFD 44 µmol m^{-2} s^{-1} and temperature 24 °C, and 10 hours of darkness at 18 °C.

The enclosures were supplied with dry compressed air which was humidified by bubbling through Milli-Q water. Prior to an experiment the outflow from an enclosure was connected to the chamber via a 6 m length of ½" outer diameter PFA Teflon tubing.

During the experiments the ToF-CIMS (Chapter 2) was used to monitor the evolution of VOCs in the gas-phase and particle-phase. Experiments were performed using the ToF-CIMS with $C_6H_6^+$ as the reagent ion, produced from a benzene permeation tube, to monitor the decay of the Spruce 1 emissions. The voltages and pressures applied to the ToF-CIMS were selected based on optimal tuning performed on 11/07/2021. The ToF-CIMS inflow was sub sampled and passed through a glass tube containing the internal mass calibrant trichlorobenzene (Sigma Aldrich, purity 99%), before

joining the remainder of the inflow at the ToF-CIMS inlet. The trichlorobenzene was replaced with a fresh sample weekly.

The experiments were repeated with the ToF-CIMS using I^- as the reagent ion, to monitor the formation of gas-phase oxidised products and to determine the composition of the particle-phase. The voltages and pressures were selected as per tuning conducted on 08/12/2020. For experiments conducted with the ToF-CIMS in I^- mode, the gas-phase inlet of the ToF-CIMS was replaced with the FIGAERO, allowing for simultaneous gas-phase and particle-phase sampling.

An SMPS (Chapter 2) was connected to the chamber during the experiments to characterise the SOA produced. The SMPS was operated with a 10 L min^{-1} sheath flow and a sample flow of 1 L min^{-1}. The voltage was scanned twice per sample over 50 s with a 10 s purge, measuring particles with geometric diameters between 7.5 nm and 273.8 nm. The two scans were averaged to give a single sample measurement every 2.5 minutes. The SMPS was connected to the chamber with a 1 m length of ¼" outer diameter stainless steel tubing.

5.2.2 Experimental Procedure

The Spruce 1 enclosure and Empty enclosure were supplied with humidified compressed air at a flow rate of 10 L min^{-1}. Depending on the degree of sealing of the enclosure, the outflow varied between 6 L min^{1} and 7 L min^{-1}. The BVOC emissions from Spruce 1 were transferred into the chamber over approximately 16 hours, which included the 14 hours with the plant growth chamber under illumination.

For experiments with the ToF-CIMS in I^- mode the FIGAERO inlet was used. Prior to commencing an experiment, a filter background measurement was performed to identify any compounds inherent to the filter. The filter was subject to the 35-minute desorption cycle (Chapter 2). The FIGAERO was not used for experiments with the

ToF-CIMS in $C_6H_6^+$ mode, as the $C_6H_6^+$ reagent ion is not suitable for detecting highly oxidised compounds which are expected to be in the particle-phase.

Prior to commencing an experiment, the inflow to the chamber from either the Spruce 1 enclosure or the Empty enclosure was supplemented with humidified compressed air, increasing the total inflow to 10 L min^{-1}. Initially the ToF-CIMS was used to measure a background of the chamber for 30 minutes. Following background measurement, dry compressed air was passed over H_2O_2 (10 µL) in a glass vessel, to carry it into the chamber. After oxidant addition the fan was turned on for a maximum of 30 s to ensure homogenisation throughout the chamber[38, 246]. All lamps were turned on 30 minutes after homogenisation to initiate oxidation via the formation of $OH^{\bullet}$ produced from H_2O_2 photolysis. The oxidation of the Spruce 1 BVOC emissions was allowed to proceed for 4 hours before flushing. All instrumentation was connected to the chamber for the duration of the experiment.

For experiments conducted with the FIGAERO inlet on the ToF-CIMS, particles were collected onto a 25 mm PTFE filter[113, 276] (pore size 1 µm, Zefon International Inc, USA). Particle collection commenced after the particle mass, as measured by the SMPS, had maximised. Particles were collected at a flow rate of 2.5 L min^{-1} until approximately 0.5 µg (determined from SMPS measurements) had been collected onto the filter[176].

The 35-minute desorption cycle was applied to the filter to enable analysis of the particle-phase. After each sample desorption the filter was cleaned by repeating the 35-minute desorption cycle, allowing the filter to be reused.

Two Sitka spruce emission photolysis experiments and a single blank photolysis experiment were performed with the ToF-CIMS in each mode. Blank experiments were performed to ensure the identified oxidation products were not artefacts. For blank experiments the outflow from the Empty enclosure was used to supply the chamber. The experimental procedure was the same as for the spruce emissions oxidation experiments.

Photolysis experiments were also conducted with the Sitka spruce emissions, to ensure products identified from $OH^{\bullet}$ oxidation were not due to photolysis. The procedure for photolysis experiments was the same as described above without the addition of H_2O_2 to the chamber. For each ToF-CIMS mode three Sitka spruce emissions experiments and two blank experiments were performed.

5.2.3 Data Analysis

5.2.3.1 ToF-CIMS

Calibrations

To quantify the concentrations of BVOC reactants in the chamber the same calibration coefficients determined for δ-3-carene, β-myrcene, camphor and piperitone, as described in Chapter 3 were used.

Experiments involving 4-methyl catechol and H_2O_2 were conducted to determine the steady state $OH^{\bullet}$ concentration in the chamber. The decay of 4-methyl catechol was monitored with the ToF-CIMS in I^- mode, and was assumed to follow a pseudo first order decay, due to reaction with $OH^{\bullet}$ only. A straight line plot of $\ln\left(\frac{[4-methyl\ catechol]_0}{[4-methyl\ catechol]_t}\right)$ as a function of time, with slope[184] equal to $\frac{[OH^{\bullet}]}{k_{4-\text{methyl catechol}}}$ was attained. The steady state $OH^{\bullet}$ concentration in the chamber was determined using k_{OH}(4-methyl catechol)[44] = 1.56×10^{-10} cm^3 $molecule^{-1}$ s^{-1}. The procedure was repeated for various H_2O_2 concentrations and a linear calibration plot was generated. All experiments were conducted with 10 µL H_2O_2, which corresponded to an $OH^{\bullet}$ concentration of 1.25×10^7 molecules cm^{-3}.

ToF-CIMS Data Analysis

ToF-CIMS gas-phase and particle-phase data were analysed with Tofware 3.2.0, operated through IGOR Pro 7.08. Initially 1 Hz data was averaged to 10 s time resolution. Following this, a mass calibration was performed. For experiments with

the ToF-CIMS in $C_6H_6^+$ mode $C_6H_6^+$ (*m/z* 78.05), $C_6H_3Cl_3^+$ (*m/z* 179.93), $C_{12}H_{23}N_2O_2^+$ (*m/z* 227.18), $C_{12}H_{21}N_2O_2^+$ (*m/z* 241.15) and $C_{18}H_{22}N_2O_2^+$ (*m/z* 303.21) were used. The C_{12} and C_{18} ions are benzene clusters with $C_6H_{11}NO$, the contaminant in the N_2 supply. For experiments with the ToF-CIMS in I^- mode NO_3^- (*m/z* 61.99), $I.H_2O^-$ (*m/z* 144.92), I_2O^-(*m/z* 269.80), I_3O^- (*m/z* 398.71) and I_4HNO^- (*m/z* 538.62) were used. The remaining data analysis steps included correction of the baseline position, peak shape and peak resolution. Following calibration, chemical formulae were assigned to peaks within the calibrated mass range. Only formulae containing the elements C, H, O and N (and Cl for experiments with the ToF-CIMS in $C_6H_6^+$ mode, and I for experiments with the ToF-CIMS in I^- mode) were assigned. If an appropriate formula could not be assigned, the peak was left unassigned.

After completing peak assignment, the remainder of the analysis was performed using R Studio 4.0.2. Initially all signals were normalised to the reagent ion signal ($C_6H_6^+$ or I^-). The data were then filtered to isolate only signals corresponding to significant reactants and products. Initially, filtering involved the removal of unassigned and calibrant signals, and for experiments with the ToF-CIMS in I^- mode, signals not clustered with I^- were removed.

During the experiments conducted with the ToF-CIMS in $C_6H_6^+$ mode, an external interference was observed to significantly increase the intensity of $C_{10}H_{15}^+$ at varying stages during the experiments. It also impacted the time series profiles of multiple other ions. The source of $C_{10}H_{15}^+$ was not identified. To maintain uniformity across all experiments with the ToF-CIMS in $C_6H_6^+$ mode, only data recorded until 75 minutes after illumination was used in the analysis.

Spruce reactants were identified from experiments conducted with the ToF-CIMS in $C_6H_6^+$ mode. A Welch T-test was performed comparing the concentrations prior to and following illumination. The period during illumination was scaled by 1.5, and only signals with a P-value below 0.05 were retained. A further Welch T-test was carried out to compare the ion signal intensities prior to illumination between the spruce emissions oxidation experiments and the blank experiments. Signals with a P-value

less than 0.05 when compared with 1.5 times the ion concentration of the blank experiments were retained as statistically significant reactants. The agreement between the identified reactants in the Spruce 1 emissions was verified by comparison with the results presented in Chapter 3.

Gas-phase oxidation products were identified from experiments conducted with the ToF-CIMS operated in both modes. A Welch T-test was performed comparing the ion signal intensities prior to and following illumination. The period prior to illumination was scaled by 1.5, and only signals with a P-value below 0.05 were retained. Another Welch T-test was carried out to compare the intensity of the ion signals during illumination between the spruce emissions oxidation experiments and the blank experiments. Signals with a P-value less than 0.05 when compared with 1.5 times the ion concentration of the blank experiments were retained as statistically significant gas-phase oxidation products.

The filtering process for the particle-phase involved the use of a Welch T-test to identify ions with a P-value below 0.05, when compared with 1.2 times the filter background, recorded prior to the experiment. The ion signal concentrations were then normalised to the mass collected on the filter. A further Welch T-test was conducted using the mass normalised ion signals from the spruce oxidation experiments compared with 1.2 times the mass normalised ion concentrations from the blank experiments. Signals with a P-value below 0.05 were removed. Further filtering was conducted to remove noisy and highly scattered signals.

Volatility Determination

The volatility of the products in the particle-phase was determined from volatility calibrations, performed by a colleague (Niall O'Sullivan) using a series of polyethylene glycols (PEGs); tetraethylene glycol, pentaethylene glycol, hexaethylene glycol and octaethylene glycol (Sigma Aldrich, purity >99%, 89%, 97%, and >95%, respectively).

A clean filter was placed into the FIGAERO and filter background was recorded using the 35-minute desorption cycle. A 2 µL aliquot of one of the PEGs was then spotted

onto the filter with a syringe[113, 276], and a 35-minute desorption cycle was performed. This procedure was repeated for all PEGs a minimum of five times.

A value for T_{max} was determined for each PEG calibration, and an average T_{max} for each PEG calibrant was calculated. A calibration plot of literature vapour pressure, at 298 K, as a function of T_{max} displayed a logarithmic relationship. The equation describing the relationship between literature vapour pressure and T_{max} was used to determine the vapour pressures of the Spruce 1 oxidation products using their measured T_{max} values.

Vapour pressures were then converted to saturation vapour concentrations (C^*), using Equation 5.1.

$$C^* = \frac{VP \times Mw \times 10^6}{R \times T} \qquad \textbf{\textit{Equation 5.1}}$$

Where: C^* is the saturation vapour concentration of the product, in µg m^{-3}; VP is the vapour pressure of the product at 298 K in J m^{-3}, determined from the PEG calibration plot using T_{max}; Mw is the molecular weight of the product in g mol^{-1}, R is the universal gas constant, 8.314 J K^{-1} mol^{-1}; and T is the temperature in K that the literature vapour pressures for the PEGs were measured at.

5.2.3.2 SMPS

A correction was applied to the SMPS number concentration data to account for chamber losses (wall, dilution and sampling), using size bin specific loss coefficients. The size bin specific coefficients were determined from chamber losses experiments performed using ammonium sulfate seed, assuming that chemical composition has a negligible impact on particle deposition. A density[122] of 1.3 g cm^{-3} was used to calculate the particle mass from the chamber losses corrected particle number.

5.2.3.3 Calculations

OH• Exposure

The effective OH• exposure experienced by the emissions was determined from the OH• concentration and the duration of the experiment, Equation 5.2[184, 205].

$$Exposure_{OH\bullet} = \frac{\left(\int_0^t [OH^\bullet]\right)}{[OH^\bullet]_a} \qquad \textit{Equation 5.2}$$

Where: $Exposure_{OH\bullet}$ is the equivalent time in hours that the BVOC emissions would be exposed to OH• for under ambient atmospheric conditions; $\int_0^t [OH^\bullet]$ is the total OH• concentration integrated over the duration of the experiment; and $[OH^\bullet]_a$ is the ambient atmospheric OH• concentration, 1.6×10^6 molecule cm^{-3} was used[27].

SOA Yield

The total reactant BVOC concentration in the chamber was determined and used to calculate the SOA yield, according to Equation 5.3[68].

$$Yield_{\mathrm{SOA}} = \frac{\Delta m}{\Delta BVOC} \qquad \textit{Equation 5.3}$$

Where: $Yield_{\mathrm{SOA}}$ is the yield of SOA mass from the oxidation of Spruce 1 BVOC emissions; Δm is the change in SOA mass during the experiment; and $\Delta BVOC$ is the change in mass concentration of reactant BVOCs emitted from Spruce 1 during the experiment.

5.3 Results and Discussion

5.3.1 Experimental Conditions

A series of $OH^{\bullet}$ oxidation experiments under low NO_x conditions was conducted using the BVOC emissions from Spruce 1 during June and July 2021, several months prior to emissions characterisation (Chapter 3). All experiments were conducted under similar initial reaction conditions and the time series profiles obtained in each ToF-CIMS ionisation mode were found to be nearly identical. As a result, the experiment with the clearest signals was selected for the detailed analysis described below. The steady state $OH^{\bullet}$ concentration in the chamber during the experiments was 1.25 x 10^7 molecule cm^{-3}. Over the 4 hours of the oxidation experiment, this corresponded to an effective $OH^{\bullet}$ exposure of 30 hours. Comparison of the results from the $OH^{\bullet}$ oxidation experiments with the photolysis experiments found that the influence of photolysis on the $OH^{\bullet}$ oxidation experiments was negligible.

Although forty-nine BVOCs were detected in the emissions from Spruce 1, only eight of these transferred into the chamber at concentrations high enough for the $C_6H_6^+$ ToF-CIMS to detect, and underwent a significant decay upon reaction with $OH^{\bullet}$, and were therefore classified as reactants. This is somewhat expected as many of the BVOCs emitted by Spruce 1 had quite low emission fluxes and would not have been expected to be detected. Also, thirty-three of the BVOCs emitted from Spruce 1 were oxygenated compounds and their ToF-CIMS signals may have experienced interference from oxidation products, causing the signals to increase which prevented their identification as “reactants”. The initial concentrations obtained for the eight BVOCs identified as reactants are provided in Table 5.1. The BVOC reactants were not detected by the ToF-CIMS when I^- was used as the reagent ion, and for these experiments it is assumed that the BVOC reactant concentrations were in the same range as those presented in Table 5.1.

Table 5.1 *Summary of initial reactant BVOC conditions prior to oxidation, for experiments with the ToF-CIMS in $C_6H_6^+$ mode.*

BVOC	15/07/2021 ppb	17/07/2021 ppb	19/07/2021 ppb
Piperitone	1.77	0.90	1.85
Sum of Monoterpenes	2.34	1.55	2.20
Isoprene	0.64	0.42	0.44
C_7H_8	0.08	0.06	0.08
$C_5H_8O_2$	0.23	0.11	0.17
C_9H_{12}	0.07	0.05	0.07
$C_{10}H_{16}O_2$	0.05	0.03	0.04
$C_{10}H_{18}O_4$	0.03	0.02	0.03
Total BVOCs	5.23	3.14	4.88

The total concentrations of the eight BVOC in the chamber were between 3.1 ppb and 5.3 ppb. This is similar to the BVOC concentrations present in an aerosol growth chamber prior to the low NO_x $OH^{\bullet}$ initiated oxidation of Holm oak[19] and Loblolly pine[73] emissions, at approximately 5 ppb and 2.5 ppb respectively.

Together, piperitone, isoprene and sum of monoterpenes accounted for over 90% of the total BVOC concentration in the chamber for all experiments. These were identified as the three main BVOCs emitted by Spruce 1 (Chapter 3). Although the sum of monoterpenes was identified as the third highest emission from Spruce 1 (Chapter 3), its concentration present in the chamber at the start of the oxidation experiments was higher than those for both piperitone and isoprene. This is likely due to the Spruce 1 emitting a slightly different emission profile than was determined for the emission characterisation measurements. Also, since piperitone has a low vapour pressure (0.053 hPa at 20 °C, Sigma Aldrich), it may have experienced deposition onto the walls of the tubing prior to reaching the chamber. The monoterpenes were not characterised, but they were assumed to have the same composition (myrcene, β-phellandrene, α-pinene, δ-limonene and camphene) and to have been present in the same proportions as was presented for the Spruce 1 emissions in Chapter 3. The concentrations of the other five Spruce 1 BVOCs in the chamber at the start of the emissions oxidation experiments were low, as was

observed for their emission fluxes in Chapter 3, but were consistently detected in the same proportions.

5.3.2 Bulk analysis

5.3.2.1 Composition

The results from all gas-phase and particle-phase analysis were combined and used to describe the bulk properties of the oxidation products. Figure 5.1 shows all reactants and products detected in the OH• oxidation of Spruce 1 emissions. The mass spectrum is composed of data from experiments performed on two separate days 15/07/2021 ($C_6H_6^+$ ToF-CIMS) and 09/06/2021 (I^- ToF-CIMS). The y-axis represents the average ion signal intensity over the duration of the experiment for gas-phase reactants and products, or the average signal intensity over the duration of the desorption cycle for particle-phase products.

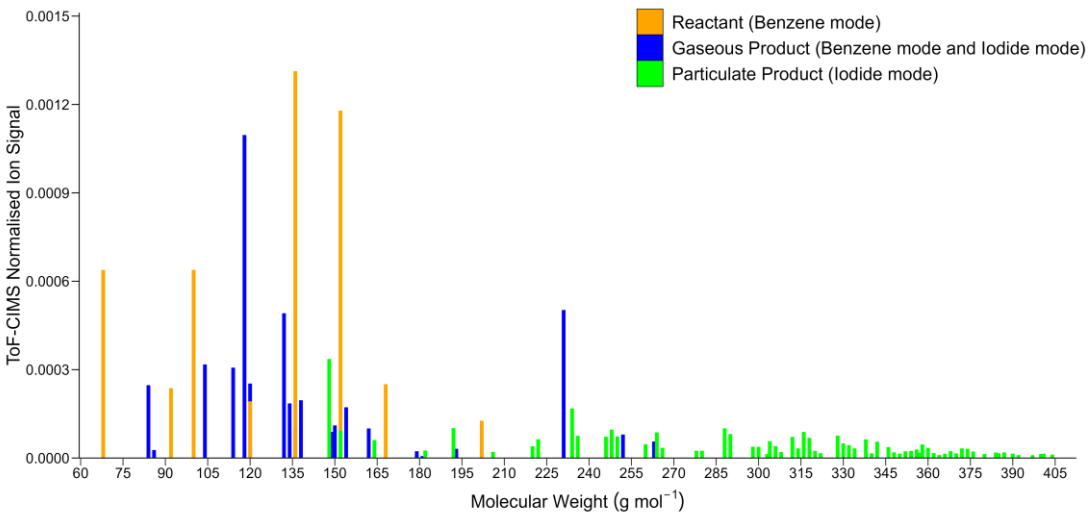

Figure 5.1 *Composite mass spectrum of all reactants and products detected in the gas-phase and particle-phase during the OH• oxidation of Spruce 1 emissions. Signal intensity refers to the average ion signal over the duration of the experiment for gas-phase products, and average ion signal over duration of the desorption cycle for particle-phase products.*

Eight BVOC reactants (orange) were detected with the ToF-CIMS in $C_6H_6^+$ mode as well as four oxidation products (blue). The reactants were dominated by the sum of

monoterpenes (*m/z* 136), piperitone (*m/z* 153), and isoprene (*m/z* 68). The composition of the BVOC reactants ranged from C_5 to C_{10} and were either hydrocarbons or had a low oxygen content. Although the reactants could not be detected during the experiments conducted with the ToF-CIMS operated in I^- mode, given the high level of reproducibility reported in Table 5.1, it is reasonable to assume that their composition would be similar to that obtained in $C_6H_6^+$ mode.

The remaining twenty-one gas-phase products (blue) and all ninety-nine products in the particle-phase (green) were detected with the ToF-CIMS in I^- mode. Figure 5.2 provides a breakdown of the composition of all gas-phase and particle-phase products, by carbon number and oxygen content.

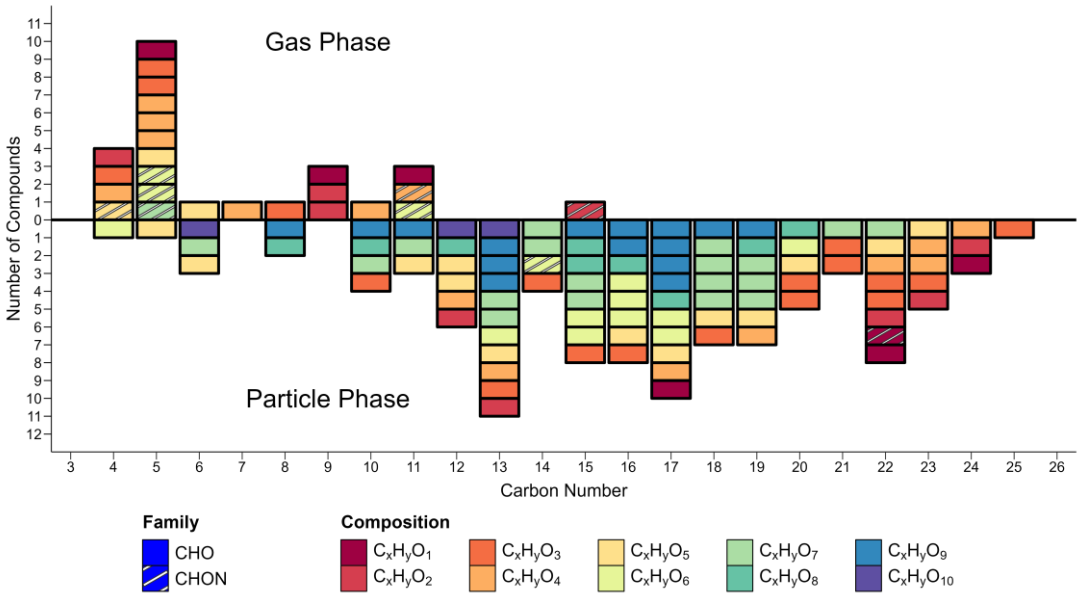

Figure 5.2 *Composition breakdown of all Spruce 1 $OH^\bullet$ oxidation products detected in the gas-phase and particle-phase. Each box represents a single product, with gas-phase products above the centre line and particle-phase products below. The colour refers to the oxygen content and striped boxes indicate the presence of nitrogen in the chemical formula.*

In total twenty-five gas-phase products were identified, with $C_5H_{10}O_3$ being the dominant product, followed by $C_{11}H_{22}NO_4$ and $C_5H_{12}O_4$. The majority of the gas-phase products have molecular weights below 200 g mol^{-1} (Figure 5.1). There is good agreement between the mass range of the Spruce 1 oxidation products and the $OH^\bullet$

and O_3 oxidation products of silver birch. The silver birch oxidation products were found between 100 g mol^{-1} and 170 g mol^{-1}, and were mainly attributed to the oxidation of monoterpenes[278]. The mass range for the particle-phase is similar to that determined from ambient SOA samples collected at a forest in Hyytiälä, which was mainly composed of Scots pine and Norway spruce, both species predominantly emit monoterpenes including α-pinene, δ-carene and limonene[71-73].

The composition of the gas-phase products ranged between C_4 and C_{15}, with C_5 compounds accounting for 40%. The three gas-phase products with carbon content above C_{10} were likely formed through oligomerisation reactions. The oxygen content of the gas-phase products varied between O_1 and O_8, with O_4 compounds dominating. Seven of the gas-phase products were found to contain nitrogen in the chemical formula. Although NO_x was not added to the chamber, a background concentration of around 0.2 ppb was present at the start of the reaction, likely due to release of NO_x from the Teflon surface of the chamber. The presence of 0.1 ppb NO_x in SAPHIR at low NO_x conditions has also been attributed to off gassing, and was shown to lead to the formation of CHON products[241, 279].

The ninety-nine products detected in the particle-phase are shown in green on the mass spectrum, Figure 5.1, and below the central line in Figure 5.2. The dominant particle-phase compound was $C_4H_4O_6$. The products in the particle-phase have higher molecular weights than the gas-phase products and are generally above 200 g mol^{-1}.

The composition of the particle-phase ranged from C_4 to C_{25}, with over half of the products between C_{13} and C_{20}. Almost 90% of particle-phase products had a carbon content greater than C_{10}. The oxidation of piperitone and monoterpenes is expected to produce high numbers of compounds with carbon content C_{10} and lower[242, 243], the scarcity of these products in the particle-phase indicates that the expected oxidation products were likely reactive intermediates that took part in combination reactions. This is supported by the high number of C_{13} to C_{20} particle-phase products and indicates that the particle-phase was mainly composed of oligomeric

compounds. The oxygen content of the particle-phase ranged from O_1 to O_{10}, with over half of the products between O_6 and O_{10}.

Partitioning between the gas-phase and particle-phase mainly occurred for compounds with oxygen contents greater than O_4 and O_5. The majority of gas-phase products had an oxygen content of O_4 or less, while almost 70% of particle-phase products had an oxygen content of O_5 or greater. Partitioning was also dependent on the carbon content. For particle-phase products less than C_{10}, the oxygen content was at least O_6, with those above C_{10} having higher variability in the oxygen content.

5.3.2.2 Product Properties

Figure 5.3 is the mass defect plot for all Spruce 1 oxidation products. The x-axis is molecular weight, and the y-axis is mass defect, which is the difference between the exact mass of a compound and its nominal mass. Each element has a set mass defect, with carbon +0.011, hydrogen +0.008 and oxygen -0.001, giving a unique mass defect for each molecular formula. Therefore mass defect plots can be used to investigate chemical composition.

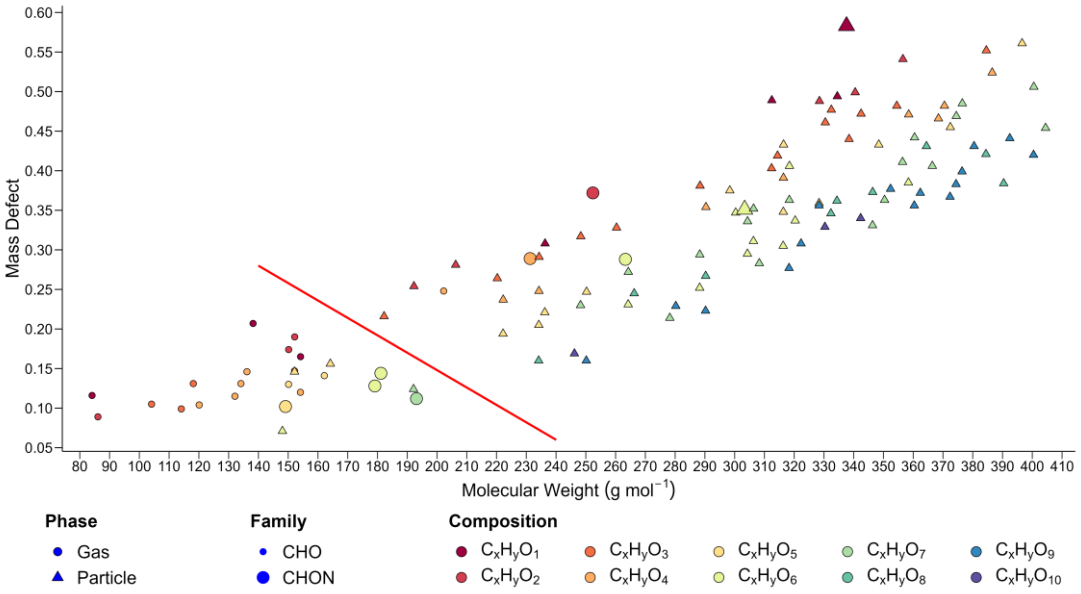

Figure 5.3 *Mass defect plot of all Spruce 1 OH• oxidation products detected in the gas-phase and particle-phase. Circle represents gaseous product and triangle represents particulate product. Colour indicates oxygen content of the product, and size refers to the nitrogen content. The red line is a rough partition between the gas-phase and particle-phase.*

All the Spruce 1 oxidation products occupy a certain area of the mass defect plot, along the positive diagonal, with an increase in molecular weight corresponding to an increase in mass defect. The mass defect plot can be split into two distinct sections, separated by the red line. The gas-phase products are mainly found below the red line, with lower molecular weights and mass defects below 0.25. Almost all particle-phase products are located above the red line, at higher molecular weights, and mass defects ranging from 0.15 to 0.6. The particle-phase products have higher mass defects than the gas-phase products, which indicates that they have a greater carbon content, suggesting the particle-phase is mainly composed of oligomers.

Oxygen has a negative mass defect, therefore for a given molecular weight a lower mass defect indicates that a compound has a higher oxygen content at the expense of having a lower carbon content. This is seen in Figure 5.3, where oxidation products along the top edge of the positive diagonal have larger mass defects and oxygen contents of O_1 to O_3, (reds) while products along the bottom edge of the positive

diagonal have lower mass defects and the oxygen content is typically O_8 and above (green, blue and purple).

Van Krevelen diagrams map the position of a compound according to its O:C and H:C, which indicates the extent to which it is oxidised. The Van Krevelen diagram of all Spruce 1 oxidation products is shown in Figure 5.4. Unlike the mass defect plot, the data is spread over the majority of the plot area, with no clear distinction between gas-phase and particle-phase products. As a compound is oxidised, in the absence of fragmentation, O:C increases and H:C decreases, yielding a negative trend with increasing O:C[280]. This was not observed for the Spruce 1 oxidation products, possibly due to presence of multiple BVOC reactants with varying oxygen content present at the start of the reaction. Each precursor BVOC would occupy a different position on the Van Krevelen diagram. The simultaneous oxidation of all Spruce 1 BVOCs and the interaction of the oxidation products may explain the deviation of the data from the expected plot shape.

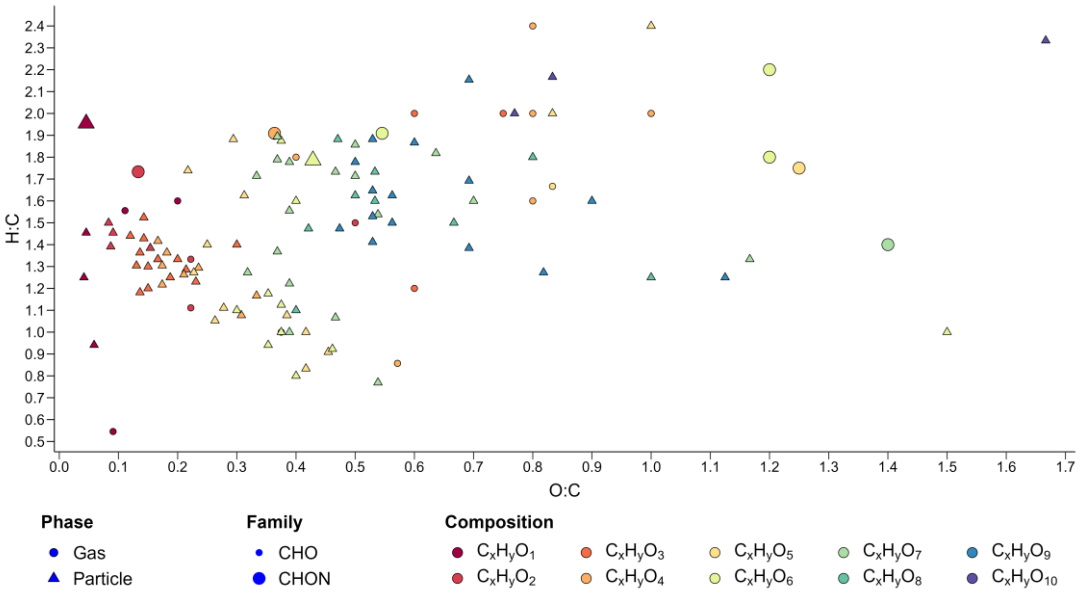

Figure 5.4 *Van Krevelen diagram of all Spruce 1 OH• oxidation products detected in both the gas-phase and particle-phase. Circle represents gaseous product and triangle represents particulate product. Colour indicates oxygen content of the product, and size refers to the nitrogen content.*

A Kroll diagram is another visualisation tool for aiding interpretation of the product distribution. Kroll diagrams are used to mark the position of compounds according to their carbon content (x-axis) and $\overline{OS}_C$ (y-axis), which was calculated according to Equation 4.11. The presence of nitrogen in the chemical formulae was not accounted for in the $\overline{OS}_C$ calculation. Inclusion requires knowledge of the oxidation state of the nitrogen, and was deemed unnecessary due to the minimal change it would have on $\overline{OS}_C$[245].

Vertical transition along the $\overline{OS}_C$ axis indicates the extent of oxidation, with a higher $\overline{OS}_C$ signifying a more oxidised compound, and a lower $\overline{OS}_C$ signifying a less oxidised compound. Lateral movement along the x-axis towards increasing carbon number corresponds to oligomerisation. Transition towards the position of CO_2 carbon number 1 and $\overline{OS}_C$ +4, indicates fragmentation[245].

Figure 5.5 shows all gas-phase and particle-phase products resulting from the oxidation of the Spruce 1 emissions. An increase in carbon number, corresponded to a decrease in $\overline{OS}_C$ across all Spruce 1 oxidation products. The colour of the symbols represents the oxygen content of the products. In general the products with lower oxygen contents (reds and oranges) have lower $\overline{OS}_C$, indicating they are less oxidised, and products with a higher oxygen content (greens, blue and purple) have a higher $\overline{OS}_C$.

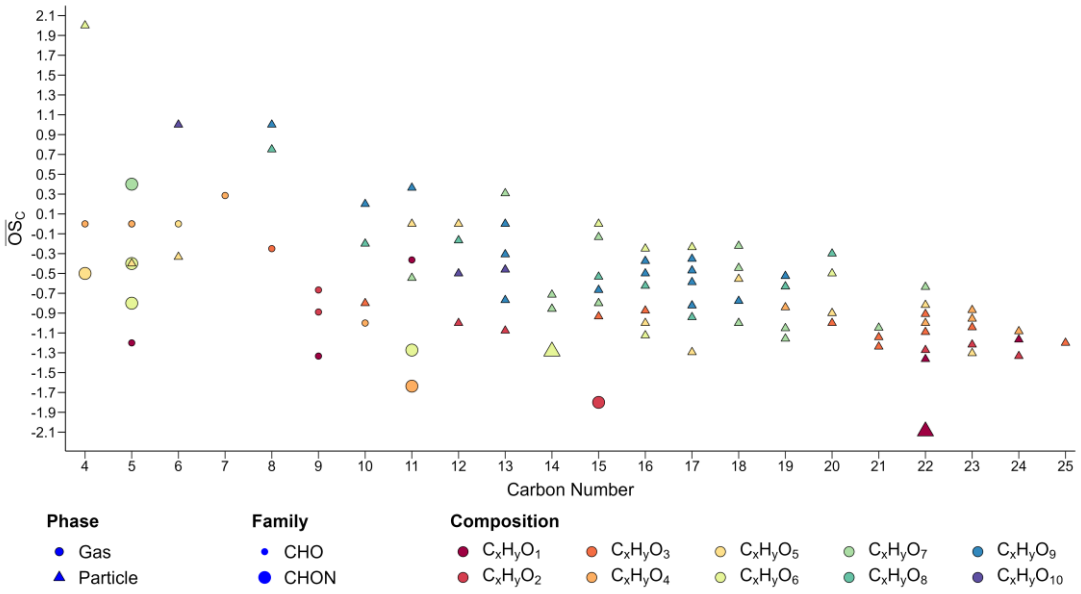

Figure 5.5 *Kroll diagram of all Spruce 1 OH• oxidation products detected in the gas-phase and particle-phase. Circle represents gaseous product and triangle represents particulate product. Colour indicates oxygen content of the product, and size refers to the nitrogen content.*

The gas-phase products and the particle-phase products generally occupy different areas of the Kroll diagram. The majority of gas-phase products have a carbon content below C_9, and $\overline{OS}_C$ -1.3 to +0.4. The particle-phase products occupy a much narrower $\overline{OS}_C$ range, mostly -1.4 to 0, with a carbon content greater than C_{10}. This is comparable to the $\overline{OS}_C$ range determined for the gas-phase products (-1.2 to +0.5) and particle-phase products (-1.4 to +2) resulting from the OH• induced oxidation of α-pinene in the presence of NO_x[281]. The $\overline{OS}_C$ range for the gas-phase products from α-pinene oxidation is similar to that from Spruce 1 BVOC oxidation, although the wider $\overline{OS}_C$ range for the α-pinene particle-phase products compared to Spruce 1 particle-phase products is possibly due to the high number of products with carbon content C_{10} and below[281] that were present in the α-pinene particle-phase.

5.3.2.3 Particle-Phase Volatility

Analysis of the particle-phase involved only data recorded during the temperature ramp phase of the desorption cycle. A thermogram is a plot of ToF-CIMS ion signal as a function of desorption temperature. Figure 5.6 shows the thermograms of the C_{10}

particle-phase products. As the temperature of the filter was increased, the compounds in the particle-phase began to desorb from the filter which led to an increase in the ToF-CIMS signals for their ions. The temperature corresponding to the maximum ToF-CIMS signal is referred to as the temperature of maximum desorption, T_{max}. It represents the temperature at which the largest amount of a product is desorbed from the filter. After reaching T_{max} the ToF-CIMS ion concentration gradually reduced to background levels.

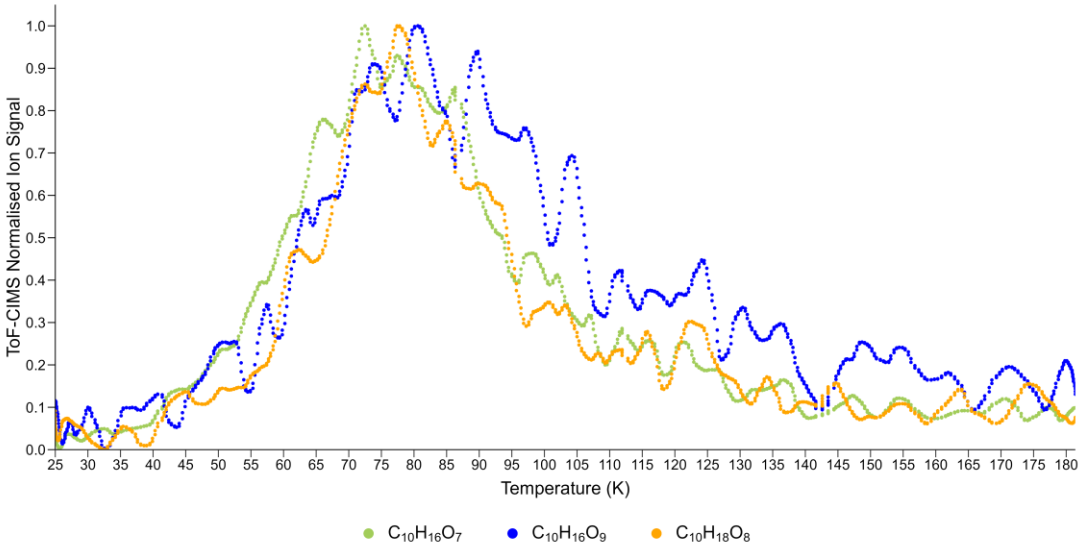

Figure 5.6 *Thermogram of $C_{10}H_{16}O_7$, $C_{10}H_{18}O_8$ and $C_{10}H_{16}O_9$ produced during the $OH^{\bullet}$ radical initiated oxidation of BVOC emission from Spruce 1.*

T_{max} can be used to derive physical properties of the products in the particle-phase, including vapour pressures and enthalpy of sublimation[111] which are useful in determining volatility and gas to particle partitioning[282]. T_{max} for the three C_{10} products in Figure 5.6 increases with increasing oxygen content. This implies that an increase in T_{max} corresponds to a reduction in volatility[111].

The T_{max} values for each product in the particle-phase were converted to C^* at 298 K (C^*_{298}) using Equation 5.1[113, 282]. The saturation vapour concentrations were then assigned to volatility bins according to the volatility basis set classifications[283, 284], Figure 5.7.

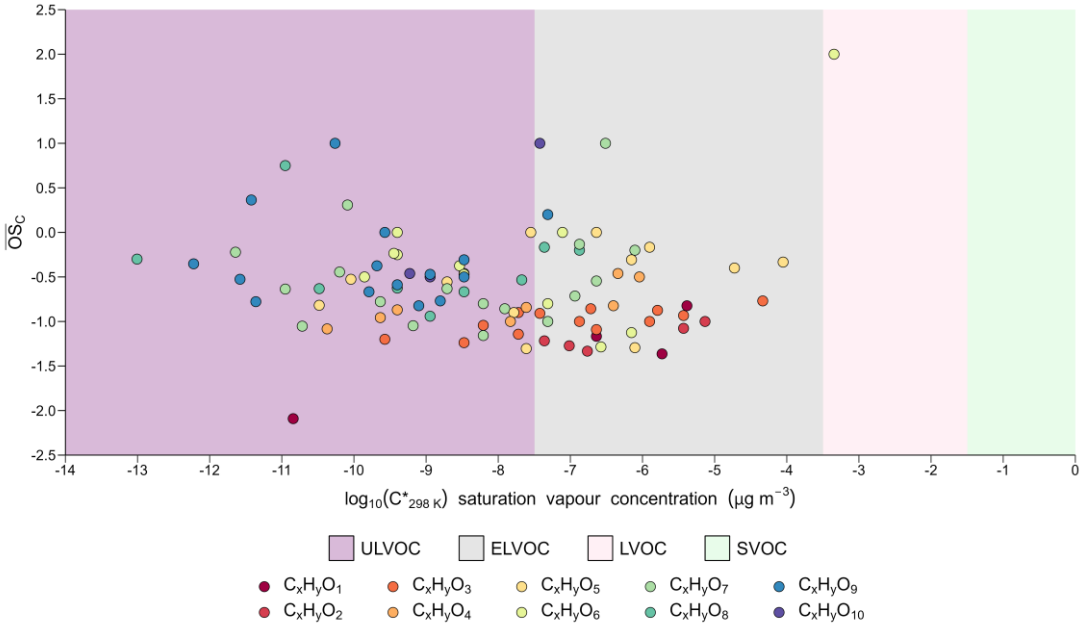

Figure 5.7. *Plot of experimentally determined C* as a function of* $\overline{OS}_C$ *for particle-phase products. Each point corresponds to a particle-phase product, with the shading referring to volatility class: purple ultra-low volatility organic compound (ULVOC); grey extremely low volatility compound (ELVOC); pink low volatility organic compound (LVOC); and green semi volatile organic compound (SVOC).*

One particle-phase product was assigned to the LVOC volatility class (pink shading), which ranges[284] between 3×10^{-4} μg m^{-3} and 0.32 μg m^{-3}. In general compounds in the LVOC class are found in the particle-phase[285]. Around half of the particle-phase products were assigned to the ELVOC class (grey shading), with *C** extending from[284] 3.2×10^{-4} μg m^{-3} to 3.2×10^{-8} μg m^{-3}. Under ambient conditions compounds in the ELVOC class are almost entirely in the particle-phase[285]. The remaining products all had *C** below 3.2×10^{-8} μg m^{-3}, and were allocated to the ULVOC class[283]. Under ambient conditions ULVOCs undergo nucleation, driving new particle formation[286].

5.3.3 Mechanistic Interpretation

Figure 5.8 shows the chamber loss corrected time series profile of the eight Spruce 1 BVOC reactants during the experiment. The data was normalised to 1 to facilitate

visualisation. Data after the appearance of the $C_{10}H_{15}$ interference was removed for clarity.

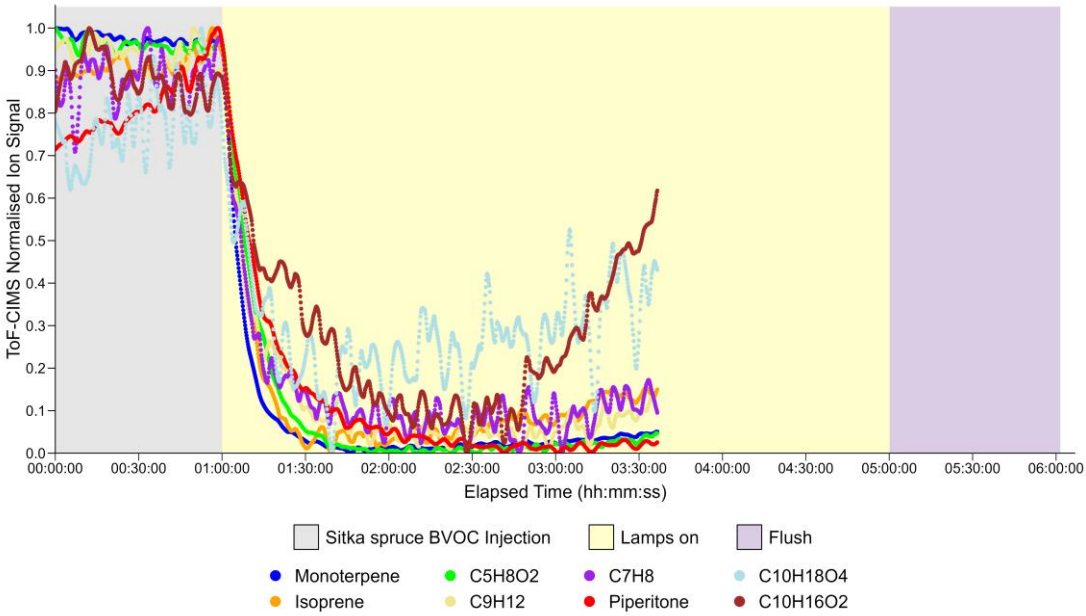

Figure 5.8 *Time series profile of reactant BVOCs from Spruce 1 during an oxidation experiment, with corrections for chamber losses applied.*

Initially the concentrations of the BVOC reactants were stable in the chamber, but then exhibited rapid decay immediately upon illumination, due to their reaction with $OH^{\bullet}$. The pseudo first-order decay rates for piperitone, isoprene and monoterpene signals were determined and compared, Table 5.2. The fastest BVOC to decay was the monoterpene (blue), followed by isoprene (orange). Due to the high abundance of myrcene in Sitka spruce emissions (Chapter 3), and the faster decay of the monoterpene signal relative to isoprene (Figure 5.8 and Table 5.2), it is assumed that myrcene was the dominant reactive monoterpene during the experiments.

Table 5.2 *Literature rate coefficients and pseudo first order decay coefficients for piperitone, isoprene, myrcene and the sum of monoterpenes. Psuedo first order decays were calculated using data obtained during the first 13 minutes of the reaction.*

BVOC	Literature Rate Coefficient cm^3 $molecule^{-1}$ s^{-1}	Absolute decay s^{-1}
Piperitone	0.99×10^{-10}	8.06×10^{-4}
Isoprene[44]	1.00×10^{-10}	9.15×10^{-4}
Myrcene[44]	2.15×10^{-10}	-
Sum of Monoterpenes	-	1.92×10^{-4}

Based on the k_{OH} values in Table 5.2, the piperitone decay (red) (Figure 5.8) would be expected to have a similar decay to isoprene (orange). However, it is noticeably slower, indicating that the signal may be affected by the appearance of some $C_{10}H_{16}O$ monoterpene oxidation products[287, 288]. Some of the other oxygenated reactants including $C_{10}H_{16}O_2$ and $C_{10}H_{18}O_4$ also exhibited a slow decay, followed by a subsequent increase. This was also likely due to interference from oxidation products[29, 288]. Due to the higher abundance of piperitone, isoprene and myrcene in the experiments, further analysis focussed on attributing the identified products from the oxidation of Spruce 1 BVOCs to known products of the $OH^{\bullet}$ initiated oxidation of these three BVOCs.

5.3.3.1 Piperitone Products

One gas-phase Spruce 1 oxidation product, $C_{10}H_{18}O_4$, was attributed as a piperitone oxidation product (Chapter 4). The formation mechanism for $C_{10}H_{18}O_4$ from piperitone is shown in Figure 5.9. The initial step is addition of $OH^{\bullet}$ to the C=C bond to produce an alkyl radical, which adds O_2 followed by reaction with $HO_2^{\bullet}$ to give a hydroperoxide. $C_{10}H_{18}O_4$ was the third oxidation product to be observed from the $OH^{\bullet}$ initiated oxidation of piperitone (Chapter 4). The first and second piperitone oxidation products to appear were $C_{10}H_{16}O_3$ and $C_{10}H_{14}O_4$, these were not observed in the oxidation of Spruce 1 emissions. The reason for the absence of these products may be due to the Spruce 1 oxidation experiments being carried out in a different facility, under slightly different oxidation conditions. The termination steps in the mechanisms for the formation of $C_{10}H_{16}O_3$ and $C_{10}H_{14}O_4$ are unimolecular

eliminations, while for $C_{10}H_{18}O_4$ it is bimolecular reaction with $HO_2^{\bullet}$. The experimental conditions for Spruce 1 oxidation experiments likely had higher $HO_2^{\bullet}$ concentrations than the piperitone experiments, due to a higher relative humidity and the use of UVC lamps[289]. This would have favoured the formation of $C_{10}H_{18}O_4$ over both $C_{10}H_{16}O_3$ and $C_{10}H_{14}O_4$. Also, $C_{10}H_{16}O_3$ and $C_{10}H_{14}O_4$ were proposed to undergo oxidation with $OH^{\bullet}$ and photolysis (Chapter 4). It is likely that $C_{10}H_{16}O_3$ and $C_{10}H_{14}O_4$ were formed during the Spruce 1 emissions oxidation, but due to limited formation and rapid decay their yields may have been below the ToF-CIMS limit of detection.

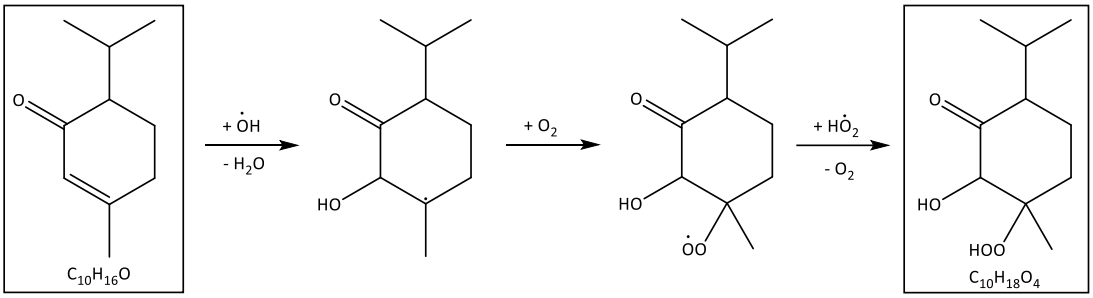

Figure 5.9 *Proposed mechanism for the formation of $C_{10}H_{18}O_4$ from the $OH^{\bullet}$ initiated oxidation of piperitone.*

Three particle-phase Spruce 1 oxidation products, $C_{10}H_{16}O_7$, $C_{10}H_{16}O_9$ and $C_{10}H_{18}O_8$ may have been formed from the oxidation of piperitone. $C_{10}H_{16}O_7$ was observed as a gas-phase piperitone oxidation product (Chapter 4), while $C_{10}H_{16}O_9$ could be produced through the further oxidation of $C_{10}H_{16}O_7$. The product $C_{10}H_{18}O_8$ could be formed via the oxidation of $C_{10}H_{18}O_4$ and $C_{10}H_{18}O_6$, both of which were detected as gas-phase piperitone oxidation products (Chapter 4), although not in the Spruce 1 oxidation experiments. The proposed oxidation mechanisms for $C_{10}H_{16}O_7$, $C_{10}H_{16}O_9$ and $C_{10}H_{18}O_8$ are shown in Figure 5.10.

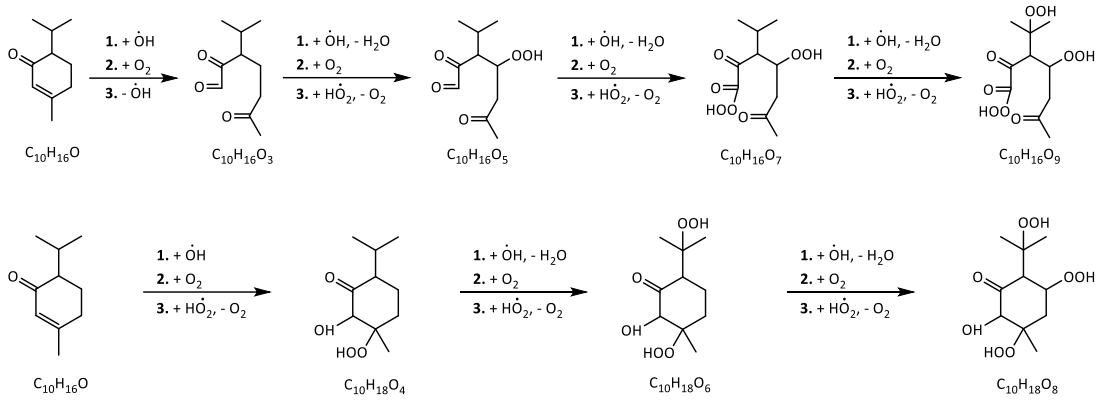

Figure 5.10 *Condensed mechanism for the proposed formation of $C_{10}H_{16}O_7$, $C_{10}H_{16}O_9$ and $C_{10}H_{18}O_8$ from piperitone, showing the most likely structures.*

Figure 5.10 shows the proposed condensed mechanism for the formation of the three particle-phase products. There are several potential isomers for $C_{10}H_{16}O_5$, $C_{10}H_{16}O_7$ and $C_{10}H_{18}O_8$, only the predicted dominant ones are shown for clarity. Since compositional analysis of the particle-phase piperitone oxidation products was not possible, a direct comparison cannot be made. However it is likely that $C_{10}H_{16}O_7$ was also present in the particle-phase during the piperitone oxidation experiments. The high oxygen contents of $C_{10}H_{16}O_9$ and $C_{10}H_{18}O_8$ indicate that these compounds would have low vapour pressures and would predominantly exist in the particle-phase[290].

5.3.3.2 Myrcene Products

One gas-phase Spruce 1 oxidation product, $C_9H_{14}O$ was identified as a potential myrcene oxidation product. $C_9H_{14}O$ is a primary Spruce 1 oxidation product and maximised within 20 minutes of reaction initiation. $C_9H_{14}O$ has two possible isomers, 1-vinyl-5-methyl-4-hexanone and 2-methylidene-6-methyl-5-heptanal. Previously proposed mechanisms for the formation both isomers[243] are shown in Figure 5.11.

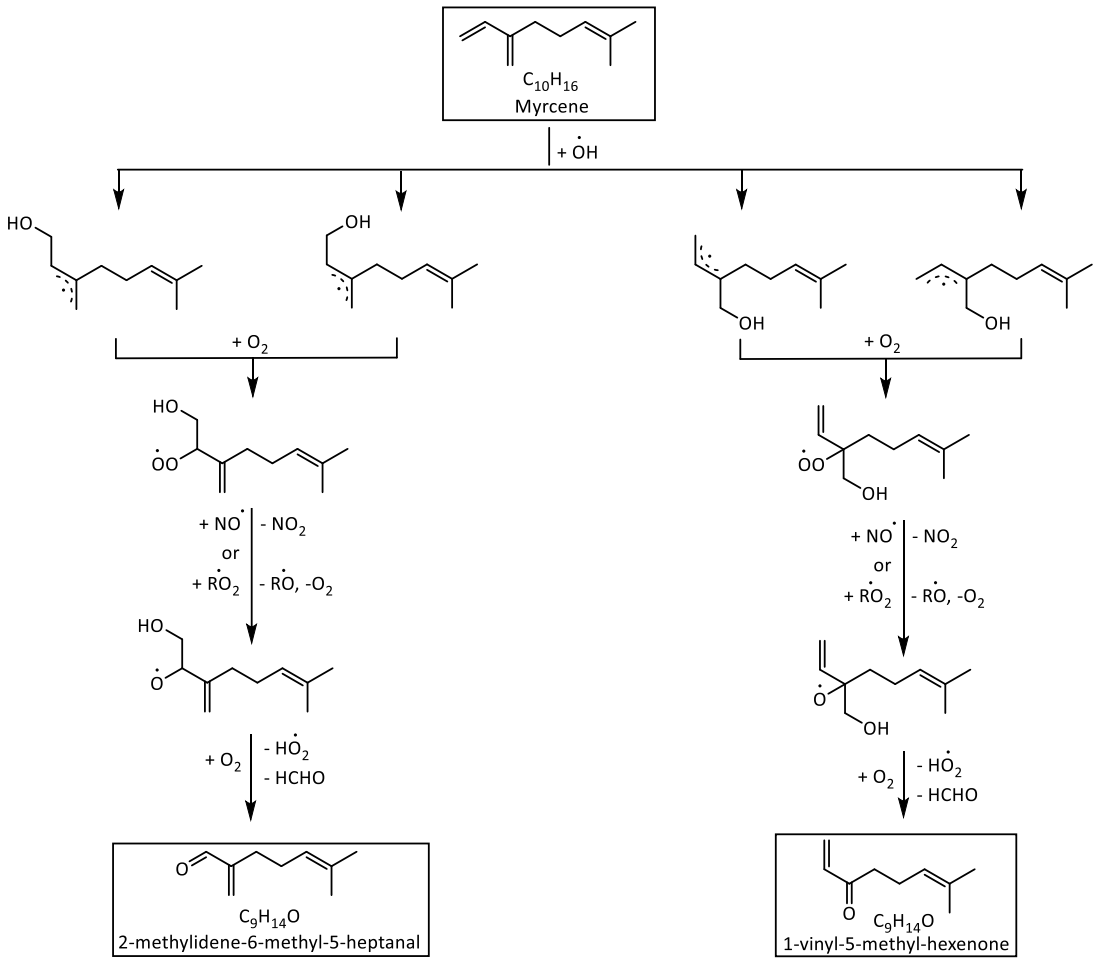

Figure 5.11 *Mechanism for the formation of $C_9H_{14}O$ from the oxidation of myrcene, adapted from Tan et al[243].*

This $C_9H_{14}O$ formation mechanism involves the reaction of the peroxy radical with either $NO^{\bullet}$ or another peroxy radical, with both reactions producing an alkoxy radical[243, 279]. It is unlikely the $C_9H_{14}O$ product detected in these experiments was formed through these mechanism, as neither of these peroxy radical reactions is likely to have occurred. An alternative mechanism is proposed here, based on the $OH^{\bullet}$ elimination from the hydroxyl peroxy radical, Figure 5.12.

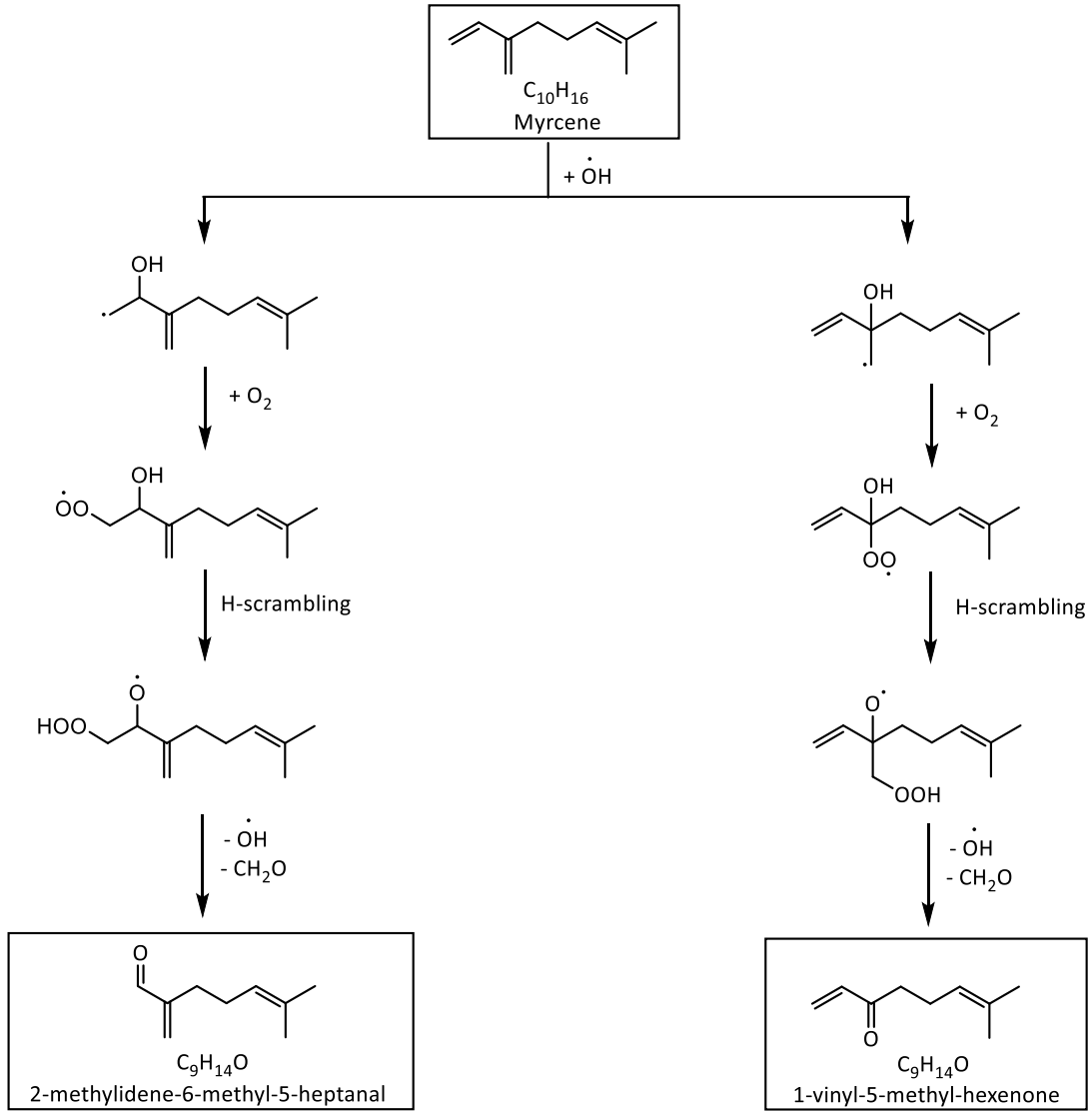

Figure 5.12 *Alternative proposed mechanism for the formation of $C_9H_{14}O$ from the oxidation of myrcene.*

This alternative mechanism for the formation of $C_9H_{14}O$, produces the same two isomers 1-vinyl-5-methyl-4-hexanone and 2-methylidene-6-methyl-5-heptanal as have previously been observed from the OH• initiated oxidation of myrcene[243]. The oxidation of myrcene proceeds via addition of OH• to any of the three C=C bonds. Addition to the isolated C=C bond is expected to dominate[9, 243], although for the formation of $C_9H_{14}O$, the reaction is initiated by addition of OH• to either internal end of the conjugated dialkene, producing an alkyl radical, Figure 5.12. The alkyl will add O_2, yielding a hydroxyl peroxy radical, which can undergo H-scrambling to produce an alkoxy radical, that can decompose leading to the formation of $C_9H_{14}O$,

formaldehyde and $OH^{\bullet}$. This kind of alkoxy decomposition has been observed for the oxidation of limonene[241] and isoprene[206, 222] under low NO_x conditions, and was also included in some of the proposed piperitone oxidation mechanisms (Chapter 4). The ToF-CIMS is not capable of separating structural isomers, although it is anticipated that both isomers contribute to the signal at $C_9H_{14}O$.

No particle-phase products were identified as originating from myrcene oxidation. Due to the linear structure of myrcene, the majority of its primary oxidation products are fragmentation products[291] that likely have higher saturation vapour pressures than myrcene, and are less likely to take part in SOA formation.

5.3.3.3 Isoprene Products

Three gas-phase products were identified as originating from the oxidation of isoprene, $C_5H_{10}O_3$ and $C_5H_{10}O_5$. $C_5H_{10}O_3$ could be ISOPOOH or IEPOX. It is likely both isomers contribute to the signal at $C_5H_{10}O_3$. Figure 5.13 shows potential formation mechanisms for both $C_5H_{10}O_3$ isomers and $C_5H_{10}O_5$.

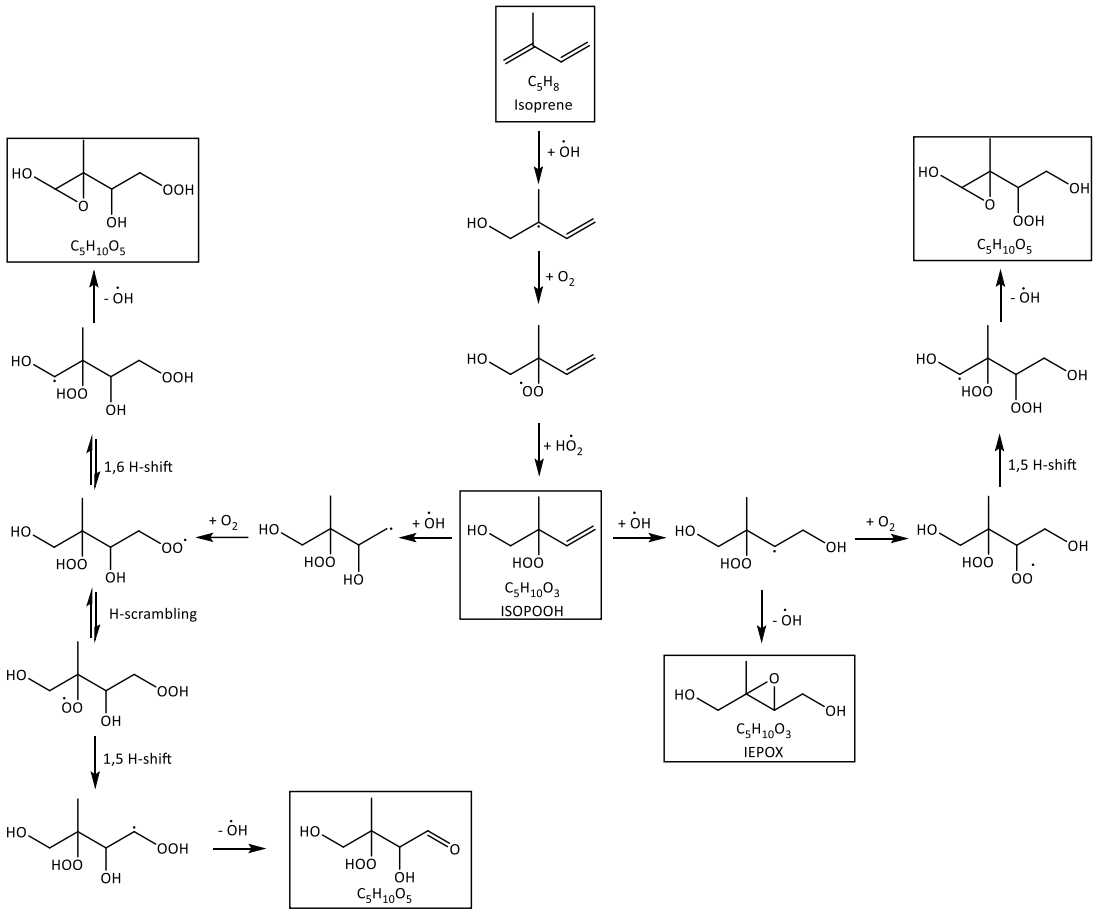

Figure 5.13 *Mechanism for the formation of ISOPOOH, IEPOX and $C_5H_{10}O_5$ from the oxidation of isoprene, adapted from D'Ambro et al*[266]*.*

ISOPOOH is a primary isoprene oxidation product, formed from the addition of OH• to one of the C=C bonds in isoprene, producing alkyl radical. Upon addition of O_2 and reaction with HO_2• a peroxide is formed giving $C_5H_{10}O_3$, ISOPOOH[206, 266]. Four possible ISOPOOH structures can be formed, only one is shown.

IEPOX is a secondary isoprene oxidation product, that is formed from the oxidation of ISOPOOH. IEPOX formation involves the addition of another OH• to the external end of the C=C bond in ISOPOOH, producing an alkyl radical. Epoxidation can occur resulting in the elimination of OH• and the formation of stable IEPOX[25, 266, 292]. Alternatively, the alkyl radical can add O_2, to produce a peroxy radical, which can undergo a 1,5-hydrogen shift followed by OH• elimination leading to the formation of $C_5H_{10}O_5$[266]. Two alternative $C_5H_{10}O_5$ isoprene oxidation products can be formed through the oxidation of ISOPOOH via similar oxidation steps, involving OH• addition

to the internal carbon of the C=C bond in ISOPOOH[266]. $C_5H_{10}O_5$ was detected in the particle-phase of the Spruce 1 emissions, and has also been identified in the SOA produced from isoprene oxidation[96, 293].

5.3.4 Particle Formation and SOA Yield

Figure 5.14 shows the particle number and mass concentrations during the Spruce 1 oxidation experiments following correction for chamber losses. The data shown is from experiment the experiment performed on 15/07/2021, with the ToF-CIMS operated in $C_6H_6^+$ mode, and is typical of all experiments. The SOA yield could not be determined for the experiments conducted with the ToF-CIMS in I^- mode as the BVOC reactants could not be detected.

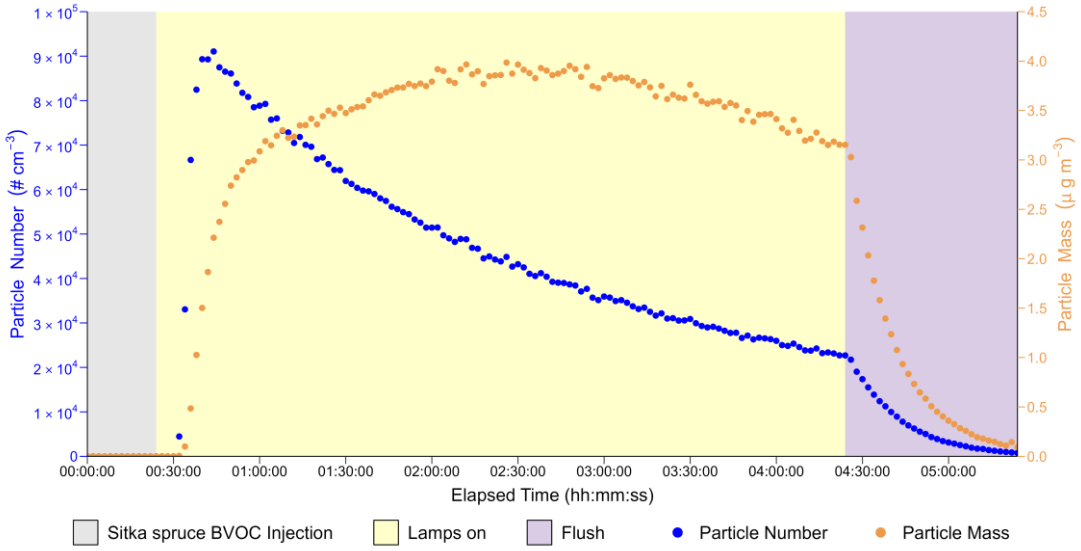

Figure 5.14. *Time series plot of particle formation measured by the SMPS during the $OH^{\bullet}$ oxidation of Spruce 1 emissions. Particle number is shown in blue and particle mass is shown in orange. Data has been corrected for chamber losses.*

Particle formation commenced within 10 minutes of reaction initiation, due to the formation of ULVOCs (Section 5.3.2.3), which undergo new particle formation[288]. Particle number underwent a rapid increase over fifteen minutes before maximising. The number concentration then exhibited a fast exponential decay, due to the

coagulation of smaller particles. Rapid SOA formation from the oxidation of BVOC emissions[52] has been observed both in the field[55] and laboratory settings[278, 294]. The rate of SOA formation from the oxidation of Spruce 1 BVOCs was faster than for piperitone (Chapter 4). This is likely due to a combination of the Spruce 1 BVOC oxidation experiments containing multiple precursors and having a higher oxidant concentration compared to the piperitone experiments.

The particle mass concentration increased more slowly than the particle number, and reached a maximum approximately 90 minutes after the initiation of particle formation. The number concentration remained stable for approximately 60 minutes before decreasing. The reason for the decrease in particle mass is unclear, one possibility is that it could be due to evaporation, resulting from an increase in temperature over the course of the experiment. There is no temperature control system for the chamber at the ERI and the temperature increased by almost 10 °C during all experiments. Evaporation from pre-existing SOA has previously been attributed to fragmentation resulting from the oxidation of the particle-phase compounds[205].

Figure 5.15 shows the particle-phase growth during the oxidation of the Spruce 1 emissions. The data shown is also from the experiment performed on 15/07/2021. At the onset of particle formation there was a high concentration of small particles, with diameter between 10 nm and 20 nm. The particles underwent rapid growth, due to coagulation, over approximately 30 minutes, to reach a mean diameter of around 40 nm. After this the rate of particle growth significantly reduced reaching a maximum mean diameter of 60 nm after 4 hours. A small number of particles with much larger diameters than the bulk SOA, greater than 100 nm were also produced soon after the initiation of particle formation, and also experienced an increase in mean diameter as the reaction progressed, due to coagulation of smaller particles. Comparison with blank experiments determined that the event only occurred during experiments involving Spruce 1 emissions.

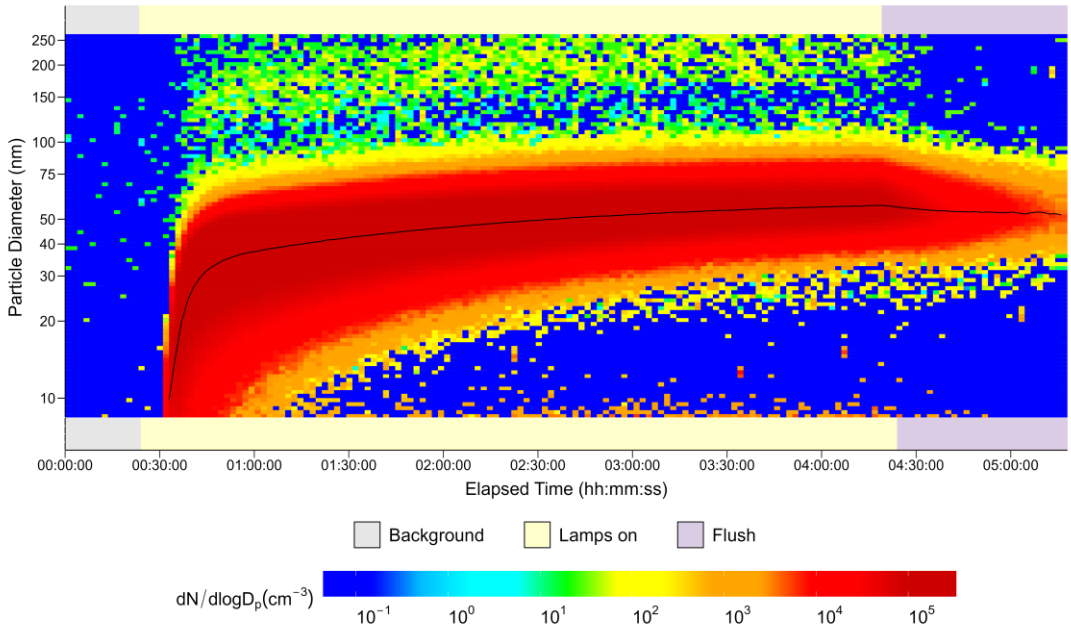

Figure 5.15 *Banana plot showing the particle-phase growth during a Spruce 1 emissions oxidation experiment. The black line represents the median particle diameter.*

The SOA yield was calculated as the ratio of the mass of SOA formed to the mass of Spruce 1 emissions reacted, at the point when the particle mass concentration maximised[18, 295]. Chamber loss corrected SMPS and ToF-CIMS data from two of the experiments with the ToF-CIMS in $C_6H_6^+$ mode were used to calculate an average SOA yield. The data from the other $C_6H_6^+$ mode ToF-CIMS Spruce 1 experiment was not included in the calculation due to interference of the ToF-CIMS signals with $C_{10}H_{15}^+$ before the particle mass maximised. The SOA yield results are shown in Table 5.3.

Table 5.3 *Summary of SOA yields for experiments conducted with the ToF-CIMS in $C_6H_6^+$ mode.*

	Reacted BVOC mass µg	**SOA mass µg**	**SOA Yield %**
1. 15/07/2021	70.2	10.5	14.9
2. 17/07/2021	43.1	6.7	15.6
Average			15.2

The average SOA yield was calculated to be 15.2%. This is comparable to the SOA yield determined from the $OH^\bullet$ oxidation of Scots pine which ranged between 13.7%

and 20%, for an SOA density of 1.3 g cm^{-3}. The BVOCs emitted from Scots pine were predominantly monoterpenes and sesquiterpenes[184], while the BVOCs emitted from Spruce 1 were mostly monoterpenes and piperitone. BVOC composition has been shown previously to have an impact on SOA yield[45, 60], with the addition of isoprene to the starting BVOC mix leading to a reduction in SOA yield. The SOA yield from the $OH^{\bullet}$ initiated oxidation of Norway spruce emissions was 13.6%. This is similar to the 15.2% calculated in this work for Sitka spruce. The main BVOC emissions from Norway spruce were α-pinene and β-pinene[296]. Overall the SOA yield from Spruce 1 is similar to that determined for other coniferous tree species, despite having different BVOC emission mixtures.

5.4 Conclusions

A series of atmospheric simulation chamber experiments were conducted on the $OH^{\bullet}$ initiated oxidation of the BVOC emissions from Spruce 1. The ToF-CIMS was able to identify eight Spruce 1 BVOCs as reactants in the chamber; piperitone, the sum of monoterpenes, isoprene, C_7H_8, $C_5H_8O_2$, C_9H_{12}, $C_{10}H_{16}O_2$ and $C_{10}H_{16}O_4$. The most reactive BVOCs were piperitone, monoterpenes and isoprene. A total of twenty-five gas-phase products were identified from the oxidation of the Spruce 1 BVOC emissions, which were mainly composed of C_5 compounds, with carbon content ranging from C_5 to C_{15}, and oxygen content O_1 to O_7 with O_4 products dominating.

Analysis of the particle-phase found ninety-nine oxidation products. The composition of the particle-phase ranged from C_4 to C_{25}, with 90% of products having a carbon content greater than C_{10}, implying the particle-phase was mostly composed of oligomers. The dominant oxygen content of the particle-phase was O_7, with 70% of the products having an oxygen content above O_3. Gas to particle partitioning was estimated to occur at an oxygen content of O_4, but was also related to carbon number, with compounds below C_{10} having a minimum oxygen content of O_6. All of the particle-phase products had low volatility, with almost all being classed as ELVOCs or ULVOCs.

The gas-phase and particle-phase products were compared with literature to identify their precursors. In the gas-phase $C_{10}H_{18}O_4$, was identified as a piperitone oxidation product. Three products in the particle-phase were identified as probable piperitone oxidation products $C_{10}H_{16}O_7$, $C_{10}H_{16}O_9$ and $C_{10}H_{18}O_8$.

$C_9H_{14}O$ was identified as a myrcene oxidation product. $C_9H_{14}O$ has previously been identified as one of the main products in the $OH^{\bullet}$ initiated oxidation of myrcene. There are two possible structural isomers for $C_9H_{14}O$, 1-vinyl-5-methyl-4-hexanone and 2-methylidene-6-methyl-5-heptanal, it is likely both isomers are present.

One gas-phase product and one particle-phase product were attributed to the oxidation of isoprene. $C_5H_{10}O_3$ has previously been identified as either the primary oxidation product ISOPOOH, or secondary oxidation product IEPOX. It is likely that both contribute to the signal at $C_5H_{10}O_3$. The particle-phase product $C_5H_{10}O_5$, is likely another secondary isoprene oxidation product, from the oxidation of ISOPOOH.

Particle formation commenced within 10 minutes of reaction initiation, with the formation of small particles less than 20 nm in diameter. Within 15 minutes of particle formation the particle number had maximised to 90,000 cm^{-3}, and the particles had undergone rapid growth to have a median diameter of 50 nm. The particle mass increased logarithmically before plateauing after 2 hours at 4 µg m^{-3}, and exhibiting a decrease 90 minutes later. The decrease in mass was possibly a result of evaporation due to the increasing temperature in the chamber during the experiment. The average SOA yield for the experiments was 15.2%.

Chapter 6 Conclusions

6.1 Summary and Perspectives

In this work different types of laboratory studies were conducted to identify the main BVOCs emitted from Sitka spruce, to assess their oxidation capacity and to determine their SOA formation potential. The work was conducted using an on-line ToF-CIMS with a flexible ionisation regime, facilitating the detection of a range of different compounds.

A series of measurements were conducted in a laboratory using a plant growth chamber with variable temperature and PPFD to study the BVOC emissions from Sitka spruce. Through a combination of on-line and off-line techniques the main BVOCs emitted from Sitka spruce at conditions relevant to the Irish climate were identified. The key finding from this work was that of the seventy-four BVOCs identified, fifty-two were oxygenated compounds. This is in contrast to many previous reports of BVOC emissions in the literature, which mainly detected hydrocarbons and small oxygenated compounds using PTR-MS and GC-MS. This work has therefore demonstrated that the combination of ToF-CIMS (utilising two ionisation modes) and TD-GC-MS is an effective method for identifying a wider range of compounds.

Assessment of the BVOC emission fluxes found that different BVOCs responded differently to changes in temperature and PPFD. Stress was also found to have a significant impact on the BVOC emissions, with the biosynthetic emission pathway making a minor contribution to the overall BVOC emission flux from a stressed Sitka spruce, and the identification of stress induced GLVs and a sesquiterpene in the emissions of the stressed tree. This is the first study to identify an oxygenated monoterpene, piperitone, as the dominant BVOC emitted from Sitka spruce, with a standardised emission flux of 17.29 μg h^{-1} g^{-1}. Isoprene and five monoterpenes, myrcene, β-phellandrene, δ-limonene, α-pinene, and camphene, were also detected as major BVOC emissions, with standardised emission fluxes of 6.3 μg h^{-1} g^{-1} for isoprene and 0.93 μg h^{-1} g^{-1} for the sum of monoterpenes. Estimates for the annual BVOC fluxes for all Sitka spruce in Ireland were 8,240 tonne $year^{-1}$ for piperitone,

13,114 tonne year^{-1} for isoprene, and 1,618 tonne year^{-1} for the sum of monoterpenes. It is important to note that the annual emission flux for isoprene is 1.6 times higher than it is for piperitone, despite piperitone having a standardised emission flux almost triple that of isoprene. This highlights the importance of determining the temperature and PPFD responses of individual BVOC emissions and the significance of calculating emission fluxes at conditions relevant to the climate the trees are subject to. Under the conditions of a warming climate, the emission of piperitone is predicted to exceed that of isoprene, and over time could become the dominant BVOC emitted from Sitka spruce in Ireland.

Due to the significant contribution of piperitone in the BVOC emission flux from Sitka spruce and the lack of knowledge regarding its atmospheric oxidation, a series of simulation chamber experiments were performed to determine piperitone kinetics, oxidation products, oxidation mechanisms and SOA formation potential. The rate coefficients for the reaction of piperitone with $OH^{\bullet}$, O_3 and $NO_3^{\bullet}$ were estimated using SAR methods, with the rate coefficient for reaction with $OH^{\bullet}$ also determined experimentally using the relative rate method. The rate coefficients were used to calculate atmospheric lifetimes of 1.7 hours, 81.1 hours and 3.1 hours for the reaction of piperitone with $OH^{\bullet}$, O_3 and $NO_3^{\bullet}$, respectively. Therefore, piperitone is not expected to be long lived in the atmosphere making its oxidation products of particular interest.

Using the ToF-CIMS thirty-three oxidation products were identified from the $OH^{\bullet}$ initiated oxidation of piperitone in a series of simulation chamber experiments, with mechanisms proposed for seventeen of the products. The main reaction pathway was found to be $OH^{\bullet}$ addition to the C=C bond, with H-abstraction also contributing to the reactivity. Some of the oxidation products were also found to be reactive, with the reactions proceeding through several pathways including $OH^{\bullet}$ addition to C=C bonds, H-abstraction and photolysis. The $OH^{\bullet}$ initiated oxidation of piperitone was found to produce SOA, which is of particular interest considering the cooling effect secondary organic aerosols have on the atmosphere.

While it is important to determine the oxidation chemistry of piperitone, it is of more atmospheric relevance to assess the oxidation chemistry of the whole BVOC Sitka spruce emissions. Twenty-five gas-phase products composed primarily of monomers and fragments, and ninety-nine particle-phase products consisting of mainly oligomers, were identified from the $OH^{\bullet}$ initiated oxidation of the whole Sitka spruce BVOC emissions. Products were attributed to the oxidation of piperitone, myrcene and isoprene across the gas-phase and particle-phase. Almost all particle-phase products were classed as ELVOCS and ULVOCs, and likely contributed to particle formation, which commenced within 10 minutes of reaction initiation. The rapid oxidation and SOA formation from the oxidation of whole Sitka spruce emissions is an important aspect that should be taken into consideration when planting Sitka spruce trees. This research therefore highlights the need for policy makers to assess the BVOC emission profile for a tree species, as well as the BVOC reactivity and SOA formation potential prior to establishing plantations.

6.2 Future Work

This study on the BVOCs emitted from Stika spruce and their oxidation has improved knowledge regarding the impact Sitka spruce plantations may have on atmospheric composition and climate. Several follow up studies could be performed to build on this work. In relation to the characterisation of BVOC emissions:

- The trees in this study had visible resin deposits on the trunks, analysis of the resin and analysis of the BVOCs emitted from the soil and fallen litter would assist in assessing the contribution each makes to the overall BVOC flux.
- A study involving different aged trees would provide insight into changes in BVOC emission profiles with age.
- Stress was found to significantly alter the BVOC emission profile from Sitka spruce, therefore it is of particular interest to assess the impacts of stresses relevant to the Irish climate. As a result of climate change Ireland is anticipated to experience higher storm prevalence in the winter months and extended periods of heat in the summer months, therefore the impacts of wounding from storm damage and drought from excessive heat should be determined for Sitka spruce.
- This work was conducted in a laboratory environment, measurements conducted in a Sitka spruce forest are necessary to determine the BVOC profile of naturally growing Sitka spruce trees.

In relation to the atmospheric reactivity of piperitone:

- The experiments conducted with piperitone were performed under dry, NO_x free conditions. Repetition of the experiments under humid conditions and in the presence of NO_x, including characterisation of the particle-phase would provide greater insight into the atmospheric chemistry of piperitone.
- Oxidation experiments could be performed with piperitone, isoprene and myrcene at concentrations proportional to their relative emission fluxes from Sitka spruce, to better reproduce ambient Sitka spruce BVOC oxidation.

- Experimental determination of the rate coefficients and oxidation products for the reaction of piperitone with O_3 and $NO_3^{\bullet}$ would improve knowledge on piperitone atmospheric reactivity.
- A UV absorption spectrum of piperitone would be useful in assessing the potential contribution photolysis makes to the overall reactivity of piperitone.

In relation to the oxidation of the whole Sitka spruce emissions:

- Experiments on the whole Sitka spruce emissions could be performed using O_3 and $NO_3^{\bullet}$ as the oxidants to provide greater insight into the atmospheric chemistry of whole Sitka spruce emissions.
- Oxidation experiments on less commonly observed BVOCs such as the other oxygenated compounds emitted from Stika spruce, would assist in the assignment of whole emission oxidation products to their precursor BVOCs.
- Whole emissions experiments including emissions from soils and fallen litter could be conducted to provide a better understanding of the oxidation products and SOA generated from Sitka spruce in real-world plantations.

Chapter 7 References

(1) Speight, J. G. 1 - Water systems. In natural water remediation, Butterworth-Heinemann, 2020; pp 1-51.
(2) Seinfeld, J. H. Atmospheric Chemistry and Physics : From air pollution to climate change; John Wiley & Sons, Incorporated, 2016.
(3) National, G., Data, Center. U.S. standard atmosphere (1976). Planetary and space science 1992, 40, 553-554. DOI: 10.1016/0032-0633(92)90203-z.
(4) Finlayson-Pitts, B. J.; James N. Pitts, Jr.; Pitts, J. J. N.; Pitts Jr, J. N. Chemistry of the Upper and Lower Atmosphere: Theory, Experiments, and Applications; Elsevier Science & Technology, 1999.
(5) Li, A. J.; Pal, V. K.; Kannan, K. A review of environmental occurrence, toxicity, biotransformation and biomonitoring of volatile organic compounds. Environmental Chemistry and Ecotoxicology 2021, 3, 91-116. DOI: https://doi.org/10.1016/j.enceco.2021.01.001.
(6) Laothawornkitkul, J.; Taylor, J.; Paul, N.; Hewitt, C. Biogenic volatile organic compounds in the Earth system. New Phytologist 2009, 183 (1), 27-51, Review. DOI: 10.1111/j.1469-8137.2009.02859.x.
(7) Andreae, M.; Crutzen, P. Atmospheric aerosols: Biogeochemical sources and role in atmospheric chemistry. Science 1997, 276 (5315), 1052-1058, Review. DOI: 10.1126/science.276.5315.1052.
(8) Misztal, P. K.; Hewitt, C. N.; Wildt, J.; Blande, J. D.; Eller, A. S. D.; Fares, S.; Gentner, D. R.; Gilman, J. B.; Graus, M.; Greenberg, J.; et al. Atmospheric benzenoid emissions from plants rival those from fossil fuels. Scientific Reports 2015, 5. DOI: 10.1038/srep12064 Scopus C7 - 12064.
(9) Boge, O.; Mutzel, A.; Iinuma, Y.; Yli-Pirila, P.; Kahnt, A.; Joutsensaari, J.; Herrmann, H. Gas-phase products and secondary organic aerosol formation from the ozonolysis and photooxidation of myrcene. Atmospheric Environment 2013, 79, 553-560, Article. DOI: 10.1016/j.atmosenv.2013.07.034.
(10) Mutzel, A.; Rodigast, M.; Iinuma, Y.; Boge, O.; Herrmann, H. Monoterpene SOA - Contribution of first-generation oxidation products to formation and chemical composition. Atmospheric Environment 2016, 130, 136-144, Article. DOI: 10.1016/j.atmosenv.2015.10.080.
(11) Guenther, A.; Hewitt, C.; Erickson, D.; Fall, R.; Geron, C.; Graedel, T.; Harley, P.; Klinger, L.; Lerdau, M.; Mckay, W.; Et Al. A global-model of natural volatile organic-compound emissions. Journal of Geophysical Research-Atmospheres 1995, 100 (D5), 8873-8892, Article. DOI: 10.1029/94JD02950.
(12) Lewis, A.; Bartle, K.; McQuaid, J.; Pilling, M.; Seakins, P.; Ridgeon, P. Atmospheric monitoring of volatile organic compounds using programmed temperature vaporization injection. Hrc-Journal of High Resolution Chromatography 1996, 19 (12), 686-690, Article.
(13) Hellén, H.; Tykkä, T.; Hakola, H. Importance of monoterpenes and isoprene in urban air in northern Europe. Atmospheric Environment 2012, 59, 59-66, Article. DOI: 10.1016/j.atmosenv.2012.04.049 Scopus.
(14) Kroflic, A.; Grilc, M.; Grgic, I. Does toxicity of aromatic pollutants increase under remote atmospheric conditions? Scientific Reports 2015, 5, Article. DOI: 10.1038/srep08859.

(15) Seco, R.; Penuelas, J.; Filella, I. Short-chain oxygenated VOCs: Emission and uptake by plants and atmospheric sources, sinks, and concentrations. Atmospheric Environment 2007, 41 (12), 2477-2499, Review. DOI: 10.1016/j.atmosenv.2006.11.029.
(16) Ebi, K.; McGregor, G. Climate change, tropospheric ozone and particulate matter, and health impacts. Environmental Health Perspectives 2008, 116 (11), 1449-1455, Review. DOI: 10.1289/ehp.11463.
(17) Espada, C.; Grossenbacher, J.; Ford, K.; Couch, T.; Shepson, P. The production of organic nitrates from various anthropogenic volatile organic compounds. International Journal of Chemical Kinetics 2005, 37 (11), 675-685, Article. DOI: 10.1002/kin.20122.
(18) Schwantes, R. H.; McVay, R. C.; Zhang, X.; Coggon, M. M.; Lignell, H.; Flagan, R. C.; Wennberg, P. O.; Seinfeld, J. H. Science of the environmental chamber. In Advances in Atmospheric Chemistry, Vol. 1; 2016; pp 1-93.
(19) VanReken, T.; Greenberg, J.; Harley, P.; Guenther, A.; Smith, J. Direct measurement of particle formation and growth from the oxidation of biogenic emissions. Atmospheric Chemistry and Physics 2006, 6, 4403-4413, Article. DOI: 10.5194/acp-6-4403-2006.
(20) Lao, M.; Crilley, L. R.; Salehpoor, L.; Furlani, T. C.; Bourgeois, I.; Neuman, J. A.; Rollins, A. W.; Veres, P. R.; Washenfelder, R. A.; Womack, C. C.; et al. A portable, robust, stable, and tunable calibration source for gas-phase nitrous acid (HONO). Atmos. Meas. Tech. 2020, 13 (11), 5873-5890. DOI: 10.5194/amt-13-5873-2020.
(21) Monks, P. Gas-phase radical chemistry in the troposphere. Chemical Society Reviews 2005, 34 (5), 376-395, Review. DOI: 10.1039/b307982c.
(22) Atkinson, R. Atmospheric chemistry of VOCs and NO_x. Atmospheric Environment 2000, 34 (12-14), 2063-2101, Review. DOI: 10.1016/S1352-2310(99)00460-4.
(23) Hofzumahaus, A.; Rohrer, F.; Lu, K.; Bohn, B.; Brauers, T.; Chang, C.; Fuchs, H.; Holland, F.; Kita, K.; Kondo, Y.; et al. Amplified Trace Gas Removal in the Troposphere. Science 2009, 324 (5935), 1702-1704, Article. DOI: 10.1126/science.1164566.
(24) Karl, M.; Dorn, H.; Holland, F.; Koppmann, R.; Poppe, D.; Rupp, L.; Schaub, A.; Wahner, A. Product study of the reaction of OH radicals with isoprene in the atmosphere simulation chamber SAPHIR. Journal of Atmospheric Chemistry 2006, 55 (2), 167-187, Article. DOI: 10.1007/s10874-006-9034-x.
(25) Peeters, J.; Müller, J.-F.; Stavrakou, T.; Nguyen, V. S. Hydroxyl radical recycling in isoprene oxidation driven by hydrogen bonding and hydrogen tunneling: the upgraded LIM1 mechanism. The Journal of Physical Chemistry A 2014, 118 (38), 8625-8643. DOI: 10.1021/jp5033146.
(26) Fuentes, J.; Lerdau, M.; Atkinson, R.; Baldocchi, D.; Bottenheim, J.; Ciccioli, P.; Lamb, B.; Geron, C.; Gu, L.; Guenther, A.; et al. Biogenic hydrocarbons in the atmospheric boundary layer: A review. Bulletin of the American Meteorological Society 2000, 81 (7), 1537-1575, Review. DOI: 10.1175/1520-0477(2000)081<1537:BHITAB>2.3.CO;2.
(27) Atkinson, R.; Arey, J.; Aschmann, S.; Corchnoy, S.; Shu, Y. Rate constants for the gas-phase reactions of cis-3-hexen-1-ol, cis-3-hexenylacetate, trans-2-hexenal, and linalool with OH and NO_3 radicals and O_3 at 296+/-2 K, and OH radical formation yields from the O_3 reactions. International Journal of Chemical Kinetics 1995, 27 (10), 941-955, Article. DOI: 10.1002/kin.550271002.

(28) Claeys, M.; Graham, B.; Vas, G.; Wang, W.; Vermeylen, R.; Pashynska, V.; Cafmeyer, J.; Guyon, P.; Andreae, M. O.; Artaxo, P.; et al. Formation of secondary organic aerosols through photooxidation of isoprene. Science 2004, 303 (5661), 1173-1176. DOI: 10.1126/science.1092805 Scopus.
(29) Hatakeyama, S.; Izumi, K.; Fukuyama, T.; Akimoto, H.; Washida, N. Reactions of OH with alpha-pinene and beta-pinene in air - estimate of global co production from the atmospheric oxidation of terpenes. Journal of Geophysical Research-Atmospheres 1991, 96 (D1), 947-958, Article. DOI: 10.1029/90JD02341.
(30) Laurila, T.; Hakola, H.; Lindfors, V.; Rinne, J.; Steinbrecher, R.; Kesselmeier, J.; Janson, R.; Kellomäki, S. Biogenic VOC emissions and photochemistry in the boreal regions of Europe. 1996.
(31) Hewitt, C.; MacKenzie, A.; Di Carlo, P.; Di Marco, C.; Dorsey, J.; Evans, M.; Fowler, D.; Gallagher, M.; Hopkins, J.; Jones, C.; et al. Nitrogen management is essential to prevent tropical oil palm plantations from causing ground-level ozone pollution. Proceedings of the National Academy of Sciences of the United States of America 2009, 106 (44), 18447-18451, Article. DOI: 10.1073/pnas.0907541106.
(32) Platt, U.; Perner, D.; Winer, A. M.; Harris, G. W.; Pitts Jr., J. N. Detection of NO3 in the polluted troposphere by differential optical absorption. Geophysical Research Letters 1980, 7 (1), 89-92. DOI: https://doi.org/10.1029/GL007i001p00089.
(33) Wu, T.; Coeur-Tourneur, C.; Dhont, G.; Cassez, A.; Fertein, E.; He, X.; Chen, W. Simultaneous monitoring of temporal profiles of NO_3, NO_2 and O_3 by incoherent broadband cavity enhanced absorption spectroscopy for atmospheric applications. Journal of Quantitative Spectroscopy & Radiative Transfer 2014, 133, 199-205, Article. DOI: 10.1016/j.jqsrt.2013.08.002.
(34) Yuan, H.; Peng, H.; Guan, J.; Liu, Y.; Dai, J.; Su, R.; Guo, Z.; Chen, Y.; Hu, Q.; Yuan, B.; et al. Photodegradation of gaseous toluene by vacuum ultraviolet light: Performance and mechanism. Engineered Science 2020, 9, 68-76. DOI: 10.30919/es8d910 Scopus.
(35) Barber, V. P.; Green, W. H.; Kroll, J. H. Screening for new pathways in atmospheric oxidation chemistry with automated mechanism generation. The Journal of Physical Chemistry A 2021, 125 (31), 6772-6788. DOI: 10.1021/acs.jpca.1c04297.
(36) Ren, Y.; El Baramoussi, E. M.; Daële, V.; Mellouki, A. Atmospheric chemistry of ketones: Reaction of OH radicals with 2-methyl-3-pentanone, 3-methyl-2-pentanone and 4-methyl-2-pentanone. Science of The Total Environment 2021, 780, 146249. DOI: https://doi.org/10.1016/j.scitotenv.2021.146249.
(37) Meylan, W.; Howard, P. A review of quantitative structure-activity relationship methods for the prediction of atmospheric oxidation of organic chemicals. Environmental Toxicology and Chemistry 2003, 22 (8), 1724-1732, Review. DOI: 10.1897/01-275.
(38) Illmann, N.; Gibilisco, R.; Bejan, I.; Patroescu-Klotz, I.; Wiesen, P. Atmospheric oxidation of alpha,beta-unsaturated ketones: kinetics and mechanism of the OH radical reaction. Atmospheric Chemistry and Physics 2021, 21 (17), 13667-13686, Article. DOI: 10.5194/acp-21-13667-2021.
(39) Atkinson, R.; Tuazon, E.; Aschmann, S. Products of the gas-phase reactions of a series of 1-alkenes and 1-methylcyclohexene with the OH radical in the presence of

NO. Environmental Science & Technology 1995, 29 (6), 1674-1680, Article. DOI: 10.1021/es00006a035.
(40) Jorga, S.; Florou, K.; Kaltsonoudis, C.; Kodros, J.; Vasilakopoulou, C.; Cirtog, M.; Fouqueau, A.; Picquet-Varrault, B.; Nenes, A.; Pandis, S. Nighttime chemistry of biomass burning emissions in urban areas: A dual mobile chamber study. Atmospheric Chemistry and Physics 2021, 21 (19), 15337-15349, Article. DOI: 10.5194/acp-21-15337-2021.
(41) Hanson, D. R.; Sawyer, A.; Long, D.; Sofio, D.; Kunz, J.; Wentzel, M. Particle formation from photooxidation of αpinene, limonene, and myrcene. The Journal of Physical Chemistry A 2022, 126 (6), 910-923. DOI: 10.1021/acs.jpca.1c08427.
(42) Tomaz, S.; Wang, D.; Zabalegui, N.; Li, D.; Lamkaddam, H.; Bachmeier, F.; Vogel, A.; Monge, M. E.; Perrier, S.; Baltensperger, U.; et al. Structures and reactivity of peroxy radicals and dimeric products revealed by online tandem mass spectrometry. Nature Communications 2021, 12 (1), 300. DOI: 10.1038/s41467-020-20532-2.
(43) Bejan, I.; Barnes, I.; Wiesen, P.; Wenger, J. C. Temperature dependent rate coefficients for the reaction of OH radicals with dimethylbenzoquinones. Chemical Physics Letters 2015, 639, 145-150. DOI: https://doi.org/10.1016/j.cplett.2015.09.010.
(44) McGillen, M.; Carter, W.; Mellouki, A.; Orlando, J.; Picquet-Varrault, B.; Wallington, T. Database for the kinetics of the gas-phase atmospheric reactions of organic compounds. Earth System Science Data 2020, 12 (2), 1203-1216, Article|Data Paper. DOI: 10.5194/essd-12-1203-2020.
(45) Kiendler-Scharr, A.; Wildt, J.; Maso, M. D.; Hohaus, T.; Kleist, E.; Mentel, T. F.; Tillmann, R.; Uerlings, R.; Schurr, U.; Wahner, A. New particle formation in forests inhibited by isoprene emissions. Nature 2009, 461 (7262), 381-384. DOI: 10.1038/nature08292 Scopus.
(46) Joutsensaari, J.; Loivamaki, M.; Vuorinen, T.; Miettinen, P.; Nerg, A.; Holopainen, J.; Laaksonen, A. Nanoparticle formation by ozonolysis of inducible plant volatiles. Atmospheric Chemistry and Physics 2005, 5, 1489-1495, Article. DOI: 10.5194/acp-5-1489-2005.
(47) Can-Terzi, B.; Ficici, M.; Tecer, L. H.; Sofuoglu, S. C. Fine and coarse particulate matter, trace element content, and associated health risks considering respiratory deposition for Ergene Basin, Thrace. Science of the Total Environment 2021, 754. DOI: 10.1016/j.scitotenv.2020.142026 Scopus C7 - 142026.
(48) Pye, H. O. T.; Ward-Caviness, C. K.; Murphy, B. N.; Appel, K. W.; Seltzer, K. M. Secondary organic aerosol association with cardiorespiratory disease mortality in the United States. Nature Communications 2021, 12 (1), 7215. DOI: 10.1038/s41467-021-27484-1.
(49) Dick, W. D.; Saxena, P.; McMurry, P. H. Estimation of water uptake by organic compounds in submicron aerosols measured during the Southeastern Aerosol and Visibility Study. Journal of Geophysical Research: Atmospheres 2000, 105 (D1), 1471-1479. DOI: https://doi.org/10.1029/1999JD901001.
(50) Hallquist, M.; Wenger, J. C.; Baltensperger, U.; Rudich, Y.; Simpson, D.; Claeys, M.; Dommen, J.; Donahue, N. M.; George, C.; Goldstein, A. H.; et al. The formation, properties and impact of secondary organic aerosol: Current and emerging issues. Atmospheric Chemistry and Physics 2009, 9 (14), 5155-5236. DOI: 10.5194/acp-9-5155-2009 Scopus.

(51) Carslaw, K. S.; Boucher, O.; Spracklen, D. V.; Mann, G. W.; L. Rae, J. G.; Woodward, S.; Kulmala, M. A review of natural aerosol interactions and feedbacks within the Earth system. Atmospheric Chemistry and Physics 2010, 10 (4), 1701-1737. DOI: 10.5194/acp-10-1701-2010 Scopus.
(52) Kulmala, M.; Suni, T.; Lehtinen, K. E. J.; Dal Maso, M.; Boy, M.; Reissell, A.; Rannik, Ü.; Aalto, P.; Keronen, P.; Hakola, H.; et al. A new feedback mechanism linking forests, aerosols, and climate. Atmospheric Chemistry and Physics 2004, 4 (2), 557-562. DOI: 10.5194/acp-4-557-2004 Scopus.
(53) Mahilang, M.; Deb, M. K.; Pervez, S. Biogenic secondary organic aerosols: A review on formation mechanism, analytical challenges and environmental impacts. Chemosphere 2021, 262. DOI: 10.1016/j.chemosphere.2020.127771 Scopus C7 - 127771.
(54) Ramaswamy, V.; Collins, W.; Haywood, J.; Lean, J.; Mahowald, N.; Myhre, G.; Naik, V.; Shine, K. P.; Soden, B.; Stenchikov, G.; et al. Radiative forcing of climate: the historical evolution of the radiative forcing concept, the forcing agents and their quantification, and applications. Meteorological Monographs 2019, 59. DOI: 10.1175/AMSMONOGRAPHS-D-19-0001.1.
(55) Spracklen, D.; Bonn, B.; Carslaw, K. Boreal forests, aerosols and the impacts on clouds and climate. Philosophical Transactions of the Royal Society a-Mathematical Physical and Engineering Sciences 2008, 366 (1885), 4613-4626, Article. DOI: 10.1098/rsta.2008.0201.
(56) IPCC, 2007: Climate Change 2007: The Physical Science Basis. Contribution of Working Group I to the Fourth Assessment Report of the Intergovernmental Panel on Climate Change [Solomon, S., D. Qin, M. Manning, Z. Chen, M. Marquis, K.B. Averyt, M. Tignor and H.L. Miller (eds.)]. Cambridge University Press, Cambridge, United Kingdom and New York, NY, USA, 996 pp.
(57) Masson-Delmotte, V.; Zhai, P.; Pirani, A.; Connors, S. L.; Péan, C.; Berger, S.; Caud, N.; Chen, Y.; Goldfarb, L.; Gomis, M. I.; et al. Climate Change 2021: The Physical Science Basis. Contribution of Working Group I to the Sixth Assessment Report of the Intergovernmental Panel on Climate Change; Cambridge University Press, 2021. DOI: 10.1017/9781009157896.
(58) Barth, M.; McFadden, J. P.; Sun, J.; Wiedinmyer, C.; Chuang, P.; Collins, D.; Griffin, R.; Hannigan, M.; Karl, T.; Kim, S. W.; et al. Coupling between land ecosystems and the atmospheric hydrologic cycle through biogenic aerosol pathways. Bulletin of the American Meteorological Society 2005, 86 (12), 1738-1742. DOI: 10.1175/BAMS-86-12-1738 Scopus.
(59) Li, K.; Zhang, X.; Zhao, B.; Bloss, W. J.; Lin, C.; White, S.; Yu, H.; Chen, L.; Geng, C.; Yang, W.; et al. Suppression of anthropogenic secondary organic aerosol formation by isoprene. npj Climate and Atmospheric Science 2022, 5 (1), 12. DOI: 10.1038/s41612-022-00233-x.
(60) Faiola, C.; Buchholz, A.; Kari, E.; Yli-Pirila, P.; Holopainen, J.; Kivimaenpaa, M.; Miettinen, P.; Worsnop, D.; Lehtinen, K.; Guenther, A.; et al. Terpene composition complexity controls secondary organic aerosol yields from scots pine volatile emissions. Scientific Reports 2018, 8, Article. DOI: 10.1038/s41598-018-21045-1.
(61) Farmer, D. K.; Riches, M. Measuring biosphere-atmosphere exchange of short-lived climate forcers and their precursors. Accounts of Chemical Research 2020, 53 (8), 1427-1435. DOI: 10.1021/acs.accounts.0c00203 Scopus.

(62) Kim, S.; Karl, T.; Guenther, A.; Tyndall, G.; Orlando, J.; Harley, P.; Rasmussen, R.; Apel, E. Emissions and ambient distributions of Biogenic Volatile Organic Compounds (BVOC) in a ponderosa pine ecosystem: interpretation of PTR-MS mass spectra. Atmospheric Chemistry and Physics 2010, 10 (4), 1759-1771, Article. DOI: 10.5194/acp-10-1759-2010.
(63) Hewitt, C. N.; Street, R. A. A qualitative assessment of the emission of non-methane hydrocarbon compounds from the biosphere to the atmosphere in the U.K.: Present knowledge and uncertainties. Atmospheric Environment. Part A. General Topics 1992, 26 (17), 3069-3077. DOI: https://doi.org/10.1016/0960-1686(92)90463-U.
(64) Llusia, J.; Penuelas, J.; Gimeno, B. Seasonal and species-specific response of VOC emissions by Mediterranean woody plant to elevated ozone concentrations. Atmospheric Environment 2002, 36 (24), 3931-3938, Article. DOI: 10.1016/S1352-2310(02)00321-7.
(65) Mermet, K.; Perraudin, E.; Dusanter, S.; Sauvage, S.; Léonardis, T.; Flaud, P.-M.; Bsaibes, S.; Kammer, J.; Michoud, V.; Gratien, A.; et al. Atmospheric reactivity of biogenic volatile organic compounds in a maritime pine forest during the LANDEX episode 1 field campaign. Science of The Total Environment 2021, 756, 144129. DOI: https://doi.org/10.1016/j.scitotenv.2020.144129.
(66) Brilli, F.; Hortnagl, L.; Bamberger, I.; Schnitzhofer, R.; Ruuskanen, T.; Hansel, A.; Loreto, F.; Wohlfahrt, G. Qualitative and quantitative characterization of volatile organic compound emissions from cut grass. Environmental Science & Technology 2012, 46 (7), 3859-3865, Article. DOI: 10.1021/es204025y.
(67) Helmig, D.; Daly, R.; Milford, J.; Guenther, A. Seasonal trends of biogenic terpene emissions. Chemosphere 2013, 93 (1), 35-46, Article. DOI: 10.1016/j.chemosphere.2013.04.058.
(68) Ylisirnio, A.; Buchholz, A.; Mohr, C.; Li, Z.; Barreira, L.; Lambe, A.; Faiola, C.; Kari, E.; Yli-Juuti, T.; Nizkorodov, S.; et al. Composition and volatility of secondary organic aerosol (SOA) formed from oxidation of real tree emissions compared to simplified volatile organic compound (VOC) systems. Atmospheric Chemistry and Physics 2020, 20 (9), 5629-5644, Article. DOI: 10.5194/acp-20-5629-2020.
(69) Konig, G.; Brunda, M.; Puxbaum, H.; Hewitt, C.; Duckham, S.; Rudolph, J. Relative contribution of oxygenated hydrocarbons to the total biogenic voc emissions of selected mid-european agricultural and natural plant-species. Atmospheric Environment 1995, 29 (8), 861-874, Article. DOI: 10.1016/1352-2310(95)00026-U.
(70) Helmig, D.; Ortega, J.; Guenther, A.; Herrick, J.; Geron, C. Sesquiterpene emissions from loblolly pine and their potential contribution to biogenic aerosol formation in the Southeastern US. Atmospheric Environment 2006, 40 (22), 4150-4157, Article. DOI: 10.1016/j.atmosenv.2006.02.035.
(71) Hakola, H.; Tarvainen, V.; Back, J.; Ranta, H.; Bonn, B.; Rinne, J.; Kulmala, M. Seasonal variation of mono- and sesquiterpene emission rates of Scots pine. Biogeosciences 2006, 3 (1), 93-101, Article. DOI: 10.5194/bg-3-93-2006.
(72) Janson, R.; De Serves, C.; Romero, R. Emission of isoprene and carbonyl compounds from a boreal forest and wetland in Sweden. Agricultural and Forest Meteorology 1999, 98-9, 671-681, Article. DOI: 10.1016/S0168-1923(99)00134-3.
(73) Mentel, T.; Wildt, J.; Kiendler-Scharr, A.; Kleist, E.; Tillmann, R.; Dal Maso, M.; Fisseha, R.; Hohaus, T.; Spahn, H.; Uerlings, R.; et al. Photochemical production of

aerosols from real plant emissions. Atmospheric Chemistry and Physics 2009, 9 (13), 4387-4406, Article. DOI: 10.5194/acp-9-4387-2009.
(74) Website. Certified sustainable palm oil and alternatives for the future | Earth.Org. (accessed 13/10/2023).
(75) Austin, K. G.; Schwantes, A.; Gu, Y.; Kasibhatla, P. S. What causes deforestation in Indonesia? Environmental Research Letters 2019, 14 (2), 024007. DOI: 10.1088/1748-9326/aaf6db.
(76) Wilcove, D.; Koh, L. Addressing threats to biodiversity from oil-palm agriculture. Biodiversity and Conservation 2010, 19, 999-1007. DOI: 10.1007/s10531-009-9760-x.
(77) O'Callaghan, C. J.; Irwin, S.; Byrne, K. A.; O'Halloran, J. The role of planted forests in the provision of habitat: an Irish perspective. Biodiversity and Conservation 2017, 26 (13), 3103-3124. DOI: 10.1007/s10531-016-1125-7.
(78) Evans, R. C.; Tingey, D. T.; Gumpertz, M. L.; Burns, W. F. Estimates of isoprene and monoterpene emission rates in plants. Botanical Gazette 1982, 143 (3), 304-310. DOI: 10.1086/botanicalgazette.143.3.2474826 Scopus.
(79) Evans, R.; Tingey, D.; Gumpertz, M. Interspecies variation in terpenoid emissions from engelmann and sitka spruce seedlings. Forest Science 1985, 31 (1), 132-142, Article.
(80) Street, R.; Duckham, S. C.; Hewitt, C. N. Measurements of non-methane hydrocarbon emissions rates from Sitka spruce in the laboratory and field; European Commission, 1993.
(81) Street, R. A.; Duckham, S. C.; Hewitt, C. N. Laboratory and field studies of biogenic volatile organic compound emissions from Sitka spruce (Picea sitchensis Bong.) in the United Kingdom. Journal of Geophysical Research Atmospheres 1996, 101 (17), 22799-22806. DOI: 10.1029/96jd01171 Scopus.
(82) Tani, A.; Hayward, S.; Hewitta, C. Measurement of monoterpenes and related compounds by proton transfer reaction-mass spectrometry (PTR-MS). International Journal of Mass Spectrometry 2003, 223 (1-3), 561-578, Article. DOI: 10.1016/S1387-3806(02)00880-1.
(83) Hayward, S.; Tani, A.; Owen, S.; Hewitt, C. Online analysis of volatile organic compound emissions from Sitka spruce (Picea sitchensis). Tree Physiology 2004, 24 (7), 721-728, Article. DOI: 10.1093/treephys/24.7.721.
(84) Lehman, A. J.; Lynn, E. V. The leaf oils of Washington conifers: V. Picea sitchensis. The Journal of the American Pharmaceutical Association (1912) 1931, 20 (1), 29-32. DOI: https://doi.org/10.1002/jps.3080200111.
(85) Rudloff, E. V. Gas–liquid chromatography of terpenes: part x. the volatile oils of the leaves of sitka and engelmann spruce. Canadian Journal of Chemistry 1964, 42 (5), 1057-1062. DOI: 10.1139/v64-161.
(86) Hrutfiord, B. F.; Hopley, S. M.; Gara, R. I. Monoterpenes in sitka spruce: Within tree and seasonal variation. Phytochemistry 1974, 13 (10), 2167-2170. DOI: 10.1016/0031-9422(74)85021-1 Scopus.
(87) von Rudloff, E. M. Variation in leaf oil terpene composition of Sitka spruce. Phytochemistry 1978, 17 (1), 127-130. DOI: https://doi.org/10.1016/S0031-9422(00)89693-4.

(88) Brooks, J.; Borden, J.; Pierce, H.; Lister, G. Seasonal-variation in foliar and bud monoterpenes in sitka spruce. Canadian Journal of Botany-Revue Canadienne De Botanique 1987, 65 (6), 1249-1252, Article. DOI: 10.1139/b87-173.
(89) Brooks, J. E.; Borden, J. H.; Jr., H. D. P.; Lister, G. R. Seasonal variation in foliar and bud monoterpenes in Sitka spruce. Canadian Journal of Botany 1987, 65 (6), 1249-1252. DOI: 10.1139/b87-173.
(90) Forrest, G. I. Seasonal and spatial variation in cortical monoterpene composition of Sitka spruce oleoresin. Canadian Journal of Forest Research 1980, 10 (4), 452-457. DOI: 10.1139/x80-074.
(91) Bertram, T.; Kimmel, J.; Crisp, T.; Ryder, O.; Yatavelli, R.; Thornton, J.; Cubison, M.; Gonin, M.; Worsnop, D. A field-deployable, chemical ionization time-of-flight mass spectrometer. Atmospheric Measurement Techniques 2011, 4 (7), 1471-1479, Article. DOI: 10.5194/amt-4-1471-2011.
(92) Ji, Y.; Gregory Huey, L.; Tanner, D. J.; Ro Lee, Y.; Veres, P. R.; Andrew Neuman, J.; Wang, Y.; Wang, X. A vacuum ultraviolet ion source (VUV-IS) for iodide-chemical ionization mass spectrometry: A substitute for radioactive ion sources. Atmospheric Measurement Techniques 2020, 13 (7), 3683-3696. DOI: 10.5194/amt-13-3683-2020 Scopus.
(93) Kim, M. J.; Zoerb, M. C.; Campbell, N. R.; Zimmermann, K. J.; Blomquist, B. W.; Huebert, B. J.; Bertram, T. H. Revisiting benzene cluster cations for the chemical ionization of dimethyl sulfide and select volatile organic compounds. Atmospheric Measurement Techniques 2016, 9 (4), 1473-1484. DOI: 10.5194/amt-9-1473-2016 Scopus.
(94) Hansel, A.; Scholz, W.; Mentler, B.; Fischer, L.; Bernd, T. Detection of RO2 radicals and other products from cyclohexene ozonolysis with NH4+ and acetate chemical ionization mass spectrometry. Atmospheric Environment 2018, 186, 248-255, Article. DOI: 10.1016/j.atmosenv.2018.04.023.
(95) Barreira, L. M. F.; Ylisirniö, A.; Pullinen, I.; Buchholz, A.; Li, Z.; Lipp, H.; Junninen, H.; Noe, S. M.; Krasnova, A.; Krasnov, D.; et al. The importance of sesquiterpene oxidation products for secondary organic aerosol formation in a spring-time hemi-boreal forest. Atmos. Chem. Phys. Discuss. 2021, 2021, 1-32. DOI: 10.5194/acp-2021-8.
(96) Liu, J.; D'Ambro, E.; Lee, B.; Lopez-Hilfiker, F.; Zaveri, R.; Rivera-Rios, J.; Keutsch, F.; Iyer, S.; Kurten, T.; Zhang, Z.; et al. Efficient isoprene secondary organic aerosol formation from a non-IEPDX pathway. Environmental Science & Technology 2016, 50 (18), 9872-9880, Article. DOI: 10.1021/acs.est.6b01872.
(97) Lee, B. H.; Lopez-Hilfiker, F. D.; D'Ambro, E. L.; Zhou, P.; Boy, M.; Petäjä, T.; Hao, L.; Virtanen, A.; Thornton, J. A. Semi-volatile and highly oxygenated gaseous and particulate organic compounds observed above a boreal forest canopy. Atmospheric Chemistry and Physics 2018, 18 (15), 11547-11562. DOI: 10.5194/acp-18-11547-2018 Scopus.
(98) Ye, C.; Yuan, B.; Lin, Y.; Wang, Z.; Hu, W.; Li, T.; Chen, W.; Wu, C.; Wang, C.; Huang, S.; et al. Chemical characterization of oxygenated organic compounds in the gas phase and particle phase using iodide CIMS with FIGAERO in urban air. Atmospheric Chemistry and Physics 2021, 21 (11), 8455-8478. DOI: 10.5194/acp-21-8455-2021 Scopus.

(99) Sanchez, J.; Tanner, D. J.; Chen, D.; Huey, L. G.; Ng, N. L. A new technique for the direct detection of HO2 radicals using bromide chemical ionization mass spectrometry (Br-CIMS): initial characterization. Atmos. Meas. Tech. 2016, 9 (8), 3851-3861. DOI: 10.5194/amt-9-3851-2016.
(100) Osuagwu, C. G. Investigation of volatile organic compounds from diesel engine emissions using H3O+ chemical ionisation mass spectrometry (H3O+-CIMS). Queensland University of Technology, 2020.
(101) Wang, M.; He, X. C.; Finkenzeller, H.; Iyer, S.; Chen, D.; Shen, J.; Simon, M.; Hofbauer, V.; Kirkby, J.; Curtius, J.; et al. Measurement of iodine species and sulfuric acid using bromide chemical ionization mass spectrometers. Atmos. Meas. Tech. 2021, 14 (6), 4187-4202. DOI: 10.5194/amt-14-4187-2021.
(102) Yatavelli, R.; Lopez-Hilfiker, F.; Wargo, J.; Kimmel, J.; Cubison, M.; Bertram, T.; Jimenez, J.; Gonin, M.; Worsnop, D.; Thornton, J. A Chemical Ionization High-Resolution Time-of-Flight Mass Spectrometer Coupled to a Micro Orifice Volatilization Impactor (MOVI-HRToF-CIMS) for Analysis of Gas and Particle-Phase Organic Species. Aerosol Science and Technology - AEROSOL SCI TECH 2012, 46. DOI: 10.1080/02786826.2012.712236.
(103) TOFWERK. Reference Guide TOF-CIMS Instrument. 2016.
(104) Junninen, H.; Ehn, M.; Petäjä, T.; Luosujärvi, L.; Kotiaho, T.; Kostiainen, R.; Rohner, U.; Gonin, M.; Fuhrer, K.; Kulmala, M.; et al. A high-resolution mass spectrometer to measure atmospheric ion composition. Atmos. Meas. Tech. 2010, 3 (4), 1039-1053. DOI: 10.5194/amt-3-1039-2010.
(105) Riva, M.; Rantala, P.; Krechmer, J. E.; Peräkylä, O.; Zhang, Y.; Heikkinen, L.; Garmash, O.; Yan, C.; Kulmala, M.; Worsnop, D.; et al. Evaluating the performance of five different chemical ionization techniques for detecting gaseous oxygenated organic species. Atmos. Meas. Tech. 2019, 12 (4), 2403-2421. DOI: 10.5194/amt-12-2403-2019.
(106) Lavi, A.; Vermeuel, M.; Novak, G.; Bertram, T. The sensitivity of benzene cluster cation chemical ionization mass spectrometry to select biogenic terpenes. Atmospheric Measurement Techniques 2018, 11 (6), 3251-3262, Article. DOI: 10.5194/amt-11-3251-2018.
(107) Breitenlechner, M.; Novak, G. A.; Neuman, J. A.; Rollins, A. W.; Veres, P. R. A versatile vacuum ultraviolet ion source for reduced pressure bipolar chemical ionization mass spectrometry. Atmos. Meas. Tech. 2022, 15 (5), 1159-1169. DOI: 10.5194/amt-15-1159-2022.
(108) Ganske, J.; Wingen, L.; Perraud, V.; Finlayson-Pitts, B. Role of Gas-Phase Halogen Bonding in Ambient Chemical Ionization Mass Spectrometry Utilizing Iodine. Acs Earth and Space Chemistry 2019, 3 (7), 1315-1328, Article. DOI: 10.1021/acsearthspacechem.9b00030.
(109) TOFWERK. Getting Started Guide
TOF-CIMS Instrument. 2016.
(110) TOFWERK. Thuner User Guide. 2014.
(111) Lopez-Hilfiker, F.; Mohr, C.; Ehn, M.; Rubach, F.; Kleist, E.; Wildt, J.; Mentel, T.; Lutz, A.; Hallquist, M.; Worsnop, D.; et al. A novel method for online analysis of gas and particle composition: description and evaluation of a Filter Inlet for Gases and AEROsols (FIGAERO). Atmospheric Measurement Techniques 2014, 7 (4), 983-1001, Article. DOI: 10.5194/amt-7-983-2014.

(112) Thornton, J.; Mohr, C.; Schobesberger, S.; D'Ambro, E.; Lee, B.; Lopez-Hilfiker, F. Evaluating organic aerosol sources and evolution with a combined molecular composition and volatility framework using the Filter Inlet for Gases and Aerosols (FIGAERO). Accounts of Chemical Research 2020, 53 (8), 1415-1426, Review. DOI: 10.1021/acs.accounts.0c00259.
(113) Ylisirnio, A.; Barreira, L.; Pullinen, I.; Buchholz, A.; Jayne, J.; Krechmer, J.; Worsnop, D.; Virtanen, A.; Schobesberger, S. On the calibration of FIGAERO-ToF-CIMS: importance and impact of calibrant delivery for the particle-phase calibration. Atmospheric Measurement Techniques 2021, 14 (1), 355-367, Article. DOI: 10.5194/amt-14-355-2021.
(114) Lopez-Hilfiker, F. D.; Iyer, S.; Mohr, C.; Lee, B. H.; D'Ambro, E. L.; Kurtén, T.; Thornton, J. A. Constraining the sensitivity of iodide adduct chemical ionization mass spectrometry to multifunctional organic molecules using the collision limit and thermodynamic stability of iodide ion adducts. Atmospheric Measurement Techniques 2016, 9 (4), 1505-1512, Article. DOI: 10.5194/amt-9-1505-2016 Scopus.
(115) Mehra, A.; Wang, Y.; Krechmer, J.; Lambe, A.; Majluf, F.; Morris, M.; Priestley, M.; Bannan, T.; Bryant, D.; Pereira, K.; et al. Evaluation of the chemical composition of gas- and particle-phase products of aromatic oxidation. Atmospheric Chemistry and Physics 2020, 20 (16), 9783-9803, Article. DOI: 10.5194/acp-20-9783-2020.
(116) WAng, S.; Flagan, R. Scanning electrical mobility spectrometer. Aerosol Science and Technology 1990, 13 (2), 230-240, Article. DOI: 10.1080/02786829008959441.
(117) Kuang, C. Scanning Mobility Particle Spectrometer Instrument Handbook. US Department of Energy, 2016.
(118) Incorporated, T. Condensation Particle Counter, Model 3750. 2017.
(119) API, T. Operation Manual Model T200 NO/NO2/NOX Analyzer. 2018.
(120) API, T. Operation Manual Model T400 Photometric Ozone Analyzer. 2018.
(121) Ashu-Ayem, E. R.; Nitschke, U.; Monahan, C.; Chen, J.; Darby, S. B.; Smith, P. D.; O'Dowd, C. D.; Stengel, D. B.; Venables, D. S. Coastal iodine emissions. 1. release of i2 by laminaria digitata in chamber experiments. Environmental Science & Technology 2012, 46 (19), 10413-10421. DOI: 10.1021/es204534v.
(122) Kesselmeier, J.; Schäfer, L.; Ciccioli, P.; Brancaleoni, E.; Cecinato, A.; Frattoni, M.; Foster, P.; Jacob, V.; Denis, J.; Fugit, J. L.; et al. Emission of monoterpenes and isoprene from a Mediterranean oak species Quercus ilex L. measured within the BEMA (Biogenic Emissions in the Mediterranean Area) project. Atmospheric Environment 1996, 30 (10), 1841-1850. DOI: https://doi.org/10.1016/1352-2310(95)00376-2.
(123) Hartikainen, K.; Riikonen, J.; Nerg, A.; Kivimaenpaa, M.; Ahonen, V.; Tervahauta, A.; Karenlampi, S.; Maenpaa, M.; Rousi, M.; Kontunen-Soppela, S.; et al. Impact of elevated temperature and ozone on the emission of volatile organic compounds and gas exchange of silver birch (Betula pendula Roth). Environmental and Experimental Botany 2012, 84, 33-43, Article. DOI: 10.1016/j.envexpbot.2012.04.014.
(124) Kerhoulas, L. P.; Weisgrau, A. S.; Hoeft, E. C.; Kerhoulas, N. J. Vertical gradients in foliar physiology of tall Picea sitchensis trees. Tree Physiology 2020, 40 (3), 321-332. DOI: 10.1093/treephys/tpz137 (acccessed 9/22/2022).
(125) Portillo-Estrada, M.; Ariza-Carricondo, C.; Ceulemans, R. Outburst of senescence-related VOC emissions from a bioenergy poplar plantation. Plant

Physiology and Biochemistry 2020, 148, 324-332. DOI: 10.1016/j.plaphy.2020.01.024 Scopus.
(126) Henriques, F. Leaf chlorophyll fluorescence: background and fundamentals for plant biologists. Botanical Review 2009, 75 (3), 249-270, Article. DOI: 10.1007/s12229-009-9035-y.
(127) Wilkinson, M.; Owen, S.; Possell, M.; Hartwell, J.; Gould, P.; Hall, A.; Vickers, C.; Hewitt, C. Circadian control of isoprene emissions from oil palm (Elaeis guineensis). Plant Journal 2006, 47 (6), 960-968, Article. DOI: 10.1111/j.1365-313X.2006.02847.x.
(128) Guenther, A. B.; Monson, R. K.; Fall, R. Isoprene and monoterpene emission rate variability: Observations with eucalyptus and emission rate algorithm development. Journal of Geophysical Research: Atmospheres 1991, 96 (D6), 10799-10808. DOI: https://doi.org/10.1029/91JD00960.
(129) Tingey, D. T.; Manning, M.; Grothaus, L. C.; Burns, W. F. The influence of light and temperature on isoprene emission rates from live oak. Physiologia Plantarum 1979, 47 (2), 112-118. DOI: https://doi.org/10.1111/j.1399-3054.1979.tb03200.x.
(130) Guenther, A. B.; Zimmerman, P. R.; Harley, P. C.; Monson, R. K.; Fall, R. Isoprene and monoterpene emission rate variability: model evaluations and sensitivity analyses. Journal of Geophysical Research 1993, 98 (D7), 12,609-"612,617". DOI: 10.1029/93jd00527 Scopus.
(131) Kesselmeier, J.; Staudt, M. Biogenic volatile organic compounds (VOC): An overview on emission, physiology and ecology. Journal of Atmospheric Chemistry 1999, 33 (1), 23-88, Review. DOI: 10.1023/A:1006127516791.
(132) Schuh, G.; Heiden, A.; Hoffmann, T.; Kahl, J.; Rockel, P.; Rudolph, J.; Wildt, J. Emissions of volatile organic compounds from sunflower and beech: Dependence on temperature and light intensity. Journal of Atmospheric Chemistry 1997, 27 (3), 291-318, Article. DOI: 10.1023/A:1005850710257.
(133) Owen, S. M.; MacKenzie, A. R.; Stewart, H.; Donovan, R.; Hewitt, C. N. Biogenic volatile organic compound (voc) emission estimates from an urban tree canopy. Ecological Applications 2003, 13 (4), 927-938. DOI: https://doi.org/10.1890/01-5177.
(134) Peñuelas, J.; Llusià, J.; Gimeno, B. S. Effects of ozone concentrations on biogenic volatile organic compounds emission in the Mediterranean region. Environmental Pollution 1999, 105 (1), 17-23. DOI: 10.1016/S0269-7491(98)00214-0 Scopus.
(135) Liao, H.; Henze, D. K.; Seinfeld, J. H.; Wu, S.; Mickley, L. J. Biogenic secondary organic aerosol over the United States: Comparison of climatological simulations with observations. Journal of Geophysical Research Atmospheres 2007, 112 (6). DOI: 10.1029/2006JD007813 Scopus C7 - D06201.
(136) Timkovsky, J.; Gankema, P.; Pierik, R.; Holzinger, R. A plant chamber system with downstream reaction chamber to study the effects of pollution on biogenic emissions. Environmental Sciences: Processes and Impacts 2014, 16 (10), 2301-2312. DOI: 10.1039/c4em00214h Scopus.
(137) Hakola, H.; Laurila, T.; Lindfors, V.; Hellen, H.; Gaman, A.; Rinne, J. Variation of the VOC emission rates of birch species during the growing season. Boreal Environment Research 2001, 6 (3), 237-249, Article.
(138) Geron, C.; Rasmussen, R.; Arnts, R. R.; Guenther, A. A review and synthesis of monoterpene speciation from forests in the United States. Atmospheric Environment 2000, 34 (11), 1761-1781. DOI: 10.1016/S1352-2310(99)00364-7 Scopus.

(139) Mofikoya, A.; Miura, K.; Ghimire, R.; Blande, J.; Kivimaenpaa, M.; Holopainen, T.; Holopainen, J. Understorey rhododendron tomentosum and leaf trichome density affect mountain birch VOC emissions in the subarctic. Scientific Reports 2018, 8, Article. DOI: 10.1038/s41598-018-31084-3.
(140) Pio, C. A.; Valente, A. R. Terpene emissions from resin tapping practices; European Commission, 1993.
(141) Street, R.; Duckham, S. C.; Hewitt, C. N. Measurements of non-methane hydrocarbon emissions rates from Sitka
spruce in the laboratory and field; European Commission, 1993.
(142) Niinemets, Ü.; Kuhn, U.; Harley, P. C.; Staudt, M.; Arneth, A.; Cescatti, A.; Ciccioli, P.; Copolovici, L.; Geron, C.; Guenther, A.; et al. Estimations of isoprenoid emission capacity from enclosure studies: measurements, data processing, quality and standardized measurement protocols. Biogeosciences 2011, 8 (8), 2209-2246. DOI: 10.5194/bg-8-2209-2011.
(143) Gomez, L. G.; Loubet, B.; Lafouge, F.; Ciuraru, R.; Bsaibes, S.; Kammer, J.; Buysse, P.; Durand, B.; Gueudet, J.-C.; Fanucci, O.; et al. Effect of senescence on biogenic volatile organic compound fluxes in wheat plants. Atmospheric Environment 2021, 266, 118665. DOI: https://doi.org/10.1016/j.atmosenv.2021.118665.
(144) Praplan, A. P.; Tykkä, T.; Schallhart, S.; Tarvainen, V.; Bäck, J.; Hellén, H. OH reactivity from the emissions of different tree species: investigating the missing reactivity in a boreal forest. Biogeosciences 2020, 17 (18), 4681-4705. DOI: 10.5194/bg-17-4681-2020.
(145) Hohaus, T.; Kuhn, U.; Andres, S.; Kaminski, M.; Rohrer, F.; Tillmann, R.; Wahner, A.; Wegener, R.; Yu, Z.; Kiendler-Scharr, A. A new plant chamber facility, PLUS, coupled to the atmosphere simulation chamber SAPHIR. Atmospheric Measurement Techniques 2016, 9 (3), 1247-1259. DOI: 10.5194/amt-9-1247-2016 Scopus.
(146) Daussy, J.; Staudt, M. Do future climate conditions change volatile organic compound emissions from Artemisia annua? Elevated CO_2 and temperature modulate actual VOC emission rate but not its emission capacity. Atmospheric Environment: X 2020, 7, 100082. DOI: https://doi.org/10.1016/j.aeaoa.2020.100082.
(147) Kainulainen, P.; Holopainen, J.; Oksanen, J. Effects of gaseous air pollutants on secondary chemistry of Scots pine and Norway spruce seedlings. Water Air and Soil Pollution 1995, 85 (3), 1393-1398, Article|Proceedings Paper. DOI: 10.1007/BF00477176.
(148) Ortega, J.; Helmig, D. Approaches for quantifying reactive and low-volatility biogenic organic compound emissions by vegetation enclosure techniques - Part A. Chemosphere 2008, 72 (3), 343-364, Review. DOI: 10.1016/j.chemosphere.2007.11.020.
(149) Kempf, K.; Allwine, E.; Westberg, H.; Claiborn, C.; Lamb, B. Hydrocarbon emissions from spruce species using environmental chamber and branch enclosure methods. Atmospheric Environment 1996, 30 (9), 1381-1389. DOI: 10.1016/1352-2310(95)00462-9 Scopus.
(150) Hao, L.; Yli-Pirila, P.; Tiitta, P.; Romakkaniemi, S.; Vaattovaara, P.; Kajos, M.; Rinne, J.; Heijari, J.; Kortelainen, A.; Miettinen, P.; et al. New particle formation from the oxidation of direct emissions of pine seedlings. Atmospheric Chemistry and Physics 2009, 9 (20), 8121-8137, Article. DOI: 10.5194/acp-9-8121-2009.

(151) Hakola, H.; Rinne, J.; Laurila, T. The hydrocarbon emission rates of tea-leafed willow (Salix phylicifolia), silver birch (Betula pendula) and European aspen (Populus tremula). Atmospheric Environment 1998, 32 (10), 1825-1833. DOI: 10.1016/S1352-2310(97)00482-2 Scopus.
(152) Tarvainen, V.; Hakola, H.; Hellen, H.; Back, J.; Hari, P.; Kulmala, M. Temperature and light dependence of the VOC emissions of Scots pine. Atmospheric Chemistry and Physics 2005, 5, 989-998, Article. DOI: 10.5194/acp-5-989-2005.
(153) Faiola, C.; Wen, M.; VanReken, T. Chemical characterization of biogenic secondary organic aerosol generated from plant emissions under baseline and stressed conditions: inter- and intra-species variability for six coniferous species. Atmospheric Chemistry and Physics 2015, 15 (7), 3629-3646, Article. DOI: 10.5194/acp-15-3629-2015.
(154) Yuan, B.; Koss, A.; Warneke, C.; Gilman, J. B.; Lerner, B. M.; Stark, H.; De Gouw, J. A. A high-resolution time-of-flight chemical ionization mass spectrometer utilizing hydronium ions (H_3O^+ ToF-CIMS) for measurements of volatile organic compounds in the atmosphere. Atmospheric Measurement Techniques 2016, 9 (6), 2735-2752. DOI: 10.5194/amt-9-2735-2016 Scopus.
(155) Bourtsoukidis, E.; Williams, J.; Kesselmeier, J.; Jacobi, S.; Bonn, B. From emissions to ambient mixing ratios: Online seasonal field measurements of volatile organic compounds over a Norway spruce-dominated forest in central Germany. Atmospheric Chemistry and Physics 2014, 14 (13), 6495-6510. DOI: 10.5194/acp-14-6495-2014 Scopus.
(156) Tingey, D. T.; Marybeth, M.; Grothaus, L. C.; Burns, W. F. Influence of Light and Temperature on Monoterpene Emission Rates from Slash Pine. Plant Physiology 1980, 65 (5), 797-801. Jstor.
(157) Bourtsoukidis, E.; Bonn, B.; Dittmann, A.; Hakola, H.; Hellen, H.; Jacobi, S. Ozone stress as a driving force of sesquiterpene emissions: a suggested parameterisation. Biogeosciences 2012, 9 (11), 4337-4352, Article. DOI: 10.5194/bg-9-4337-2012.
(158) PHCBi. MLR-352 Operating Instructions Versatile Environmental Test Chamber. 2018.
(159) MLR-352, P. Akribis Scientific Ltd., (accessed 2023 24/07/2023).
(160) Marková, I.; Kubásek, J. Transmittance of young norway spruce stand canopy for photosynthetically active radiation during the growing season. Acta Universitatis Agriculturae et Silviculturae Mendelianae Brunensis 2013, 61 (1), 129-135. DOI: 10.11118/actaun201361010129 Scopus.
(161) Byrne, K. A.; Kiely, G.; Leahy, P. CO2 fluxes in adjacent new and permanent temperate grasslands. Agricultural and Forest Meteorology 2005, 135 (1-4), 82-92. DOI: 10.1016/j.agrformet.2005.10.005 Scopus.
(162) Kelly., P. c. w. C. Met Éireann. 2023.
(163) Staudt, M.; Joffre, R.; Rambal, S. How growth conditions affect the capacity of Quercus ilex leaves to emit monoterpenes. New Phytologist 2003, 158, 61-73.
(164) Reissell, A.; Harry, C.; Aschmann, S.; Atkinson, R.; Arey, J. Formation of acetone from the OH radical- and O-3-initiated reactions of a series of monoterpenes. Journal of Geophysical Research-Atmospheres 1999, 104 (D11), 13869-13879, Article. DOI: 10.1029/1999JD900198.
(165) Vilar, E. G.; Ouyang, H.; O'Sullivan, M. G.; Kerry, J. P.; Hamill, R. M.; O'Grady, M. N.; Mohammed, H. O.; Kilcawley, K. N. Effect of salt reduction and inclusion of 1%

edible seaweeds on the chemical, sensory and volatile component profile of reformulated frankfurters. Meat Science 2020, 161, 108001. DOI: https://doi.org/10.1016/j.meatsci.2019.108001.
(166) Purser, G.; Drewer, J.; Heal, M.; Sircus, R.; Dunn, L.; Morison, J. Isoprene and monoterpene emissions from alder, aspen and spruce short-rotation forest plantations in the United Kingdom. Biogeosciences 2021, 18 (8), 2487-2510, Article. DOI: 10.5194/bg-18-2487-2021.
(167) Janson, R. W. Monoterpene emissions from Scots pine and Norwegian spruce. Journal of Geophysical Research 1993, 98 (D2), 2839-2850. DOI: 10.1029/92JD02394 Scopus.
(168) Haapanala, S.; Ekberg, A.; Hakola, H.; Tarvainen, V.; Rinne, J.; Hellen, H.; Arneth, A. Mountain birch - potentially large source of sesquiterpenes into high latitude atmosphere. Biogeosciences 2009, 6 (11), 2709-2718, Article. DOI: 10.5194/bg-6-2709-2009.
(169) Scala, A.; Allmann, S.; Mirabella, R.; Haring, M. A.; Schuurink, R. C. Green leaf volatiles: A plant's multifunctional weapon against herbivores and pathogens. International Journal of Molecular Sciences 2013, 14 (9), 17781-17811. DOI: 10.3390/ijms140917781 Scopus.
(170) Kännaste, A.; Vongvanich, N.; Borg-Karlson, A. K. Infestation by a Nalepella species induces emissions of α- and β-farnesenes, (-)-linalool and aromatic compounds in Norway spruce clones of different susceptibility to the large pine weevil. Arthropod-Plant Interactions 2008, 2 (1), 31-41. DOI: 10.1007/s11829-008-9029-4 Scopus.
(171) Hayward, S.; Hewitt, C. N.; Sartin, J. H.; Owen, S. M. Performance characteristics and applications of a proton transfer reaction-mass spectrometer for measuring volatile organic compounds in ambient air. Environmental Science and Technology 2002, 36 (7), 1554-1560. DOI: 10.1021/es0102181 Scopus.
(172) Filella, I.; Wilkinson, M. J.; Llusià, J.; Hewitt, C. N.; Peñuelas, J. Volatile organic compounds emissions in Norway spruce (Picea abies) in response to temperature changes. Physiologia Plantarum 2007, 130 (1), 58-66. DOI: 10.1111/j.1399-3054.2007.00881.x Scopus.
(173) Lang-Yona, N.; Rudich, Y.; Mentel, T.; Bohne, A.; Buchholz, A.; Kiendler-Scharr, A.; Kleist, E.; Spindler, C.; Tillmann, R.; Wildt, J. The chemical and microphysical properties of secondary organic aerosols from Holm Oak emissions. Atmospheric Chemistry and Physics 2010, 10 (15), 7253-7265, Article. DOI: 10.5194/acp-10-7253-2010.
(174) Zhang, Q.; Birgersson, G.; Zhu, J.; Lofstedt, C.; Lofqvist, J.; Schlyter, F. Leaf volatiles from nonhost deciduous trees: Variation by tree species, season and temperature, and electrophysiological activity in Ips typographus. Journal of Chemical Ecology 1999, 25 (8), 1923-1943, Article. DOI: 10.1023/A:1020994119019.
(175) Liu, B.; Kaurilind, E.; Jiang, Y.; Niinemets, U. Methyl salicylate differently affects benzenoid and terpenoid volatile emissions in Betula pendula. Tree Physiology 2018, 38 (10), 1513-1525, Article. DOI: 10.1093/treephys/tpy050.
(176) Mehra, A.; Krechmer, J. E.; Lambe, A.; Sarkar, C.; Williams, L.; Khalaj, F.; Guenther, A.; Jayne, J.; Coe, H.; Worsnop, D.; et al. Oligomer and highly oxygenated organic molecule formation from oxidation of oxygenated monoterpenes emitted by

California sage plants. Atmos. Chem. Phys. 2020, 20 (18), 10953-10965. DOI: 10.5194/acp-20-10953-2020.
(177) Pettersson, M. Stress Related Emissions of Norway Spruce Plants. Trita-CHE-Report 2007. DiVA.
(178) Mäntylä, E.; Alessio, G. A.; Blande, J. D.; Heijari, J.; Holopainen, J. K.; Laaksonen, T.; Piirtola, P.; Klemola, T. From plants to birds: Higher avian predation rates in trees responding to insect herbivory. PLoS ONE 2008, 3 (7). DOI: 10.1371/journal.pone.0002832 Scopus C7 - e2832.
(179) Portillo-Estrada, M.; Niinemets, Ü. Massive release of volatile organic compounds due to leaf midrib wounding in Populus tremula. Plant Ecology 2018, 219 (9), 1021-1028. DOI: 10.1007/s11258-018-0854-y Scopus.
(180) Hellén, H.; Praplan, A. P.; Tykkä, T.; Helin, A.; Schallhart, S.; Schiestl-Aalto, P. P.; Bäck, J.; Hakola, H. Sesquiterpenes and oxygenated sesquiterpenes dominate the VOC (C5–C20) emissions of downy birches. Atmos. Chem. Phys. 2021, 21 (10), 8045-8066. DOI: 10.5194/acp-21-8045-2021.
(181) Mentel, T.; Kleist, E.; Andres, S.; Dal Maso, M.; Hohaus, T.; Kiendler-Scharr, A.; Rudich, Y.; Springer, M.; Tillmann, R.; Uerlings, R.; et al. Secondary aerosol formation from stress-induced biogenic emissions and possible climate feedbacks. Atmospheric Chemistry and Physics 2013, 13 (17), 8755-8770, Article. DOI: 10.5194/acp-13-8755-2013.
(182) Heiden, A.; Hoffmann, T.; Kahl, J.; Kley, D.; Klockow, D.; Langebartels, C.; Mehlhorn, H.; Sandermann, H.; Schraudner, M.; Schuh, G.; et al. Emission of volatile organic compounds from ozone-exposed plants. Ecological Applications 1999, 9 (4), 1160-1167, Article|Proceedings Paper. DOI: 10.1890/1051-0761(1999)009[1160:EOVOCF]2.0.CO;2.
(183) Li, Z.; Ratliff, E. A.; Sharkey, T. D. Effect of Temperature on Postillumination Isoprene Emission in Oak and Poplar. Plant Physiology 2010, 155 (2), 1037-1046. DOI: 10.1104/pp.110.167551 (acccessed 10/30/2022).
(184) Faiola, C.; Pullinen, I.; Buchholz, A.; Khalaj, F.; Ylisirnio, A.; Kari, E.; Miettinen, P.; Holopainen, J.; Kivimaenpaa, M.; Schobesberger, S.; et al. Secondary Organic Aerosol Formation from Healthy and Aphid-Stressed Scots Pine Emissions. Acs Earth and Space Chemistry 2019, 3 (9), 1756-1772, Article. DOI: 10.1021/acsearthspacechem.9b00118.
(185) Brown, K. R.; Thompson, W. A.; Weetman, G. F. Effects of N addition rates on the productivity ofPicea sitchensis,Thuja plicata, andTsuga heterophylla seedlings. Trees 1996, 10 (3), 189-197. DOI: 10.1007/BF02340771.
(186) Bouvier-Brown, N.; Schade, G.; Misson, L.; Lee, A.; McKay, M.; Goldstein, A. Contributions of biogenic volatile organic compounds to net ecosystem carbon flux in a ponderosa pine plantation. Atmospheric Environment 2012, 60, 527-533, Article. DOI: 10.1016/j.atmosenv.2012.06.070.
(187) Mochizuki, T.; Tani, A.; Takahashi, Y.; Saigusa, N.; Ueyama, M. Long-term measurement of terpenoid flux above a Larix kaempferi forest using a relaxed eddy accumulation method. Atmospheric Environment 2014, 83, 53-61, Article. DOI: 10.1016/j.atmosenv.2013.10.054.
(188) Tani, A.; Mochizuk, T. Review: Exchanges of volatile organic compounds between terrestrial ecosystems and the atmosphere. Journal of Agricultural Meteorology 2021, 77 (1), 66-80, Review. DOI: 10.2480/agrmet.D-20-00025.

(189) Maxwell, K.; Johnson, G. Chlorophyll fluorescence - a practical guide. Journal of Experimental Botany 2000, 51 (345), 659-668, Review. DOI: 10.1093/jexbot/51.345.659.
(190) Ibrahim, M.; Maenpaa, M.; Hassinen, V.; Kontunen-Soppela, S.; Malec, L.; Rousi, M.; Pietikainen, L.; Tervahauta, A.; Karenlampi, S.; Holopainen, J.; et al. Elevation of night-time temperature increases terpenoid emissions from Betula pendula and Populus tremula. Journal of Experimental Botany 2010, 61 (6), 1583-1595, Article. DOI: 10.1093/jxb/erq034.
(191) Neilson, R. E.; Ludlow, M. M.; Jarvis, P. G. Photosynthesis in Sitka Spruce (Picea sitchensis (Bong.) Carr.). II. Response to Temperature. 9 (3), 721-745. From JSTOR http://www.jstor.org JSTOR.
(192) van Meeningen, Y.; Schurgers, G.; Rinnan, R.; Holst, T. Isoprenoid emission response to changing light conditions of English oak, European beech and Norway spruce. Biogeosciences 2017, 14 (18), 4045-4060, Article. DOI: 10.5194/bg-14-4045-2017.
(193) Laurila, T.; Hakola, H.; Lindfors, V. Biogenic VOCs in continental Northern Europe-concentrations and Photochemistry. Physics and Chemistry of the Earth, Part B: Hydrology, Oceans and Atmosphere 1999, 24 (6), 689-693. DOI: 10.1016/S1464-1909(99)00066-0 Scopus.
(194) Faiola, C.; Jobson, B.; VanReken, T. Impacts of simulated herbivory on volatile organic compound emission profiles from coniferous plants. Biogeosciences 2015, 12 (2), 527-547, Article. DOI: 10.5194/bg-12-527-2015.
(195) Eireann, M. Historical Data. https://www.met.ie/climate/available-data/historical-data (accessed 26/03/2019).
(196) Tobin, B.; Black, K.; Osborne, B.; Reidy, B.; Bolger, T.; Nieuwenhuis, M. Assessment of allometric algorithms for estimating leaf biomass, leaf area index and litter fall in different-aged Sitka spruce forests. Forestry 2006, 79 (4), 453-465, Article. DOI: 10.1093/forestry/cpl030.
(197) Barton, C.; Jarvis, P. Growth response of branches of Picea sitchensis to four years exposure to elevated atmospheric carbon dioxide concentration. New Phytologist 1999, 144 (2), 233-243, Article. DOI: 10.1046/j.1469-8137.1999.00520.x.
(198) Meir, P.; Kruijt, B.; Broadmeadow, M.; Barbosa, E.; Kull, O.; Carswell, F.; Nobre, A.; Jarvis, P. Acclimation of photosynthetic capacity to irradiance in tree canopies in relation to leaf nitrogen concentration and leaf mass per unit area. Plant Cell and Environment 2002, 25 (3), 343-357, Article. DOI: 10.1046/j.0016-8025.2001.00811.x.
(199) Norman, J.; Jarvis, P. Photosynthesis in sitka spruce (picea-sitchensis (bong) carr) .3. measurements of canopy structure and interception of radiation. Journal of Applied Ecology 1974, 11 (1), 375-398, Article. DOI: 10.2307/2402028.
(200) Dengel, S.; Grace, J.; MacArthur, A. Transmissivity of solar radiation within a Picea sitchensis stand under various sky conditions. Biogeosciences 2015, 12 (14), 4195-4207, Article. DOI: 10.5194/bg-12-4195-2015.
(201) P. Duffy, K. B., D. Fahey, B. Hyde, A. Kehoe, J. Murphy, B. Quirke, A.M. Ryan and J. Ponzi. Ireland's Informative Inventory Report 2022. EPA website, 2022.
(202) Agency, E. E. EMEP/EEA air pollutant emission inventory guidebook 2019. Publications Office of the European Union: 2019.
(203) Portillo-Estrada, M.; Zenone, T.; Arriga, N.; Ceulemans, R. Contribution of volatile organic compound fluxes to the ecosystem carbon budget of a poplar short-

rotation plantation. Global Change Biology Bioenergy 2018, 10 (6), 405-414, Article. DOI: 10.1111/gcbb.12506.
(204) IPCC. Climate Change 2023: Synthesis Report. A Report of the Intergovernmental Panel on Climate Change. Contribution of Working Groups I, II and III to the Sixth Assessment Report of the Intergovernmental Panel on Climate Change [Core Writing Team, H. Lee and J. Romero (eds.)]. IPCC, Geneva, Switzerland, (in press). 2023.
(205) Zhao, D.; Kaminski, M.; Schlag, P.; Fuchs, H.; Acir, I.; Bohn, B.; Haseler, R.; Kiendler-Scharr, A.; Rohrer, F.; Tillmann, R.; et al. Secondary organic aerosol formation from hydroxyl radical oxidation and ozonolysis of monoterpenes. Atmospheric Chemistry and Physics 2015, 15 (2), 991-1012, Article. DOI: 10.5194/acp-15-991-2015.
(206) Peeters, J.; Nguyen, T.; Vereecken, L. HOx radical regeneration in the oxidation of isoprene. Physical chemistry chemical physics : PCCP 2009, 11, 5935-5939. DOI: 10.1039/b908511d.
(207) Atkinson, R. A structure-activity relationship for the estimation of rate constants for the gas-phase reactions of oh radicals with organic-compounds. International Journal of Chemical Kinetics 1987, 19 (9), 799-828, Article. DOI: 10.1002/kin.550190903.
(208) Kwok, E.; Atkinson, R. Estimation of hydroxyl radical reaction-rate constants for gas-phase organic-compounds using a structure-reactivity relationship - an update. Atmospheric Environment 1995, 29 (14), 1685-1695, Article. DOI: 10.1016/1352-2310(95)00069-B.
(209) Atkinson, R.; Carter, W. P. L. Kinetics and mechanisms of the gas-phase reactions of ozone with organic compounds under atmospheric conditions. Chemical Reviews 1984, 84 (5), 437-470. DOI: 10.1021/cr00063a002.
(210) Kerdouci, J.; Picquet-Varrault, B.; Doussin, J.-F. Structure–activity relationship for the gas-phase reactions of NO_3 radical with organic compounds: Update and extension to aldehydes. Atmospheric Environment 2014, 84, 363–372. DOI: 10.1016/j.atmosenv.2013.11.024.
(211) Klamt, A. Estimation of gas-phase hydroxyl radical rate constants of oxygenated compounds based on molecular orbital calculations. Chemosphere 1996, 32 (4), 717-726. DOI: https://doi.org/10.1016/0045-6535(95)00352-5.
(212) Güsten, H.; Klasinc, L.; Marić, D. Prediction of the abiotic degradability of organic compounds in the troposphere. Journal of Atmospheric Chemistry 1984, 2 (1), 83-93. DOI: 10.1007/BF00127264.
(213) Zhang, Q.; Lin, X.; Gai, Y.; Ma, Q.; Zhao, W.; Fang, B.; Long, B.; Zhang, W. Kinetic and mechanistic study on gas phase reactions of ozone with a series of cis-3-hexenyl esters. Rsc Advances 2018, 8 (8), 4230-4238, Article. DOI: 10.1039/c7ra13369c.
(214) Atkinson, R. Kinetics and mechanisms of the gas-phase reactions of the hydroxyl radical with organic-compounds under atmospheric conditions. Chemical Reviews 1986, 86 (1), 69-201, Review. DOI: 10.1021/cr00071a004.
(215) King, M. The relative-rate technique for determining rate constants. ECG Environmental Briefs: Royal Society of Chemistry—Environmental Chemistry Group, 2016; p 2.
(216) Leighton, P. A. The mechanism of aldehyde and ketone photolysis1. The Journal of Physical Chemistry 1938, 42 (6), 749-761. DOI: 10.1021/j100901a006.

(217) Zborowska, A. G.; MacInnis, C. Y.; Ye, C. Z.; Osthoff, H. D. On the photolysis branching ratio of methyl ethyl ketone. Atmospheric Environment 2021, 254, 118383. DOI: https://doi.org/10.1016/j.atmosenv.2021.118383.
(218) Jiménez, E.; Lanza, B.; Antiñolo, M.; Albaladejo, J. Photooxidation of Leaf-Wound Oxygenated Compounds, 1-Penten-3-ol, (Z)-3-Hexen-1-ol, and 1-Penten-3-one, Initiated by OH Radicals and Sunlight. Environmental Science & Technology 2009, 43 (6), 1831-1837. DOI: 10.1021/es8027814.
(219) O'Connor, M. P.; Wenger, J. C.; Mellouki, A.; Wirtz, K.; Muñoz, A. The atmospheric photolysis of E-2-hexenal, Z-3-hexenal and E,E-2,4-hexadienal. Physical Chemistry Chemical Physics 2006, 8 (44), 5236-5246. DOI: 10.1039/B611344C.
(220) Newland, M. J.; Rea, G. J.; Thüner, L. P.; Henderson, A. P.; Golding, B. T.; Rickard, A. R.; Barnes, I.; Wenger, J. Photochemistry of 2-butenedial and 4-oxo-2-pentenal under atmospheric boundary layer conditions. Physical Chemistry Chemical Physics 2019, 21 (3), 1160-1171. DOI: 10.1039/C8CP06437G.
(221) Hasson, A. S.; Tyndall, G. S.; Orlando, J. J. A Product Yield Study of the Reaction of HO2 Radicals with Ethyl Peroxy ($C_2H_5O_2$), Acetyl Peroxy ($CH_3C(O)O_2$), and Acetonyl Peroxy ($CH_3C(O)CH_2O_2$) Radicals. The Journal of Physical Chemistry A 2004, 108 (28), 5979-5989. DOI: 10.1021/jp048873t.
(222) Wennberg, P.; Bates, K.; Crounse, J.; Dodson, L.; McVay, R.; Mertens, L.; Nguyen, T.; Praske, E.; Schwantes, R.; Smarte, M.; et al. Gas-Phase Reactions of Isoprene and Its Major Oxidation Products. Chemical Reviews 2018, 118 (7), 3337-3390, Review. DOI: 10.1021/acs.chemrev.7b00439.
(223) McVay, R.; Zhang, X.; Aumont, B.; Valorso, R.; Camredon, M.; La, Y.; Wennberg, P.; Seinfeld, J. SOA formation from the photooxidation of alpha-pinene: systematic exploration of the simulation of chamber data. Atmospheric Chemistry and Physics 2016, 16 (5), 2785-2802, Article. DOI: 10.5194/acp-16-2785-2016.
(224) Mellouki, A.; Le Bras, G.; Sidebottom, H. Kinetics and mechanisms of the oxidation of oxygenated organic compounds in the gas phase. Chemical Reviews 2003, 103 (12), 5077-5096, Review. DOI: 10.1021/cr020526x.
(225) Atkinson, R. Gas-phase tropospheric chemistry of volatile organic compounds .1. Alkanes and alkenes. Journal of Physical and Chemical Reference Data 1997, 26 (2), 215-290, Review. DOI: 10.1063/1.556012.
(226) Blanco, M. B.; Barnes, I.; Wiesen, P. Kinetic Investigation of the OH Radical and Cl Atom Initiated Degradation of Unsaturated Ketones at Atmospheric Pressure and 298 K. The Journal of Physical Chemistry A 2012, 116 (24), 6033-6040. DOI: 10.1021/jp2109972.
(227) Grimsrud, E.; Westberg, H.; Rasmussen, R. Atmospheric reactivity of monoterpene hydrocarbons, NO_x photooxidation and ozonolysis. International Journal of Chemical Kinetics 1975, 1, 183-195, Article.
(228) Atkinson, R.; Aschmann, S. M. Rate constants for the reaction of OH radicals with a series of alkenes and dialkenes at 295 ± 1 K. International Journal of Chemical Kinetics 1984, 16 (10), 1175-1186. DOI: https://doi.org/10.1002/kin.550161002.
(229) Atkinson, R.; Arey, J. Atmospheric Degradation of Volatile Organic Compounds. Chemical Reviews 2003, 103 (12), 4605-4638. DOI: 10.1021/cr0206420.
(230) Blanco, M.; Teruel, M. Atmospheric photodegradation of ethyl vinyl ketone and vinyl propionate initiated by OH radicals. Chemical Physics Letters 2011, 502 (4-6), 159-162, Article. DOI: 10.1016/j.cplett.2010.12.059.

(231) Gaona-Colman, E.; Blanco, M.; Teruel, M. Kinetics and product identification of the reactions of (E)-2-hexenyl acetate and 4-methyl-3-penten-2-one with OH radicals and Cl atoms at 298 K and atmospheric pressure. Atmospheric Environment 2017, 161, 155-166, Article. DOI: 10.1016/j.atmosenv.2017.04.033.
(232) McGillen, M.; Percival, C.; Shalleross, D.; Harvey, J. Is hydrogen abstraction an important pathway in the reaction of alkenes with the OH radical? Physical Chemistry Chemical Physics 2007, 9 (31), 4349-4356, Article. DOI: 10.1039/b703035e.
(233) McQuaid, J.; Stocker, D.; Pilling, M. Kinetics of the reactions of OH with 3-methyl-2-cyclohexen-1-one and 3,5,5-trimethyl-2-cyclohexen-1-one under simulated atmospheric conditions. International Journal of Chemical Kinetics 2002, 34 (1), 7-11, Article. DOI: 10.1002/kin.10018.
(234) Atkinson, R.; Aschmann, S. M.; Carter, W. P. L.; Pitts Jr., J. N. Rate constants for the gas-phase reaction of OH radicals with a series of ketones at 299 ± 2 K. International Journal of Chemical Kinetics 1982, 14 (8), 839-847. DOI: https://doi.org/10.1002/kin.550140804.
(235) Stewart, D. J.; Almabrok, S. H.; Lockhart, J. P.; Mohamed, O. M.; Nutt, D. R.; Pfrang, C.; Marston, G. The kinetics of the gas-phase reactions of selected monoterpenes and cyclo-alkenes with ozone and the NO_3 radical. Atmospheric Environment 2013, 70, 227-235. DOI: https://doi.org/10.1016/j.atmosenv.2013.01.036.
(236) Atkinson, R.; Aschmann, S. M.; Winer, A. M.; Pitts Jr., J. N. Rate constants for the gas-phase reactions of O_3 with a series of carbonyls at 296 K. International Journal of Chemical Kinetics 1981, 13 (11), 1133-1142. DOI: https://doi.org/10.1002/kin.550131104.
(237) Grosjean, E.; Grosjean, D. Rate constants for the gas-phase reaction of ozone with unsaturated oxygenates. International Journal of Chemical Kinetics 1998, 30 (1), 21-29, Article.
(238) Jenkin, M. E.; Valorso, R.; Aumont, B.; Newland, M. J.; Rickard, A. R. Estimation of rate coefficients for the reactions of O3 with unsaturated organic compounds for use in automated mechanism construction. Atmos. Chem. Phys. 2020, 20 (21), 12921-12937. DOI: 10.5194/acp-20-12921-2020.
(239) Kerdouci, J.; Picquet-Varrault, B.; Doussin, J.-F. Prediction of Rate Constants for Gas-Phase Reactions of Nitrate Radical with Organic Compounds: A New Structure–Activity Relationship. ChemPhysChem 2010, 11 (18), 3909-3920. DOI: https://doi.org/10.1002/cphc.201000673.
(240) Atkinson, R.; Aschmann, S. M.; Pitts Jr., J. N. Rate constants for the gas-phase reactions of the OH radical with a series of monoterpenes at 294 ± 1 K. International Journal of Chemical Kinetics 1986, 18 (3), 287-299. DOI: https://doi.org/10.1002/kin.550180303.
(241) Luo, H.; Vereecken, L.; Shen, H.; Kang, S.; Pullinen, I.; Hallquist, M.; Fuchs, H.; Wahner, A.; Kiendler-Scharr, A.; Mentel, T. F.; et al. Formation of highly oxygenated organic molecules from the oxidation of limonene by OH radical: significant contribution of H-abstraction pathway. Atmos. Chem. Phys. Discuss. 2022, 2022, 1-23. DOI: 10.5194/acp-2022-803.
(242) Eddingsaas, N.; Loza, C.; Yee, L.; Seinfeld, J.; Wennberg, P. alpha-pinene photooxidation under controlled chemical conditions - Part 1: Gas-phase

composition in low- and high-NO_x environments. Atmospheric Chemistry and Physics 2012, 12 (14), 6489-6504, Article. DOI: 10.5194/acp-12-6489-2012.
(243) Tan, Z.; Hantschke, L.; Kaminski, M.; Acir, I.; Bohn, B.; Cho, C.; Dorn, H.; Li, X.; Novelli, A.; Nehr, S.; et al. Atmospheric photo-oxidation of myrcene: OH reaction rate constant, gas-phase oxidation products and radical budgets. Atmospheric Chemistry and Physics 2021, 21 (20), 16067-16091, Article. DOI: 10.5194/acp-21-16067-2021.
(244) Bianchi, F.; Kurten, T.; Riva, M.; Mohr, C.; Rissanen, M.; Roldin, P.; Berndt, T.; Crounse, J.; Wennberg, P.; Mentel, T.; et al. Highly Oxygenated Organic Molecules (HOM) from Gas-Phase Autoxidation Involving Peroxy Radicals: A Key Contributor to Atmospheric Aerosol. Chemical Reviews 2019, 119 (6), 3472-3509, Review. DOI: 10.1021/acs.chemrev.8b00395.
(245) Kroll, J.; Donahue, N.; Jimenez, J.; Kessler, S.; Canagaratna, M.; Wilson, K.; Altieri, K.; Mazzoleni, L.; Wozniak, A.; Bluhm, H.; et al. Carbon oxidation state as a metric for describing the chemistry of atmospheric organic aerosol. Nature Chemistry 2011, 3 (2), 133-139, Article. DOI: 10.1038/nchem.948|10.1038/NCHEM.948.
(246) Banco, M.; Barnes, I.; Wiesen, P. Kinetic Investigation of the OH Radical and Cl Atom Initiated Degradation of Unsaturated Ketones at Atmospheric Pressure and 298 K. Journal of Physical Chemistry a 2012, 116 (24), 6033-6040, Article. DOI: 10.1021/jp2109972.
(247) Vereecken, L.; Nozière, B. H migration in peroxy radicals under atmospheric conditions. Atmos. Chem. Phys. 2020, 20 (12), 7429-7458. DOI: 10.5194/acp-20-7429-2020.
(248) Khanniche, S.; Green, W. H. Reaction pathways, thermodynamics, and kinetics of cyclopentanone oxidation intermediates: A theoretical approach. The Journal of Physical Chemistry A 2019, 123 (45), 9644-9657. DOI: 10.1021/acs.jpca.9b05806.
(249) Jørgensen, S.; Knap, H. C.; Otkjær, R. V.; Jensen, A. M.; Kjeldsen, M. L. H.; Wennberg, P. O.; Kjaergaard, H. G. Rapid hydrogen shift scrambling in hydroperoxy-substituted organic peroxy radicals. The Journal of Physical Chemistry A 2016, 120 (2), 266-275. DOI: 10.1021/acs.jpca.5b06768.
(250) Rio, C.; Flaud, P.-M.; Loison, J.-C.; Villenave, E. Experimental Revaluation of the Importance of the Abstraction Channel in the Reactions of Monoterpenes with OH Radicals. ChemPhysChem 2010, 11 (18), 3962-3970. DOI: https://doi.org/10.1002/cphc.201000518.
(251) Shen, H.; Vereecken, L.; Kang, S.; Pullinen, I.; Fuchs, H.; Zhao, D.; Mentel, T. F. Unexpected significance of a minor reaction pathway in daytime formation of biogenic highly oxygenated organic compounds. Science Advances 2022, 8 (42), eabp8702. DOI: doi:10.1126/sciadv.abp8702.
(252) Praske, E.; Otkjær, R. V.; Crounse, J. D.; Hethcox, J. C.; Stoltz, B. M.; Kjaergaard, H. G.; Wennberg, P. O. Intramolecular hydrogen shift chemistry of hydroperoxy-substituted peroxy radicals. The Journal of Physical Chemistry A 2019, 123 (2), 590-600. DOI: 10.1021/acs.jpca.8b09745.
(253) Vereecken, L.; Peeters, J. Nontraditional (per)oxy ring-closure paths in the atmospheric oxidation of isoprene and monoterpenes. The Journal of Physical Chemistry A 2004, 108 (24), 5197-5204. DOI: 10.1021/jp049219g.
(254) Vereecken, L.; Vu, G.; Wahner, A.; Kiendler-Scharr, A.; Nguyen, H. M. T. A structure activity relationship for ring closure reactions in unsaturated alkylperoxy

radicals. Physical Chemistry Chemical Physics 2021, 23 (31), 16564-16576. DOI: 10.1039/D1CP02758A.
(255) Staffelbach, T. A.; Orlando, J. J.; Tyndall, G. S.; Calvert, J. G. The UV-visible absorption spectrum and photolysis quantum yields of methylglyoxal. Journal of Geophysical Research: Atmospheres 1995, 100 (D7), 14189-14198. DOI: https://doi.org/10.1029/95JD00541.
(256) Kyle, E.; Orchard, S. W. The photolysis of methyl glyoxal vapour at 436 nm. Journal of Photochemistry 1977, 7 (5), 305-317. DOI: https://doi.org/10.1016/0047-2670(77)80012-9.
(257) Tadić, J.; Moortgat, G. K.; Wirtz, K. Photolysis of glyoxal in air. Journal of Photochemistry and Photobiology A: Chemistry 2006, 177 (2), 116-124. DOI: https://doi.org/10.1016/j.jphotochem.2005.10.010.
(258) Raber, W. H.; Moortgat, G. K. Photooxidation of selected carbonyl compounds in air: methyl ethyl ketone, methyl vinyl ketone, methacrolein and methylglyoxal. In Progress and Problems in Atmospheric Chemistry, pp 318-373.
(259) Bonn, B.; Moortgat, G. New particle formation during alpha- and beta-pinene oxidation by O_3, OH and NO_3, and the influence of water vapour: particle size distribution studies. Atmospheric Chemistry and Physics 2002, 2, 183-196, Article. DOI: 10.5194/acp-2-183-2002.
(260) Kammer, J.; Perraudin, E.; Flaud, P. M.; Lamaud, E.; Bonnefond, J. M.; Villenave, E. Observation of nighttime new particle formation over the French Landes forest. Science of The Total Environment 2018, 621, 1084-1092. DOI: https://doi.org/10.1016/j.scitotenv.2017.10.118.
(261) Sindelarova, K.; Markova, J.; Simpson, D.; Huszar, P.; Karlicky, J.; Darras, S.; Granier, C. High resolution biogenic global emission inventory for the time period 2000-2019 for air quality modelling. Earth System Science Data 2022, 14 (1). DOI: https://doi.org/10.5194/essd-14-251-2022.
(262) Peñuelas, J.; Staudt, M. BVOCs and global change. Trends in Plant Science 2010, 15 (3), 133-144. DOI: https://doi.org/10.1016/j.tplants.2009.12.005.
(263) Lohmann, U.; Feichter, J. Global indirect aerosol effects: a review. Atmos. Chem. Phys. 2005, 5 (3), 715-737. DOI: 10.5194/acp-5-715-2005.
(264) Orlando, J.; Noziere, B.; Tyndall, G.; Orzechowska, G.; Paulson, S.; Rudich, Y. Product studies of the OH- and ozone-initiated oxidation of some monoterpenes. Journal of Geophysical Research-Atmospheres 2000, 105 (D9), 11561-11572, Article. DOI: 10.1029/2000JD900005.
(265) Jaoui, M.; Kleindienst, T.; Docherty, K.; Lewandowski, M.; Offenberg, J. Secondary organic aerosol formation from the oxidation of a series of sesquiterpenes: alpha-cedrene, beta-caryophyllene, alpha-humulene and alpha-farnesene with O_3, OH and NO_3 radicals. Environmental Chemistry 2013, 10 (3), 178-193, Article. DOI: 10.1071/EN13025.
(266) D'Ambro, E. L.; Møller, K. H.; Lopez-Hilfiker, F. D.; Schobesberger, S.; Liu, J.; Shilling, J. E.; Lee, B. H.; Kjaergaard, H. G.; Thornton, J. A. Isomerization of Second-Generation Isoprene Peroxy Radicals: Epoxide Formation and Implications for Secondary Organic Aerosol Yields. Environmental Science & Technology 2017, 51 (9), 4978-4987. DOI: 10.1021/acs.est.7b00460.
(267) Wang, Y.; Zhao, Y.; Li, Z.; Li, C.; Yan, N.; Xiao, H. Importance of Hydroxyl Radical Chemistry in Isoprene Suppression of Particle Formation from α-Pinene Ozonolysis.

ACS Earth and Space Chemistry 2021, 5 (3), 487-499. DOI: 10.1021/acsearthspacechem.0c00294.
(268) Hakola, H.; Arey, J.; Aschmann, S. M.; Atkinson, R. Product formation from the gas-phase reactions of OH radicals and O_3 with a series of monoterpenes. Journal of Atmospheric Chemistry 1994, 18 (1), 75-102. DOI: 10.1007/BF00694375.
(269) McFiggans, G.; Mentel, T.; Wildt, J.; Pullinen, I.; Kang, S.; Kleist, E.; Schmitt, S.; Springer, M.; Tillmann, R.; Wu, C.; et al. Secondary organic aerosol reduced by mixture of atmospheric vapours. Nature 2019, 565 (7741), 587-593, Article. DOI: 10.1038/s41586-018-0871-y.
(270) Kourtchev, I.; Giorio, C.; Manninen, A.; Wilson, E.; Mahon, B.; Aalto, J.; Kajos, M.; Venables, D.; Ruuskanen, T.; Levula, J.; et al. Enhanced Volatile Organic Compounds emissions and organic aerosol mass increase the oligomer content of atmospheric aerosols. Scientific Reports 2016, 6 (1), 35038. DOI: 10.1038/srep35038.
(271) Hakola, H.; Tarvainen, V.; Praplan, A.; Jaars, K.; Hemmila, M.; Kulmala, M.; Back, J.; Hellen, H. Terpenoid and carbonyl emissions from Norway spruce in Finland during the growing season. Atmospheric Chemistry and Physics 2017, 17 (5), 3357-3370, Article. DOI: 10.5194/acp-17-3357-2017.
(272) Kiendler-Scharr, A.; Zhang, Q.; Hohaus, T.; Kleist, E.; Mensah, A.; Mentel, T.; Spindler, C.; Uerlings, R.; Tillmann, R.; Wildt, J. Aerosol Mass Spectrometric Features of Biogenic SOA: Observations from a Plant Chamber and in Rural Atmospheric Environments. Environmental Science & Technology 2009, 43 (21), 8166-8172, Article. DOI: 10.1021/es901420b.
(273) Heiden, A.; Kobel, K.; Langebartels, C.; Schuh-Thomas, G.; Wildt, J. Emissions of oxygenated volatile organic compounds from plants - part I: Emissions from lipoxygenase activity. Journal of Atmospheric Chemistry 2003, 45 (2), 143-172, Article. DOI: 10.1023/A:1024069605420.
(274) Bilde, M.; Barsanti, K.; Booth, M.; Cappa, C. D.; Donahue, N. M.; Emanuelsson, E. U.; McFiggans, G.; Krieger, U. K.; Marcolli, C.; Topping, D.; et al. Saturation vapor pressures and transition enthalpies of low-volatility organic molecules of atmospheric relevance: from dicarboxylic acids to complex mixtures. Chemical Reviews 2015, 115 (10), 4115-4156. DOI: 10.1021/cr5005502.
(275) D'Ambro, E.; Schobesberger, S.; Zaveri, R.; Shilling, J.; Lee, B.; Lopez-Hilfiker, F.; Mohr, C.; Thornton, J. Isothermal evaporation of alpha-pinene ozonolysis SOA: Volatility, phase state, and oligomeric composition. Acs Earth and Space Chemistry 2018, 2 (10), 1058-1067, Article. DOI: 10.1021/acsearthspacechem.8b00084.
(276) Bannan, T. J.; Le Breton, M.; Priestley, M.; Worrall, S. D.; Bacak, A.; Marsden, N. A.; Mehra, A.; Hammes, J.; Hallquist, M.; Alfarra, M. R.; et al. A method for extracting calibrated volatility information from the FIGAERO-HR-ToF-CIMS and its experimental application. Atmos. Meas. Tech. 2019, 12 (3), 1429-1439. DOI: 10.5194/amt-12-1429-2019.
(277) Donahue, N.; Epstein, S.; Pandis, S.; Robinson, A. A two-dimensional volatility basis set: 1. organic-aerosol mixing thermodynamics. Atmospheric Chemistry and Physics 2011, 11 (7), 3303-3318, Article. DOI: 10.5194/acp-11-3303-2011.
(278) Wyche, K.; Ryan, A.; Hewitt, C.; Alfarra, M.; McFiggans, G.; Carr, T.; Monks, P.; Smallbone, K.; Capes, G.; Hamilton, J.; et al. Emissions of biogenic volatile organic compounds and subsequent photochemical production of secondary organic aerosol

in mesocosm studies of temperate and tropical plant species. Atmospheric Chemistry and Physics 2014, 14 (23), 12781-12801, Article. DOI: 10.5194/acp-14-12781-2014.
(279) Pang, J. Y. S.; Novelli, A.; Kaminski, M.; Acir, I. H.; Bohn, B.; Carlsson, P. T. M.; Cho, C.; Dorn, H. P.; Hofzumahaus, A.; Li, X.; et al. Investigation of the limonene photooxidation by OH at different NO concentrations in the atmospheric simulation chamber SAPHIR (Simulation of Atmospheric PHotochemistry In a large Reaction Chamber). Atmos. Chem. Phys. 2022, 22 (13), 8497-8527. DOI: 10.5194/acp-22-8497-2022.
(280) He, Q.; Bluvshtein, N.; Segev, L.; Meidan, D.; Flores, M.; Brown, S.; Brune, W.; Rudich, Y. Evolution of the Complex Refractive Index of Secondary Organic Aerosols during Atmospheric Aging. Environmental Science & Technology 2018, 52. DOI: 10.1021/acs.est.7b05742.
(281) Voliotis, A.; Wang, Y.; Shao, Y.; Du, M.; Bannan, T. J.; Percival, C. J.; Pandis, S. N.; Alfarra, M. R.; McFiggans, G. Exploring the composition and volatility of secondary organic aerosols in mixed anthropogenic and biogenic precursor systems. Atmos. Chem. Phys. 2021, 21 (18), 14251-14273. DOI: 10.5194/acp-21-14251-2021.
(282) Gkatzelis, G.; Hohaus, T.; Tillmann, R.; Gensch, I.; Muller, M.; Eichler, P.; Xu, K.; Schlag, P.; Schmitt, S.; Yu, Z.; et al. Gas-to-particle partitioning of major biogenic oxidation products: a study on freshly formed and aged biogenic SOA. Atmospheric Chemistry and Physics 2018, 18 (17), 12969-12989, Article. DOI: 10.5194/acp-18-12969-2018.
(283) Huang, W.; Li, H.; Sarnela, N.; Heikkinen, L.; Tham, Y. J.; Mikkilä, J.; Thomas, S. J.; Donahue, N. M.; Kulmala, M.; Bianchi, F. Measurement report: Molecular composition and volatility of gaseous organic compounds in a boreal forest – from volatile organic compounds to highly oxygenated organic molecules. Atmos. Chem. Phys. 2021, 21 (11), 8961-8977. DOI: 10.5194/acp-21-8961-2021.
(284) Murphy, B. N.; Donahue, N. M.; Robinson, A. L.; Pandis, S. N. A naming convention for atmospheric organic aerosol. Atmos. Chem. Phys. 2014, 14 (11), 5825-5839. DOI: 10.5194/acp-14-5825-2014.
(285) Donahue, N.; Kroll, J.; Pandis, S.; Robinson, A. A two-dimensional volatility basis set - Part 2: Diagnostics of organic-aerosol evolution. Atmospheric Chemistry and Physics 2012, 12 (2), 615-634, Article. DOI: 10.5194/acp-12-615-2012.
(286) Schervish, M.; Donahue, N. M. Peroxy radical chemistry and the volatility basis set. Atmos. Chem. Phys. 2020, 20 (2), 1183-1199. DOI: 10.5194/acp-20-1183-2020.
(287) Eddingsaas, N.; Loza, C.; Yee, L.; Chan, M.; Schilling, K.; Chhabra, P.; Seinfeld, J.; Wennberg, P. alpha-pinene photooxidation under controlled chemical conditions - Part 2: SOA yield and composition in low- and high-NOx environments. Atmospheric Chemistry and Physics 2012, 12 (16), 7413-7427, Article. DOI: 10.5194/acp-12-7413-2012.
(288) Lee, A.; Goldstein, A. H.; Kroll, J. H.; Ng, N. L.; Varutbangkul, V.; Flagan, R. C.; Seinfeld, J. H. Gas-phase products and secondary aerosol yields from the photooxidation of 16 different terpenes. Journal of Geophysical Research: Atmospheres 2006, 111 (D17). DOI: https://doi.org/10.1029/2006JD007050.
(289) Vaghjiani, G. L.; Turnipseed, A. A.; Warren, R. F.; Ravishankara, A. R. Photodissociation of H2O2 at 193 and 222 nm: Products and quantum yields. The Journal of Chemical Physics 1992, 96 (8), 5878-5886. DOI: 10.1063/1.462684 (acccessed 10/19/2023).

(290) Li, Y.; Pöschl, U.; Shiraiwa, M. Molecular corridors and parameterizations of volatility in the chemical evolution of organic aerosols. Atmos. Chem. Phys. 2016, 16 (5), 3327-3344. DOI: 10.5194/acp-16-3327-2016.
(291) Reissell, A.; Aschmann, S.; Atkinson, R.; Arey, J. Products of the OH radical- and O-3-initiated reactions of myrcene and ocimene. Journal of Geophysical Research-Atmospheres 2002, 107 (D12), Article. DOI: 10.1029/2001JD001234.
(292) Kjaergaard, H. G.; Knap, H. C.; Ørnsø, K. B.; Jørgensen, S.; Crounse, J. D.; Paulot, F.; Wennberg, P. O. Atmospheric Fate of Methacrolein. 2. Formation of Lactone and Implications for Organic Aerosol Production. The Journal of Physical Chemistry A 2012, 116 (24), 5763-5768. DOI: 10.1021/jp210853h.
(293) Riva, M.; Budisulistiorini, S.; Chen, Y.; Zhang, Z.; D'Ambro, E.; Zhang, X.; Gold, A.; Turpin, B.; Thornton, J.; Canagaratna, M.; et al. Chemical characterization of secondary organic aerosol from oxidation of isoprene hydroxyhydroperoxides. Environmental Science & Technology 2016, 50 (18), 9889-9899, Article. DOI: 10.1021/acs.est.6b02511.
(294) Ng, N.; Kroll, J.; Keywood, M.; Bahreini, R.; Varutbangkul, V.; Flagan, R.; Seinfeld, J.; Lee, A.; Goldstein, A. Contribution of first- versus second-generation products to secondary organic aerosols formed in the oxidation of biogenic hydrocarbons. Environmental Science & Technology 2006, 40 (7), 2283-2297, Article. DOI: 10.1021/es052269u.
(295) Griffin, R. J.; Cocker Iii, D. R.; Flagan, R. C.; Seinfeld, J. H. Organic aerosol formation from the oxidation of biogenic hydrocarbons. Journal of Geophysical Research Atmospheres 1999, 104 (D3), 3555-3567. DOI: 10.1029/1998JD100049 Scopus C7 - 1998JD100049.
(296) Hao, L.; Romakkaniemi, S.; Yli-Pirila, P.; Joutsensaari, J.; Kortelainen, A.; Kroll, J.; Miettinen, P.; Vaattovaara, P.; Tiitta, P.; Jaatinen, A.; et al. Mass yields of secondary organic aerosols from the oxidation of alpha-pinene and real plant emissions. Atmospheric Chemistry and Physics 2011, 11 (4), 1367-1378, Article. DOI: 10.5194/acp-11-1367-2011.